N° Ordre...../FT/UMBB/2024

PEOPLE'S DEMOCRATIC REPUBLIC OF ALGERIA

MINISTRY OF HIGHER EDUCATION AND SCIENTIFIC RESEARCH

UNIVERSITY M'HAMED BOUGARA OF BOUMERDES

Faculty of Technology

Doctoral Thesis

Presented by:

Ms. Amina NOUAL

Submitted for the Fulfilment of the Requirements of the **DOCTORAT-LMD** degree in

Field: Telecommunications

Specialty: Telecommunications Systems

Study of Electrical and Radio Frequency Properties of Structures (IIIA-N) for Filter Applications for GNSS Receivers

In front of a jury composed of

Pr. Yassine	MERAIHI	Professor	Univ. Boumerdes	President
Dr. Zitouni	MESSAI	MCA	Univ. Borj Bou Arreridj	Supervisor
Dr. Noureddine	MESSAOUDI	Professor	Univ. Boumerdes	Examiner
Dr. Samia	BELKACEM	MCA	Univ. Boumerdes	Examiner
Dr. Mustapha	FLISSI	MCA	Univ. Borj Bou Arreridj	Examiner

Academic Year: 2023/2024

Acknowledgment

First and foremost, I would like to thank Allah for granting me the health and patience to complete this research. This thesis is the result of a long journey of study, from primary school to postgraduate studies, and I am grateful to the many teachers and professors who have guided me to reach this point.

I would like to express my deepest gratitude to my thesis advisor, Dr Zitouni MESSAI, for his guidance, support, and encouragement throughout the entire process of this thesis. The direction and outcomes of my research have been greatly influenced by his invaluable insights and expertise.

I would like to thank Dr. Zineeddine TOUATI, Dr. Abderrahim YOUSFI, and Dr. Okba SAIDANI for their unwavering support, guidance, ideas, and suggestions during this PhD experience. Their contributions have greatly enhanced the quality of my thesis.

I would also like to extend my sincere thanks to Pr. Dalila Acheli and Pr. Yassine MERAIHI, who directed the doctoral formation, for all the support they provided.

I express my gratitude to the thesis committee members, Pr. Yassine MERAIHI, Dr. Samia BELKACEM, Pr. Noureddine MESSAOUDI, and Dr. Mustapha FLISSI, for their interest in this work and for agreeing to examine it. Their contribution has significantly improved the quality of my thesis.

Also, throughout my Ph.D. career, my parents, “Nacer” and “Souhila”, have supported and encouraged me to carry out my work and achieve my dreams. Their unconditional love and encouragement have been a constant source of motivation and inspiration for me. I would also like to express my deepest thanks to my husband “Hichem RIAL” and my dear son “Yasser” for being by my side throughout this crucial period of our life. I could not have completed this study without their unwavering love, patience, tolerance, and support.

After several years of research, I would like to thank all those who have contributed in any way to the success of this work from far or near. There are many names to mention. I will limit myself to those who made a positive impression on me and gave me moral and psychological support, in particular:

- My grandmother “Baya”, my siblings “Mohamed”, “Meriem”, “Ahlem”, and “Ikrem”, and my niece “Rihem”.
- My family-in-law, exceptionally my mother-in-law “Yamina”, my father-in-law “Ali”, “Imene”, “Amira” and “Yasmine”.
- My aunts and uncles. - My friends Nor El-houda and Selma.

I dedicate this thesis to my Parents, my Husband, and my dear Son.

Abstract

Satellite positioning and navigation systems (GNSS) are among the fastest-growing technologies of the 21st century. They face new challenges such as improving receiver sensitivity, acquiring precise positions, reducing production costs, and lowering energy consumption. To meet these challenges, current research is focusing on the use of high-quality high-frequency devices. Unfortunately, interference in GNSS receivers can arise either from the mixing of spurious harmonics from adjacent transmitters or from intentional interference. Consequently, in most GNSS receivers, the application of filtering is essential and must be applied to the RF input. The study in question is based on the design of an RF filtering block for the GNSS receiver, consisting of two bandpass filters (BPFs) and a low-noise amplifier (LNA). The basic element of the low-noise amplifier is the transistor, which largely determines the performance of the final block. To meet current and future challenges, a substitute for the silicon-based transistor is being considered. To date, transistors based on compounds in class IIIA-N of the Mendeleyev table have been presented as the most promising for radio frequency applications, thanks to their exceptional physical and electrical characteristics. Different AlGaN/GaN MOSHEMT (Metal-Oxide-Semiconductor High Electron Mobility Transistor) structures were investigated in this thesis using the TCAD SILVACO software, and finally, the AlGaN/AlInGaN/GaN MOSHEMT on 4H-SiC substrate was chosen for implementation in the single-stage LNA circuit. To this end, we are interested in the design of two filtering block (BPF + LNA + BPF), which operate in the two spectral bands used by the GNSS system: [1190 MHz -1300 MHz] and [1550 MHz -1610 MHz] using the ADS simulator. The first frequency band corresponds to the L2-GPS and L2-GLONASS signals. The second corresponds to the L1-GPS, B1-COMPASS and E1-GALILEO signals.

Keywords: IIIA-Nitride semiconductor, MOSHEMT transistor, RF filtering block, LNA, BPF, GNSS receiver, SILVACO, ADS.

Résumé

Les systèmes de navigation et de positionnement par satellite (GNSS) font partie des technologies qui connaissent la croissance la plus rapide au 21ème siècle. Ils sont confrontés à des nouveaux défis tels que l'amélioration de la sensibilité des récepteurs, l'acquisition des positions précises, la réduction des coûts de production et la diminution de la consommation d'énergie. Pour relever ces défis, la recherche actuelle se concentre sur l'utilisation de dispositifs haute fréquence de haute qualité. Malheureusement, les interférences dans les récepteurs GNSS peuvent provenir soit du mélange d'harmoniques parasites provenant d'émetteurs adjacents, soit d'interférences intentionnelles. Par conséquent, dans la plupart des récepteurs GNSS, l'application d'un filtrage est essentielle et doit être appliquée à l'entrée RF. L'étude en question est basée sur la conception d'un bloc de filtrage RF pour le récepteur GNSS, composé de deux filtres passe-bande (FPB) et d'un amplificateur à faible bruit (LNA). L'élément de base de l'amplificateur à faible bruit est le transistor, qui détermine largement les performances du bloc final. Pour relever les défis actuels et futurs, on envisage de remplacer le transistor à base de silicium. À ce jour, les transistors basés sur des composés de la classe IIIA-N du tableau de Mendeleïev ont été présentés comme les plus prometteurs pour les applications radiofréquences, grâce à leurs caractéristiques physiques et électriques exceptionnelles. Différentes structures AlGaN/GaN MOSHEMT (Transistor à métal-oxyde-semi-conducteur à haute mobilité d'électron) ont été étudiées dans cette thèse à l'aide du logiciel TCAD SILVACO, et finalement, le MOSHEMT AlGaN/AlInGaN/GaN sur substrat 4H-SiC a été choisi pour l'implémentation dans le circuit LNA à un seul étage. À cette fin, nous nous intéressons à la conception de deux systèmes de filtrage (FPB + LNA + FPB), qui fonctionnent dans les deux bandes spectrales utilisées par le système GNSS : [1190 MHz -1300 MHz] et [1550 MHz -1610 MHz] en utilisant le simulateur ADS. La première bande correspond aux bandes de fréquences L2-GPS et L2-GLONASS. La seconde correspond aux bandes L1-GPS, B1-COMPASS et E1-GALILEO.

Mots clés : Semi-conducteur IIIA-N, transistor MOSHEMT, bloc de filtrage, LNA, FPB, récepteur GNSS, SILVACO, ADS.

ملخص

تعد أنظمة تحديد المواقع والملاحة عبر الأقمار الصناعية (GNSS) من بين أسرع التقنيات نموًا في القرن الحادي والعشرين. حيث تواجه تحديات جديدة مثل تحسين حساسية جهاز الاستقبال والحصول على مواقع دقيقة وتقليل تكاليف الإنتاج وخفض استهلاك الطاقة. ولمواجهة هذه التحديات، تركز الأبحاث الحالية على استخدام أجهزة عالية الجودة وعالية التردد. ولسوء الحظ، يمكن أن ينشأ التداخل في مستقبلات GNSS إما عن خلط التوافقيات الهامشية من أجهزة الإرسال المجاورة أو عن التداخل المتعمد. وبالتالي، في معظم أجهزة استقبال GNSS، يعد تطبيق الترشيح ضروريًا ويجب تطبيقه على مدخل التردد اللاسلكي. تعتمد الدراسة المعنية على تصميم وحدة ترشيح التردد الراديوي لمستقبل GNSS، والتي تتألف من مرشحي تمرير النطاق (BPFs) ومضخم منخفض الضوضاء (LNA). العنصر الأساسي لمضخم منخفض الضوضاء هو الترانزستور، الذي يحدد إلى حد كبير أداء الوحدة النهائية. ولمواجهة التحديات الحالية والمستقبلية، يجري النظر في بديل للترانزستور القائم على السيليكون. حتى الآن، تم تقديم الترانزستورات المعتمدة على مركبات من الفئة N-IIIA من جدول مندلييف باعتبارها الترانزستورات الواعدة لتطبيقات الترددات الراديوية، وذلك بفضل خصائصها الفيزيائية والكهربائية الاستثنائية. تم دراسة هياكل AlGaN/GaN MOSHEMT (ترانزستور التنقل الإلكتروني العالي لأكسيد المعادن وأشباه الموصلات) مختلفة في هذه الأطروحة باستخدام برنامج TCAD SILVACO، وأخيرًا، تم اختيار AlGaN /AlInGaN/GaN MOSHEMTعلى الركيزة 4H-SiC من أجل تنفيذها في دائرة مضخم منخفض الضوضاء. ولتحقيق هذه الغاية، نهتم بتصميم نظامي وحدة مرشح (BPF + LNA + BPF)، يعملان في نطاقي التردد اللذين يستخدمهما نظام GNSS : [1190 MHz -1300 MHz] و [1550 MHz -1610 MHz] باستخدام جهاز المحاكاة ADS. الأول يتوافق مع نطاقات التردد L2-GLONASS و L2-GPS والثاني يتوافق مع نطاقي L1-GPS وB1-COMPASS وE1-GALILEO.

.

الكلمات المفتاحية: أشباه الموصلات N-IIIA، ترانزستورMOSHEMT، وحدة مرشح الترددات اللاسلكية، LNA، BPF، مستقبل GNSS، SILVACO، ADS.

Acronyms

2DEG Two-dimensional electron gas

a Lattice matching

AC Alternating current

ADC Analog/digital converter

ADS Advanced design system

Ag Gate area

Al Aluminum

Al_2O_3 Aluminum oxide

AlGaAs Aluminum gallium arsenide alloy

AlGaN Aluminum gallium nitride alloy

AlN Aluminum nitride

AlInGaN Aluminum indium gallium nitride alloy

Au Gold

b_1, b_2 Progressive waves of reflected power in port 1 and 2

BFOM Baliga's Figure of Merit

BPF Bandpass filter

BW Bandwidth

c Height of a one-unit hexagonal cell

C_{13}, **C_{33}** Elastic constants

C_{GS}, C_{GD}, C_{DS} Intrinsic gate-source, gate-drain, and drain-source capacitances

C_G Gate capacitance

C_{PG}, C_{PD} Extrinsic parasitic gate and parasitic drain capacitances

DC Direct current

DD Drift-Diffusion

D-mode Depletion mode

e_{31}, **e_{33}** Piezoelectric constants

E Electric field

E_{BR} Critical breakdown field

E_c Conduction band energy

E_F Fermi energy

E_g Gap band energy

E-mode Enhancement mode

eV Electron volte

E_V Valence band energy

Fc Center frequency

FET Field effect transistor

f_{max} Maximum oscillation frequency

f_t Cut-off frequency

Ga Gallium

GaAs Gallium arsenide

GaN Gallium nitride

Ga_2O_3 Gallium oxide

Gd Drain conductance

GHz Gigahertz

GLONASS Global navigation satellite system

G_m Transconductance

GNSS Global navigation satellite system

GPa Giga pascal

GPS Global positioning system

H_{21} Current gain

HEMT High electron mobility transistor

HFET Heterojunction field effect transistor

HfO_2 Hafnium oxide

I_D Drain current

IF Intermediate frequency

In Indium

InAlAs Indium aluminum arsenide

InGaAs Indium gallium arsenide

InN Indium nitride

InP Indium phosphor

IP1dB Compression point at 1dB

IRNSS Indian regional navigation satellite system

JFoM Johnson's figure of merit

k Dielectric constant

K Stability factor

Lg Gate length

L_G, L_S, L_D Gate, source, and drain parasitic inductance

L_{GS}, L_{GD}, L_{SD} Gate-source, Gate-drain, and source-drain length

LNA Low noise amplifier

LO Local oscillator

MBE Molecular beam epitaxy

MESFET Metal semiconductor field effect transistor

MMIC Mono monolithic microwave integrated circuit

MOCVD Metal organic chemical vapor deposition

MODFET Modulation doped field effect transistor

MOSHEMT Metal oxide semiconductor high electron mobility transistor

MOSFET Metal oxide semiconductor field effect transistor

MOVPE Metal organic vapor phase epitaxy

NF Noise figure

NH3 Ammonia

Ni Nickel

P_{in} Input power

P_{out} Output power

P_{PZ} Piezoelectric polarization

Psp Spontaneous Polarization

Pt Platinum

q Elementary charge

R_c Ohmic contact resistance

R_{ch} Channel resistance under the gate

RF Radio frequency

Ri Channel resistance

R_g, R_s, R_d Gate, source, and drain resistances

R_{GS}, R_{GD}, R_{DS} Intrinsic gate-source, gate-drain, and drain-source resistances

R_{ON} Access resistance

S_{11}, S_{12} Input and output reflection coefficients

S_{21}, S_{22}Direct and reverse transmission coefficients

S Simens

SAW Surface acoustic wave

SBF Stop band filter

Si Silicon

SiC silicon carbide

SiGe Silicon-germanium

SILVACO Silicon valley corporation

SiO_2 Silicon dioxide

Si_3N_4 Silicon nitride

SNR Signal-to-noise ratio

SRH Shockley-read hall

TCAD Technology computer aided design

THz Terahertz

Ti Titanium

TiO_2 Titanium dioxide

u Distance between nitrogen and IIIA-atoms

U_g Unilateral power gain

V_{BR} Breakdown voltage

V_{DS} Drain source voltage

V_{GS} Gate source voltage

V_{Knee} Knee voltage

V_p Pinch-off voltage

V_{sat} Saturation velocity

V_{TH} Threshold voltage

Wg Gate width

Y Admittance

Z Impedance

Z_S Source impedance

Z_L Load impedance

α, β(K) Varshni coefficients

ε_{bar}, χ Permittivity and affinity

τ Time delay

Φ_b Schottky barrier hight

Δχ Electronegativity

κ Thermal conductivity

μ_n Electron mobility

η Basal strain

Contents

List of figures

List of tables

General Introduction

General introduction

The last century has witnessed impressive evolution in the fields of science and technology, including mobile networks, aeronautics, space applications, and satellite positioning systems. In recent years, GNSS systems have attracted worldwide attention and have been widely applied in many strategic areas. They are used to determine the position of a receiver on earth using a constellation of multiple satellites. The list of GNSS systems includes more than one satellite system: the American Global Positioning System (GPS), the European Galileo system, the Russian Global Navigation system (GLONASS), the Chinese COMPASS system, and the Indian Regional Navigation Satellite System (IRNSS) [1].

GNSS receivers must detect and amplify the power of incoming RF signals without adding excessive noise that interferes with the utile signals. For GNSS signals, it is intended to cover the allocated frequency band (approximately 1.1-1.6 GHz). Therefore, to ensure frequency selectivity by passing through the main spectral components while attenuating the others, an RF filtering block is placed directly after the receiver antenna, containing bandpass filters (BPF) and a low-noise amplifier (LNA) [2].

Precise GNSS receivers require bandpass filters with narrow bandwidths and appropriate operating frequencies. Furthermore, LNA is the basic active functional block of GNSS receivers. Its performance is closely linked to the transistors that make it up. For practical reasons, an LNA must possess the following characteristics: low noise, sufficient gain, good linearity, unconditional stability, and minimal power consumption.

The basic element of this LNA is the transistor. Various design and implementation approaches have been adopted depending on the type of application. Heterojunction field-effect transistors of the HEMT (High Electron Mobility Transistors) type based on IIIA-N semiconductor materials have shown interesting and remarkable performance for radio frequency applications [3]. Improving the electrical performance of IIIA-N-based HEMT transistors is still the subject of major research efforts, with the incorporation of new materials and the adoption of new structures.

Unfortunately, the leakage currents of conventional AlGaN/GaN HEMTs are relatively high. Significant progress has been made to improve device characteristics. The metal-oxide-semiconductor HEMT structure (MOSHEMT) has been developed by introducing various oxide materials such as SiO_2, Al_2O_3, HfO_2, TiO_2, and Ga_2O_3 to reduce leakage current [4].

In this context, the aim of our thesis is to design an RF filtering block based on GaN MOSHEMT transistor for GNSS receiver, providing the following contributions:

- In the first contribution, we performed a numerical simulation of AlGaN/GaN MOSHEMT transistors using the TCAD SILVACO simulator. Different structures and substrates are proposed to achieve enhancement mode, high on-state current, and microwave frequency characteristics. To this end, we are interested in:
  - A recessed T-gate β-Ga_2O_3/AlGaN/GaN/AlGaN MOSHEMT on GaN substrate.
  - A T-gate TiO_2/AlGaN/AlInGaN/GaN MOSHEMT on 4H-SiC substrate.
  - A T-gate HfO_2/AlGaN/AlInGaN/GaN MOSHEMT on β-Ga_2O_3substrate.
- In our second contribution, we presented a new design of a radio frequency filtering block for GNSS receiver using Advanced Design System (ADS), this filtering block must be set at the frequency centers of 1557.42 MHz and 1227 MHz corresponding to the GNSS carrier frequency. This contribution consists of examining and simulating the characteristics of the LNA amplifier based on the MOSHEMT transistor designed in this thesis, which demonstrate the best performance.

The thesis is divided into four chapters:

Chapter I presents a theoretical study of the main structural and electrical properties of IIIA nitride semiconductor materials, including binary (GaN, AlN, and InN), ternary (AlGaN), and quaternary (AlInGaN) alloys. Next, the state-of-the-art in heterojunction transistors, mainly AlGaN/GaN HEMTs, will be discussed.

Chapter II describes the main challenges and limitations of HEMT technology and the proposed solutions. It will be followed by a theoretical study of the chosen device, which is the MOSHEMT. Finally, we will study the electrical characteristics of a new AlGaN/GaN MOS-HEMT structure. The excellent performance of this MOSHEMT is part of our study.

The third chapter reports the numerical simulation of two proposed AlGaN/AlInGaN/GaN MOSHEMTs on 4H-SiC and β-Ga_2O_3 substrates, using TCAD-SILVACO software. This modeling provides information on the static and dynamic behavior of the MOSHEMTs studied, as well as on the influence of certain technological parameters.

In the fourth chapter, the theories of GNSS receivers, and the fundamental principles of low-noise amplifiers and passive bandpass filters will be presented first. Secondly, the extraction of the small signal equivalent linear model of MOSHEMT transistor will be studied. Finally, a new prototype of RF filtering block (Filters+LNA) of the GNSS receiver is designed using ADS designer. This filtering block operates at the frequency bands corresponding to the majority of GNSS signals. Finally, the thesis is concluded with a general conclusion and future perspectives.

Chapter I An overview of IIIA-N semiconductors and HEMT transistors

I.1 Introduction

Group IIIA-N materials are one of the most promising semiconductor families for high-power electronic, microwave, and optoelectronic applications. They are composed of elements from groups III-A and V-A of the periodic table (Appendix A). The most common IIIA-nitride materials are gallium nitride (GaN), aluminum nitride (AlN), and indium nitride (InN), which form the lower and upper limits of the band gap height, which extends from 0.68 to 6.2 eV [1]. Creating ternary and even quaternary materials is feasible by combining binary compounds. Overall, the distinctive qualities of IIIA-nitride materials, including their abilities to operate at high voltages and high frequencies, stem from their remarkable properties.

This chapter presents a brief overview of the basic structural, electrical, and electronic properties of group IIIA-nitride materials, including binary (GaN, AlN, and InN), ternary (AlGaN), and quaternary (AlInGaN) alloys. We will then establish the main characteristics of the AlGaN/GaN and AlInGaN/GaN heterojunctions. Finally, a concise overview of the operating principle of the HEMT transistor will be provided in detail as the key applications of IIIA-N semiconductor materials.

I.2 Basic properties of group IIIA-N semiconductors

All the electronic devices investigated in this thesis are based on IIIA-nitride semiconductor materials, which enjoy a remarkable combination of high electrical characteristics and superior material qualities. The following section provides an overview of the fundamental characteristics that enable us to assess the performance of IIIA-N materials.

I. 2. 1 Band gap energy and critical breakdown field

The band gap energy, denoted E_g (eV), is one of the most important parameters characterizing IIIA-N semiconductors. The gap energy refers to the difference in energy between the top of the valence band (E_v) and the bottom of the conduction band (E_c).

This difference corresponds to the energy required by an excited electron to move from the valence band to the conduction band and participate in the current flow. If the value of this energy is greater than 2 eV, the material is considered to be a wide-gap semiconductor [1].

The use of a wide band gap material will affect the critical breakdown field (E_{BR}) of the device, which indicates the maximum voltage withstood by a device before it deteriorates. This parameter is directly proportional to the gap energy (E_g) as $E_{BR} = E_g^{3/2}$ [2]. By increasing the critical breakdown field, a smaller transistor can be produced with a higher level of doping[3].

As a result, the component will have better power gain efficiency and higher frequencies. On the other hand, wide band gap materials permit the creation of heterojunctions with strong band discontinuities between atoms, which gives the material chemical and thermal stability.

Despite all the benefits of wide bandgap materials, there are some drawbacks, the high stability of the materials makes the manufacturing process more complicated and time-consuming, while the doping profile is frequently challenging, especially a p-type doping [4].

I. 2. 2 Saturation velocity and electron mobility

The saturation velocity represents the ability of the material to operate at high frequencies while accepting high power. In other words, it is a measure of the maximum speed that carrier charge can achieve in response to the application of an electric field before reaching a state of saturation.

The variation of the electron velocity (V) and the electron mobility (μ_n) as a function of the applied electric field (E) is expressed as $V = \mu_n \times E$. When the electric field is intense, the velocity of the carriers tends towards a saturation value (V_{sat}) [5].

I. 2. 3 Thermal conductivity

The thermal conductivity (κ) is a very important parameter. It reflects a material's aptitude to conduct heat. Poor thermal conductivity leads to power dissipation, with some of the power dissipated as heat and the rest converted into stored heat. The undissipated heat leads to a rise in temperature in the device, then to a drop in electron mobility and a reduction in energy efficiency [6].

I. 2. 4 Dielectric constant

The dielectric constant, also known as the relative permittivity (ε_r), is a measure of how a material responds to an electric field by allowing or resisting its passage through it; hence, a low value of semiconductor permittivity is desired [7].

I. 2. 5 Electron affinity

The electron affinity refers to the energy change that occurs when an electron is added to a semiconductor atom, forming a negatively charged ion. It is an important parameter for understanding the electronic properties of IIIA-N semiconductors [7].

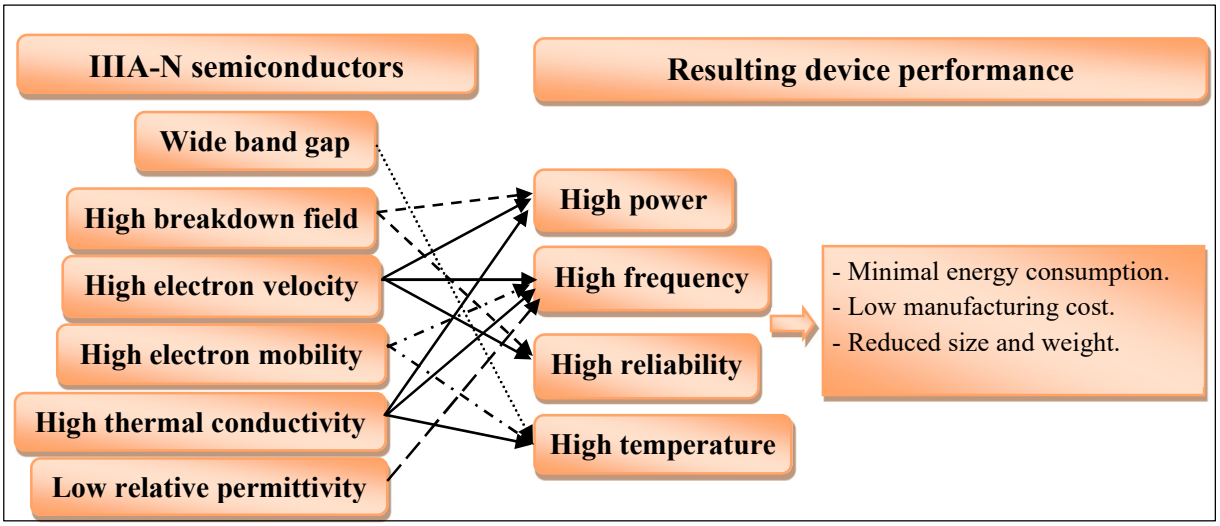

Figure I.1 Summary of the IIIA-N semiconductors properties and resulting device performance.

I.3 Overview of the IIIA-nitride materials used

I. 3. 1 Binary semiconductors: GaN, AlN, and InN

In the solid state, atoms of gallium (Ga), aluminum (Al), or indium (In) are linked to nitrogen (N) by covalent bonds to form binary nitride semiconductor materials, namely gallium nitride (GaN), aluminum nitride (AlN), and indium nitride (InN) [9]. The following section will discuss their principal properties.

I.3.1.1 Background

Binary IIIA-N semiconductors were first synthesized at the beginning of the 20th century. For over thirty years, there were no significant innovations until the 1960s, when Maruska and Tietjen developed the first use of hybrid vapor phase epitaxy (HVPE) enabling the growth of centimeter-sized monocrystalline alloys. Throughout the 1980s and beyond, the quality of the nitride growth described an excellent surface morphology by using modern growth procedures such as metal-organic chemical vapor deposition (MOCVD) [10] and the molecular beam epitaxy (MBE) [11].

The research is continuing to obtain materials of high crystalline quality. To date, MOCVD growth is the most widely used industrial process for producing binary semiconductors and devices destined for the market [12].

I.3.1.2 Crystallographic properties

Binary IIIA-N materials can exist in a variety of crystal structures, the two most common being the zinc blende and wurtzite [13], as shown in Figure I.2.

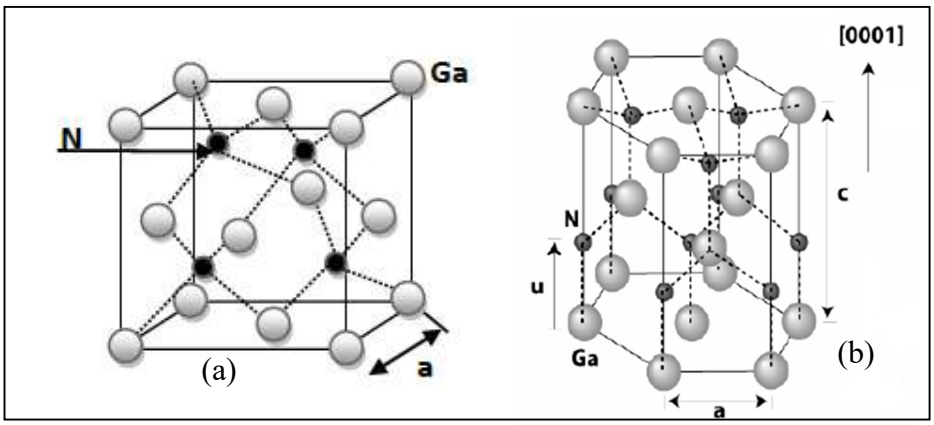

Figure I.2 IIIA-nitride crystal structures (a) Zinc-blend, (b) Wurtzite [9].

- **Zinc-blend structure:** It is a type of crystal in which Ga, Al, or In and nitrogen atoms are arranged in a face-centered cubic lattice. It is characterized by the symmetry of their unit cells, which have all edges of equal length (a) and all angles equal to 90 degrees. Although it is the thermodynamically metastable polytype of binary nitride crystals.
- **Wurtzite structure:** It is the most commonly employed crystal structure in IIIA-nitride compounds, as it is the most stable phase at room temperature and atmospheric pressure due to its excellent structural characteristics [9].

  In wurtzite crystal, the arrangement of the atoms forms a hexagon. It is characterized by two sub-lattices: c and a, which respectively represent the height of a one-unit hexagonal cell along the [0001] growth axis and the separation between each atom in the same plane [14]. Moreover, u is the distance in the [0001] direction between the nitrogen atom and the IIIA-element atom. The lattice parameters of binary single-crystals GaN, AlN, and InN in wurtzite form are listed in Table I.1.

Table I.1 Lattice parameters of binary wurtzite single-crystals GaN, AlN, and InN [15].

Parameters	GaN	AlN	InN
a (nm)	0.1389	0.3111	0.3544
c (nm)	0.5185	0.4978	0.5718
u (nm)	0.376	0.380	0.377

I.3.1.3 Electrical properties: Polarization effect

The binary nitride semiconductors belong to the pyroelectric class of materials. Pyroelectric materials are capable of generating an electric charge and exhibit both large spontaneous (P_{sp}) and piezoelectric polarization (P_{pz}) [16]. The total polarization charge of the material is the sum of these polarizations as follows:

$$P_{Total} = P_{sp} + P_{pz} \qquad \text{I.1}$$

a. Spontaneous polarization

Spontaneous polarization is a microscopic polarization that exists naturally in the relaxed material [15]. The binary IIIA-N materials exhibit a high value of spontaneous polarization charge, which is present without any external stress. The main structural parameter that is responsible for creating this polarization is the difference in electronegativity between nitrogen ($\Delta\chi$(N) = 3.04) and metal ($\Delta\chi$ (Ga)=1.23, and $\Delta\chi$ (Al)=1.43), so a negative charge (-q) appears around the nitrogen atoms and a positive charge (+q) appears around the metal atoms, leading to the appearance of strong electrostatic dipole moments oriented towards the IIIA-element atom, and the creation of an electric field in the opposite direction to this polarization.

Figure I.3 illustrates the distribution of the dipole moments responsible for spontaneous polarization on an elementary lattice of GaN. As can be seen, the gallium atom is bonded to four nitrogen atoms. Each of these atoms generates a dipole moment directed at Ga-atoms. The spontaneous polarization is the result of the sum of these dipole moments and is given by:

$$P_{sp} = P_1 + P_2 + P_3 + P_4 \qquad \text{I. 2}$$

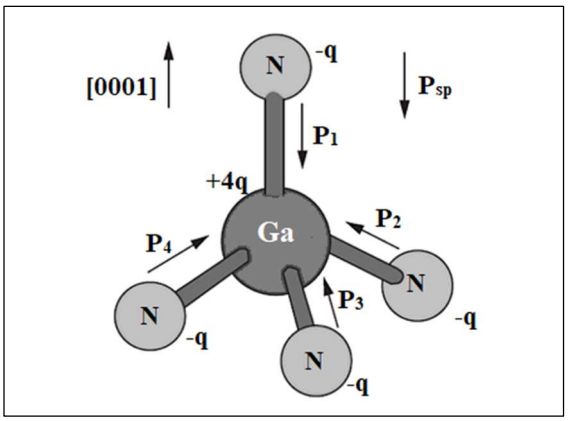

Figure I.3 Ball-and-stick configuration of spontaneous polarization of relaxed GaN [17].

The electronegativity and the spontaneous polarization values for all binary alloys are given in Table I.2. It can be seen that AlN exhibits the lowest spontaneous polarization compared to GaN and InN [14].

Table I.2 Spontaneous polarization values for all binary alloys [15].

Parameters	GaN	AlN	InN
$\Delta\chi$	1.23	1.43	1.26
P_{sp} (C.m^{-2})	-0.029	-0.081	-0.032

b. Piezoelectric Polarization

Another very interesting property of element IIIA-nitrides is the piezoelectric polarization (P_{pz}), which only occurs when external stress is exerted, leading to further deformation of the hexagon [17].

There are two piezoelectric polarization effects:

- **Direct piezoelectric effects:** It defines the ability of IIIA-nitride materials to generate an electric charge under the action of compressive stress. In this case, P_{pz} is oriented in the opposite direction to that of spontaneous polarization.
- **Inverse piezoelectric effects:** It presents the ability of a material to deform when an electric field acts upon it. In general, when a tensile stress is applied, the P_{pz} and P_{sp} vectors are oriented in the same direction.

Figure I.4 [17] shows the possible orientations for the P_{pz} as a function of the applied stress.

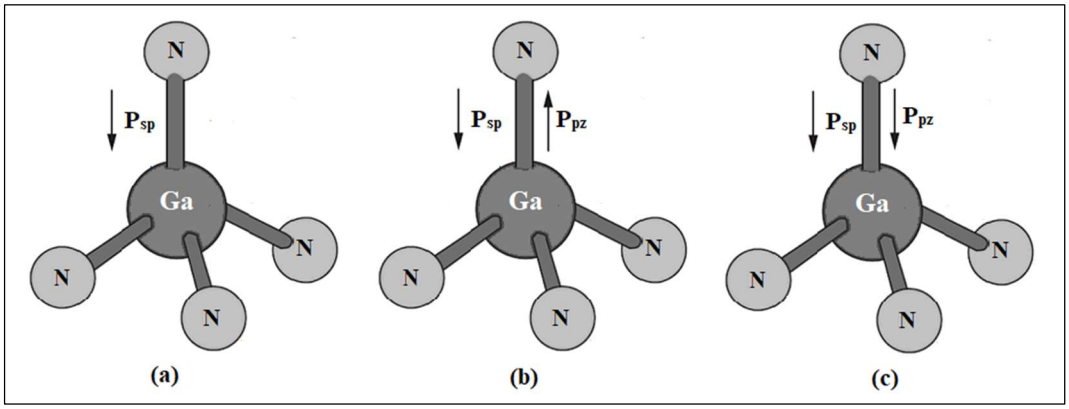

Figure I.4 Possible orientations of P_{pz} (a) No stress, (b) Compressive stress, (c)Tensile stress.

The piezoelectric polarization (P_{pz}) depends linearly on the deformation of the lattice constant (a) and is modeled according to Hooke's formalism. The following equation allows the P_{pz} of the binary nitrides to be calculated using the coefficients defined in Table I.3.

I.3

Where: $\eta = \frac{a - a_0}{a_0}$ represents the Basal strain, with a_0 is the lattice constant of the relaxed material, a is the lattice constant of the constrained material. From Equation I.3, $e_{31,}$ and e_{33} are the piezoelectric constants, and C_{13} and C_{33} are the elastic constants. These constants are still the subject of debate, and different experimental measurements gave results [18].

Table I.3 Relative parameters of the piezoelectric polarization of binary compounds [18].

Constants	GaN	AlN	InN
e_{31} (C/m²)	-0.49	-0.60	-0.57
e_{33} (C/m²)	0.73	1.46	0.97
C_{31} (GPa)	106	99	92
C_{33} (GPa)	398	389	224

The developed values of the piezoelectric polarization of GaN, AlN, and InN compounds are given as a function of Basal strain in Table I.4. In power devices such as HEMTs, the total polarization charge has an importance in increasing the density of the 2D electron gas.

Table I.4 Piezoelectric polarization of binary compounds [19].

Parameters	Equations
$P_{pz}^{GaN,\eta}$ (C.m-²)	$-0.918\eta + 9.541\eta^2$
$P_{pz}^{AlN,\eta}$ (C.m-²)	$-1.808\eta + 5.624\eta^2$ for $\eta < 0$ $-1.808\eta - 7.888\eta^2$ for $\eta > 0$
$P_{pz}^{InN,\eta}$ (C.m-²)	$-1.373\eta + 7.559\eta^2$

I.3.1.4 Electronic properties

To investigate the electrical properties of the binary nitrides, it is important to know all the features that offer this important quality. The binary IIIA-N materials present a large band gap energy. The high gap of GaN and AlN offers a very high breakdown field (E_{BR}) compared with conventional semiconductors such as silicon (Si) and gallium arsenide (GaAs). Whereas InN shows the lowest band gap of 0.69eV and is generally destined for optoelectronic applications.

The band gap energy decreases slightly with increasing temperature. The temperature-dependent band gap energy is calculated according to the equation established by the Varshni model as follows:

$$E_g(T) = E_g(0) - \frac{\alpha . T^2}{T + \beta} \qquad \text{I.4}$$

Where $E_g(0)$ is the band gap energy at T=0 K, α is the gap linear regression coefficient, while β(K) is the temperature from which the slope is changing [20]. Table I.5 compares the Varshni coefficients of binary alloys, Si, and GaAs.

Table I.5 Band gaps values and Varshni coefficients of binaries and their concurrent [20].

Parameters	GaN	AlN	InN	Si	GaAs
E_g (eV)	3.4	6.2	0.69	1.17	1.4
α (meV/K)	7.32	17.99	0.41	4.73	5.4
β(K)	700	1432	454	636	204

Figure I.5 shows the temperature-dependent evolution by experimental data of the band gap height of binary nitrides. E_g slightly decreases at elevated temperatures.

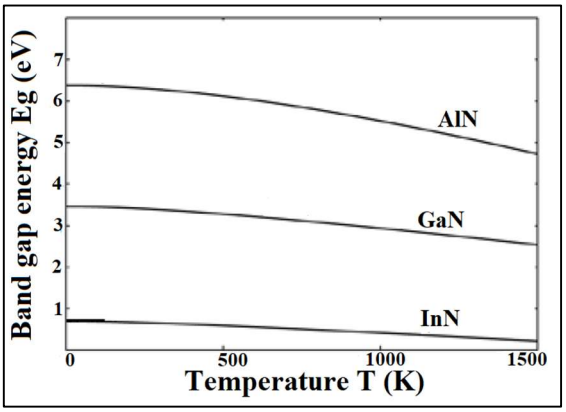

Figure I.5 Temperature-dependent evolution of the bandgap height of binary materials [21].

Table I.6 compares the basic material properties of GaN, AlN, and InN with conventional semiconductors. A major drawback in the fabrication of wide bandgap IIIA-N-based transistors is the relatively low mobility, which is 900 and 135 $cm^2.V^{-1}.\ s^{-1}$ for GaN and AlN. However, these values are sufficient for transistors specifically designed for high-frequency operation [7].

Moreover, the saturation velocity and the thermal conductivity for binary compounds are excellent compared to conventional materials, providing high chemical and thermal stability at elevated temperatures. Research on IIIA-N-binary materials continues, with efforts aimed at improving their quality and exploring their use in advanced electronic devices [8].

Table I.6 Comparison of electronic properties of binaries with Si and GaAs [22].

Parameters	GaN	AlN	InN	Si	GaAs
Critical breakdown field E_{BR} (MV/cm)	3.3	8.4	1.2	1.1	1.4
Saturation velocity V_{sat} (107 cm/s)	2.5	2.1	1.8	1	1
Electron mobility μ_n ($cm^2/v.s$)	990	135	3.6	1500	8500
Thermal conductivity λ (W/cm.K)	1.3	2	0.45	1.5	0.5
Relative permittivity ε	9.5	9.14	15.3	11.8	11.5

- **Unintentional doping of GaN**

Controlling the type of doping is a big challenge faced by nitride research technology. In particular, all the analyses carried out prove that GaN is an unintentionally doped material, which generally turns out to be a residual n-type semiconductor in the $10^{16}cm^{-3}$ concentration range. The origin of this n-type conduction is often associated with 'self-doping' attributed to

defects in the crystal unintentionally incorporated during GaN growth, such as nitrogen vacancies or residual impurities [23].

I. 3. 2 Ternary semiconductor: $Al_xGa_{1-x}N$

Aluminum gallium nitride (AlGaN) is a versatile ternary IIIA-nitride semiconductor. The development and research on AlGaN began in the 1990s as an alternative to other ternary semiconductors such as AlGaAs and InGaAs. The properties of AlGaN can be tuned by altering the ratio of aluminum to gallium in the material, thus tailoring its structural, electrical, and electronic characteristics for a specific application [24]. AlGaN alloys are often used as a confinement barrier in HEMT transistors. Here are some key points about AlGaN properties.

I.3.2.1 Crystallographic properties

The $Al_xGa_{1-x}N$ ternary alloys, where "x" is the Al mole fraction ($0 \leq x \leq 1$), typically adopt the hexagonal wurtzite structure. The crystallographic properties can vary depending on the Al-content. The compositional dependence of the calculated lattice parameters of this crystal has been measured by Yoshida and Khan [25], it can be deduced from the lattice parameters of GaN and AlN by linear interpolation. This is referred to Vegard's law, as:

$$a_{Al_xGa_{1-x}N} = xa^{AlN} + (1 - x)a^{GaN} = 3.112x + 3.189(1-x) \quad \text{I.5}$$

$$c_{Al_xGa_{1-x}N} = xc^{AlN} + (1 - x)c^{GaN} = 4.982x + 5.184(1-x) \quad \text{I.6}$$

$$u_{Al_xGa_{1-x}N} = 0.3819x + 0.3772(1 - x) - 0.0032x(1 - x) \quad \text{I.7}$$

Figure I.6 shows the variation of the lattice parameters (a and c) of AlGaN with respect to Al-content. As the Al-mole fraction increases, the lattice constants slightly decrease.

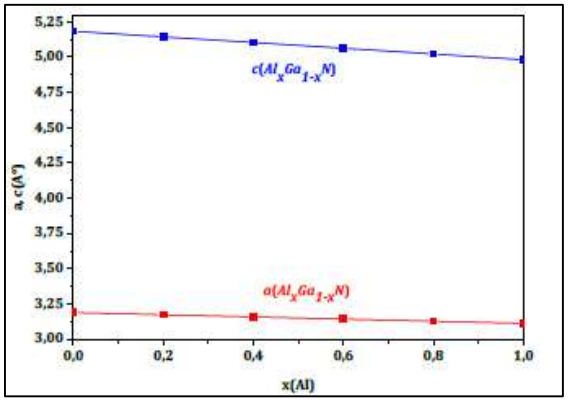

Figure I.6 Variation of AlGaN lattice constants as a function of x-mole fraction [26].

I.3.2.2 Electrical properties: Polarization effect

The ternary AlGaN is a pyroelectric semiconductor. The total polarization presented in the crystal is the summation of its spontaneous and piezoelectric polarizations as:

$$P_{AlGaN} = P_{sp}^{AlGaN} + P_{pz}^{AlGaN} \quad \text{I.8}$$

a. Spontaneous polarization

It is expected that for AlGaN ternary compounds, the variation in Al-constituent will lead to a non-linear behavior of spontaneous polarization. This non-linear behavior is explained by Bernardini et al. [27]. The P_{sp} of an AlGaN nitride can be described as follows:

$$P_{sp}^{AlGaN} = xP_{sp}^{AlN} + (1-x)P_{sp}^{GaN} + x(1-x)b_{AlGaN} \quad \text{I.9}$$

The first two terms are the usual spontaneous polarization of the binary nitrides. The third term shows the non-linear law for polarization: is the so-called bowing parameter; this parameter depends on the microscopic structure and represents the difference in contribution between the volume deformation and the internal deformation of the alloy [28]. The P_{sp}^{AlGaN} can be expressed by the non-linear interpolation of Vegard's law as follows [18]:

$$P_{sp}^{AlGaN} = (-0.052x - 0.029) \quad \text{I.10}$$

b. Piezoelectric Polarization

The piezoelectric polarization effect in $Al_XGa_{1-X}N$ alloy occurs when the material is strained. This means that it can generate an electrical charge in response to mechanical stress. The P_{pz}^{AlGaN} can be calculated by linear interpolation of the piezoelectric polarization values of GaN and AlN binaries as a function of the Basal strain, as follows:

$$P_{pz}^{AlGaN} = xP_{pz}^{AlN,\eta} + (1-x)P_{pz}^{GaN,\eta} \quad \text{I.11}$$

Here, the Basal strain is:

$$\eta = \frac{a(AlGaN\ strained) - a(AlGaN)}{a(AlGaN)} \quad \text{I.12}$$

I.3.2.3 Electronic properties

The band gap energy of ternary AlGaN varies linearly with the percentage of aluminum. At ambient temperature, the compositional dependency of the energy band gap of $Al_xGa_{1-x}N$ can be estimated from the following empirical expression; where b is the bowing parameter:

$$E_g^{Al_xGa_{1-x}N} = x\,E_g^{AlN} + (1-x)E_g^{GaN} - x(1-x)b_{AlGaN} \quad \text{I.13}$$

Figure I.7 shows the value of the AlGaN bandgap with respect to x content (from 0 to 1), the effective band gap is tuned from 3.4 eV to 6.2 eV. This property allows the AlGaN's band gap to be engineered, making the material suitable for high-performance devices [29].

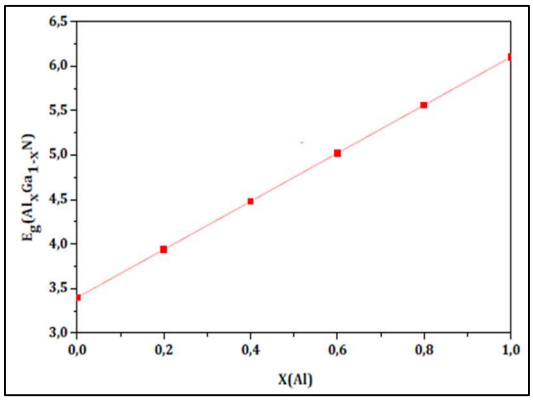

Figure I.7 Variation of the AlGaN's bandgap energy as a function of Al composition [26].

The relative permittivity and the electron affinity of AlGaN alloy are a function of x content, they are expressed as:

$$\varepsilon_{Al_xGaN} = 8.5x + 8.9(1-x) \quad \text{I.14}$$

$$\chi_{Al_xGaN} = 1.89x + 0.91x(1-x) \quad \text{I.15}$$

I. 3. 3 Quaternary semiconductor: $Al_xIn_yGa_zN$

Aluminum indium gallium nitride (AlInGaN) is an important IIIA-N quaternary semiconductor. The first report on the growth of the AlInGaN layer was in 1992 [30]. The great tunable wide bandgap and desirable material properties make the AlInGaN a key material in the advanced semiconductor technology. Additionally, quaternary nitride is frequently used as a barrier or spacer layer in HEMT structures. Here are the main properties of AlInGaN:

I.3.3.1 Crystallographic properties

The crystallographic properties of $Al_xIn_yGa_{1-x-y}N$ alloy can vary depending on the specific composition and growth conditions. The hexagonal wurtzite structure is the most frequently used, its lattice constant changes with the aluminum and indium contents, is calculated by Vegard's method as follows:

$$a_{Al_xIn_yGa_zN} = xa^{AlN} + ya^{GaN} + za^{InN} \quad \text{I. 16}$$

Achieving high-quality $Al_xIn_yGa_zN$ crystals can be technically challenging due to the complexities introduced by varying compositions and strain effects. Figure I.8 shows the possible lattice constant values of AlInGaN as a function of x, y, and z (with z = 1- x - y).

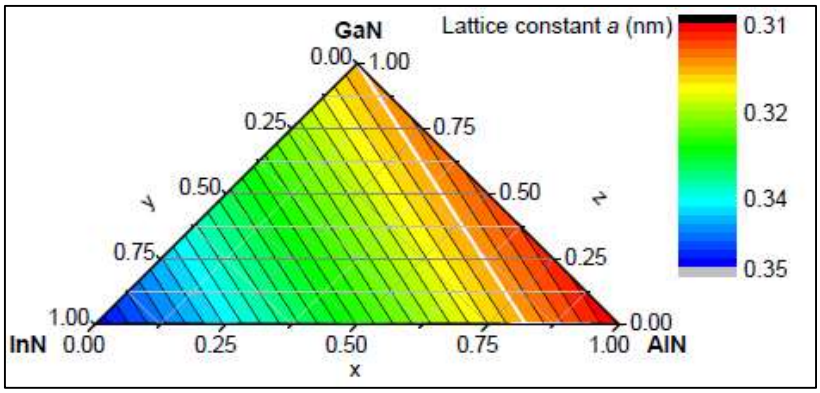

Figure I.8 AlInGaN lattice constant for different alloy constituents [31].

I.3.3.2 Electrical properties: Polarization effect

Based on the aforementioned features of IIIA-nitride semiconductors, quaternary AlInGaN is considered to be a pyroelectric material. As a consequence, AlInGaN exhibits a strong polarization charge, represented by inherent spontaneous polarization ($P_{sp}^{AlInGaN}$) and induced piezoelectric polarization ($P_{pz}^{AlInGaN}$), which depend on the Al and In mole fractions:

$$P_{AlInGaN} = P_{pz}^{AlInGaN} + P_{sp}^{AlInGaN} \qquad \text{I. 17}$$

a. Spontaneous Polarization

The spontaneous polarization of AlInGaN shows the polarization inherent in an unstressed alloy [32]. Vegard's law and bowing approach are utilized, giving:

$$P_{sp}^{AlInGaN} = xP_{sp}^{AlN} + yP_{sp}^{InN} + zP_{sp}^{GaN} + xz.\, b_{AlGaN} + yzb_{InGaN} + xyb_{AlInN} \qquad \text{I. 18}$$

The detailed formulas for the bowing parameters and the spontaneous polarization for ternaries (AlGaN, AlInN, and InGaN) are mentioned below in Table I.7**:**

Table I.7 Bowing parameters and spontaneous polarization for ternary alloys [15].

Parameters	Equations
$\mathbf{b_{AlGaN}}$	$4P_{sp}^{AlGaN} - 2(P_{sp}^{AlN} + P_{sp}^{GaN})$
$\mathbf{b_{InGaN}}$	$4P_{sp}^{InGaN} - 2(P_{sp}^{InN} + P_{sp}^{GaN})$
$\mathbf{b_{AlInN}}$	$4P_{sp}^{AlInN} - 2(P_{sp}^{AlN} + P_{sp}^{InN})$
$\mathbf{P_{sp}^{AlGaN}}$	-0.081x - 0.029(1-x) + 0.021x(1-x)
$\mathbf{P_{sp}^{InGaN}}$	-0.042x - 0.034(1-x) + 0.037x(1-x)
$\mathbf{P_{sp}^{AlInN}}$	-0.090x - 0.042(1-x) + 0.070x(1-x)

After developing Equation (I.18), $P_{sp}^{AlInGaN}$ (x,y) at zero strain is given by:

$$P_{sp}^{AlInGaN} = -0.081x - 0.032y - 0.029z \quad \text{I.19}$$

b. Piezoelectric polarization

In a quaternary AlInGaN, a piezoelectric polarization is present when the crystal is under strain, it can produce an electric charge that can be influenced by the percentage of the compounds in the material (x and y). The P_{pz} charge can be calculated using the equation below:

$$P_{pz}^{AlInGaN,\eta} = x.P_{pz}^{AlN,\eta} + y.P_{pz}^{InN,\eta} + z.\ P_{pz}^{GaN,\eta} \quad \text{I. 20}$$

The Basal strain $\eta(x, y, z)$ of the AlInGaN is calculated by Equation (I.21) with nominal lattice constants ($a_{Al_xIn_yGa_zN}$) [33] as follows:

$$\eta(x,y,z) = \frac{a_{Al_xIn_yGa_zN,\ strained} - a_{Al_xIn_yGa_zN}}{a_{Al_xIn_yGa_zN}} \quad \text{I. 21}$$

I.3.3.3 Electronic properties

Quaternary AlInGaN materials represent a new class of wide band gap nitride semiconductors, which can be used in power electronic devices establishing several advantages. One of the main advantages is its tunable band gap that can be adjusted over a wide range of compositions demonstrating a high degree of freedom, which contributes to the reduction of the defects in the alloy.

The quaternary band gap is mathematically expressed as a sum of the linear band gap energies of the binary semiconductors (Table I.2) with the appropriate non-linear bowing parameters of ternary compounds (Table I.7) [34], and is given by:

$$E_g^{Al_xIn_yGa_zN} = x\ E_g^{AlN} + yE_g^{Gan} + zE_g^{InN} - xy(1-z)b_{AlGaN} - xz(1-y)b_{AlInN} - yz(1-x)b_{InGaN} \quad \text{I.22}$$

In addition, the relative permittivity and the electron affinity of AlInGaN [33] depend on x, y, and z, as:

$$\varepsilon_{Al_xIn_yGa_zN} = 8.5x + 15.3y + 8.9z \quad \text{I.23}$$

$$\chi_{Al_xIn_yGa_zN} = 2.05x + 5.75y + 4.16z \quad \text{I.24}$$

Figure I.9 illustrates the AlInGaN band gap. From this figure, the bandgap of the resulting crystal can be augmented from 0.63 eV to 6.23 eV [9].

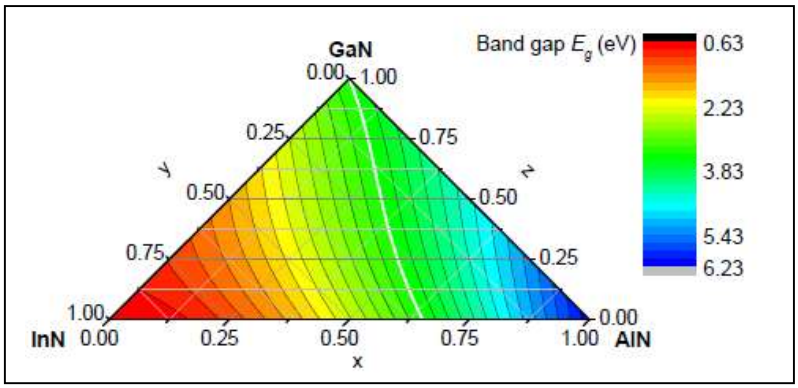

Figure I.9 AlInGaN band gap variation as function of x, y, and z [31].

I.4 Structural defects in group IIIA-N semiconductor

The presence of defects in the crystal can be introduced unintentionally during the fabrication process [35]. In a flawless crystal, atoms occupy precise crystallographic sites. Nevertheless, for a variety of reasons; several point defects can occur, including:

- **Vacancies:** They refer to missing atoms at specific sites, creating localized regions of deformation-strain.
- **Substitutional impurities:** Foreign impurities are incorporated during the crystal growth, involving the replacement of one or more atoms, leading to a change in the mobility[36].
- **Interstitial defects:** In the crystal, the atoms can be arranged outside of their designated locations forming interstitial sites.
- **Dislocations:** It occurs when there is a discontinuity in the crystalline atomic planes. They can be viewed as irregularities in the normal arrangement of atoms, which can propagate through the crystal and lead to significant deformation of the material [37].

Figure I.10 shows some of the structural point defects present in a crystal.

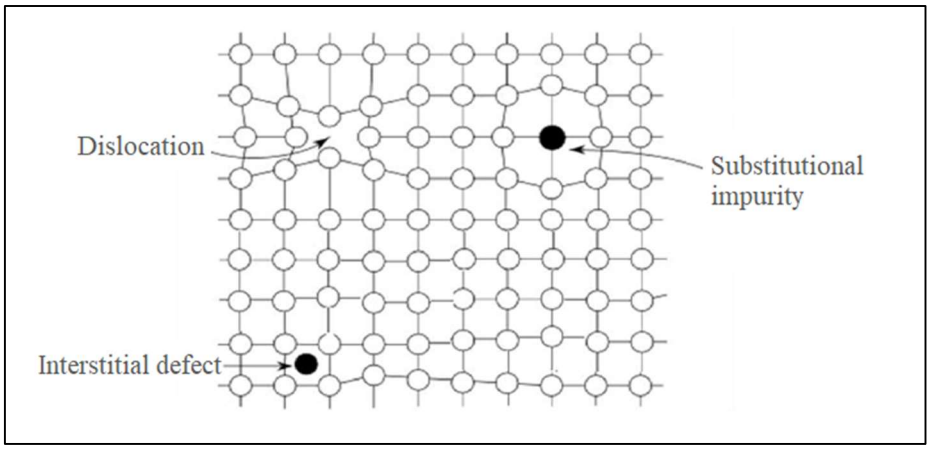

Figure I.10 Some structural defects present in a semiconductor crystal.

I.5 GaN-based heterostructures and two-dimensional electron gas

In this fifth section, the main characteristics of IIIA-nitride-based heterostructures will be examined, in particular AlGaN/GaN and AlInGaN/GaN. At present, these heterostructures are the focus of the majority of extensive research into the fabrication of HEMT transistors.

I. 5. 1 Polarization effect

Nitride-based heterostructure is created when two crystalline layers with distinct band gaps stack on top of each other and form a net charge (σ_{int}) at the interface due to the polarization difference, as shown in Figure I.11 [31]. The charge density (σ_{int}) in this interface manifests as the difference between the polarization-induced charge in the barrier ($P_{Barrier}$) and the channel (P_{GaN}), where the total polarization of the barrier represents the sum of the piezoelectric polarization ($P_{pz}^{Barrier,\eta}$)and the spontaneous polarization ($P_{sp}^{Barrier}$) [29].

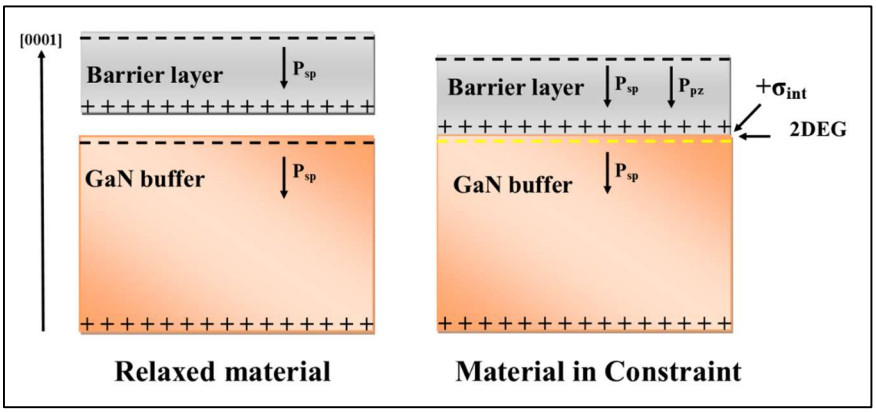

Figure I.11 Cross section of a barrier and GaN buffer at relaxed and constraint case [31].

In the case of a typical IIIA-nitride-based heterostructure, with the growth of the barrier on GaN, a compressive strain is created leading to a net negative piezoelectric polarization charge at the heterointerface, while the interface charge is positive.

In general, the GaN layer is about 100 times thicker than the barrier layer, to the point where it can be considered relaxed from any mechanical stress, so its piezoelectric polarization is zero. In the [0001] direction, the interface charge is calculated as:

$$\sigma_{int} = P_{GaN} - P_{Barrier} \quad \text{I.25}$$

$$\sigma_{int} = P_{sp}^{GaN} - (P_{pz}^{Barrier} + P_{sp}^{Barrier}) \quad \text{I.26}$$

In this work, the barrier material could be AlGaN or AlInGaN, the analytical expressions to calculate their polarization charges have already been mentioned in section I.3.

I. 5. 2 2D electron gas formation

Due to this localized interface charge and the difference in the band gaps between the barrier and GaN, a conduction band discontinuity (ΔE_c) is created, leading to the formation of a triangular-shaped quantum well for the conduction band at the heterointerface AlGaN/GaN or AlInGaN/GaN, generating a two-dimensional electron gas (2DEG) [38].

All the electrons present in the structure stockpiled within this quantum well and lead to band bending in the buffer. The use of wide band gap materials allows the creation of heterojunctions with strong band discontinuities, increasing the carrier density in the channel.

I. 5. 3 Potential quantum well and charge density

In the conduction band diagram (Figure I.12), the remarkable depth penetration relative to the Fermi level (E_f) and the accumulated 2DEG are related to the surface boundary conditions.

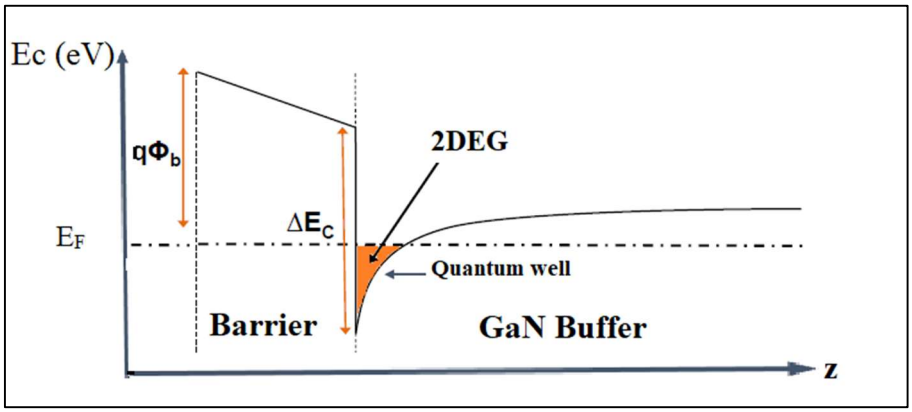

Figure I.12 Schematic conduction band diagram for a typical GaN-based HEMT [22].

In this case, the heavily doped barrier layer is a source of electrons in the GaN channel, which is assumed to provide a higher density of the 2DEG. The resulting equations for the maximum sheet carrier concentration (n_s) for a typical heterostructure with an Al_xGaN or Al_xIn_yGaN barrier layer are given by:

$$n_s^{AlGaN}(x) = \frac{\sigma_{int}(x)}{q} - \left(\frac{\varepsilon_0 \varepsilon(x)}{q^2 d_{bar}}\right)(q\Phi_b + E_F + \Delta E_c(x)) \qquad \text{I.27}$$

$$n_s^{AlInGaN}(x,y) = \frac{\sigma_{int}(x,y)}{q} - \left(\frac{\varepsilon_0 \varepsilon(x,y)}{q^2 d_{bar}}\right)(q\Phi_b + E_F + \Delta E_c(x,y)) \qquad \text{I.28}$$

Where d_{bar} represents the barrier thickness, ε_0 is the dielectric constant of the vacuum, and q is the elementary charge [39]. The average value of n_s is around 10^{13} cm^{-2}. The following table lists the other parameters used in Equations I.27 and I.28.

Table I.8 Parameters used in the sheet charge density equations [29, 40].

Parameter terms	AlxGa1-xN barrier	AlxInyGa1-x-yN barrier
Band discontinuity(eV)	$\Delta E_c(x)=0.7\,(E_g^{AlGaN} - E_g^{GaN})$	$\Delta E_c(x,y)=0.7\,(E_g^{AlInGaN} - E_g^{GaN})$
Schottky barrier height (eV)	$q\Phi_b(x) = 0.84 + 1.3x$	$q\Phi_b(x,y) = 0.94 + 2.11x - 1.59y$
Fermi level energy (eV)	$E_F(x)=E_0(x) + \frac{\pi h^2 n_s(x)}{m^*(x)}$ With: $E_0(x)= \frac{9\pi h q^2 n_s(x)}{8\varepsilon_0\varepsilon(x)\sqrt{8m^*(GaN)}}$ $m^*(x) = m_e[0.314x + 0.2(1-x)]$	$E_F(x,y)=E_0(x,y) + \frac{\pi h^2 n_s(x,y)}{m^*(x,y)}$ With: $E_0(x,y)= \frac{9\pi h q^2 n_s(x,y)}{8\varepsilon_0\varepsilon(x,y)\sqrt{8m^*(GaN)}}$ $m^*(x,y)=m_e[0.35x+0.1y+0.2(1-x-y)]$

From Table I.8, E_0 displays the ground state sub-band level of the 2DEG, h is the Planck constant, m_e is the elementary electron mass, and m^* is the effective electron mass.

I. 5. 4 Impact of the barrier on the 2DEG charge density

The presence of a 2DEG and its sheet carrier density depends strongly on the crystal quality and material constituents of the nitride layers. In general, if the amount of the barrier composition is increased the overall polarization will be increased, hence, the sheet carrier concentration.

On the other hand, the thickness of the barrier layer is also important when considering the 2DEG formation, see Figure I.13 [41]. The value of n_s will rise with the critical barrier thickness. However, if the barrier thickness is increased too much, it will become relaxed, which will lessen the polarization effect and quickly drop the n_s value. Typically, the barrier thickness in the most heterostructures is in the range of 5 to 30 nm.

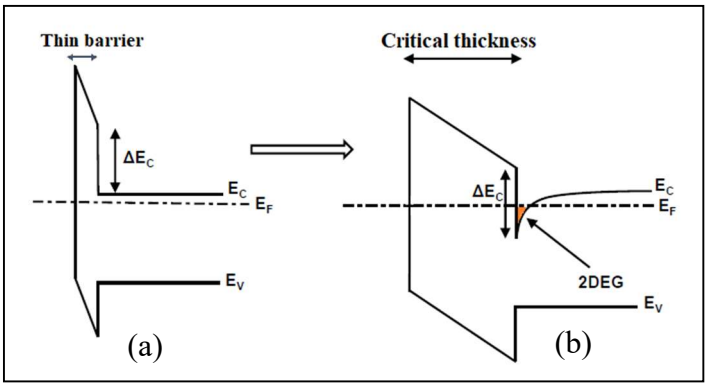

Figure I.13 Schematic band diagram with (a) Thin barrier layer, (b) Critical barrier height.

I. 5. 5 Advantage of AlInGaN-based heterostructure

The performance of HEMTs can be further optimized by employing multiple barrier materials. Experimental and theoretical studies have demonstrated that replacing the ternary

barrier material, such as AlGaN, with the quaternary AlInGaN alloy can significantly improve the electrical characteristics, enabling speed-power operations [31, 42].

The use of AlInGaN alloy with an appropriate mole fraction can be grown as a lattice-matched with substrate and between the adjacent layers, holding exceptional promise to achieve higher 2DEG density ($n_s \geq 1.8\times10^{13}$ cm^{-2}) and higher mobility ($\mu_n \geq 1800$ cm^2/Vs) [43].

Additionally, the quaternary lattice-matched offers an additional degree of freedom by tuning different band gaps and controlling the strain in the crystal, thus mitigating dislocations and the inverse piezoelectric field [44]. Finally, the insertion of a very thin barrier of AlInGaN with high Al-content demonstrated excellent power and frequency operation [45].

I.6 Applications of IIIA-N semiconductor materials

The excellent physical properties of IIIA-nitride elements are exploited in two main fields of application: optoelectronics and power RF electronics. For optoelectronics, most nitrides have a wide band gap that makes them appropriate for the production of optical components covering a wide range of applications from near-infrared through visible to deep ultraviolet emission and detection, including laser diodes, LEDs (Light-emitting Diodes), and photodetectors. We won't dwell on this subject, as our principal focus is on electronic applications, in particular high electron mobility transistors (HEMTs).

I. 6. 1 High electron mobility transistor (HEMT)

- **Background**

The high electron mobility transistor (HEMT), also known as the MODFET (Modulation Doped Field Effect Transistor), TEGFET (Two-dimensional Electron Gas Field Effect Transistor), and HFET (Heterojunction Field Effect Transistor), is a field-effect transistor that operates based on the principles of heterostructure design and high mobility.

The first HEMTs were created in the 1980s, with the idea of using the AlGaAs/GaAs heterojunction to generate high electron mobility. The GaAs-based HEMT device has witnessed technological advancements since the first two-dimensional electron gas (2DEG) was observed [46]. In 1985, GaAs HEMT was first employed as a microwave circuit in television receivers and radio telescopes.

The existence of a 2DEG in HEMT devices has been established in other structures such as InAlAs/InGaAs, InGaAs/InP, and of course, AlGaN/GaN and AlInGaN/GaN (late 1990s). Compared with their counterparts in terms of power and frequency, GaN HEMTs make it

possible to produce devices that are more robust, smaller, more efficient, and capable of withstanding high temperatures. The following section provides a detailed explanation.

➢ **What is HEMT?**

HEMT transistors are based on the heterojunction design, consisting generally of IIIA-nitride semiconductor materials. By selecting the right material, a two-dimensional electron gas (2DEG) can form at the barrier/channel heterointerface because of the different band gaps and doping levels between junctions, which allow us to create a localized potential region of the conduction band below the Fermi level and stoke the carriers into a quantum well. This 2DEG is made up of an electron sheet that is contained in an extremely thin layer with an electron concentration that can reach up to 2×10^{13} cm^{-2}.

In this heterointerface, electrons can move rapidly through the material, providing an electric current flow between the source and drain electrodes under the control of the gate electrode, enabling HEMTs to operate efficiently, particularly at high frequencies [11].

I. 6. 2 Description of HEMT structure

In this section, we will describe the complete structure of the HEMT including the contacts, the layers, and the substrate, as it is illustrated in Figure 1.14. The source length (L_s), gate length (L_g), drain length (L_d), source-gate distance (L_{SG}), and gate-drain distance (L_{GD}) are indicated in the schematic.

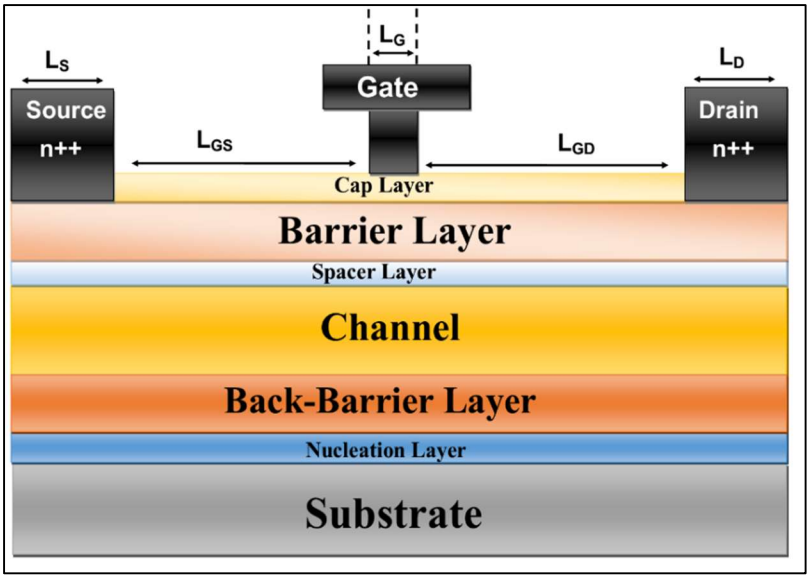

Figure I.14 Cross schematic horizontal structures of a typical HEMT device.

I.6.2.1 Contact

In the GaN-based HEMT structure, two appropriate electrical contacts are established:

- **Schottky contact:** It is the metal gate electrode whose function is to control the electron density in the channel by varying its potential. In order to achieve a high-quality Schottky contact, the barrier height between the gate metal and the semiconductor should be as high as possible, and the use of high work function metal is essential.
- **Ohmic contact:** It is the access point of the device and is characterized by low resistance in the source and drain regions to enable efficient current to flow through the device.

Most metallic contacts on GaN-based HEMTs are based on titanium (Ti), aluminum (Al), nickel (Ni), gold (Au), and platinum (Pt). Table I.9 shows the work function and barrier height of several metals commonly used. The metallization contact used on our devices is gold that anneals an excellent Schottky contact, with a work function of 5.1eV [47].

Table I.9 Work function and barrier height for metal Schottky contact [47].

Metal	Work function (eV)	Barrier height (eV)
Ni	5.15	2.35
Pt	5.65	1.85
Ti	4.33	0.23
Au	5.1	2.4
Al	4.28	0.18

To achieve good ohmic behavior, several techniques are often employed to lower the contact resistance between the source/drain and the semiconductor layers. One of the most interesting methods is the insertion of a heavily doped n++ GaN layer under the source/drain electrode to reduce the contact resistivity, known as the regrown source/drain technique.

I.6.2.2 Layers

- **Passivation layer**

The passivation layer is a thick film that is deposited on the surface of a semiconductor material to shield it from environmental factors when it comes into contact with air such as oxidation, damage, or contaminants, which can adversely affect the electrical characteristics of the device, causing leakage current or interface traps. Choosing the right passivation material is crucial; SiN, SiO_2, and Si_3N_4 are the most common in use due to their beneficial impact to achieve good insulating qualities and reduced surface traps [48].

- **Cap layer**

The cap layer is the topmost surface of the structure, formed usually by an extra thin GaN nitride. It serves to protect the underlying layers and ensure the reliability and stability of the device by improving the surface quality between the different layers [11].

- **Barrier layer**

The barrier layer represents a few nanometers of doped or undoped wide band gap semiconductor, it plays a vital role in confining and controlling the movement of electrons that are required for the formation of the 2DEG on which the operation of HEMTs relies. In this thesis, the barrier layer is composed of ternary AlGaN or quaternary AlInGaN alloys, whose content and thickness can be modified to obtain the desired electronic properties [11].

- **Spacer layer**

The spacer layer is an ultra-thin film with the largest bandgap, adding between the barrier and the channel regions in order to improve the electron confinement in the 2DEG potential well. It also provides better separation between the electrons present in the gas and the electrons from the doped barrier [14]. AlN and AlInGaN alloys are utilized as spacers in our devices.

- **Channel layer**

The channel layer is a thick region where electron conduction occurs and the 2DEG is formed, it is made from a non-doped GaN material with the highest possible crystalline quality. The channel layer is the most important part of the HEMT, as it provides the conductive path for the electrons and influences their mobility [11].

- **Back-barrier layer**

In the so-called double hetero-junction (DH) HEMT, a thick layer (> 1 μm) is placed beneath the channel produced from an undoped AlGaN material, resulting in a second AlGaN/GaN/AlGaN heterojunction. The term "back-barrier" refers to this enhanced potential barrier. The main objective of the back-barrier is to prevent the electrons from getting to the substrate. It helps to improve the carrier confinement of the device and stops the unwanted leakage current that might deteriorate device performance [14].

- **Nucleation layer**

The channel or the back-barrier, cannot be deposited directly on a foreign substrate because of the large lattice mismatch that can induce a high density of dislocations and wafer cracking during the epitaxial growth. Therefore, a very thin nucleation layer is deposited immediately on the substrate to absorb the majority of the stresses [14].

I.6.2.3 Substrate

The substrate layer in the HEMT component is the underlying solid on which the other semiconductor layers are superimposed. The discrepancies in lattice mismatch between the substrate and the layers are responsible for the creation of dislocations. The selection of an appropriate substrate is critical [23].

I. 6. 3 How the HEMT works?

The working principle of a HEMT is based on modulating the electron density (flow line current) between the source and drain contacts and controlling the gate voltage via the gate [49]. Employing a gate-source voltage ($V_{GS} \neq 0$) will affect the energy position of the conduction band relative to the Fermi level leading to 2D electron gas accumulation. The conduction band position (E_c) and the 2DEG density at different V_{GS} of a typical AlGaN/GaN HEMT are depicted in Figure I.15 [23].

- At $V_{GS} < 0$, the conduction band is lifted with respect to the Fermi level up to a point where the quantum well decreases. Consequently, there is no charge left in the channel.
- At $V_{GS} = 0V$, the conduction band is at the same position as the fermi level, leading to generate a moderate 2DEG density thanks to the direct formation of the Schottky contact.
- At $V_{GS} > 0$, the conduction band moves in the direction of the Fermi level. As a result, the quantum well below the Fermi level is enlarged and the 2DEG is highly accumulated.

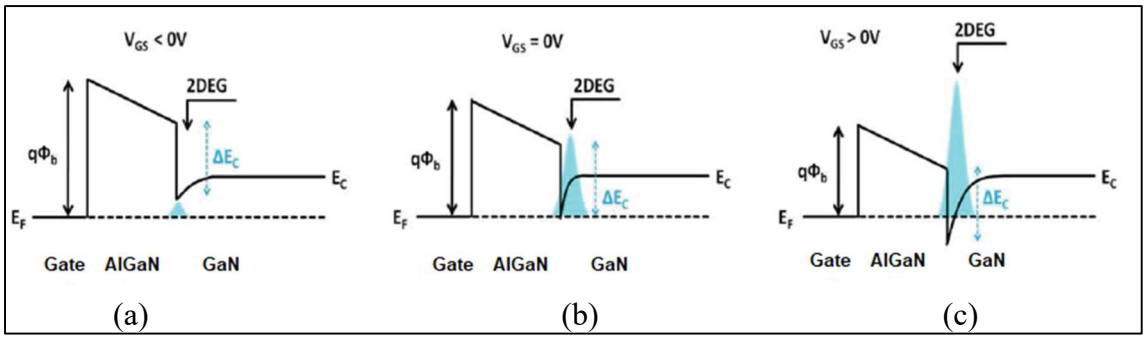

Figure I.15 Conduction band and 2DEG diagrams as function of V_{GS} of an AlGaN/GaN HEMT [23].

I. 6. 4 Electrical Characterization of HEMT devices

The analysis of a HEMT transistor consists of determining its electrical characteristics by means of static (DC) and dynamic (AC) measurements, as well as determining the intrinsic and extrinsic parameters of its equivalent small signal diagram.

I.6.4.1 Static characteristics

In general, two types of analog measurement are carried out, known as I-V output characteristics and input transfer characteristics.

- **I-V output characteristics**

Figure I.16 shows the output drain current (I_D) as a function of the drain-source voltage (V_{DS}) while maintaining the gate voltage (V_{GS}) at a constant value. This gives three possible zones representing the transistor's operating regime:

a. **Ohmic zone**: In this zone, the I_D current increases linearly as a function of V_{DS}. As the speed of the electrons in the channel is proportional to the applied electric field, the current increases with this field, as shown by the following equation:

$$I_D = qn_s V_{eff} W_g \quad \text{I.29}$$

Where V_{eff} is the effective speed of the electrons, W_g is the width of the gate [50]. This zone is limited by the knee voltage (V_{Knee}) which is defined as the voltage at which the current undergoes a break between the linear zone and the saturation zone.

b. **Saturation zone:** In this zone, the I_D is practically constant but varies according to the gate-source voltage, i.e., the I_D current is independent of the V_{DS} voltage. By increasing the applied field, the electrons in the channel reach their saturation speed (V_{sat}), as a result, the I_D current reaches saturation, and is given by:

$$I_{D,\,sat} = qn_s V_{sat} W_g \quad \text{I.30}$$

c. **Avalanche zone:** In this zone, the drain current rises suddenly and sharply until the component can no longer withstand it and is destroyed. This phenomenon occurs when the field in the channel reaches the critical breakdown value.

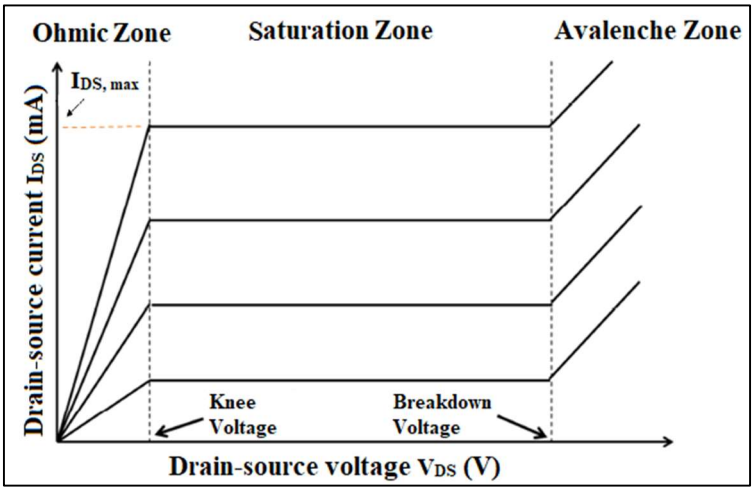

Figure I.16 I_D-V_{DS} output characteristic [50].

In addition, an important parameter can be extracted from these output characteristics: is the on-resistance "R_{on}" value, which can be extracted from the intersection between the tangent and the x-axis in the linear region of the $I_D(V_{DS})$ curve, or by plotting its inverse derivative by Equation I.31 below:

$$R_{on}= \frac{\Delta V_{DS}}{\Delta I_D}\Big|_{V_{GS}=cste} \quad \text{I.31}$$

- **Input transfer characteristics**

The input transfer curve is obtained by measuring the drain current I_D at a given voltage V_{DS} and varying V_{GS}. This variation reveals two operating zones as a function of the pinch-off voltage (V_p) (See Figure I.17.(a) [51].), which can be defined as the voltage transition from the off-state to the on-state:

a. For $V_{GS} < V_p$: In this zone, the carrier density in the channel is zero, i.e., deserted channel and the component is in the blocked state.

b. For $V_{GS} > V_p$: As the gate voltage increases, both the electron density and the drain current in the channel increase until the operating point at maximum current is reached, this bias point presents the beginning of the saturation zone.

Several parameters can be determined graphically from the $I_D(V_{GS})$ curve:

a. The threshold voltage (V_{th}) is the gate voltage at the moment the channel begins to open allowing the carriers to conduct. It can be extracted from the intersection between the tangent and the x-axis in the linear region of the $I_D(V_{GS})$.

b. The transconductance (g_m), in Simens, is an important parameter that can be determined from the first derivative of the $I_D(V_{GS})$ characteristic and reflects the capacity of the gate to control the drain current, is given by:

$$g_m= \frac{\Delta I_D}{\Delta V_{GS}}\Big|_{V_{DS}=cste} \quad \text{I.32}$$

c. The drain leakage current by logarithmic scaling plot of the transfer characteristics (Log (I_{DS}) versus (V_{GS})) to determine the drain leakage current (Figure I.17 (b)).

d. The I_{on}/I_{off} ratio is an important figure of merit for HEMT transistors. It is the ratio between the I_D drain currents in the on-state and in the off-state. This ratio is intended to be as high as possible.

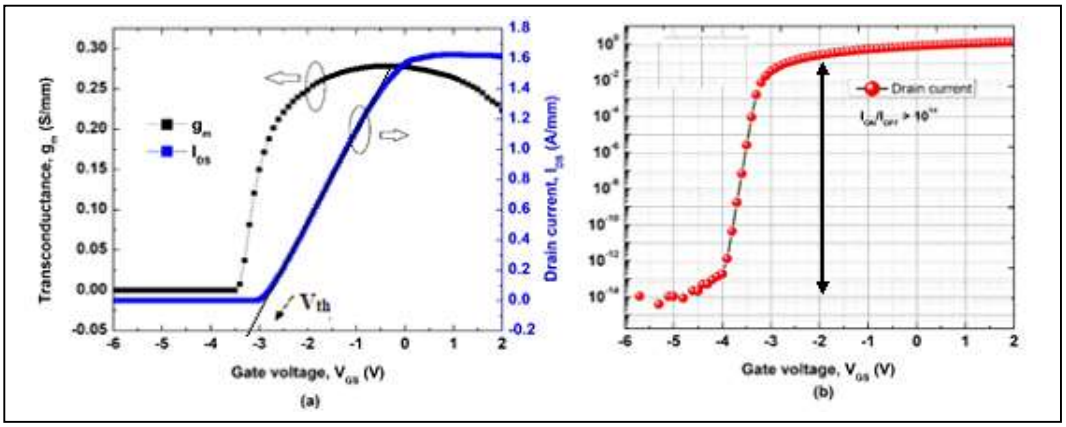

Figure I.17 (a) I_D (V_{GS}) and g_m curves in linear scale, (b) I_D (V_{GS}) curve in logarithmic scale.

I.6.4.2 Dynamic characteristics (AC)

- **Gate-source capacitance (C_{GS})**

The gate-source capacitance describes the capacitive interaction between the gate and the source at the input of the component as a function of the charge under the gate, as follows:

$$C_{GS}= \frac{\partial Q}{\partial V_{GS}} \qquad \text{I.33}$$

- **Gate-drain capacitance (CGD)**

This reflects the capacitive interaction in the semiconductor between the gate and the drain. Analytically, the C_{GD} capacitance is defined by:

$$C_{GD}= \frac{\partial Q}{\partial V_{GD}} \qquad \text{I.34}$$

This capacitance degrades the dynamic performance of the device at high frequencies in different ways. Firstly, due to the Miller effect: part of the C_{GD} is transferred to the input of the transistor and added to the C_{GS} capacitance, resulting in a reduction in extrinsic gain. In addition, this parasitic capacitance short-circuits the source by direct coupling [22].

- **Drain-source capacitance (CDS)**

The origin of C_{DS} is the capacitive interaction between the two regions of the channel under the drain and source ohmic contacts.

- **Transition frequencies**

In the small signal regime, the transistor can be likened to a quadripole nerwerk, as shown in Figure I.18.

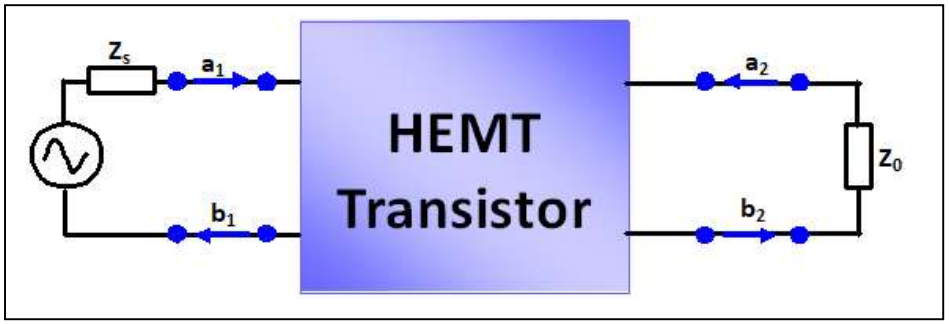

Figure I.18 Quadripole representation, adapted from [52].

The input of the quadripole is connected to an alternating current generator and impedance Z_s and is loaded onto an impedance Z_0. This diagram is adapted to determine the current gain $|H_{21}|$ and the unilateral power gain U_g of the HEMT device [52]. The progressive waves of power incident and reflected by the HEMT ports a_i and bi, make it possible to establish the S-parameters dispersion of the quadripole via the following equations [53]:

$$b_1 = S_{11}a_1 + S_{12}a_2 \quad \text{I.35}$$

$$b_2 = S_{21}a_1 + S_{22}a_2 \quad \text{I.36}$$

The S-parameters dispersion are therefore complex wave ratios at a given frequency:

$$S_{11} = \frac{b_1}{a_1}\Big|_{a_2=0}, S_{12} = \frac{b_1}{a_2}\Big|_{a_1=0}, S_{21} = \frac{b_2}{a_1}\Big|_{a_2=0}, S_{22} = \frac{b_2}{a_2}\Big|_{a_1=0} \quad \text{I.37}$$

Where,

- S_{11} = Input reflection coefficient.
- S_{22} = Output reflection coefficient.
- S_{21} = Forward voltage gain.
- S_{12} = Reversed voltage gain.

The current and the unilateral power gains are expressed as a function of S-parameters:

$$H_{21} = \left|\frac{-2S_{21}}{(1-S_{11})(2-S_{22})-(S_{12}S_{21})}\right| \quad \text{I.38}$$

$$U_g = \frac{|S_{21}|^2}{(1-|S_{11}|^2)(1-|S_{22}|^2)} \quad \text{I.39}$$

These two gains are used to define the two operating frequencies of a HEMT, which are:

- Cut-off frequency (f_t) defined as the frequency at which the modulus of the current gain ($|H_{21}|$) equals 0dB. This frequency corresponds to the time taken for the electrons in the 2D gas to transit under the gate. Mathematically, the cut-off frequency is given by:

$$f_t = \frac{G_m}{2\pi\,(C_{GS} + C_{GD})} \qquad \text{I.40}$$

Therefore, to obtain a maximum transition frequency, it is necessary to maximize the transconductance and reduce the gate length [54].

- Maximum frequency (f_{max}) for which the power gain (U_g) equals 0dB, is given by:

$$f_{max} = \frac{f_t}{2\sqrt{G_d\,(R_G+R_S) + 2\pi f_t\,(R_G C_{GD})}} \qquad \text{I.41}$$

Where Gd is the output conductance, RG and RS are the gate and the source resistances, respectively. Based on these equations, improving the RF performance requires a reduction in other parameters, namely: the output conductance and the input resistances [33, 55].

I.6.4.3 Small signal linear equivalent diagram

The small-signal equivalent diagram of a HEMT exposed to a low-amplitude sinusoidal wave can be drawn using the intrinsic and extrinsic elements. These parameters describe the HEMT effect and the parasitic elements resulting from its structure. Figure I.19 shows a schematic representation of the basic elements of a small-signal linear equivalent diagram.

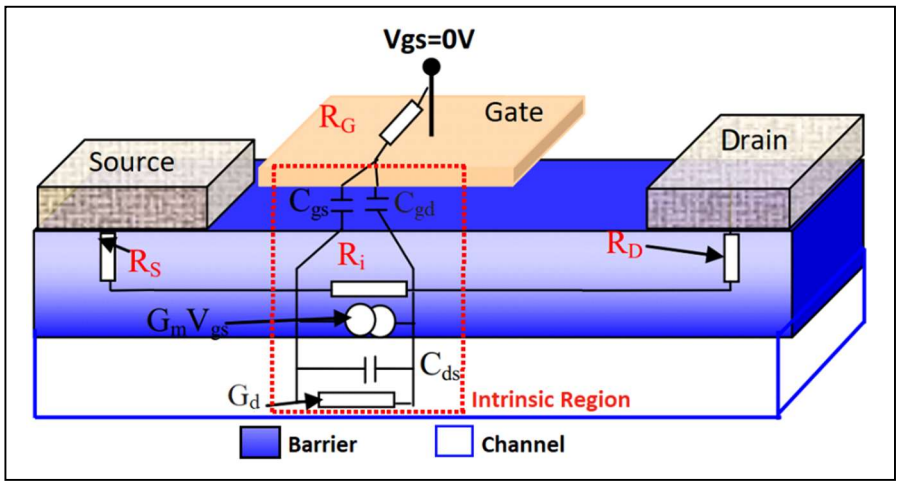

Figure I.19 Schematic of the basic elements of small signal equivalent diagram [22].

These elements are :

- **Intrinsic elements:** They characterize the active aspect of the transistor (fit inside the dotted box in Figure I.19), they depend on the bias applied to the transistor, including:
  a. **The transit time of the electrons under the gate (τ):** It represents the delay time taken for the charge to redistribute after a fluctuation in the gate voltage.
  b. **The transconductance (G_m):** It is a crucial transistor parameter reflecting the gate's ability to control the current.

c. **The output conductance (G_d):** It represents the inverse of the drain-source resistance (R_{DS}), it should be minimized, as it opposes current control by the gate [22].

d. **The intrinsic capacitance**: including the gate-source capacitance (C_{GS}), the gate-drain capacitance (C_{GD}), and the drain-source capacitance (C_{DS}).

e. **The channel resistance (R_i):** It is adapted to the source-gate length and source-gate capacitance. The smaller this resistance is, the faster the device becomes [56].

- **Extrinsic elements:** They represent the parasitic elements in the access zones between the active part and the metal contacts connecting the transistor to the rest of the circuit. They are assumed to be independent of the transistor's polarization and operating regime.

  There are various extrinsic parameters:

  Figure I.20 shows the extrinsic elements outside the dotted box.

a. **Extrinsic resistances:** They represente by the ohmic contact resistances which are the source (R_s) and drain (R_d) resistances. In addition, the Schottky gate resistance (R_g).

b. **The parasitic capacitances C_{PG} and C_{PD}**: They are the capacitances induced by the gate and drain accesses with respect to the substrate.

c. **The parasitic inductance L_G, L_D, and L_G**: These inductances model the effect of the device's electrode connection wires, which depend on the dimensions of the transistor.

.

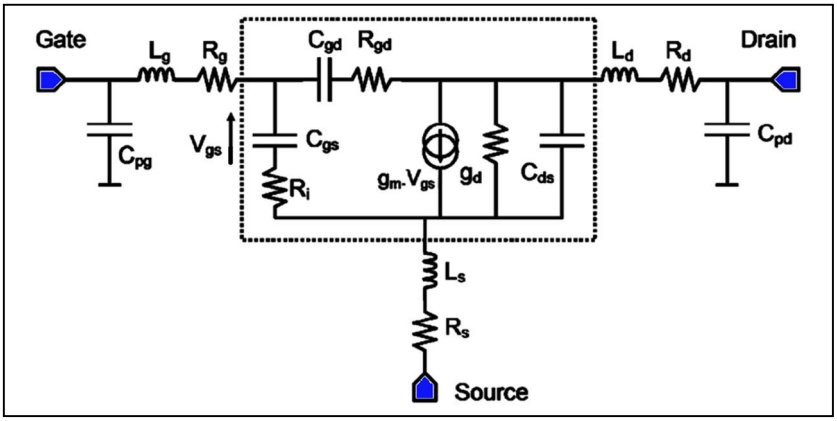

Figure I.20 Complete small signal equivalent circuit of transistor [57].

I.7 Conclusion

In this first chapter, we studied the main structural, electrical, and electronic properties of binary ternary and quaternary materials. The studied materials will be used in the characterization of our transistors. After a brief evaluation of the peculiarities of structure and growth specifics of IIIA-nitride materials the principle of AlGaN/GaN and AlInGaN/GaN heterojunction is reviewed. Finally, high electron mobility transistor (HEMT) is presented in detail as the main applications of the studied materials.

Chapter II Normally-off AlGaN/GaN MOSHEMT transistor

II.1 Introduction

GaN-based HEMTs have evolved considerably since their inception. After a brief assessment, in the previous chapter, of the particularities of the IIIA-N materials and the properties of heterojunction devices, we review here our choice of research. To improve performance, technological advances need to be incorporated into the basic structure of HEMTs. One of the difficulties encountered with this technology is the creation of an enhancement-mode transistor with a low leakage current. The solution adopted is to design HEMT structures by adding oxide materials, thus forming a MOSHEMT (Metal-Oxide-Semiconductor-HEMT) heterostructure [1].

This chapter discusses several challenges and limitations of GaN-based HEMTs. For most of these challenges, different technological solutions have been proposed. This is followed by a theoretical study of the MOSHEMT transistor and their applications. We will then study the electrical characteristics of a new MOSHEMT structure using a new oxide material, namely β-Ga_2O_3, the results of which form part of this study.

II.2 New challenges for HEMT devices and the available solutions

Despite the remarkable performance of HEMT transistors, understanding the fundamental properties of materials and devices remains an open question. These include not only material selection and device geometry but also other important properties such as leakage current sources, mode of operation, and degradation mechanisms [58]. This section describes the main challenges posed by HEMTs and the available technical solutions.

II. 2. 1 Device geometry

For GaN-based HEMTs, the device geometry must be optimized to achieve high breakdown voltage and high-frequency performance. The main objective of HEMT design is to maximize breakdown voltage (V_{BR}) while minimizing on-resistance (R_{on}). This can be achieved by increasing the scale of the device by extending the gate-to-drain distance.

Furthermore, the distribution of the electric field in the channel is not homogeneous. When the transistor is biased by a drain-source voltage (V_{DS}), the electric field in the gate-drain region increases drastically. This sudden increase in the electric field causes an electrical overload that could destroy the component. Therefore, widening the gate-drain distance provides better electric field distribution, leading to higher breakdown voltage. This in turn increases the size of the access region, which raises R_{on} and therefore on-state losses.

In a HEMT device, the relationship between the specific on-state resistance ($R_{on,\,sp}$) and the breakdown voltage (V_{BR}) is given by the following expression:

$$R_{ON,sp} = \frac{V_{BR}}{q\mu_n n_s E_c} \ (m\Omega.cm^2) \qquad \text{II.1}$$

Where:

$$R_{on,\,sp} = R_{on} \times L_{SD} \qquad \text{II.2}$$

Figure II.1 presents a comparison between Si, GaAs, and GaN technology in terms of their specific on-resistance and breakdown voltage. GaN has potentially the lowest on-resistance and the highest breakdown voltage thanks to its superior material quality.

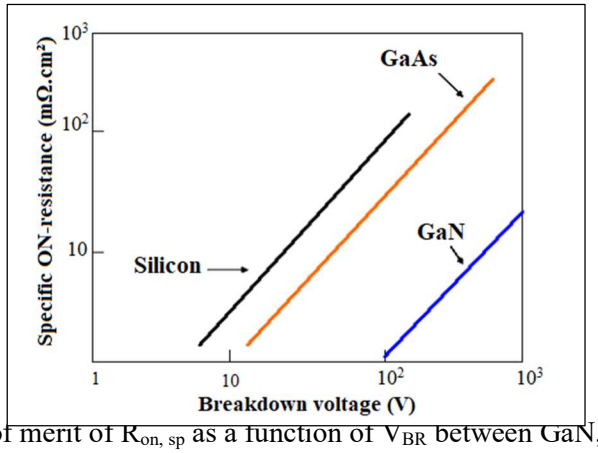

Figure II.1 Figure of merit of $R_{on,\,sp}$ as a function of V_{BR} between GaN, GaAs, and Si.

The on-resistance is a figure of merit of the GaN-based HEMTs that characterizes its breakdown voltage and reliability [59]. It depends on the resistance and length of the device regions, as shown in the cross-section of Figure II.2.

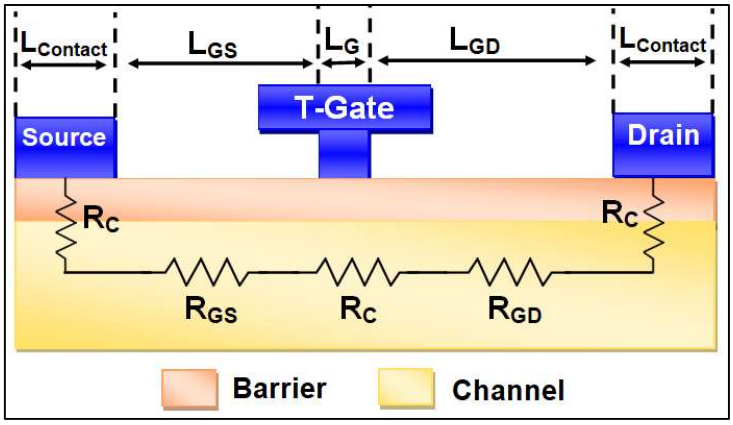

Figure II.2 Schematic of a HEMT demonstrating the total access resistance, adapted from [60].

The total access resistance (R_{on}) can be calculated using Equation II.3 [61]:

$$R_{on} = 2R_C + R_{GS} + R_{GD} + R_{CH} \qquad \text{II.3}$$

Where R_C is the ohmic contact resistance, R_{GS} and R_{GD} are the gate source and the gate-drain resistances, and R_{CH} is the resistance of the channel under the gate foot.

All of these resistances are calculated based on the fundamental geometrical parameters of the HEMT structure, namely: gate length (L_g), gate-drain length (L_{GD}), gate-source length (L_{GS}), and barrier height (d_{bar}). Initially, R_{GS} and R_{GD} were introduced by Saito et al. [61]:

$$R_{GS}= \frac{L_{GS}}{q\mu_n n_{S,1}} \quad \text{II.4}$$

$$R_{GD}= \frac{L_{GD}}{q\mu_n n_{S,2}} \quad \text{II.5}$$

With $n_{s,1}$ and $n_{s,2}$ are the 2DEG density in the active region between source and gate and between gate and drain, respectively. Furthermore, the calculation of the channel resistance R_{CH} varies depending on the device technology, e.g. HEMT or MOSHEMT, the latter is the case of this research. First, for HEMT structures R_{CH} is given by:

$$R_{CH} = \frac{L_G}{\mu_n C_G (V_{G,ON} - V_{TH} - \Phi_b)} \quad \text{II.6}$$

Where $V_{G,ON}$ is the on-state gate voltage. C_G is the gate capacitance [61], it is calculated as a function of the gate area ($A_G=L_G \times W$, W is the device width), the permittivity and thickness of the barrier as follows:

$$C_G= \frac{A_G \varepsilon_{bar}}{d_{bar}} \quad \text{II.7}$$

For MOSHEMT devices, the equation of the R_{CH} changes due to the presence of an oxide layer between the gate and the layers that directly influence the gate capacitance $C_{G,oxide}$), and metal-oxide barrier height ($\Phi_{b/oxide}$) [62], as follows:

$$R_{CH}= \frac{L_g}{\mu_n C_{G,oxide} (V_{G,ON} - V_{TH} - \Phi_{b/oxide})} \quad \text{II.8}$$

Where:

$$C_{G,oxide}= \frac{\varepsilon_{bar} \times \varepsilon_{oxide}}{\varepsilon_{bar} \times d_{oxide} + \varepsilon_{oxide} \times d_{bar}} \quad \text{II.9}$$

With ε_{oxide} and d_{oxide} represent dielectric constant and thickness of the oxide.

For high-power devices, the R_C, R_{GS}, R_{GD}, and R_{CH} resistances must be minimized as much as possible, here are several technical solutions:

- R_C is minimized by adding a heavily doped n++ GaN layer to optimize the ohmic contacts, this method is known as regrown source/drain technology [63].
- R_{GS} and R_{GD} can be minimized by employing a barrier thickness that creates high 2DEG.
- R_{CH} can be decreased by using short gate lengths [64].

For instance, Dong-Seup et al. experimentally demonstrate a low R_{on} of 0.4 Ω.mm and a high transition frequency of 317 GHz using regrown source/drain AlInGaN/GaN MOSHEMT with a short gate length of 26nm [65].

The field plate gate structure is another method to achieve higher breakdown voltage. It consists of extending the metal from the gate to the drain. It has been used to improve the electric field distribution at high-bias voltage. As the technology studied in this thesis aims to create RF transistors, this method is not used as it significantly increases the gate-drain capacitance, resulting in increased transit time and reduced frequency performance [8].

For this reason, the ultra-short gate length with T-shape structures technique is adopted, leading to a significant decrease in gate capacitance and thus allowing higher frequency to be achieved. To date, most papers have focused on assessing the reliability of ultra-short gates with T-shaped structures. [48]. Next figure shows a flow chart of the main geometrical impact on HEMT transistor performance.

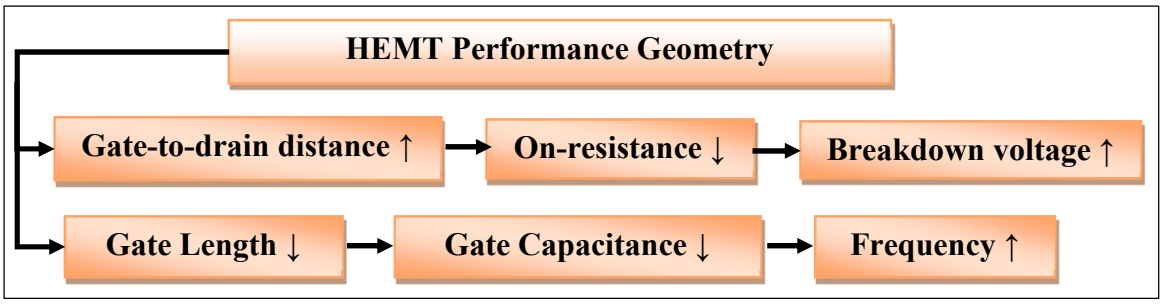

Figure II.3 Flow chart of the principal geometrical effects on HEMT device performance.

II. 2. 2 Substrate choice

Heteroepitaxy of GaN crystals on alternative substrates is becoming a real challenge due to some critical factors that will be discussed in this section. The HEMT transistors on Silicon, sapphire, SiC, GaN, diamond, and more recently β-Ga_2O_3 substrates are studied and experimented by many researchers. Table II.1 contains a list of the main characteristics of the majority of prevalent substrates in terms of material availability, manufacturing cost, electrical and thermal properties. Each of these substrates has benefits and drawbacks [66].

The key parameter for obtaining good heteroepitaxy is the lattice mismatch. This parameter guarantees superior crystalline quality because the smaller it is, the lower the

dislocation density. It is defined as the difference in spacing in the Basal plane between the GaN layer and the substrate and is expressed as:

$$a = \frac{a_{sub} - a_{GaN}}{a_{GaN}} \qquad \text{II.10}$$

The thermal expansion mismatch coefficient (CTE) must also be taken into account; it can be used to measure the deformation in the crystal between two materials as a function of temperature change [67].

Silicon and sapphire were the first substrates used for GaN growth because of their relatively low cost, availability in large wafers, and high thermal and mechanical stability. However, they have the largest lattice mismatch with GaN, 17% and 14%, respectively, resulting in considerable mechanical stresses and dislocations densities ($\approx 10^{10} cm^{-2}$) [23, 48].

Diamond substrates, renowned for their ultra-high bandgap, exhibit the highest thermal conductivity among all known materials, which significantly mitigates the self-heating effect. Nevertheless, the fabrication of GaN on diamond substrate poses certain problems: the large lattice mismatch (around 13%), and very high costs [68].

Intensive research and development are conducted to improve the growth quality of GaN as a substrate because of its excellent properties. With no lattice mismatch, the homoepitaxy of GaN on a bulk GaN substrate has advantages in terms of structural defect reduction and dislocation suppression, making it a preferred choice for GaN HEMTs [69]. However, large-scale production of GaN substrates is technically challenging and overpriced.

The availability of other substrates with the same lattice parameter as GaN could help reduce manufacturing costs by simplifying the growth process. One of the main areas of scientific interest is silicon carbide (4H-SiC), which has a closer lattice match to GaN, only 3.5%, resulting in reduced defects and improved crystal quality, and is the best choice for RF operation [70]. Thanks to its excellent thermal conductivity, the 4H-SiC substrate provides better heat dissipation and withstand high temperatures [31]. Unfortunately, the size of this substrate available on the market is relatively small and its cost remains considerably high.

As a result, finding an alternative substrate that is inexpensive, easy to produce, and widely available is becoming increasingly important. It has recently been shown that GaN-based HEMTs are being developed using an emerging substrate, namely β-Ga_2O_3 (beta-phase gallium oxide), which has an ultra-wide band gap and a large breakdown field [51, 71, 72].

The use of β-Ga_2O_3 substrate remains an area of development in the next generation of RF circuits, as it has all the qualities required to be a high-performance substrate. The potential advantage of using β-Ga_2O_3 is its closest lattice match to GaN and AlN with only 4.7% and 2.4% mismatch [73]. In addition, β-Ga_2O_3 exhibits good thermal conductivity and can dissipate heat efficiently. Therefore, β-Ga_2O_3 can offer two fundamental advantages over SiC and GaN: fewer defects in the structure and ease of large-scale production at low cost.

When choosing the substrate, only materials with lattice constants relatively close to that of GaN are preferred in practice. This limits the excellent substrate used to 4H-SiC, GaN, and β-Ga_2O_3, and so these substrates will be utilized for the remainder of this thesis.

The properties presented in Table II.1 can be used to calculate Baliga's Figure of Merit (BFOM) defined as follows: $BFOM = \varepsilon \mu E_{BR}^3$. The BFOM of β-$Ga_2O_3$ is about 4 times greater than that of GaN and more than 200 times greater than that of silicon [74].

Table II.1 Principal properties of substrate materials [3, 22, 75].

Substrate	Si	Sapphire	GaN	4H-SiC	β-Ga_2O_3	Diamond
Cost	low	low	high	moderate	low	high
a	17%	14%	0%	3.5%	4.7%	13%
E_g (eV)	1.1	6.1	3.4	3.2	4.9	5.5
ε	11.8	8.5	9	9.7	10	5.5
E_{BR} (MV/cm)	0.3	12	3.3	2.2	8	10
μ_n ($cm^2/V.s$)	1500	4000	1000	1250	140-300	2000
V_{sat} ($10^7 cm/s$)	1	1.5	2	2.5	1.8-2	1
κ (W/cm K)	1.5	0.5	1.3	3-3.8	3.7-4.5	22.9
CTE ($10^{-6}/K$)	2.59	7.5	5.59	4.2		1
BFOM	1	-	870	340	3444	24664

II. 2. 3 Leakage current

The off-state leakage current must be kept to a minimum in any transistor configuration. Generally, there are three possible tunneling leakage current paths in HEMTs as shown in Figure II.4. Several techniques have been proposed to suppress these leakage currents [75]. The following paragraphs detail these limitations and the corresponding solutions:

a. **Substrate leakage current (type (1)):** these leakage currents flow through the lower part of the channel and penetrate the substrate. This is due to the low crystalline quality in this area, because of the large lattice mismatch between the semiconductor layers and the substrate material. Many solutions were proposed to reduce this leakage, including: increasing the thickness of the GaN channel, inserting the nucleation layer, and using an appropriate substrate with a lattice parameter close to the GaN channel [76].

b. **Channel leakage current (type (2)):** this leakage passes through the channel, due to the weaker confinement of electrons in the 2DEG quantum well. To solve this problem, two solutions have been proposed. The first is to separate the barrier layer and the GaN channel with a thin spacer layer, the material inserted should have broad bandgap energy to enhance the stockpiled of electrons such as AlN or AlInGaN. The second solution consists of introducing an AlGaN back-barrier under the channel [76].

c. **Gate leakage currents (types (3)):** in this leakage current, the electrons come straight from the gate and pass the barrier, causing higher power consumption and strong noise. To reduce these leakage currents, it is necessary to increase the insulation of the Schottky contact by adding a GaN cap layer or by depositing an oxide layer under the gate, creating a metal-oxide-semiconductor (MOS)-HEMT [22].

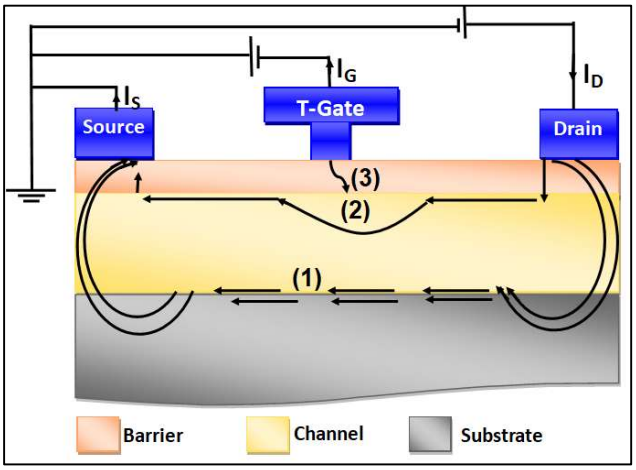

Figure II.4 Leakage current path in HEMT design, adapted from [75].

II. 2. 4 HEMT operating mode

The operating mode of the standard GaN-based HEMTs is normally-on due to the natural creation of 2DEG gas even in the absence of gate voltage, i.e., it naturally conducts current. Consequently, the application of a negative voltage to the gate is then necessary to cut the channel and place the HEMT in the off-state. Others use the term depletion mode (D-mode) to indicate that the action of VGS is to deplete the channel of its carriers with a negative threshold voltage (V_{TH}<0) [17].

However, the D-mode operation is not suitable for RF applications since an additional current is required to bias the device in the off-state, making it unsafe. This mode is the opposite of the enhancement mode (E-mode). Initially, the device is in the off state (normally-off mode); as soon as a positive voltage is applied to the gate, the 2DEG channel is confined and enhanced,

placing the HEMT in an on-state so that the device begins to conduct current. [77]. Figure II.5 shows the different ways in which HEMT works, showing its input and output characteristics.

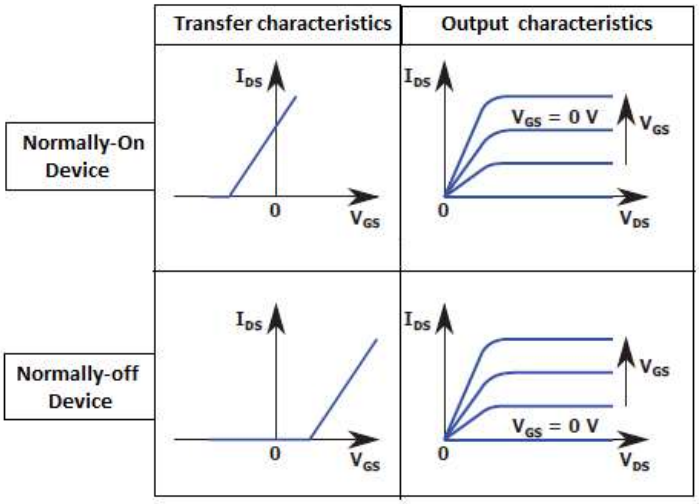

Figure II.5 Input/Output characteristics of normally-on and normally-off operations [62].

II.2.4.1 Benefits of normally-off HEMTs

The main advantage of normally-off HEMTs is the higher safety that they provide for both the equipment and its users, i.e., if there is no input voltage the device acts as an open circuit without risk of runaway, protecting the circuit from any further damage. Unlike their D-mode counterparts, E-mode devices only operate with positive gate voltage, which is advantageous to simplify the integration of HEMTs into MMIC circuits and reduce manufacturing costs [14].

II.2.4.2 Methods to achieve the enhancement mode

Numerous technological solutions have been proposed to realize the enhancement mode. Analysis of the classic model of the threshold voltage (Equation II.11) enables us to identify the various ways of moving it toward positive values:

$$V_{th} = \frac{1}{q}\left(\Phi_b - \Delta E_C - \frac{q d_{bar}}{\varepsilon_{bar}}\sigma_{int}\right) \qquad \text{II.11}$$

It is possible to positively shift V_{th} by decreasing the barrier layer thickness or by acting on the Schottky barrier height. Among the many methods proposed in the literature:

- **Thin barrier layer**

The use of a thin barrier brings the gate electrode closer to the 2DEG channel. Thus, if the gate is close enough, the depletion zone generated by the metal-semiconductor Schottky contact can extend as far as the electron gas and therefore cause the threshold voltage to rise [78]. Nevertheless, using a thin barrier will decrease the sheet charge density to solve this

problem a barrier richer in aluminum is adequate, leading to a change in polarization effects and therefore an increase in n_s despite the thin barrier thickness [14].

- **Recess gate**

In the recessed gate structure, the barrier is locally etched under the gate foot with a size of a few nanometers, as illustrated in Figure II.6. The manufacturing principle of the recessed gate consists of locally reducing the thickness of the AlGaN barrier layer under the gate foot. As a result, a high 2DEG density is maintained in the source and drain access area, while gate control is carried out on a thinned barrier, thus retaining a normally-off functionality [17].

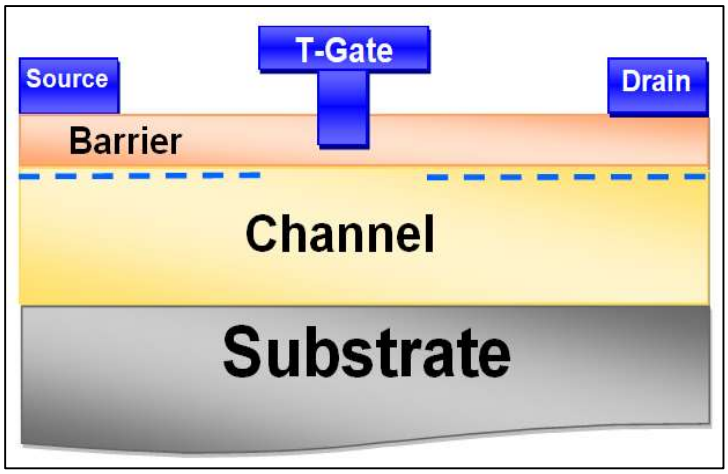

Figure II.6 Schematic configurations for normally-off approaches using a recessed gate.

- **P-doped GaN cap**

This method involves growing a p-doped GaN cap only where the gate is deposited.

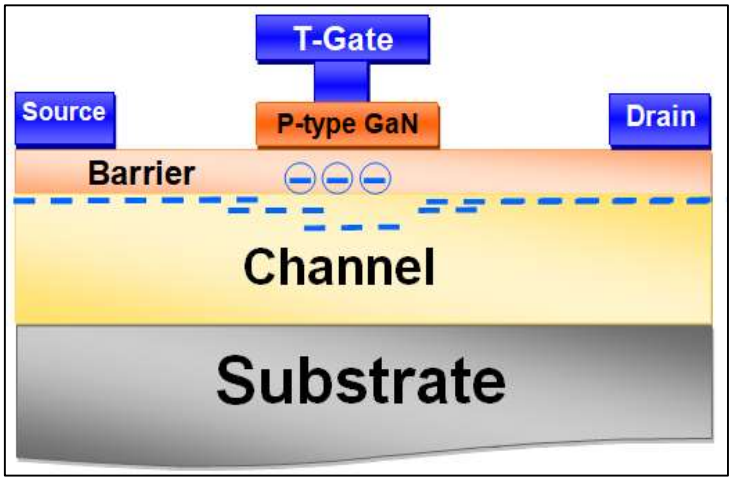

Figure II.7 Schematic configurations for normally-off approaches using p-GaN cap.

In this case, at zero bias, the depletion region can extend as far as the 2DEG channel, thus making the transistor normally-off, as shown in Figure II.7. The thickness and doping level of the p-GaN cap must be kept low enough to allow the gate to modulate the voltage [79].

- **Fluorine ions implantation**

This method is based on the implantation of a negative charge fluoride ions below the gate. These F-ions act as fixed charges in the barrier and thus induce a conduction band and therefore the creation of the 2DEG potential well. The introduced negative charge produces a positive shift of the V_{th} [79]. Figure II.8 is a schematic of the F-ions technique.

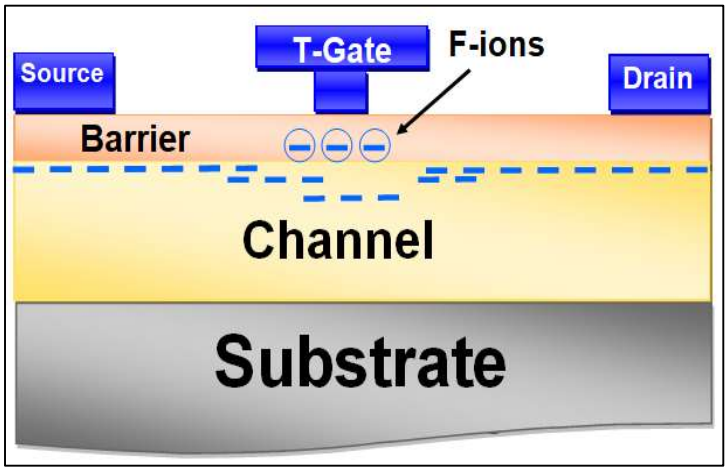

Figure II.8 Schematic configurations for E-mode HEMT using Fluorine ions technique.

- **Bande engineering**

The solutions presented here use additional epitaxial layers in the basic structure of a HEMT in order to raise the conduction band. In reality, the introduction of this method is not sufficient in itself to achieve E-mode operation. It is almost exclusively used in conjunction with one or more other techniques

a. **GaN cap layer:** The addition of a thin GaN cap layer leads to an increase in the effective height of the Schottky barrier, thereby raising the conduction energy band [49].
b. **Gate dielectric layer**: The deposition of a dielectric between the barrier and the gate is necessary for E-mode devices to accumulate carriers in the channel without drawing excessive leakage current. [49].
c. **Back-barrier**: This layer presents a second barrier that can raise the conduction band at the 2DEG channel, facilitating normally-off operation, especially with thin channels [49].
d. **AlInGaN barrier:** A new approach to realize E-mode operation is to replace the ternary AlGaN barrier with a quaternary AlInGaN barrier. Based on the polarization engineering

method that leads to reduce the polarization in the barrier, and the dependence on V_{TH} and barrier thickness to maintain a sufficient conduction band offset [31].

- **Recapitulative table**

Table II.2 summarizes the advantages and disadvantages of each of the E-mode techniques presented above.

Table II.2 Advantages and disadvantages of the enhancement mode technological solutions.

Normally-off Design	Advantages	Disadvantages
Thin barrier	- Achieve E-mode operation - Enhance the frequency performance.	- Reduce the 2DEG, hence, the drain current. - High access resistance.
Recessed gate	- Achieve E-mode operation. - Ameliorate the drain current density. - Reduce the access resistance.	- High leakage current. - High trap density.
P-doped GaN cap	- Achieve E-mode operation.	- Difficulty of doping p.
F'ions implantation	- Achieve E-mode operation.	- High trap density.
GaN cap	- Help to achieve E-mode operation. - High Schottky barrier.	- Not enough to normally-off.
Gate dielectric	- Help to achieve E-mode operation. - Reduce the gate leakage current.	- Not enough to normally-off.
Back-barrier	- Help to achieve E-mode operation. - Reduce the substrate leakage current.	- Not enough to normally-off. - Need for a thin channel.

II.3 Intrinsic limitation of GaN-based HEMT

The aforementioned technological challenges can be avoided by selecting an appropriate material and designing the device correctly [80]. There are other device degradation factors, known as intrinsic limitations that cannot be avoided. These degradation processes have a negative effect not only on the electrical characteristics but also on the durability and reliability of the device, resulting in shorter lifetimes and failures.

Furthermore, the theoretical maximum output power that can be delivered by an AlGaN/GaN HEMT can be estimated from its $I_D(V_{DS})$ output characteristics as follows:

$$P_{out} = \frac{1}{8} I_{D,max} - (V_{BR} - V_{KNEE}) \qquad \text{II.12}$$

The mechanisms of intrinsic degradation of HEMTs will then be detailed.

II. 3. 1 Trapping effects

At strong polarization, it has been demonstrated that the drain current is temporarily reduced. This reduction is the direct result of traps at the surface and in the deep levels of the

HEMT transistor. In general, the physical origin of these trapping phenomena is the presence of impurities located on the surface of the device. These impurities capture and then re-emit charge carriers. As a result, the charge carriers do not participate in conduction and the drain current is reduced [81]. As shown in Figure II.9, two groups of traps can be considered:

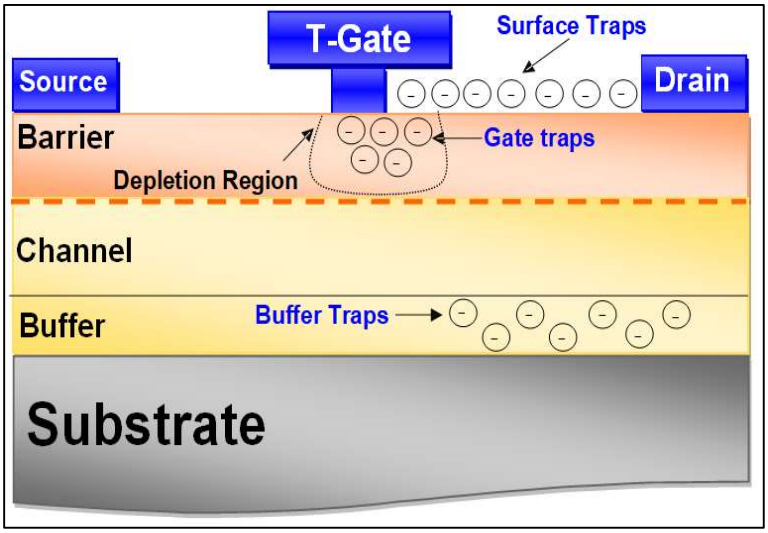

Figure II.9 Descriptive scheme of the trapping mechanisms in the HEMT transistor [60].

- **Gate-lag mechanism:** It reacts when there is an abrupt variation in the gate voltage that causes electrons to leak onto the surface of the component, in particular between the gate and the drain. As a result, the ionized surface donors capture these electrons, creating a new depletion region of the channel [56]. This effect was considered as a "virtual gate" which describes the accumulation of electrons in the proximity of the gate caused by surface traps.
- **Drain-Lag mechanism:** It reacts to sudden changes in the drain voltage that increase the electric field significantly across the device, hence, the electrons in the channel become excited. As a result, these electrons can leak out in the depth of the channel (the buffer), prompting a considerable reduction in the drain current [60].

II. 3. 2 Current collapse

Another important parameter in assessing the reliability of HEMTs is the current collapse, which is defined as the reduction in the drain current after the application of high voltage. The origin of the current collapse has been attributed to trap mechanisms [82]. The possible preventive mechanisms for minimizing this phenomenon are as follows:

- Using a passivation layer to prevent electrons from passing through the gate and becoming trapped in the surface [60].
- Depositing a gate dielectric layer to reduce the gate leakage current [83].
- Using a gate field plate to cause relaxation of the electric field at the side of the drain [84].

Figure II.10 shows the impact of the current collapse on the output characteristics.

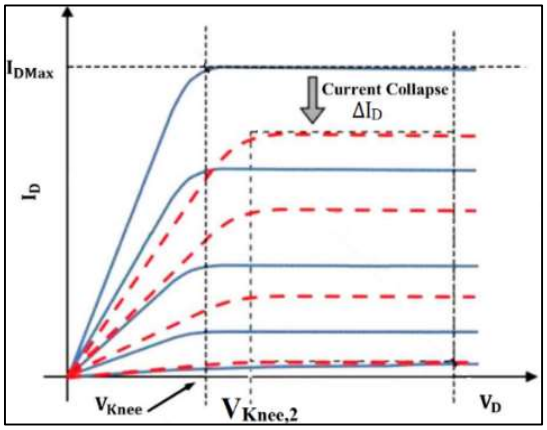

Figure II.10 $I_D(V_D)$ characteristics showing the impact of the current collapse effect; before (solid lines) and after (graded lines) traps [33].

II. 3. 3 Self-heating

At room temperature, when high current flows for a long time, thermal effects are generated due to increased collisions between the free electrons and the crystal lattice, i.e., an increase in the internal temperature of the component. This phenomenon, known as self-heating, is a serious problem in GaN devices, as it can alter the temperature-dependent properties of the material, such as bandgap and mobility, hence, decreasing in the drain current, as shown in Figure II.11. Using a suitable substrate with the highest thermal conductivity, such as 4H-SiC, β-Ga_2O_3, or diamond (see Table II.1) will reduce the self-heating effect [56].

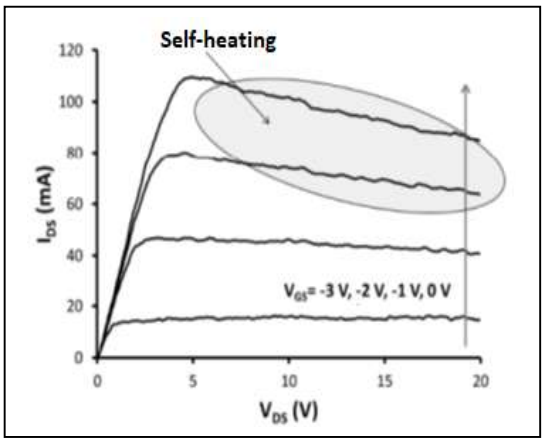

Figure II.11 $I_D(V_D)$ characteristics showing the impact of the self-heating effect [85].

II. 3. 4 Kink effect

The Kink effect occurs when the gate voltage is higher than the pinch-off voltage. It is linked to the presence of surface traps in the semiconductor. This effect is attributed to impact ionization, resulting in an accumulation of holes that modify the surface potentials [86].

The Kink effect is an abnormal phenomenon, demonstrating an increase in the I_{DS} current with V_{DS} pumping down and up, as shown in Figure II.12. The Kink effect leads to an increase

in the output conductance and dispersion between the DC and RF characteristics. Passivation can eliminate this phenomenon.

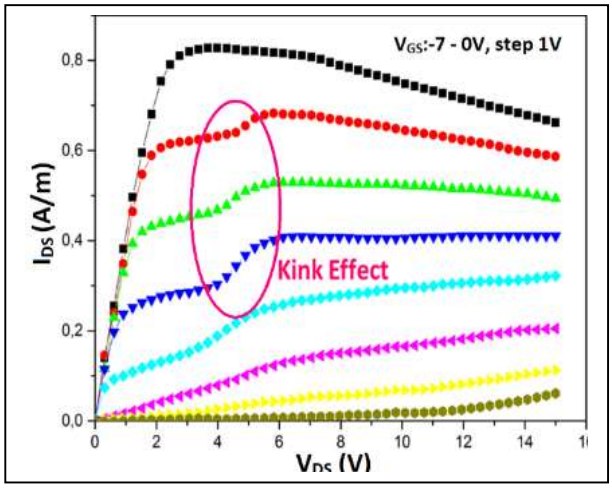

Figure II.12 $I_D(V_D)$ output characteristics showing the impact of the Kink effect [1].

II.4 MOSHEMT device

This thesis aims to create AlGaN/GaN transistors with outstanding performance to realize RF filtering bloc for GNSS receiver applications. To this end, a MOSHEMT structure is used, which involves adding an oxide material between the semiconductor and the gate metal. This technique is strongly advised in order to reduce gate leakage current and boost the component's normally-off operation [23].

The oxide/semiconductor interface is a new interface that forms when the oxide is introduced into the structure. The mechanical stress of this additional layer causes the AlGaN barrier to become piezoelectrically polarized. It is feasible to lessen the contribution of the piezoelectric polarization by decreasing the thickness of the AlGaN barrier layer. For this reason, an optimal barrier thickness is required to promote the formation of the 2DEG [49].

Normally-off MOSHEMT structure is a structure with an open channel between source and drain for any negative or zero gate bias, i.e., no channel is formed (Figure II.13 (a)). increasing the magnitude of the gate voltage ($V_{GS} > 0$) increases the electric field and therefore attracts more free electrons towards the gate [23]. This in turn increases the electron density in the channel and hence the current flow (Figure II.13 (b)).

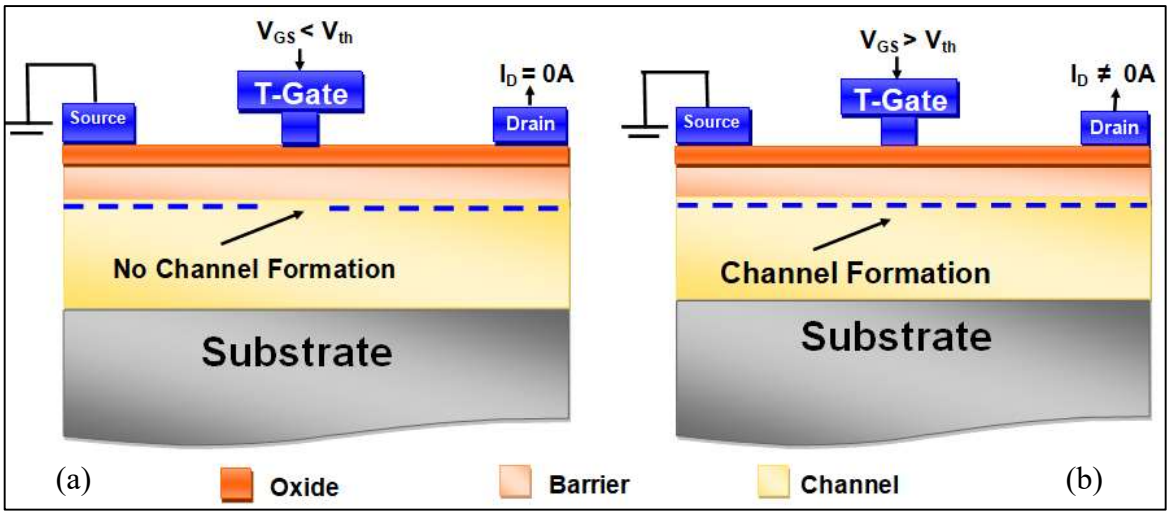

Figure II.13 Operation principle of MOSHEMT device (a) at $V_{GS}<V_{th}$, (b) at $V_{GS}>V_{th}$ [47].

II. 4. 1 High-K materials

The electrical properties of the oxide materials strongly influence the behavior of the MOSHEMT. A wide variety of oxides have been studied. The most promising are: aluminum oxide (Al_2O_3) [39, 87], gallium oxide (Ga_2O_3) [88, 89], hafnium oxide (HfO_2) [90] and titanium dioxide (TiO_2) [91, 92]. Additionally, insulators may be utilized such as silicon nitride (Si_3N_4). Table II.2 lists the main characteristics of various dielectric materials used during this thesis. Their potential advantage is the high dielectric constants combined with good contact insulation

High-k materials are preferable because they do not require a large thickness to significantly reduce the leakage currents. In addition, they prevent the negative V_{th} shift. On the other hand, the bandgap energy and the critical breakdown field of the oxide materials must be higher than that of the barrier in order to withstand the peak electric field [23].

Table II.3 Crystalline and electrical properties for different dielectric materials [22].

Gate dielectrics	k constant	Eg (eV)	E_{BR} (MV/cm)
Si_3N_4	7	5.3	-
Al_2O_3	9	8.7	>10
HfO_2	25	5.5	4
TiO_2	80	3.5	5
β-Ga_2O_3	10	4.8/4.9	8

Unlike the other materials, β-Ga_2O_3 and Al_2O_3 have ultra-wide bandgaps and large breakdown fields, but they have moderate dielectric constants of 10 and 9. On the other hand, HfO_2 and TiO_2 have respectively higher dielectric constants of 25 and 80, but their breakdown fields are relatively low. Considering the criteria that a gate dielectric must meet, HfO_2 and TiO_2 appear to be a suitable material to perform the function of a gate dielectric. It is important

to note that β-Ga_2O_3 is also a perfect contender for use as a gate oxide [93, 94], thanks to its good chemical and thermal stability and excellent cost/performance ratio

II. 4. 2 MOSHEMT applications

GaN-based MOSHEMTs become essential components in many areas of modern electronics thanks to their unique properties and performance [60]. Integrating GaN-based MOSHEMTs into MMIC circuits improves the overall performance of these circuits. Here are just a few of the common applications for (MOS)HEMTs:

- Wireless communications: MOSHEMTs are used in RF amplifiers for wireless applications such as cell phones, Wi-Fi, cellular networks and satellite networks, radars. Their high frequencies and low noise make them ideal choices for these applications.
- Low-noise amplifiers: MOSHEMTs are often used in low-noise amplifiers for applications sensitive to weak signals, such as radio receivers and antennas.
- Power electronics: MOSHEMTs are used in RF switches for power electronics applications such as DC-DC converters and inverters. Their high breakdown voltage and low on-resistance make them effective for power conversion.
- Optoelectronics: MOSHEMTs are used in semiconductor lasers and optical detectors because of their high speed and low noise.

II.5 MOSHEMT simulation

In recent years, due to the high cost of experimentation, researchers have turned to simulation to predict the performance of the nano-electrical components before they are manufactured. The TCAD (Technology Computer-Aided Design) simulators can be used to model and optimize the electrical behavior of an electronic component, identify weak points, and save development time and costs.

In our thesis, we have used the 2D ATLAS-SILVACO tool to study the performance of

ur transistors [29] (see Appendix B). Our work consists of designing MOSHEMT structures by performing the following simulations:

- Energy band diagram, sheet charge density, 2DEG concentration, electric field.
- Static regime: output/input characteristics and transconductance.
- Dynamic regime: capacitance curves and gain frequency characterizations.

II.6 Simulation and characterization of a new β-Ga_2O_3 AlGaN/GaN/AlGaN MOSHEMT (Device A)

In order to confirm the theoretical concepts addressed in this thesis, we have proposed an innovative structure, in which we have integrated several technologies in order to obtain a component that guarantees high performance and may work in the enhancement mode, which is preferable for simplifying the switching circuit and providing greater safety.

Numerous techniques are adopted to achieve normally-off operations such as a thin barrier layer, a recessed gate, a back-barrier, and gate dielectric material. In our first work, we combine all these techniques into a single structure and interpret the results.

The current method used in this section depends primarily on gate foot recess techniques. From the literature, the recessed gate process can lead to an increase in gate current density and therefore in leakage current, but this increase can be contained by deposition of a dielectric under the gate, which is the case of our study

Several conventional oxide materials were widely used in MOSHEMT structure, especially HfO_2, TiO_2, and Al_2O_3. Today, an emerging material has appeared as a key focus of research, thanks to its excellent properties to minimize the gate current losses. Therefore, the novelty in our structure is the use of an UWBG β-Ga_2O_3 as an oxide layer.

We carried out digital simulations of an AlGaN/GaN MOSHEMT transistor using the TCAD ATLAS-SILVACO. Our numerical simulation consists of first designing the structures and then performing numerical resolutions, the steps are mentioned in Appendix B. The numerical resolution involves determining the choice of physical models and mathematical methods used to find the solution. All the physical models mentioned in Appendix B are evoked during the simulation using the Newton method. Our simulations of consists of two steps:

a. Comparison study between conventional and recess gate structures to achieve E-mode.

b. Impact of Al-content of the barrier layer on the electrical characteristics of the device.

And finally, we compare our results with other similar publications.

II. 6. 1 Device Description

Figure II.14 shows a 2D schematic cross section of our first transistor; AlGaN/GaN MOSHEMT grown on GaN substrate (device A). Table II.3 shows its various geometric parameters.

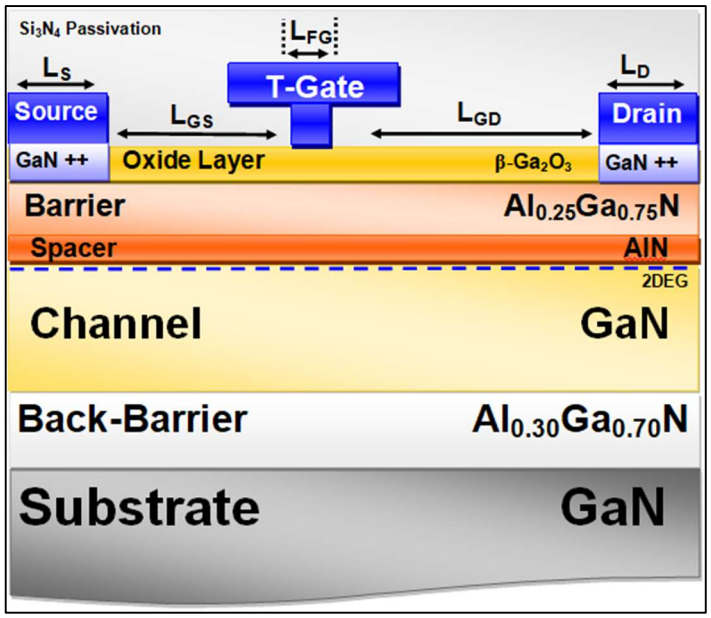

Figure II.14 Structure of the proposed β-Ga_2O_3/AlGaN/GaN MOSHEMT.

An Au-T-gate electrode with 70 nm foot-length is implemented and passivated with Si_3N_4, with a metal work function equal to 5.1 eV. The main advantage of T-shape gate technology is that enable the use of an ultrashort gate length while optimizing gate resistance and capacitance, thereby, alleviating overall device performance. The L_{SG} and L_{GD} are 1.545 µm and 2.042 µm. Low access resistance contact is obtained by regrown source/drain regions with a layer of GaN heavily doped, with 10^{20} cm^{-3} of n-type impurities.

Table II.4 Geometrical specifications of the studied device.

Gate specifications		**Structure specifications**	
Parameter	**Dimension**	**Layer**	**Height**
Gate foot length	70 nm	β-Ga_2O_3 oxide layer	3 nm
Gate head length	300 nm	$Al_{0.25}Ga_{0.75}N$ barrier	13.5 nm
Gate stem height	50 nm	AlN spacer	1.2 nm
Gate-drain distance	2.042 µm	GaN channel	1.9 µm
Gate-source distance	1.545 µm	$Al_{0.30}Ga_{0.70}N$ back-barrier	1.3 µm
Gate work function	5.1 eV	GaN substrate	< 3µm

During the simulation, the electrical parameters of the IIIA-nitride materials used are defined by default by the software. Whereas the electrical and structural parameters of β-Ga_2O_3 are not defined, so we take them from [95]. These parameters play a critical role in determining the overall electrical characteristics of the simulated device. Table II.4 lists the β-gallium oxide parameters used in the simulation.

Table II.5 Electrical and structural parameters of β-Ga_2O_3 oxide layer [95].

Parameters	Value	Parameters	Value
Energy band gap E_g	4.8 eV	Electron mobility μ_n	118 $cm^2/V.s$
Electron affinity χ	4 eV	Hole mobility μ_p	50 $cm^2/V.s$
Electron effective masse m_e^*	$0.25m_0$	Conduction band density of state E_c	3.72×10^{18} cm^{-3}
Relative permittivity ε	10	Valence band density of state E_v	3.72×10^{18} cm^{-3}
Thermal conductivity κ	0.13 W/cm.k	Length	3 nm

The layer sequence arrangement starts with a thin 3nm β-Ga_2O_3 oxide layer followed by a 2 nm GaN cap. Then the device consists of an $Al_{0.25}Ga_{0.75}N$ barrier layer doped with a donor concentration equal to 10^{19} cm^{-3}, and an ultra-short AlN spacer is added, followed by an undoped GaN channel. To improve the confinement of the electrons in the channel, an undoped $Al_{0.30}Ga_{0.70}N$ back-barrier layer is inserted.

II. 6. 2 Results and discussion

- **Energy Band Diagram**

Figure II.15 shows the conduction band energy beneath the gate electrode. This band diagram is used to explain the formation of the 2DEG channel in the MOSHEMT. Our findings on the conduction band diagram are correct, the band curvature seems good because it corresponds to what is expected in theory. The triangular quantum well appears clearly at the interface between the spacer and the channel, with sufficient depth below the fermi level.

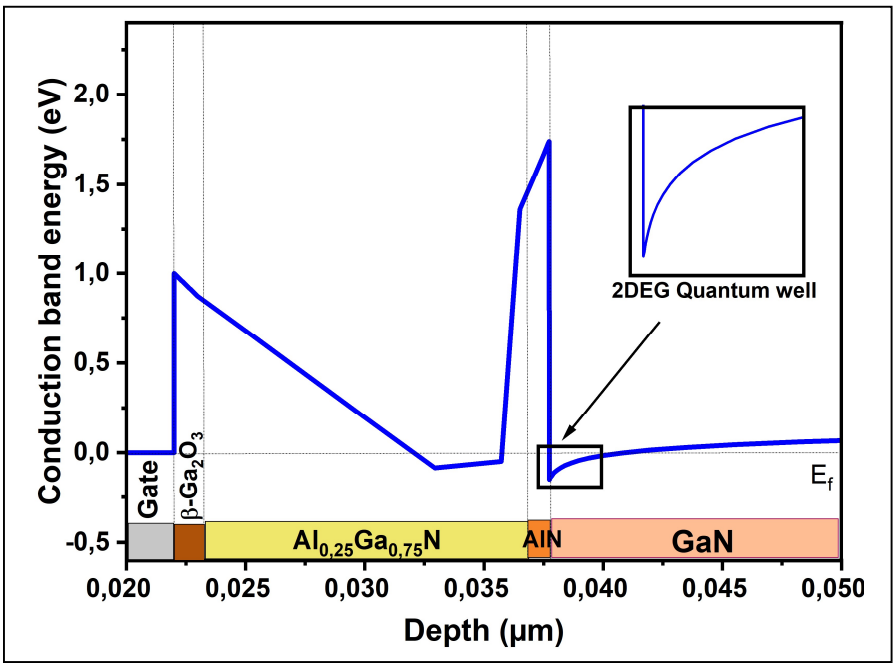

Figure II.15 Simulated conduction band diagram of the proposed device.

II. 6. 3 Comparative study of conventional and recess gate structure of device A

In this section, a comparison study between a recess gate structure and a non-recess gate was performed. Figure II.16 depicts a comparison scheme between the conventional (denoted as β-Ga_2O_3-MOSHEMT) and the recess gate (denoted as β-Ga_2O_3-RGMOSHEMT). As can be seen, the metal gate is recessed into the β-Ga_2O_3 oxide layer to a depth of 2 nm.

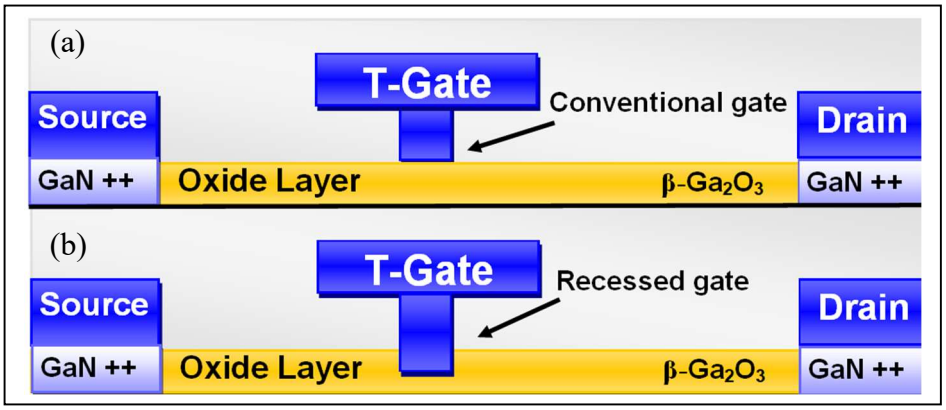

Figure II.16 Scheme of the device's electrodes with conventional (a) and recessed gate(b).

- **Transfer characteristics**

Figure II.17 (a) shows the input characteristics (Drain current versus gate voltage at V_{DS}=10V) of Device A. The two different structures show different mode operations, a positive threshold voltage of +0.56V was extracted for the recessed gate device, hence, the mode functioning of this structure is the enhancement mode, which is preferable. While the conventional MOSHEMT exhibits a depletion mode with a negative V_{TH} of -0.25V. As a result, the recess gate technique is well adapted to obtain the normally-off functionality of the proposed device by boosting the threshold voltage to a positive value.

Another parameter can be observed, which is the maximum drain current achieved by this device. As can be seen, the recess gate diminishes the value of the current output of the device because it depletes the 2DEG channel.

Figure II.17 (b) shows the transconductance for the suggested devices. At V_{GS}=1.1V, a high value of 1.170 S/mm is achieved for β-Ga_2O_3-RGMOSHEMT, while β-Ga_2O_3-MOSHEMT only reaches 1.003 S/mm at V_{GS} = 0.8V. The transconductance reaches high values due to several technological effects, citing the good controllability of the short T-gate structure, the thin barrier layer, and the potential effect of the back-barrier.

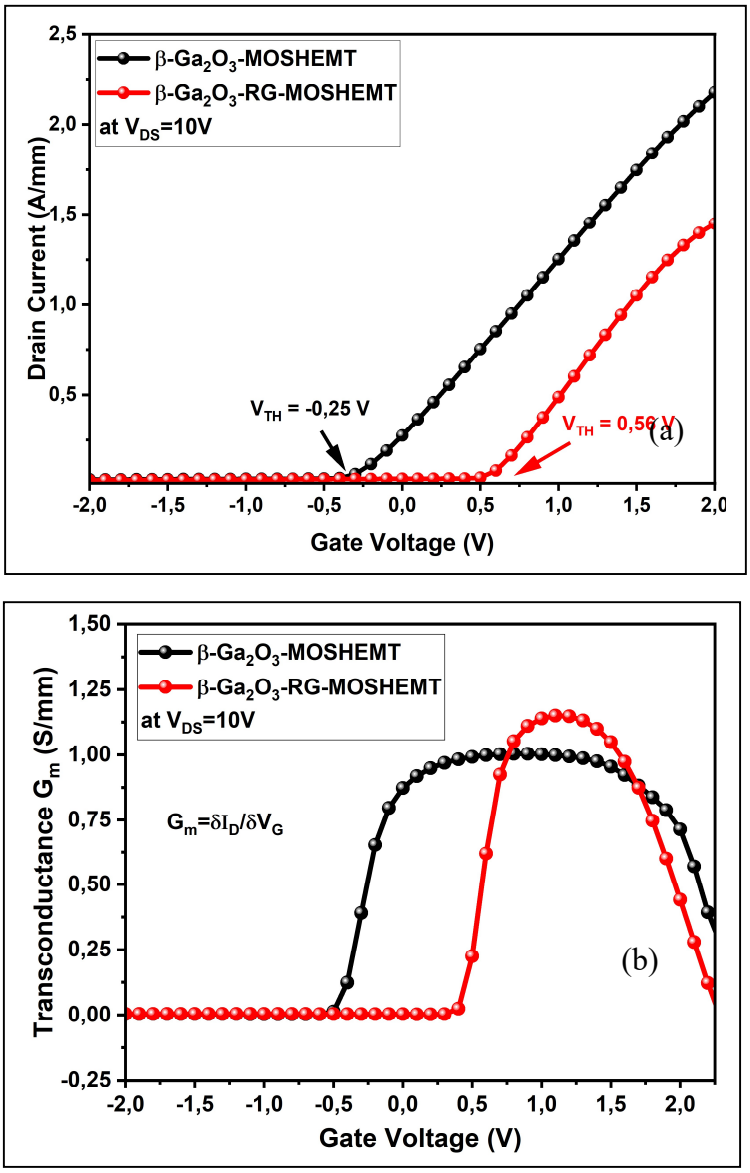

Figure II.17 Simulation comparison between conventional and recessed gate β-Ga_2O_3- MOSHEMT of (a) Transfer characteristics at V_{DS}=10V, (b) Transconductance G_m.

- **RF characteristics**

The cut-off frequency (f_t) and the maximum oscillation frequency (f_{max}) are key factors for microwave applications, they are defined as the frequencies for which the modulus of the current gain and the modulus of the power gain equal 0 dB. Figures II.18 (a) and (b) show the variation of H_{21} and U gains as a function of frequency on a logarithmic scale at room temperature. The results are described as a function of two gate lengths (50nm and 70nm).

For conventional gate MOSHEMT, the simulation was carried out at V_{GS} = 0.8V, corresponding to the maximum of the peak transconductance. This gives a cut-off frequency of 38 GHz and a maximum oscillation frequency of 47 GHz. For the MOSHEMT with a recessed gate, and at V_{GS} = 1.1 V, the cut-off frequency is 49 GHz and the maximum oscillation

frequency is around 60 GHz. Compared with the normally-on MOSHEMT, the normally-off device has a higher performance frequency than the normally-on MOSHEMT.

In addition, Figure II.18 shows the relationship between the gate length and the frequencies. As it can be seen, when L_g decreases the frequency increases, as this leads to a decrease in the gate capacitance. Furthermore, the maximum speed of the electrons depends on the material used and the device geometry, which means that to increase the operating frequency and therefore reduce the time taken for an electron to pass under the gate, a short gate length must be employed.

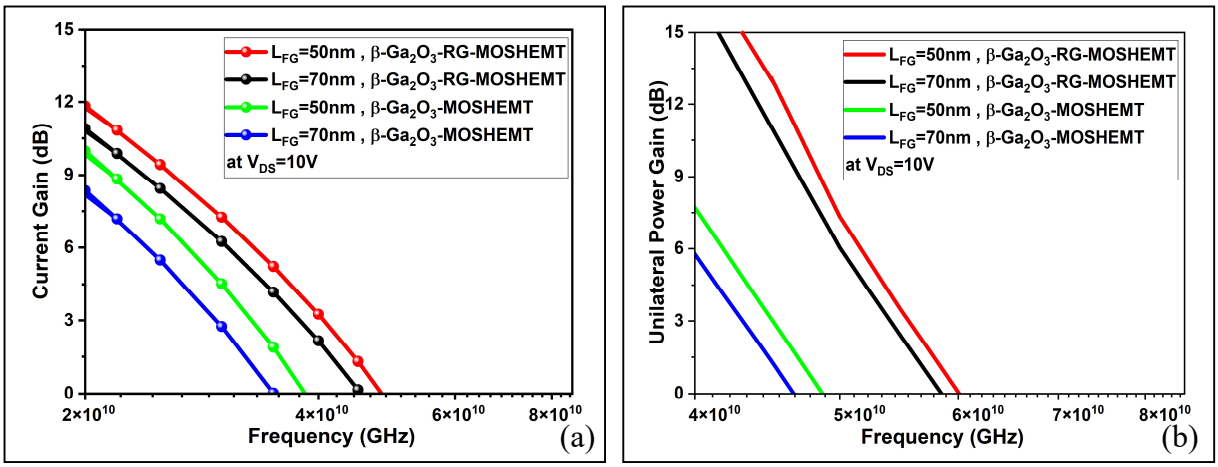

Figure II.18 RF performance at Lg=50 and 70nm (a) Current gain (b) power gain.

II. 6. 4 Impact of Al-content of a recessed-gate Device A

In this section, we are going to study the electrical characteristics of the E-mode 50 nm-recessed gate β-Ga_2O_3-AlGaN/GaN MOSHEMT as a function of the barrier constituent.

- **Effect of Al% on the physical parameters**

The principal physical parameters of the Al_xGaN barrier are extracted by varying the mole fraction (x) from 0.23 to 0.31, and are mentioned in Table II.5.

Table II.6. Electrical parameters of AlGaN barrier material at different aluminum contents.

Aluminum mole fraction %	**23%**	**25%**	**27%**	**29%**	**31%**
Band Gap E_g (eV)	4.36	4.46	4.57	4.69	4.80
Permittivity ε	8.72	8.70	8.68	8.66	8.65
Electron density of state E_c ($\times 10^{18}cm^{-3}$)	3.18	3.27	3.36	3.44	3.53
Hole density of state E_v ($\times 10^{19}\ cm^{-3}$)	1.57	1.50	1.42	1.35	1.28
Electron velocity v_{sat} ($\times 10^{8}$ cm/s)	4.63	4.80	4.98	5.14	5.31

It can be seen that the band gap, the electron density of state, and the electron velocity increase with increasing Al composition, while the permittivity and the hole density of state decrease, demonstrating the large tunability of the device depending on the target application.

- **Effect of Al% on the energy band diagram and the 2DEG density**

The conduction band profile and the electron concentration at different aluminum contents are compared and plotted in Figures II.19 and II.20.

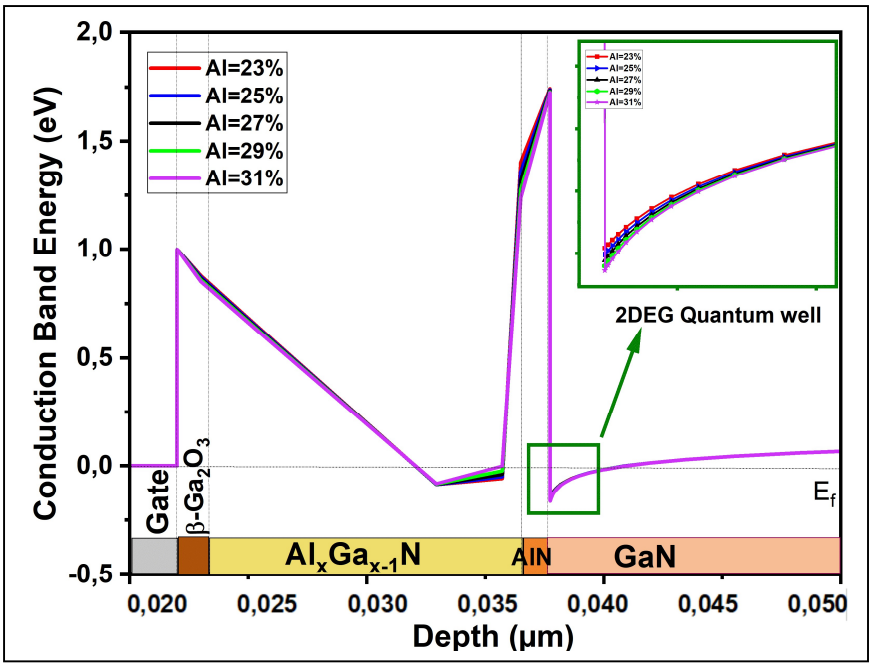

Figure II.19 Simulated conduction band energy at different aluminum contents.

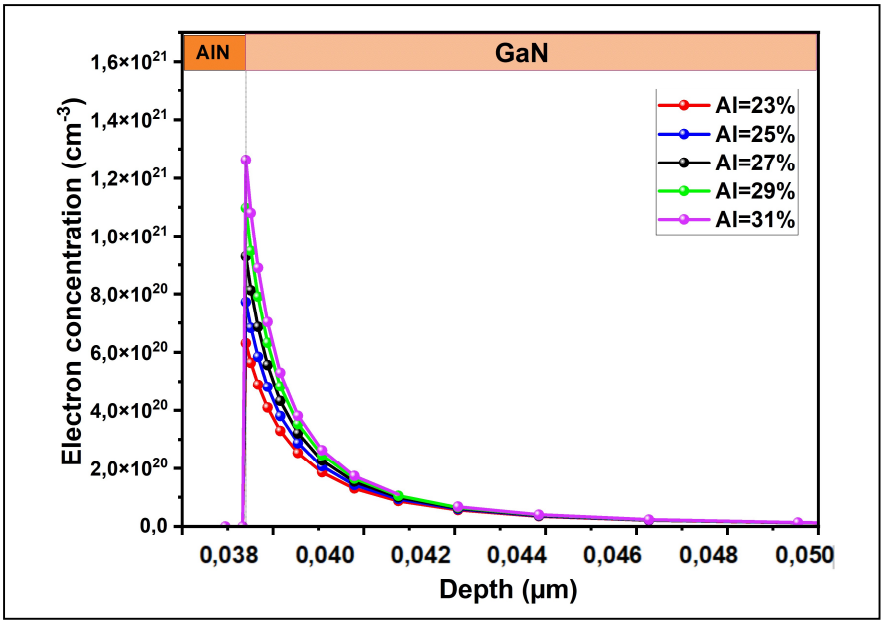

Figure II.20 Simulated electron concentrations at different aluminum contents.

The depth of the triangular quantum well below the fermi level is greater with a higher percentage of aluminum. The value of the sheet charge density is largely influenced by the critical value of the barrier composition due to the impact of the polarization. According to the literature, the 2DEG charge may be absent at very low aluminum values (Al<10%), whereas it is always present when the AlGaN constituent is increased above a certain percentage of aluminum (x>30%).

If we exceed 30-31%, interlayer mismatch and dislocations will be observed. It should be noted that it is easier to grow AlGaN barriers with an Al-content of 20-31% than barriers with a high Al content [96, 97]. The extracted value of the sheet charge density n_s and the electron concentration of the proposed MOSHEMT are observed with Al percent of 23%, 25%, 27%, 29%, and 31%, and are listed in Table II.7. The use of a spacer significantly enhances the electron confinement.

Table II.7. Sheet charge density and electron concentration at different aluminum contents.

Aluminum mole fraction %	**23%**	**25%**	**27%**	**29%**	**31%**
Sheet charge density n_s ($\times 10^{13}$ cm^{-2})	1.34	1.4	1.60	1.73	1.85
Electron concentration ($\times 10^{20}$ cm^{-3})	6.3	7.72	9.29	10.96	12.63

- **Effect of Al% on the electric field**

The device's electric field is shown in Figure II.21. The electric field is high at the AlN/GaN interface due to the strong polarization. It is observed that the peak electric field also increases with increasing Al-content, reaching a maximum value of 4.3 MV.

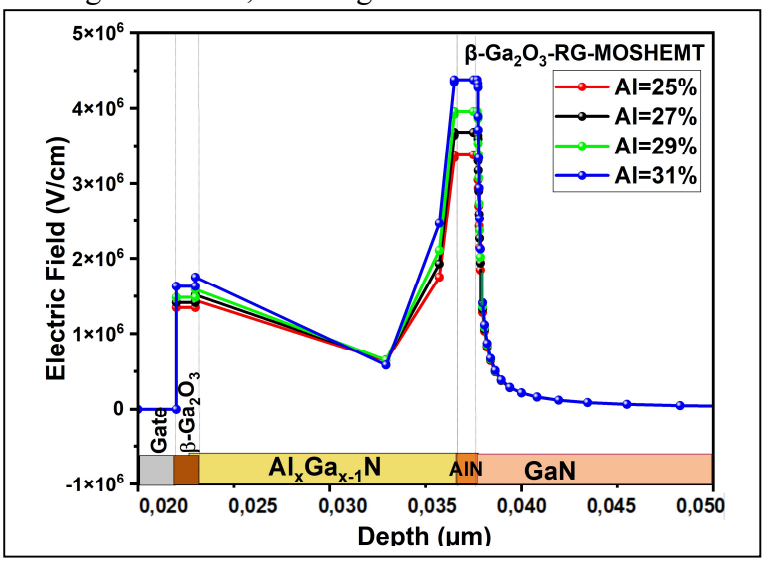

Figure II.21. The electric field of the proposed device at different aluminum contents.

- **Effect of Al% on the transfer characteristics**

The transfer characteristics of the recess gate β-Ga_2O_3-MOSHEMT are presented in this section with the variation of aluminum percentage from 25% to 31% with steps of 2%. Figure II.22 depicts the linear transfer characteristics at V_{DS} = 10V as a function of Al percent. A positive value of V_{th} about 0.56V was extracted for Al=25%, while around 0.52V was achieved for Al = 31%. As can be seen, V_{th} depends inversely on Al-content. On the other hand, the saturation drain current density increases with increasing the Al-composition.

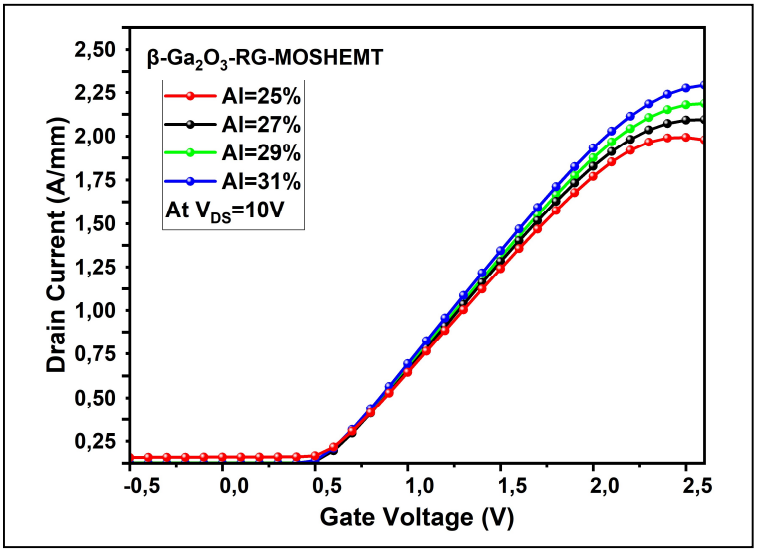

Figure II.22 Linear transfer characteristics of the device at Al=25, 27, 29, and 31%.

Figure II.23 displays the $I_d(V_{GS})$ curve in a semi-logarithmic scale and further compares the drain leakage current of the sample under consideration. The sample with the highest Al-mole fraction is fully functional with the lowest drain leakage current of more than 10^{-5} A/mm and the highest I_{ON}/I_{OFF} ratio, due mainly to the β-Ga_2O_3 gate oxide.

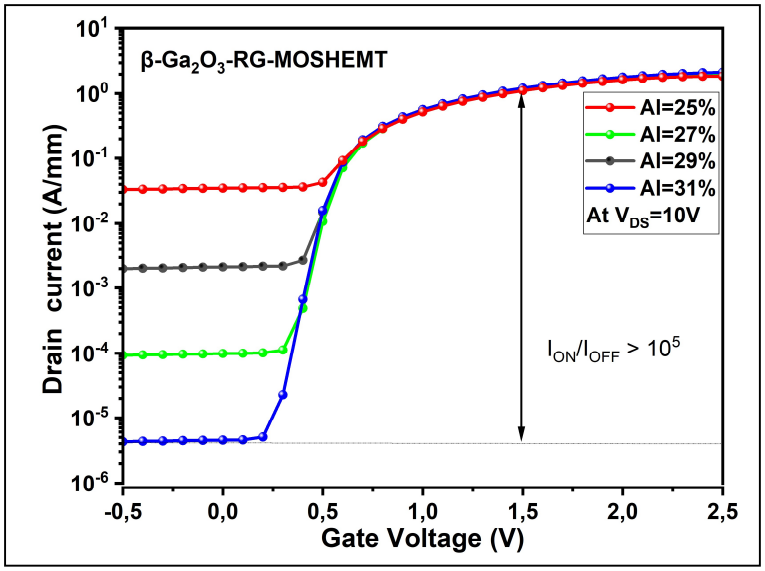

Figure II.23. Semi-logarithmic scale of the I_D-V_{GS} at Al=25, 27, 29, and 31%

Figure II.24 shows the G_m-V_{GS} curve at V_{DS} = 1V. High peak transconductance are obtained of 1170, 1260, 1280, and 1308 mS/mm for Al% of 25, 27, 29, and 31%, respectively. Improved results of G_m are obtained by increasing the molar fraction of AlGaN barrier. This is due to the higher concentration of electrons available for conduction and the excellent β-Ga_2O_3/AlGaN interface inducing high controllability of the short T-gate [98, 99]

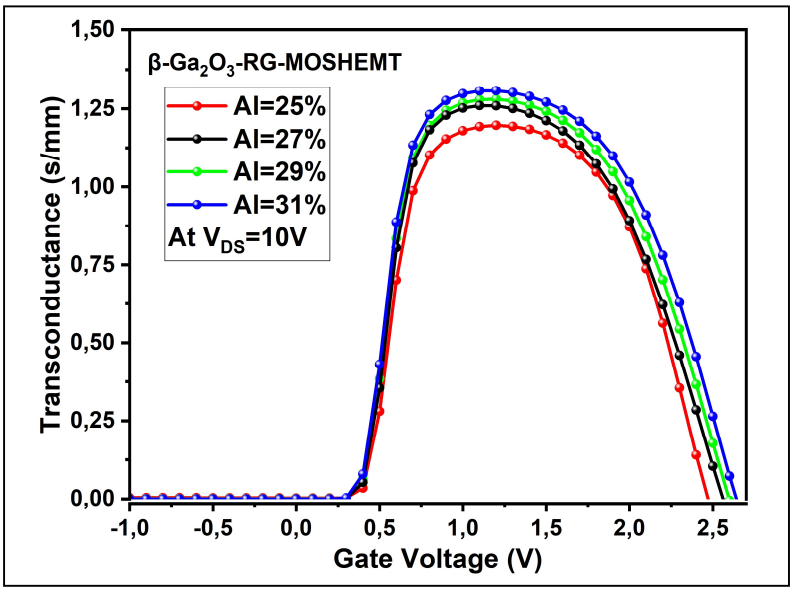

Figure II.24 Transconductance of the proposed device at V_{DS}=10V as a function of Al%.

As a result, high barrier composition leads to an increase in the drain current saturation and the peak G_m, but substantially shifts V_{TH} in the negative direction. These results demonstrate the strong dependence between the electrical characteristics and the aluminum composition of the $Al_xGa_{1-x}N$ barrier.

- **Recapitulative table**

The studied AlGaN/AlN/GaN MOSHEMT demonstrates surprisingly improved DC and RF performance when utilizing ultra-wideband β-Ga_2O_3, the use of thins barrier and recess gate technologies allow us to easily obtain a device that is normally-off.

Table II.8 compares the performance of the proposed MOSHEMT with previously published devices that use β-Ga_2O_3 as oxide layer. Therefore, our first results show that the proposed RG-MOSHEMT produced on GaN substrate may offer greater scalability in terms of future ultra-high frequency technology.

Table II.8. Comparison of our results with similar reports using β-Ga_2O_3 oxide layer.

References	MOSHEMT Devices	Substrate	Parameters					
			$I_{d,sat}$ A	$n_s \times 10^{13}$ cm^{-2}	V_{th} V	g_m mS	f_t GHz	f_{max} GHz
[100].2021 fabrication	i-Ga_2O_3 /AlGaN/GaN	Saphire		1.1	-3.5	85	5.7	11
[101].2016 fabrication	Ga_2O_3/AlGaN/GaN	Si	0.72	1.02	-4.2	200	--	--
[102], 2021 simulation	β-Ga_2O_3 /P-GaN /$Al_{0.25}Ga_{0.75}N$ /GaN	--	0.35	--	2.8	--	--	--
[103], 2023 fabrication	k-Ga_2O_3 AlGaN/GaN	GaN	0.7	1.24	-4.7	140	9.1	14.5
[104], 2021 fabrication	Ga_2O_3/$In_{0.83}Al_{0.17}N$/GaN/$Al_{0.18}Ga_{0.82}N$/GaN	Si	0.81	1.11	-3.2	149	6.5	12.6
This work simulation	Un-recessed β-Ga_2O_3 /AlGaN/AlN/GaN	GaN	2.2	1.4	-0.2	1003	38	47
	Recessed β-Ga_2O_3 /AlGaN/AlN/GaN	GaN	1.4	1.4	0.6	1170	49	60

II.7 Conclusion

In this chapter, we discuss the various challenges and limitations that exist in HEMT technology. Then, we briefly presented our choice of investigation based on the enhancement mode MOSHEMT transistor. Finally, we presented our first simulation results, obtained in the static and dynamic regime using the SILVACO ATLAS environment for a new AlGaN/GaN MOSHEMT design. Firstly, we carried out a comparative study between recess and non-recess gate structure. Secondly, we investigate the impact of the barrier composition.

Thanks to the interesting properties of the materials used and also to the mathematical models and methods of the SILVACO software. Our study shows excellent results, offering a research opportunity for developing and manufacturing normally-off MOSHEMT with β-Ga_2O_3 oxide layer.

Chapter III TCAD simulation of AlGaN/AlInGaN/GaN MOSHEMTs grown on 4H-SiC and β-Ga_2O_3 substrates

III.1 Introduction

MOSHEMTs are components of major importance in various domains of RF electronic circuits. The approach discussed in this thesis is to expand the conventional MOSHEMT structure to a more complex structure in order to reach a wider range of applications. The main motivation behind this project was to utilize new materials to release high RF components that are reliable, reproducible, and do not require expensive materials. Similarly, the structures should be capable of delivering, in enhancement mode, high output current and high frequencies.

In this chapter, we carry out DC and AC simulations using ATLAS-SILVACO tool on two types of MOSHEMTs based on AlGaN/AlInGaN/GaN structure, with AlInGaN being used as a spacer layer. We start this chapter by describing a single-barrier and double-barrier AlGaN/AlInGaN/GaN MOSHEMT on a 4H-SiC substrate (Device B). In the second part, we simulate the AlGaN/AlINGaN/GaN MOSHEMT on β-Ga_2O_3 substrate (Device C). Different geometrical and physical factors are investigated, such as the number of barriers, the gate length, the type of oxide, the spacer composition, and the effect of temperature.

III.2 Radio-frequency MOSHEMT devices

Since the first demonstration of GaN-based MOSHEMTs, research activities have focused mainly on improving the radio-frequency features of these devices, which are still in great demand as their most outstanding feature. In particular, for RF amplifiers, which is the focus of our research. Today, AlGaN/GaN MOSHEMTs are commercially available from several suppliers. They can reach operating frequencies above 500 GHz.

Nevertheless, the next generation of GaN-based RF transistors is likely to be realized through the integration of new IIIA-N materials, oxides, and substrates such as GaN, AlGaN, AlInGaN, 4H-SiC, and β-Ga_2O_3. The high compatibility between these materials allows intentional defects to be minimized and surface roughness to be reduced during manufacture. In this case, maximizing f_t and f_{max} frequencies is our major interest, and each parameter in Equation (I-41) must be carefully optimized. In this thesis, we have successfully designed RF MOSHEMT transistors operating in a spectrum range above 1000 GHz. by optimizing overall intrinsic and extrinsic parameters.

III.3 Device B: AlGaN/AlInGaN/GaN MOSHEMT on 4H-SiC substrate

III. 3. 1 Concept of double barrier heterostructure

Traditionally, since 1991, HEMTs have been designed and fabricated with a single barrier layer [16]. In 1999, Gaska et al. designed and manufactured a double barrier AlGaN structure for the first time [17]. Subsequently, various designs with $Al_{x1}Ga_{y1}N/Al_{x2}Ga_{y2}N/GaN$ double heterojunctions have been explored theoretically and experimentally, showcasing a high current and high-frequency performance [18-20]. Recent research has focused on bilayer barriers with quaternary $Al_{x1}In_{y1}Ga_{z1}N/Al_{x2}In_{y2}Ga_{z2}N/GaN$ HEMTs, with high current density [21, 22].

Numerous studies have verified that the quaternary AlInGaN material, which is strongly matched to GaN, exhibits notably stronger spontaneous polarization than the ternary AlGaN. This is attributed to the much higher concentration of aluminum. In addition, by adding a second barrier, the height between the gate electrode and the 2DEG channel will increase, inhibiting the channel from forming at zero bias and enabling enhancement mode operation.

To date, most experimental and theoretical studies of HEMTs or MOSHEMTs have focused on double AlGaN barriers or double AlInGaN barriers. In our work, we success to combine these two barriers, i.e. AlGaN and AlInGaN, into a single structure. This structure is capable of combining the advantages of both ternary and quaternary barriers and it can enable simple processing of E-mode operation. The concept of a novel double barrier AlGaN/AlInGaN/GaN MOSHEMT will be discussed.

III. 3. 2 Device description

A 3D view of the proposed structures is shown in figures III.1 (a) and (b), with:

- Single barrier $Al_{0.30}Ga_{0.70}N/Al_{0.36}In_{0.08}Ga_{0.56}N/GaN$ MOSHEMT (labeled STR01-SB).
- Double barrier $Al_{0.30}Ga_{0.70}N/Al_{0.80}In_{0.18}Ga_{0.02}N/Al_{0.36}In_{0.08}Ga_{0.56}N/GaN$ MOSHEMT (labeled STR02-DB).

However, MOS-HEMTs exhibit high contact resistance due to the alloyed ohmic contacts. A layer of heavily doped n ++ GaN layer with $2\times10^{19}cm^{-3}$ donors is regrown under the source-drain junction to minimize access resistance [64]. In addition, a 10 nm T-gate technology is employed to enhance the RF device performance [105].

Looking at the schematic design from top to bottom, a silicon dioxide (SiO_2) passivation layer is implemented to minimize surface traps. High-k titanium dioxide TiO_2 is deposited under the gate as an oxide layer, followed by a thin (2nm) GaN cap. A non-doped AlGaN barrier

layer with 30% aluminum concentration is placed under the cap, a 2nm-thin quaternary $Al_{0.36}In_{0.08}Ga_{0.56}N$ spacer is inserted between the GaN channel and AlGaN barrier.

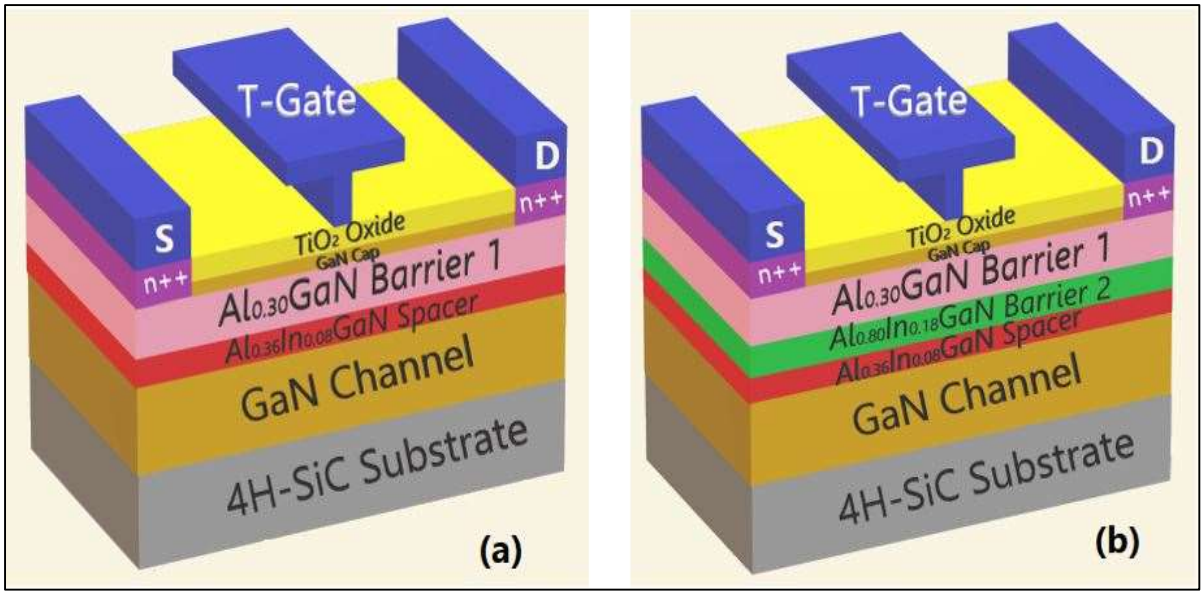

Figure III.1 3D view design of MOSHEMTs with (a) Single barrier, (b) Double barrier.

Depending on the choice of material, the spacer layer can help to manage deformation in the device, which is critical for obtaining high-quality epitaxial layers and improving device reliability.

Recent researches indicate that the 2D electron gas formation in the AlInGaN/GaN interface, associated with the AlInGaN spacer layer, is more than AlN/GaN interface (AlN spacer Layer). This is attributed to the induction of a high polarization charge, resulting in enhanced carrier transport properties and current flow between the source and drain region [106, 107], which is why we choose $Al_{0.36}In_{0.08}GaN$ as a spacer layer in our structures.

To further improve the 2DEG confinement in the quantum well, an $Al_{0.80}In_{0.18}GaN$ second barrier layer with high aluminum/indium content is interposed between the first barrier and the $Al_{0.36}In_{0.08}GaN$ spacer (as shown in Figure III.1 (b)). The Al, In, and Ga composition chosen for the AlInGaN materials guarantees lattice-matching with the GaN channel [108].

These simulated devices are deposed on one of the preferred substrates, which is silicon carbide (4H-SiC), as experimentally confirmed by Nanjo et al [109]. The geometrical specifications of these structures are listed in Table III.1.

Table III.1 Geometrical specifications of the studied devices: STR01-SB and STR02-DB.

Gate specifications		**Structure specifications**		
Parameter	Dimension	Layer	STR01-SB	STR02-DB
Gate structure	T-shape	TiO_2 oxide layer	5 nm	5 nm
Gate foot length	10 nm	GaN cap layer	2 nm	2 nm
Gate head length	400 nm	$Al_{0.30}GaN$ 1st barrier	20 nm	20 nm
Gate stem height	50 nm	$Al_{0.80}In_{0.18}GaN$ 2nd barrier	--	4 nm
Gate-drain distance	355 nm	$Al_{0.36}In_{0.08}GaN$ spacer	2 nm	2 nm
Gate-source distance	355 nm	GaN channel	796 nm	796 nm
Gate work function	5.1	4H-SiC substrate	2161 nm	2165 nm

We design and simulate these transistors in 2D using the ATLAS-SILVACO tool. The mesh must be dense at the spacer/channel interface to target the two-dimensional gas along the y-axis. The designed structures and the mesh view of the different regions of the proposed MOSHEMT are presented by the Tony plot tool and illustrated in Figures III.2 (a) and (b).

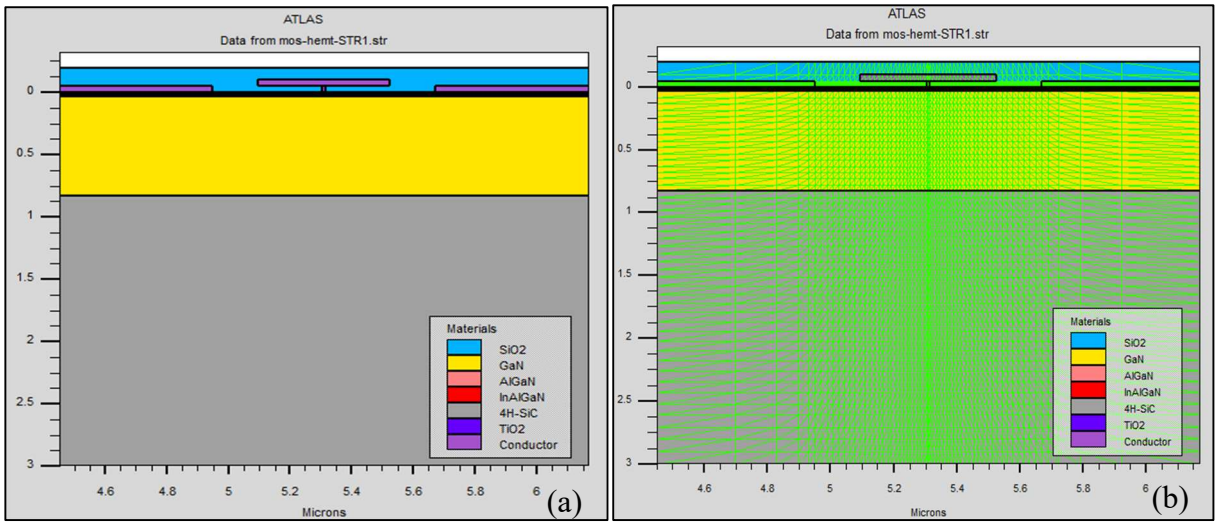

Figure III.2 (a) Structure regions from Tonyplot tool, (b) Structure mesh.

In our study, we simulated two different structures, one with a single barrier and the second with two barriers. The electrical characteristics of the suggested MOSHEMTs are evaluated on the basis of the physical models given in Appendix A. These models are solved using Newton's method at room temperature. The following figures show a zoom on the active regions of these devices.

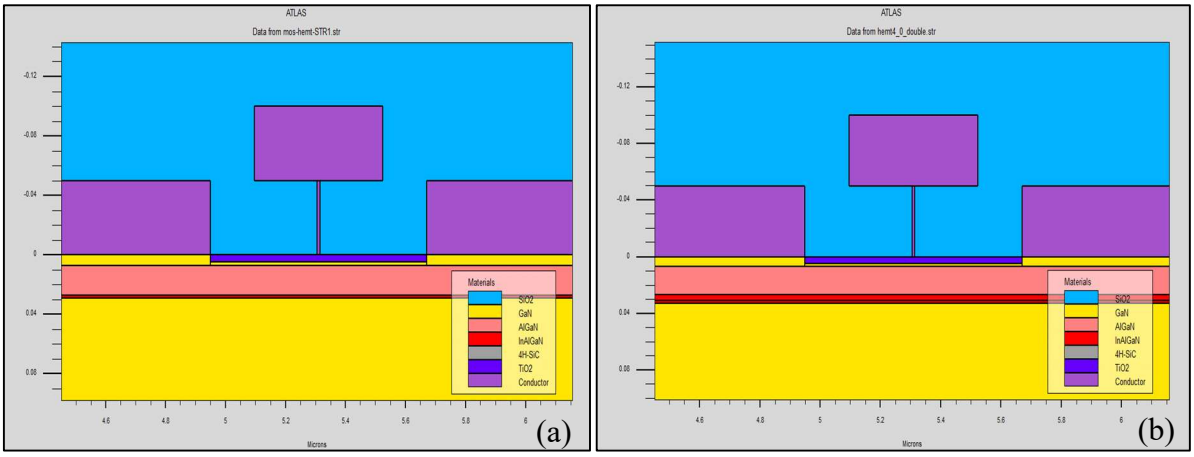

Figure III.3 Zoom on the electrodes of (a) STR01-SB, and (b) STR02-DB.

The main physical parameters of the material used during the Deckbuild simulation are extracted and listed in Table III.2.

Table III.2 The extracted physical parameters used in this work at 300k.

Parameters	$Al_{0.30}GaN$ 1st barrier	$Al_{0.8}In_{0.18}GaN$ 2nd barrier	$Al_{0.36}In_{0.08}GaN$ spacer	GaN channel	4H-SiC
ε	8.8	9.73	9.27	9.5	9.7
E_g (eV)	3.42	4.55	3.71	3.55	3.23
N_c ($\times 10^{18}cm^{-3}$)	2.02	3.01	2.45	1.07	16.6
N_v ($\times 10^{19}cm^{-3}$)	9.08	3.30	2.10	1.16	3.3
μ_e ($cm^2/V.S$)	985.5	1280	1280	1350	1250
χ (eV)	3	2.8	3.53	4.2	3.2
V_{sat} ($\times 10^6 cm/S$)	11.2	1	1	19.1	19.1
P_{sp} ($\times 10^{13}$ cm^{-2})	-1.698	-2.736	-4.007	-1.698	--

- **Polarization model**

The confinement of a large 2DEG density in the heterojunction is the most important operation of the polarization charge. For sample-I (STR01-SB), two polarization-induced negative charges are present at the $Al_{0.30}Ga_{0.70}N/Al_{0.36}In_{0.08}Ga_{0.56}N$ interface and $Al_{0.36}In_{0.08}Ga_{0.56}N/GaN$ interface (noted σ'_1 and σ'_2, respectively). Due to the lattice matching between AlInGaN and GaN, the piezoelectric polarization effect is neglected. Therefore, the total polarization σ'_{int} is a function of spontaneous polarization (P_{sp}) as $\sigma'_{int} = \sigma'_1 + \sigma'_2$ with:

$$\sigma'_1 = P_{sp}(Al_{0.36}In_{0.08}Ga_{0.56}N) - P_{sp}(Al_{0.30}Ga_{0.70}N) \quad \text{III.1}$$

$$\sigma'_2 = P_{sp}(GaN) - P_{sp}(Al_{0.36}In_{0.08}Ga_{0.56}N) \quad \text{III.2}$$

For sample-II (STR02-DB), the total polar charge density σ''_{int} is defined as the summation of three (3) polarization interface charges, σ''_1, σ''_2 and σ''_3, as follows:

$$\sigma''_1 = P_{sp}(Al_{0.80}In_{0.18}Ga_{0.02}N) - P_{sp}(Al_{0.30}Ga_{0.70}N) \quad \text{III.3}$$

$$\sigma''_2 = P_{sp}(Al_{0.36}In_{0.08}Ga_{0.56}N) - P_{sp}(Al_{0.80}In_{0.18}Ga_{0.02}N) \quad \text{III. 4}$$

$$\sigma''_3 = P_{sp}(GaN) - P_{sp}(Al_{0.36}In_{0.08}Ga_{0.56}N) \quad \text{III.5}$$

The AlInGaN material has a higher spontaneous polarization due to the additional contribution of spontaneous polarization and the bowing parameter corresponding to the indium content. The mathematical equations for the spontaneous polarization of AlGaN and AlInGaN alloys are presented in Chapter I. Figure III.4 shows the desired polarization of the structures with single and double barriers.

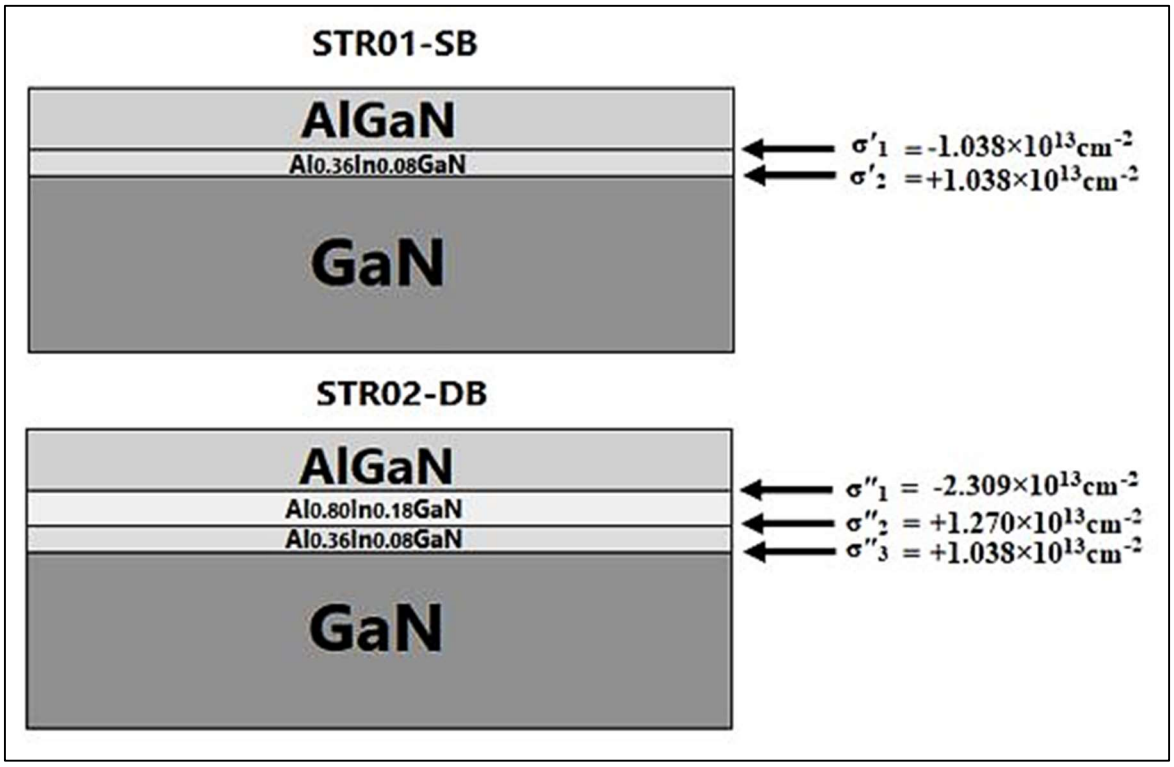

Figure III.4 Polarization interface charge of the two samples, STR01-SB and STR02-DB.

III. 3. 3 Results and discussion

III.3.3.1 Comparison between single and double barriers

- **Energy band diagram**

As discussed, the core principle of the MOSHEMT's function is the 2DEG created at the interface of the top channel and bottom barrier. As a result, a quantum well is created in the band energy profiles. The entire conduction and valence band energies are shown in Figure III.5 (a), the electron concentration is shown in Figure III.5 (b).

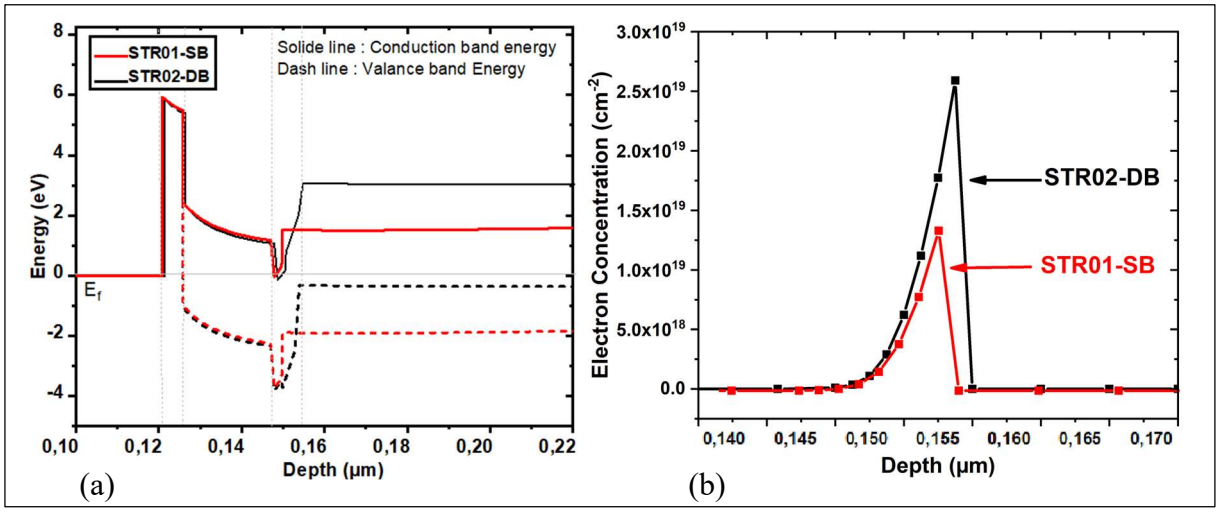

Figure III.5 (a) Conduction and valence band diagram (b) Electron concentration of the studied device with single and double barriers.

Due to the band gap difference between the AlInGaN spacer and GaN, electrons are stockpiled in the quantum well and create a 2D electron gas, which allows faster surface conduction. It is visible that the use of second barrier layer generates a large conduction band offset and higher sheet density, hence, the quantum well's depth below the Fermi level is greater.

According to the numerical simulation, the sheet 2DEG density is observed to be 4.97×10^{12} cm^{-2} for STR02-DB compared with 2.3×10^{12} cm^{-2} for STR01-SB. Moreover, the extrinsic peak of the electron concentration increases, it is around 1.2×10^{19} cm^{-2} and 2.5×10^{19} cm^{-2} for samples I and II respectively, which favors the adoption of the STR02-DB structure.

- **DC characteristics**

We simulated the DC characteristics of the TiO_2-based MOSHEMT with single and double barriers, including output characteristics, on-resistance, transfer characteristics, threshold voltage, I_{on}/I_{off} ratio, and transconductance.

Figure III.6 illustrates the I-V output characteristics at V_{GS} = 1, 2, and 3 V. Three operating regimes can be distinguished, linear regime (I_D increases linearly with V_{DS} voltage), saturation regime (I_D is substantially independent of V_{DS}), and transition regime (intermediate operating zone between the two above-mentioned regimes).

The maximum drain currents ($I_{D,max}$) obtained for the STR01-SB and STR02-DB structures give values of 3300mA and 3780 mA/mm respectively, at V_{GS} = 3 V and V_{DS} = 8 V. Notably, the use of a high percentage of Al in the first barrier (x = 30%) and the second barrier (x = 80%) significantly improves the drain current.

The I_D-V_{DS} characteristic of the STR02-DB structure shows an increase of almost 15% in max current ($I_{D\ max}$) compared with that of the STR01-SB structure. We note that the two designed structures operate in power. We can also see from the curves that we have an excellent electron saturation speed (V_{sat}).

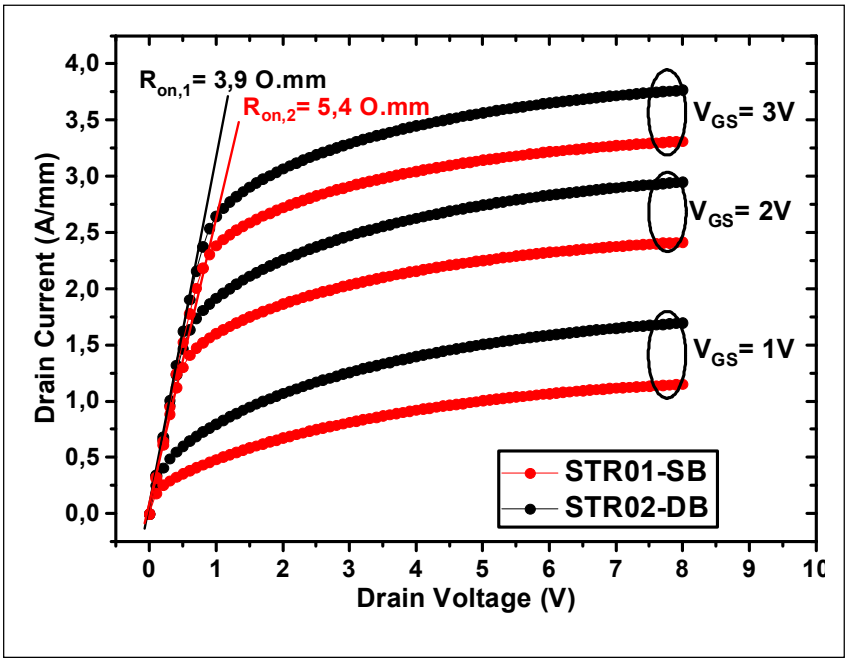

Figure III.6 I_D-V_D results of single (STR01-SB) and double (STR02-DB) barrier devices.

The on-resistance is determined from the linear region of the I_D-V_{DS} curve and amounts to 5.4 and 3.9 Ω.mm for STR01-SB and STR02-DB, respectively. The SiO_2 passivation layer and regrown source drain have a significant impact on optimizing the access resistance.

The linear transfer characteristics are plotted in Figure III.7 (a) at V_{DS} = 3V. The high threshold voltage (V_{th}) of +2.8 V and +3.2 V was extracted for samples STR01-SB and STR02-DB, respectively. From the linear plot; it shows that the mode of operation of the simulated MOSHEMTs is an enhancement mode.

The positive shift of V_{th} is mainly due to the large Schottky height between the gate and channel due to the use of a dielectric, cap, double barrier, and spacer. Thus, the 2DEG charge is depleted and V_{th} shifts more positively. In addition, the use of AlInGaN material.

Figure III.7 (b) further compares the drain leakage current of the considered samples at V_{DS} = 3V, by displaying the I_D-V_{GS} curve in a semi-logarithmic scale. All the suggested devices are fully functional with low drain leakage current and high I_{ON}/I_{OFF} ratio, greater than 10^{14}, with excellent pinch-off properties. This is due mainly to the high-k-TiO_2 oxide.

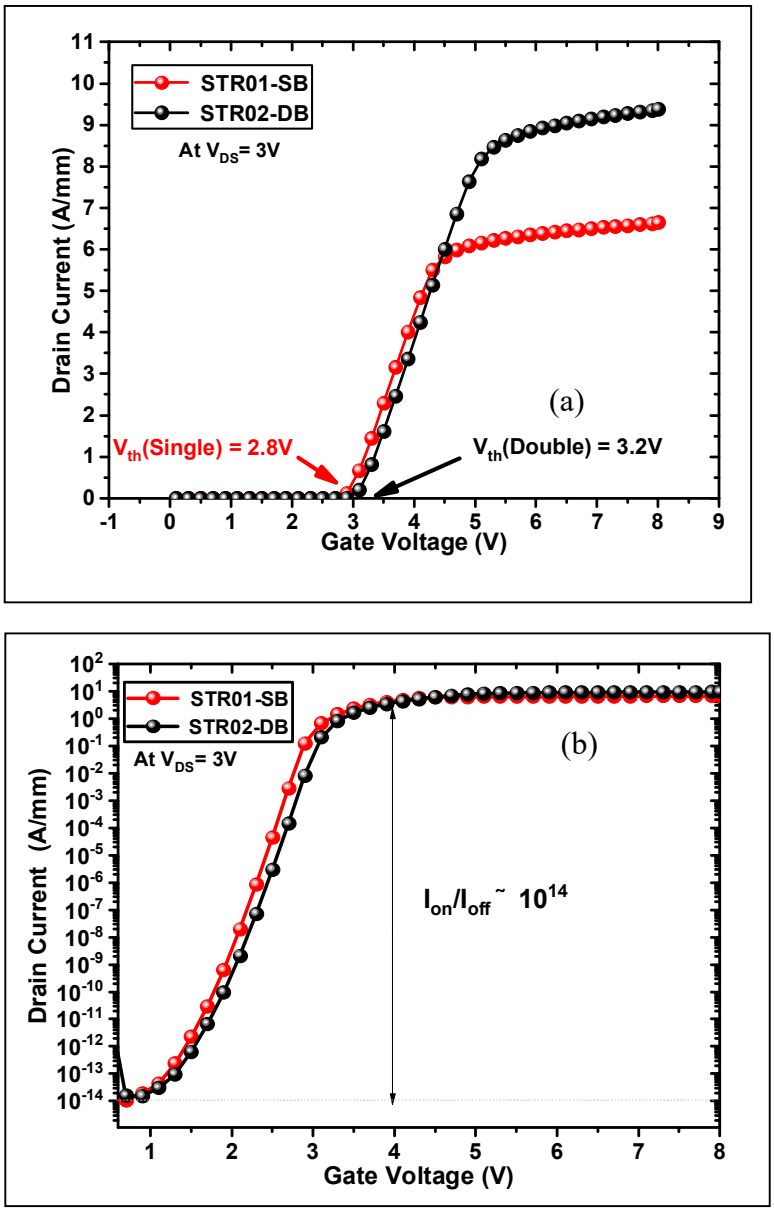

Figure III.7 Transfer characteristics of the proposed nano-MOSHEMTs at V_{DS} = 3 V, (a) I_D-V_{GS} in a linear scale, (b) I_D -V_{GS} in a logarithmic scale.

Figure III.8 shows simulated intrinsic transconductance as a function of gate voltage at V_{DS} = 3 V. Sample-II (STR02-DB) recorded a high peak extrinsic transconductance of ~ 4470 mS/mm, while sample-I (STR01-SB) demonstrates 4320 mS/mm. Beyond this maximum, the transconductance decreases as the gate-source polarization increases. This decrease is linked to the increase in the charge density in the barrier, i.e. as charge density increases, mobility decreases.

In our structures, the high g_m values can be attributed to the correct layering of the heterojunction with the high lattice matched between IIIA-N materials, inducing high 2DEG density and strong controllability of the short gate, providing further superior frequency

performance. The transition frequency of a MOSHEMT is directly proportional to the transconductance (Equation I.40); it will therefore be beneficial to have a large g_m value if the transistor is required to operate at high frequencies.

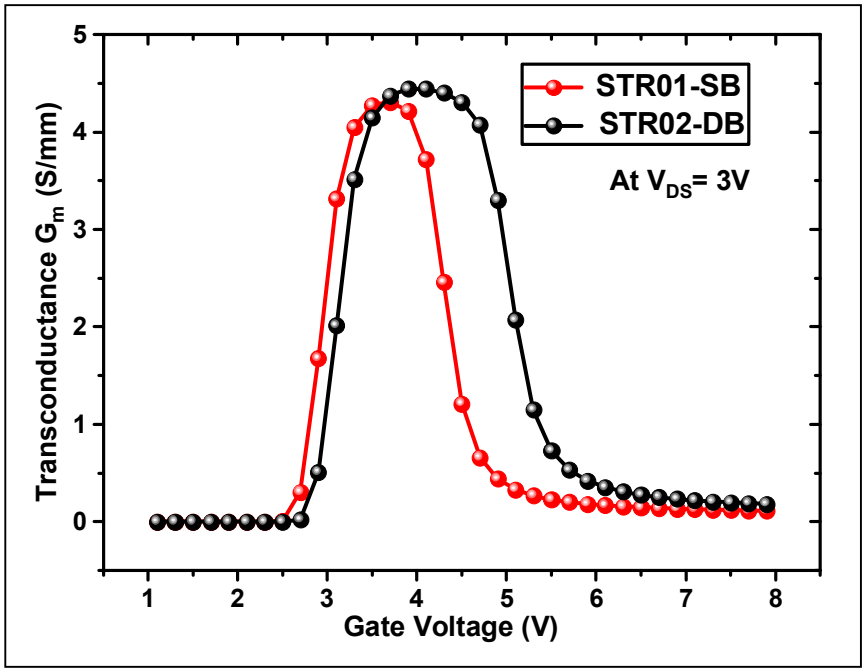

Figure III.8 Transconductance variation of STR01-SB and STR02-DB structures.

- **Breakdown voltage**

When the electric field in the channel reaches a critical value, an avalanche phenomenon occurs, inducing breakdown, i.e., the component is destroyed. In RF applications, the breakdown voltage (V_{BR}) of the MOSHETs transistors plays a critical role and is primarily influenced by the impact ionization phenomenon.

Figure III.9 shows the variation in drain-source current as a function of drain-source voltage (I_{DS}-V_{DS}) at V_{GS} = 2V. This allows us to find the breakdown voltage of the transistors.

According to Selberherr's model simulation « impact Selb », the breakdown voltage for STR01-SB and STR02-DB is significantly improved. The breakdown voltage is measured at 126 V for STR01-SB and 140 V for STR02-DB.

It is worth noting that employing a single barrier MOSHEMT results in 10% decrease in breakdown voltage compared to a double barrier. The improvement in V_{BR} of the device was achieved by smoothening the electric field profile between the gate and drain by using passivation and high-k oxide layers.

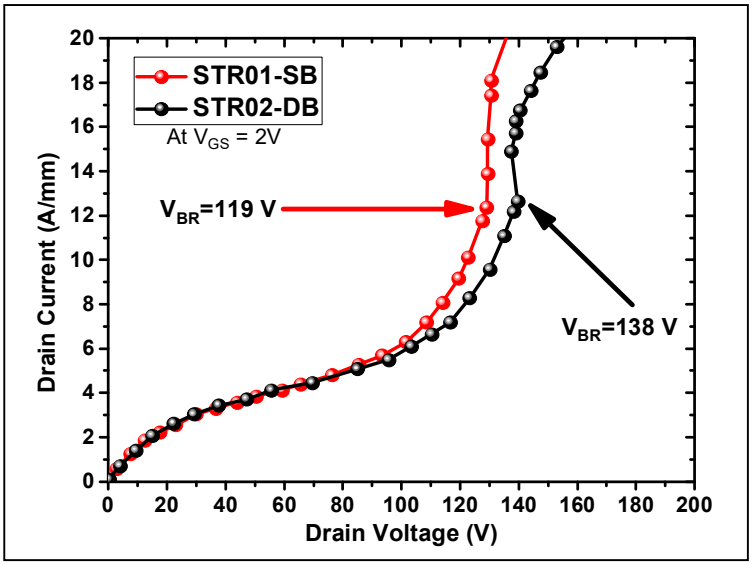

Figure III.9 Breakdown voltage of STR01-SB and STR02-DB structures at V_{GS} = 2V.

- **AC characteristics**

In this section, the AC and RF simulation results have been carried out for the proposed devices with single and double barriers. An alternating signal with a frequency of 1 MHz is applied to the gate level of each device to measure these parameters.

a. Capacitance (C_{GS}, C_{GD}, and C_G)

To analyze the capacitance-voltage characteristics C= f(V_{GS}). Figures III.10 (a) and (b) illustrate the variation of the gate-to-source capacitance (C_{GS}) and gate-to-drain capacitance (C_{GD}) as a function of V_{GS} at a fixed V_{DS}=5V. The obtained results are resumed is Table III.3. The total gate capacitance, C_G, is defined as the sum of C_{GS} and C_{GD}. It is observed that the device with a double barrier exhibits a lower total gate capacitance of 1.453 pF compared to 1.767 pF for the single barrier design. This reduction in total gate capacitance indicates a positive impact on high-frequency operation

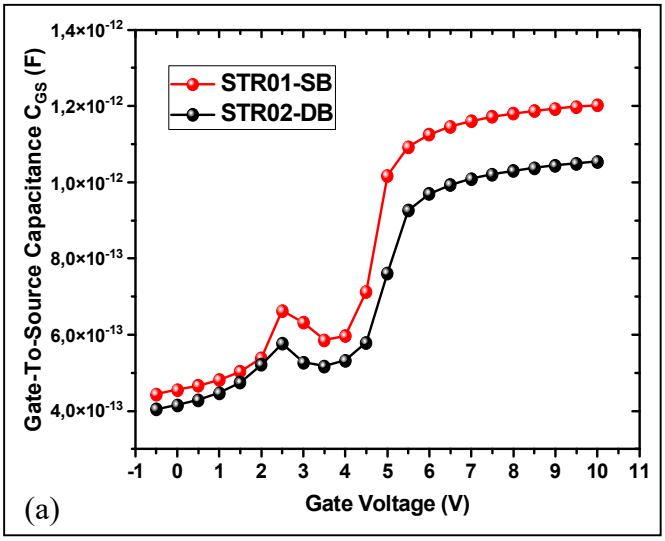

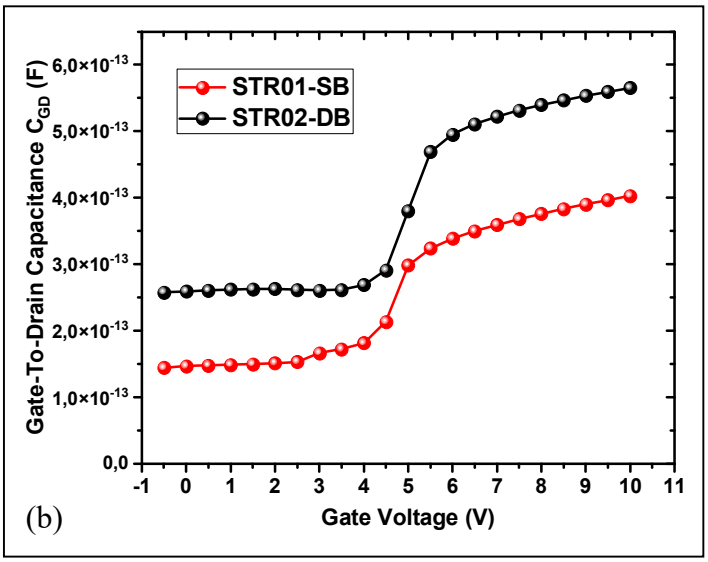

Figure III.10 C-V characteristics of the simulated devices (a) C_{GS}, (b) C_{GD}.

b. Radio frequency performance

The transition frequency (f_t) and the maximum frequency (f_{max}) are the key RF parameters, Figures III.11 (a) and (b) show the current gain and power gain of the devices under consideration at V_{DS} = 8 V and V_{GS} = 4 V corresponding to the highest peak of g_m.

The transistor's frequencies are extracted at a gain modulus equal to zero. The f_t/f_{max} values obtained for STR01-SB and STR02-DB are 812/1023 GHz and 891/1148 GHz, respectively. These are new records for the highest f_t/f_{max} reported to date in double barrier GaN-based MOSHEMTs. The superior f_t/f_{max} performance can be attributed to the utilization of a short 10 nm T-gate, a TiO_2 oxide, and thin barriers layers.

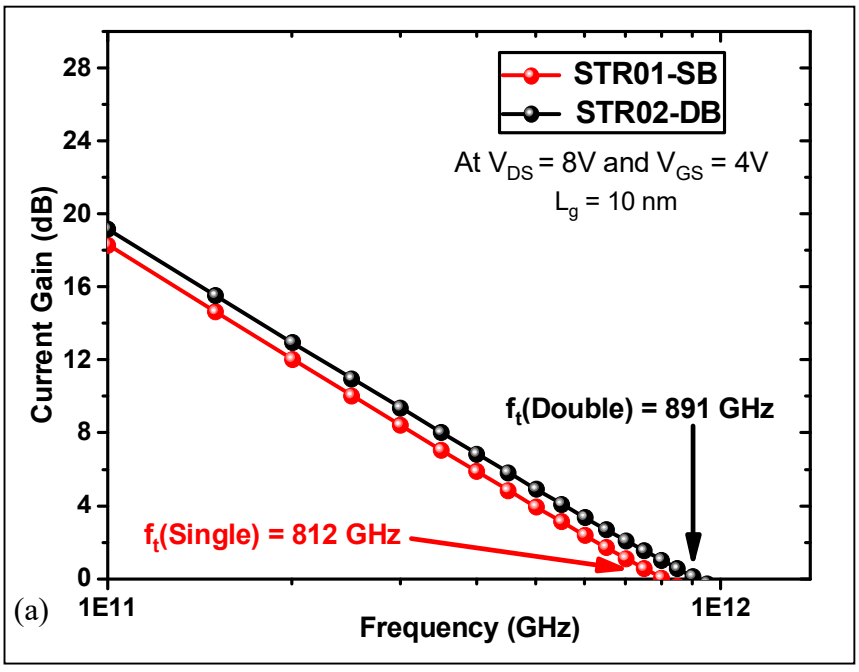

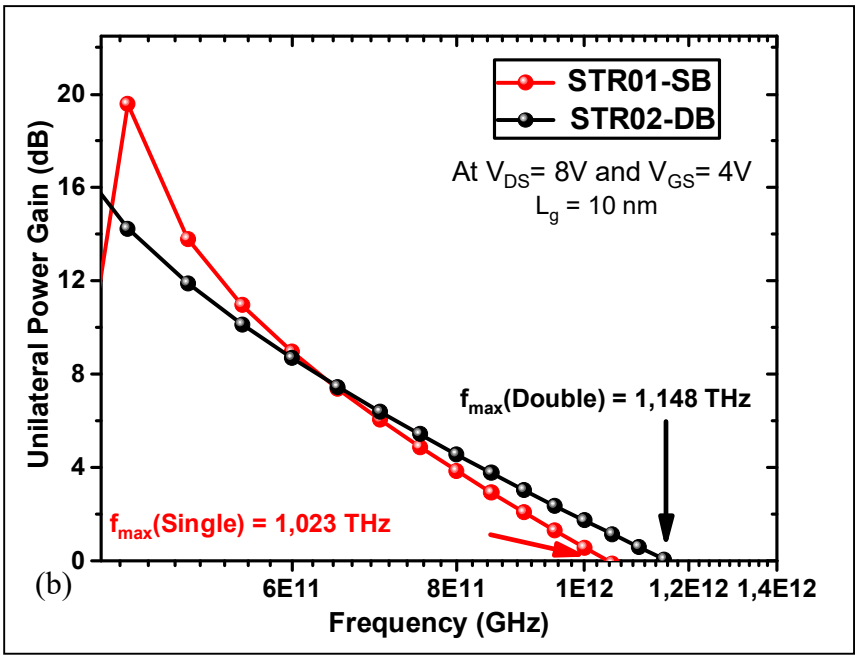

Figure III.11 Radio frequency characteristics with single and double barriers at V_{GS} = 4 V, V_{DS} = 8 V, (a) Current gain, (b) Unilateral power gain.

Furthermore, another parameter taken into account when evaluating and analyzing RF characteristics is the transit time (τ), which is defined as the minimum time required for the electron charge to move from the source electrode to the drain electrode. The total transit time is inversely proportional to the transition frequency, and is given by:

$$\tau = \frac{1}{2\pi f_t} \qquad \text{III.6}$$

For best performance, the transit time should be as low as possible. Calculated values of the transit time for STR01-SB and STR02-DB demonstrate that STR02-DB reaches a minimum transit time of 17.8 pS compared with 16.5 pS for STR01-SB. The proposed devices exhibit extremely short transit times thanks to the high transition frequencies.

To gather information on the frequency characteristics, Johnson's figure of merit of MOSHEMT transistors is also a key parameter to evaluate high-power microwave components and is measured by:

$$JFoM = V_{BR} \times f_t \qquad \text{III.7}$$

From the calculated JFoM of the proposed MOSHEMT, it is observed that double barrier AlGaN/AlInGaN/GaN MOSHEMT demonstrates the highest JFoM, approximately 125 THz, compared with 102 THz for the single AlGaN/GaN MOSHEMT.

Table III.3 summarizes a comparison of the major microwave performances established in this work. Based on the simulation results, using a short T-gate and two barriers with high composition and thin thickness enhance the speed of electrons along the channel, resulting in record values of g_m and f_t/f_{max} with very short transition time.

Table III.3 Comparative analysis of AC characteristics of the proposed devices.

Parameters	C_{GS} (pF)	C_{GD} (pF)	C_G (pF)	f_t (GHz)	f_{max} (GHz)	τ (pS)	JFoM (THz)
STR01-SB	1.2	0.55	1.45	812	1023	19.6	102
STR02-DB	1.03	0.39	1.76	891	1148	17.8	125

III.3.3.2 Impact of the gate length on the RF performance

Figures III.12 (a) and (b) showcase the optimization of the current gain and power gain for STR02-DB structure at different gate lengths (Lg = 10, 20, 35, 50 nm). Through simulation analysis, it is evident that the device with the shortest gate length exhibits excellent RF efficiency.

Reducing the gate length is a typical means for reaching a high cut-off frequency. This behavior can be attributed to the reduction in the gate capacitance. On the other hand, the transition frequency as function of gate length is expressed as follows:

$$f_t = \frac{V_{Sat}}{2\pi L_g} \qquad \text{III.8}$$

Where V_{sat} is the electron speed saturation. The length of the gate is an important parameter to tune when optimizing the structure of the component, therefore, the gate is chosen at a length of 10 nm so that we get the best possible frequencies.

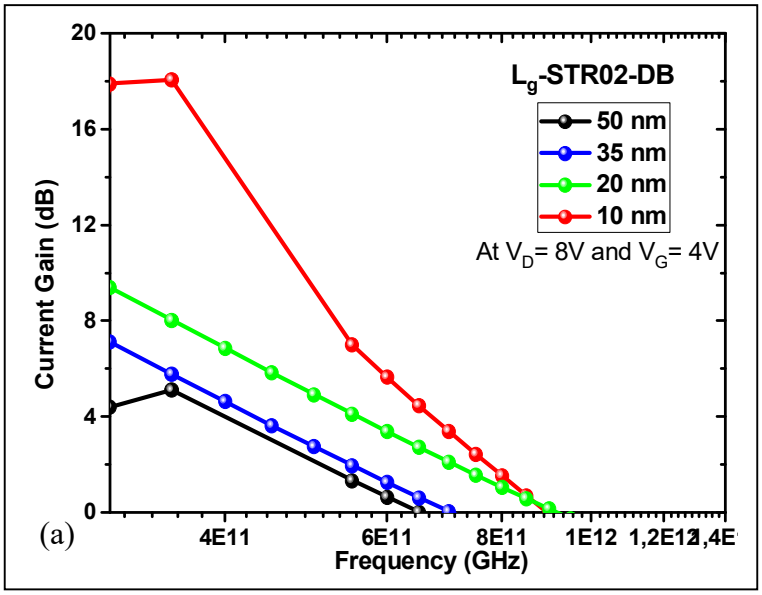

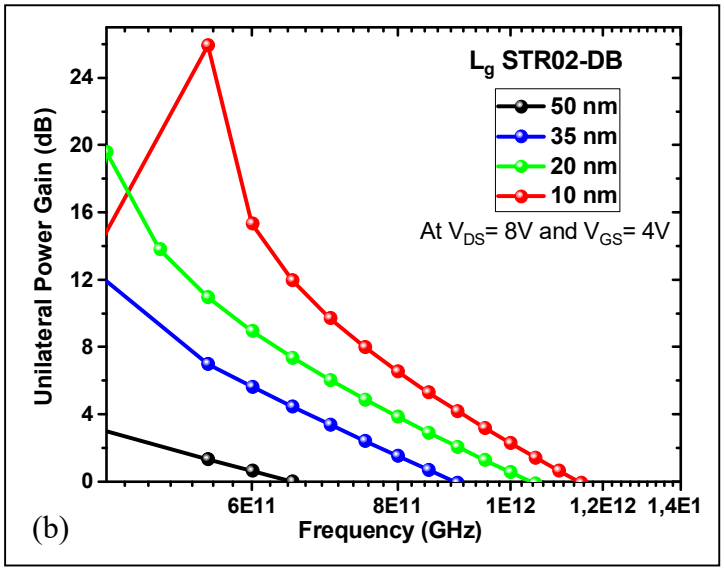

Figure III.12 RF characteristics of double barrier GaN-based MOSHEMT with respect to T-gate length (Lg = 10, 20, 35, and 50 nm) (a) Current gain, (b) Unilateral power gain.

➢ **Recapitulative table**

Table III.4 shows the main physical parameters obtained with our designed MOSHEMTs, compared with other results reported in various references using double barriers.

Table III.4 Performance comparison of our results with similar experimental reports.

Ref	(MOS)HEMT Transistor Device	$n_s \times 10^{13}$ cm^{-2}	I_D A	V_{th} V	g_m mS	V_{BR} V	C_G pF	f_t GHz	f_{max} GHz
[110], 2020	$Al_{0.30}GaN/Al_{0.20}GaN$/ GaN	--	--	0	68.9	--	220	--	--
[111], 2015	$Al_{0.85}In_{0.10}GaN$/ $Al_{0.15}GaN$/AlN/GaN	3.5	0.73	+1.1	--	--	--	--	--
[44], 2019	$Al_{0.54}In_{0.12}GaN$/ $Al_{0.18}In_{0.04}GaN$ /GaN	--	0.76	+0.4	493	--	--	--	--
[112], 2020	$Al_{0.72}In_{0.16}GaN$/ $Al_{0.18}In_{0.04}GaN$/ $Al_{0.80}In_{0.18}GaN$ /GaN	1.2	0.11	+0.2	358	--	--	--	--
[113], 2021	$Al_{0.20}GaN/Al_{0.07}GaN$/ $Al_{0.20}GaN$/GaN	--	0.74	+0.3	370	--	--	--	--
[114], 2022	$Al_{0.165}In_{0.775}GaN$/ $Al_{0.60}GaN$ /GaN	1.6	0.2	-1.5	--	--	38	0.95	4.5
[115], 2019	$Al_{0.74}In_{0.16}GaN$/AlN/ GaN/$Al_{0.08}GaN$	1.81	2.9	-2.8	900	38	0.275	310	425
Our work	STR 01-SB	0.23	3.30	+2.8	4320	126	1.767	812	1023
	STR 02-DB	0.49	3.78	+3.2	4470	140	1.453	891	1148

The characterization of the proposed MOSHEMTs on 4H-SiC substrate, demonstrates a superior DC and AC performances, setting new records for GaN-based MOSHEMTs in terms of high-speed, high current and terahertz frequency operations.

III.4 Device C: AlGaN/AlInGaN/GaN MOSHEMT on β-Ga_2O_3 substrate

III. 4. 1 Device Description

In this part of our research, we simulate the same structure as Device B with a single barrier, and make some modifications to improve the RF performance of the device using new materials. Figure III.13 shows the 2D schematic structure that we simulated.

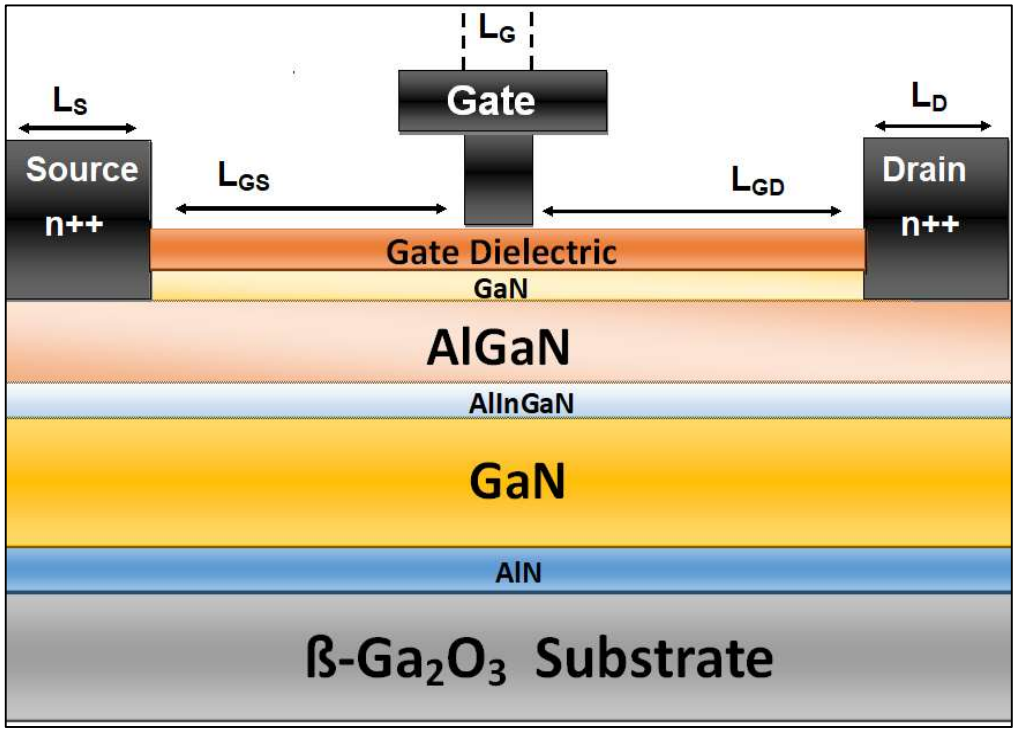

Figure III.13. 2D design of AlGaN/AlInGaN/GaN MOSHEMT on β-Ga_2O_3 substrate.

The modifications made are as follows:

- Change the passivation material from silicon oxide (SiO_2) to silicon nitride (Si_3N_4) based on the work of Bernat et al [116]. A detailed comparative study of an AlGaN/GaN HEMT passivated with SiO_2 and Si_3N_4 has been carried out, demonstrating that the performance improvements are greater using Si_3N_4 passivation than using SiO_2 passivation.
- Increase the composition of the AlInGaN spacer layer by raising the aluminum and indium contents to 0.8 and 0.18 to increase the 2DEG confinement.
- Deposit the device on a new substrate material, namely β-Ga_2O_3. Below the GaN channel, an AlN nucleation layer is grown on a UWBG- β-Ga_2O_3 substrate. This substrate is doped

with n-type impurities of 1.5×10^{15} cm^{-3} to accommodate the standard melt-growth technique introduced by the Czochralski process to ensure both low power consumption and low-cost manufacturing [117, 118]. The electrical parameters of the β-Ga_2O_3 substrate used during the simulation are the same as those listed in Table II.5.

III. 4. 2 Result and discussion

In order to evaluate the performance of the proposed device C, we will observe the effects of varying some geometric and physical parameters of our structure on its performance. We varied each of the parameters independently and observed the impact of these variations on the DC and RF characteristics. The results obtained are presented below.

III.4.2.1 Variation of the nature of the gate dielectric

The choice of oxide material in MOS structures plays a key role in reducing the leakage current and improving overall device performance. In this section, we simulate our structure using different gate dielectrics to see which one would improve its performance. These high-k materials are Si_3N_4, Al_2O_3, HfO_2, and TiO_2, and their electrical parameters are compared in Table II.3. In our work, the thickness of the dielectric layer is fixed at 5 nm and its permittivity is varied. We perform various simulations to study the impact of these materials:

- **Transfer characteristics**

Figure III.14 (a) shows the I_{DS}-V_{GS} transfer curve of the MOSHEMT on β-Ga_2O_3 at different dielectrics, at V_{DS} = 1V.

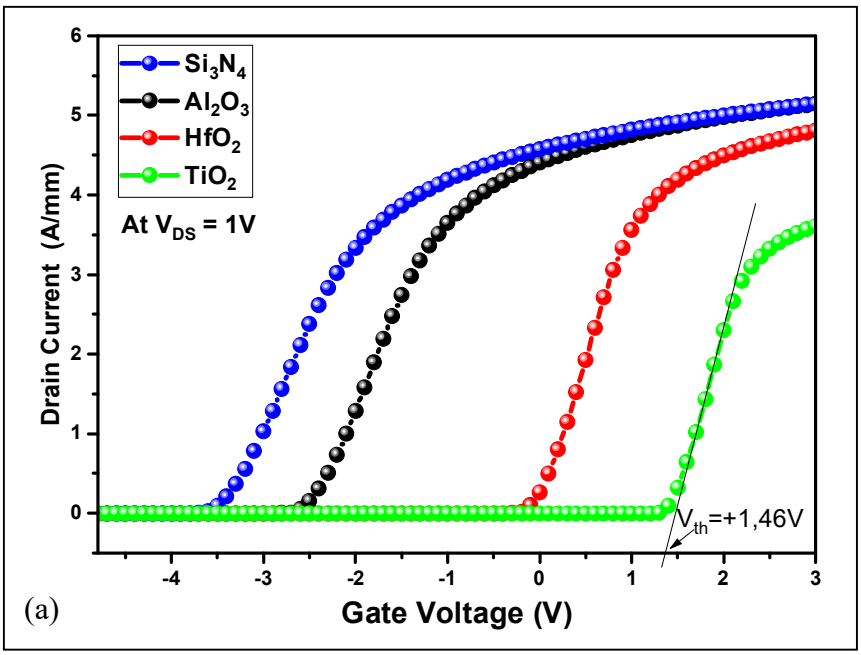

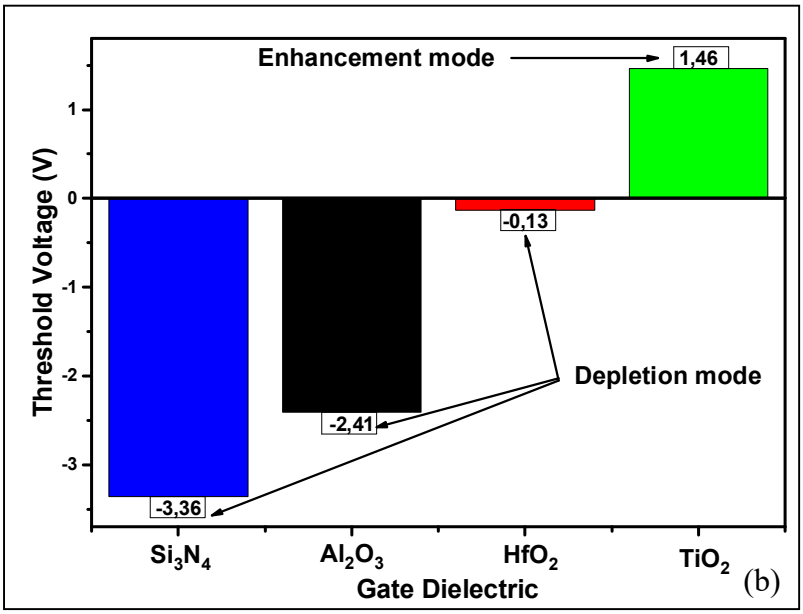

Figure III.14 (a) Linear transfer characteristics for different dielectrics (b) V_{th} comparison.

From our simulations, the extracted values of the threshold voltage are -3.36, - 2.41, -0.13, and +1.46 for gate oxides: Si_3N_4, Al_2O_3, HfO_2, and TiO_2, respectively. However, the V_{th} drops beyond a critical value of the permittivity, whereas the device with the highest-k achieves the E-mode operation, as compared in Figure III.14 (b).

Figure III.15 presents log (I_d) as a function of V_{GS}, it shows that the β-Ga_2O_3-MOSHEMT with TiO_2 turns off at a higher gate voltage than Si_3N_4. This is the consequence of high permittivity material, resulting in a reduced carrier concentration. For all scenarios, the extracted values of the I_{on}/I_{off} ratio are greater than 10^{12}.

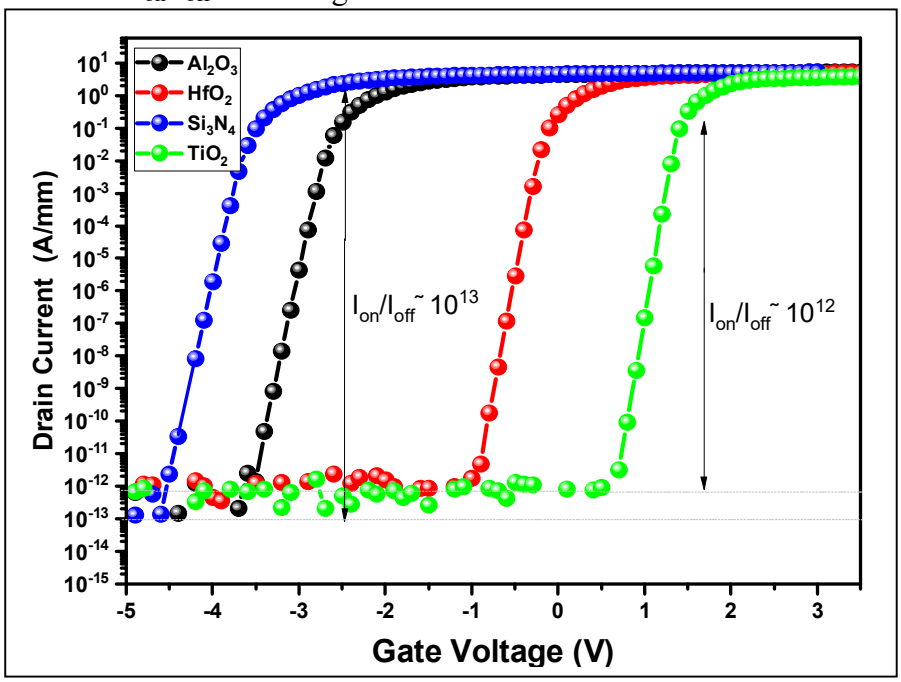

Figure III.15 Transfer characteristics in the logarithmic scale.

The comparison of DC transconductance versus gate voltage for different high-k materials is depicted in Figure III.16 at V_{DS}=1V.

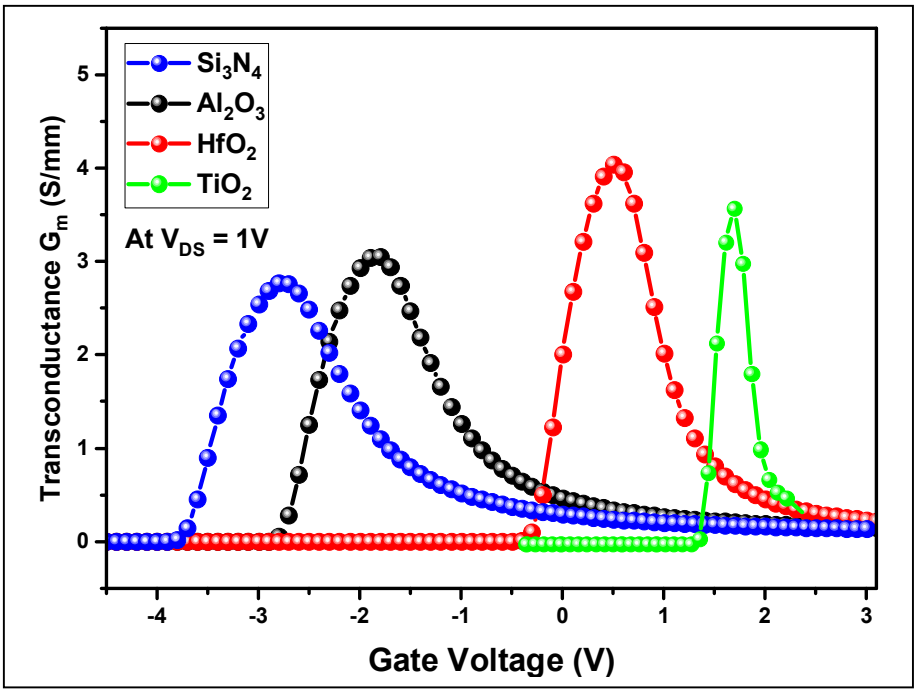

Figure III.16 DC transconductance variation for different dielectrics.

A higher transconductance value indicates better device response and allows operation in a high-frequency range. Our simulation shows that a peak g_m of 4 S/mm for HfO_2 oxide is obtained. Similarly, the MOSHEMT with TiO_2 oxide material exhibits a high g_m of 3.4 S/mm. In the case of Si_3N_4 and Al_2O_3, the peak transconductances show moderate values.

- **Output characteristics**

According to equation I.29, the drain current is directly proportional to the 2DEG density, and the threshold voltage for a transistor is defined as the minimum gate-to-source voltage (V_{GS}) needed to create a conducting charge between the source and drain. Therefore, to obtain an acceptable value of drain current, we need to determine the gate-source voltage near the threshold voltage value. In our case, we aim to design MOSHEMT with high RF performance, for that we choose V_{GS} = 0.5 V for each simulation

Regarding the I_{DS}-V_{DS} curves shown in Figure III.17, the device exhibits a maximum drain current of 9.5 A/mm for gate oxide Si_3N_4 (V_{TH} = -3.36V), and 6.5 A/mm for gate oxide Al_2O_3 (V_{TH} = -2.41V). In these cases, we observed that V_{GS}>>V_{TH}, these values are unacceptable and also show negative effects due to current collapse and kink effect, with highest pinch-off voltage. Furthermore, the MOSHEMT with high-k oxide TiO_2 exhibits a

much lower drain current of 0.047 A/mm compared to others, because V_{GS}<<V_{TH} we should increase the gate voltage.

At the same gate bias, the drain current of the HfO_2-MOSHEMT reaches a maximum value at 1A/mm, at $V_{GS} \approx V_{TH}$. In addition, HfO_2-MOSHEMT shows a low pinch-off voltage and the highest transconductance, hence, it has the best static performance.

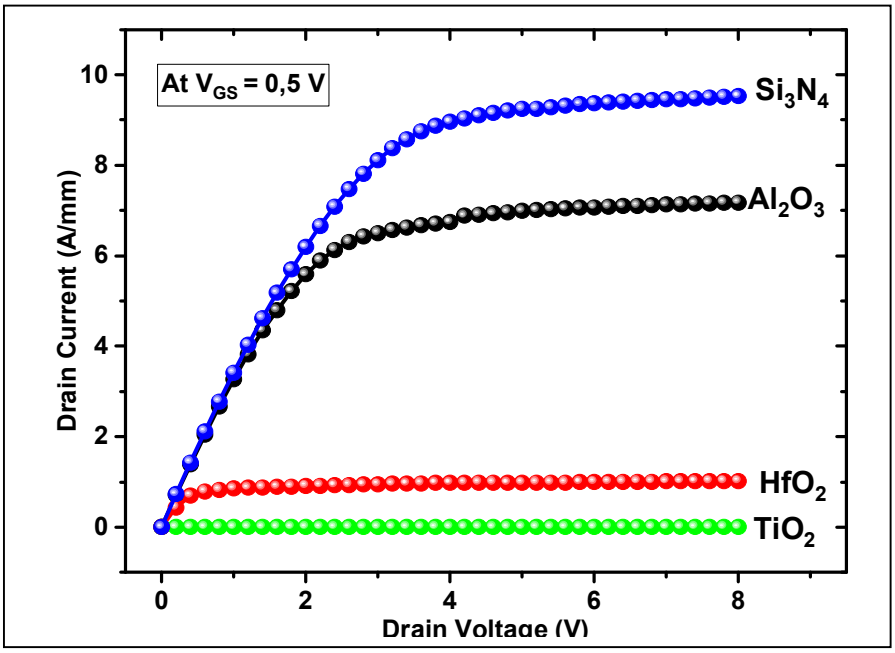

Figure III.17 Output characteristics at V_{GS} =0.5V.

➢ **Capacitance characteristics**

We have simulated the device's capacitance as a function of V_{GS} (see Figure III.18). The device demonstrates low capacitance with all-gate oxides materials. The gate oxide Si_3N_4 capacitance shows the minimum values of C_G compared to other dielectrics materials used, as shown in Table III.5.

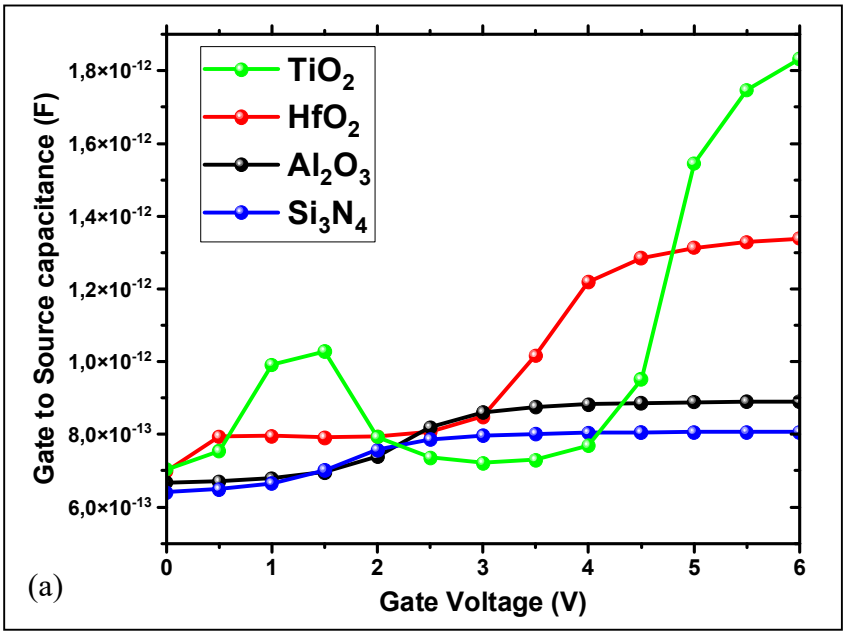

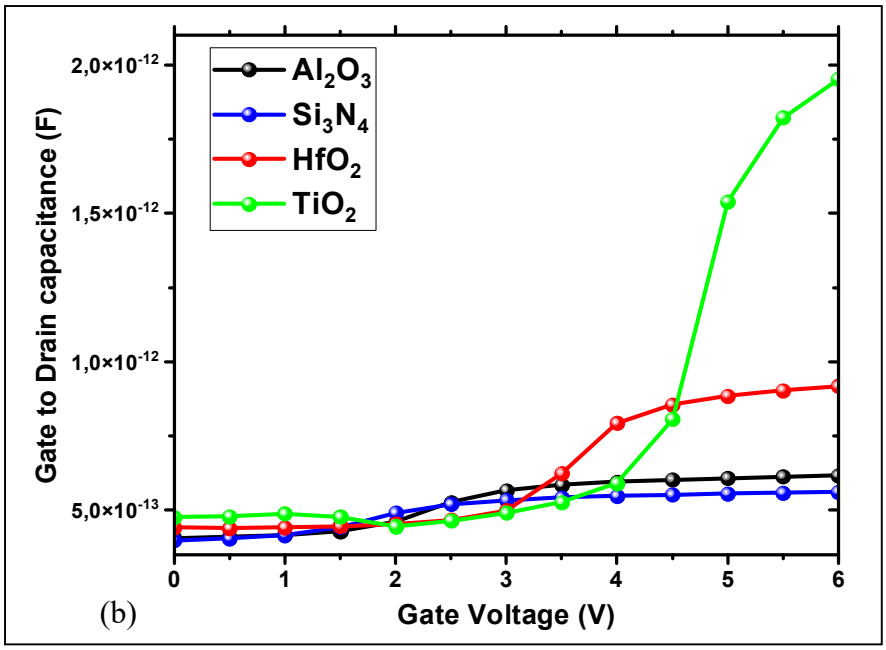

Figure III.18 (a) C_{GS}, (b) C_{GD}, for oxides gates: Si_3N_4, Al_2O_3, HfO_2, and TiO_2

➢ **RF characteristics**

The optimal current and power gains of different high-k dielectric materials are depicted in Figure III.19. Device B shows outstanding frequency performances thanks to the short T-gate and the sequence layer of the device on the β-Ga_2O_3 substrate. In particular, HfO_2-based MOSHEMT exhibits the greatest frequencies thanks to its stability, strong efficiency, high band gap, and high permittivity. Table III.5 summarizes the AC characteristics of all the dielectrics, including the capacitances, the frequencies, and the transition time of the proposed device (Device-C).

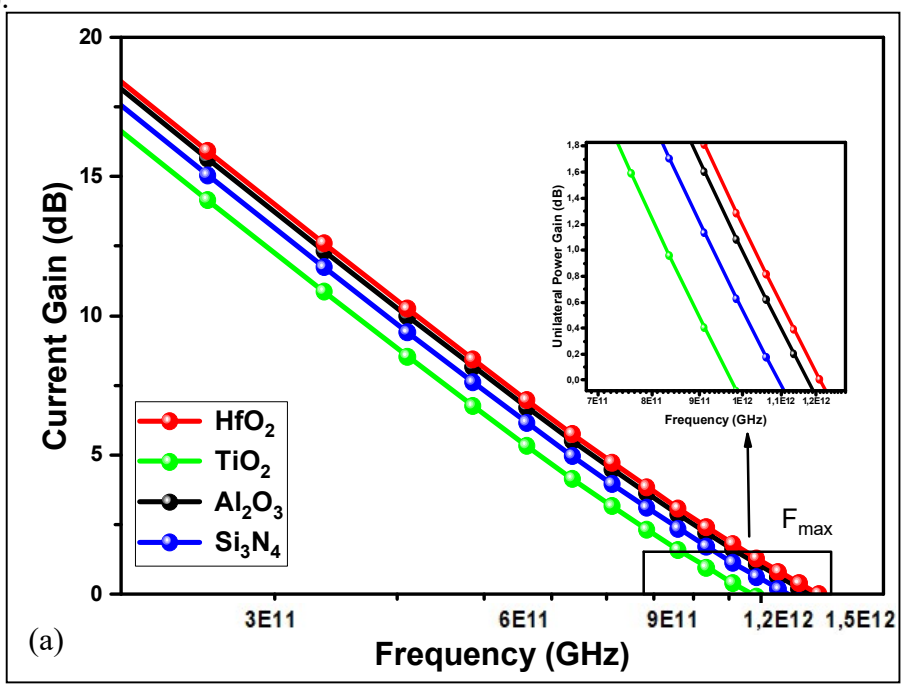

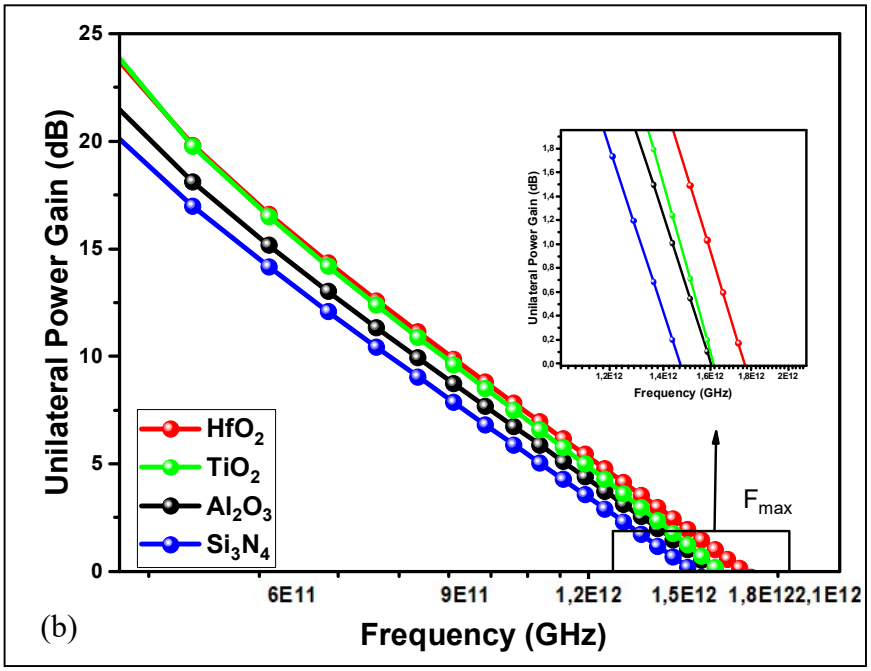

Figure III.19 Current (a) and power (b) gain for different gate oxides with L_g= 50nm.

Table III.5 AC characteristics results of the studied MOSHEMT on β-Ga_2O_3 substrate.

Oxide	C_{GS} (F)	C_{GD} (F)	C_G (F)	f_t (THz)	f_{max} (THz)	τ (pS)
Si_3N_4	8.068×10^{-13}	5.779×10^{-13}	$1{,}38 \times 10^{-12}$	1.093	1.468	0.145
Al_2O_3	8.91×10^{-13}	6.37×10^{-13}	$1{,}53 \times 10^{-12}$	1.174	1.603	0.135
TiO_2	2.035×10^{-12}	2.336×10^{-12}	$4{,}37 \times 10^{-12}$	0.972	1.614	0.163
HfO_2	$1{,}37 \times 10^{-12}$	$9{,}79 \times 10^{-13}$	$2{,}35 \times 10^{-12}$	1.216	1.770	0.130

We note that our proposed gate oxide HfO_2-based MOSHEMT exhibits excellent drain current with low pinch-off voltage, threshold voltage very close to positive values, highest transconductance and record frequency performance compared to other devices. We conclude that the choice of the oxide material must be such that:

- Its permittivity must be high enough to ensure its miniaturization.
- The oxide must behave like a good insulator (band gap > 5 eV).
- The oxide must be not only stable but also compatible with current manufacturing techniques.

Consequently, for the rest of our simulation, we choose HfO_2 as the oxide layer, because it guarantees both high current and high frequency.

III.4.2.2 Impact of AlInGaN spacer composition

Using quaternary AlInGaN as a spacer layer significantly increases the transport charge in the device and provides good interface charges for electron flow. Standard thickness of a spacer layer should not be greater than 2 nm, so we will not change this parameter. On the other hand, the constituent of this spacer layer will significantly affect the overall DC and RF

characteristics. In this case, we will study the impact of varying the percentage of In mole fraction when leaving the Al value as high as possible of the HfO_2-based MOSHEMT. The spacer compositions are $Al_{0.80}In_{0.18}GaN$, $Al_{0.80}In_{0.14}GaN$, $Al_{0.80}In_{0.10}GaN$, and $Al_{0.80}In_{0.7}GaN$.

- **Electronic parameters**

First of all, we will see the impact of decreasing the spacer composition on the 2DEG electrons confinement in the channel formed and the main physical parameters such as the band gap and polarization charge at T=300K. Figure III.20 shows the electron concentration in the AlInGaN/GaN interface, decreasing the spacer layer constituent will decrease the electron concentration and the confinement of electrons, hence the current density, which is detrimental.

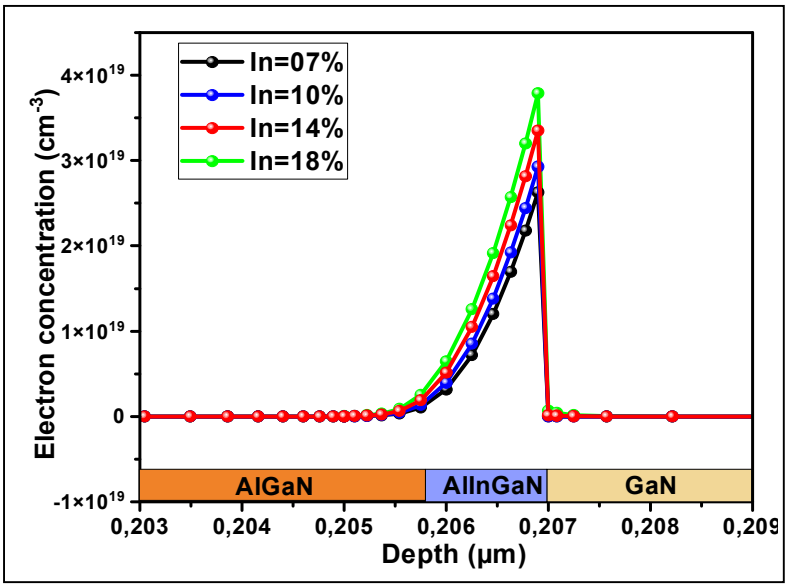

Figure III.20 Electron concentration at the spacer/channel interface as a function of In%.

Table III.6 lists the electrical and physical parameters of the AlInGaN spacer as a function of In-content. All the parameters increase with increasing indium, except for permittivity and piezoelectric polarization, which decrease, which is preferable. We cannot increase the indium by more than 20%, as this would lead to deformation of the crystal [119] and create a dislocations in the crystal lattice.

Table III.6 Electrical parameters of AlInGaN spacer as a function of indium mole fraction.

Indium mole fraction	**07%**	**10%**	**14%**	**18%**
n_s ($\times 10^{12}cm^{-2}$)	1.360	1.561	1.853	2.175
2DEG ($\times 10^{19}$ cm^{-2})	2.62	2.90	3.35	3.78
E_g (eV)	4.61	4.71	4.80	4.91
ε	9.73	9.48	9.22	9.03
P_{sp} ($\times 10^{13}$ cm^{-2})	-4.007	-3.991	-3.975	-3.963
P_{pz} ($\times 10^{13}$ cm^{-2})	-4.226	-4.437	-6.33	-7.391

- **Output characteristics**

The drain current density depends strongly on the effective speed of the electrons in the channel and the sheet charge density as shown in Equation I.29. Figure III.21 shows the I-V output current at V_{GS} = 0.5V and 1V. The device has good behavior, and the voltage knee is extremely low thanks to the layer passivation. Decreasing the In% will decrease significantly the drain current density. The access resistance of the device is extremely low.

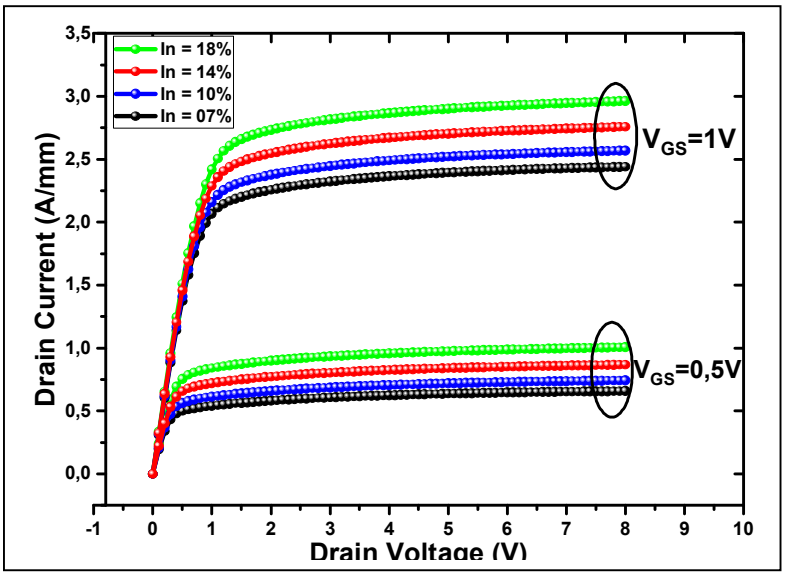

Figure III.21 I_D-V_D characteristics as a function of indium mole fraction.

- **Transfer characteristics**

Figure III.22 shows the transfer characteristics as a function of indium composition.

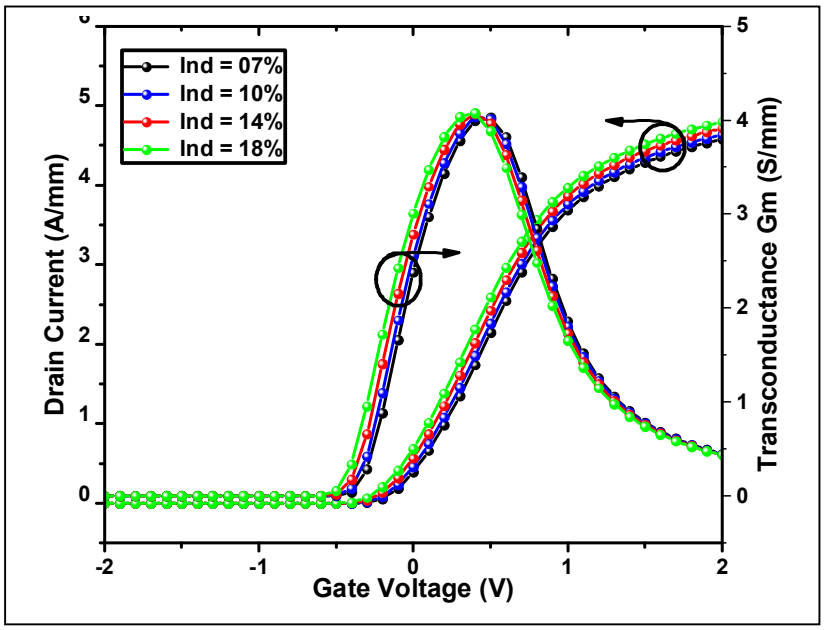

Figure III.22 I_D-V_G and g_m characteristics as a function of indium mole fraction.

As can be seen, decreasing the In-content on the spacer leads to a shift in threshold voltage towards positive values. In addition, the slope of the transconductance curve is practically constant, a slight decrease is observed. Therefore, the indium mole fraction for the spacer has little influence on the gate control and the operating frequency. Results are summarized in Table III.7.

Table III.7 Input/output characteristics at different Indium mole fractions.

Indium mole fraction	$I_{d,max}$ (A/mm) at V_{GS}= 0.5V	$I_{d,max}$ (A/mm) at V_{GS}= 1V	R_{on} (Ω/mm)	V_{TH} (V)	$G_{m,max}$ (S/mm)
18%	1.00	2.96	0.173	-0.13	4.08
14%	0.867	2.75	0.177	-0.09	4.05
10%	0.742	2.56	0.176	-0.05	4.03
7%	0.658	2.44	0.182	-0.01	3.98

➢ **RF characteristics**

Figure III.23 shows the current gain and power gain as a function of frequency, clearly, high frequency was obtained for a high In-content. The $Al_{0.30}GaN/Al_{0.80}In_{0.18}GaN/GaN$ MOSHEMT on β-Ga_2O_3 substrate shows excellent performance. We conclude that the content of the indium mole fraction of the spacer layer has a strong impact on the 2DEG surface density of the channel and on the drain current. Decreasing indium content has little effect on the transconductance and the frequencies (f_t and f_{max}) provided by our designed device.

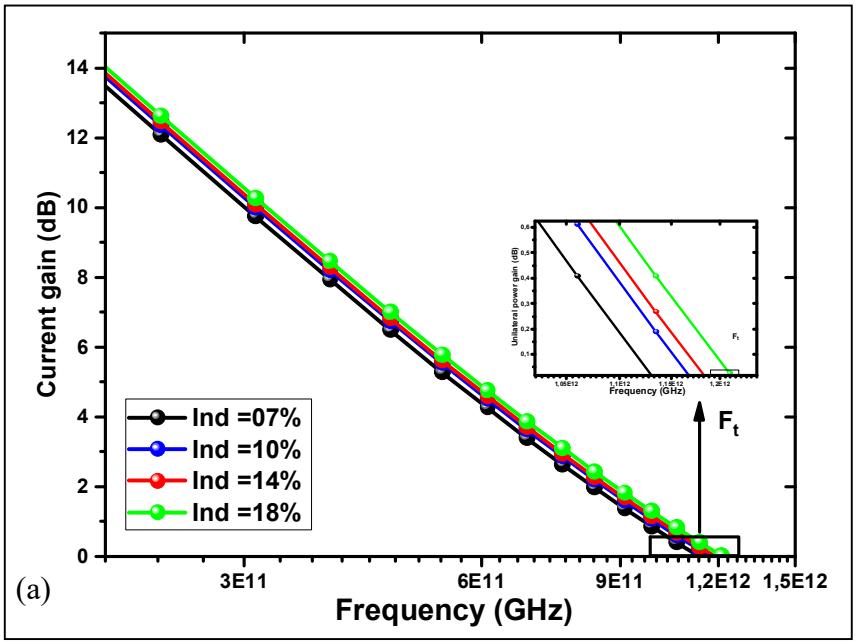

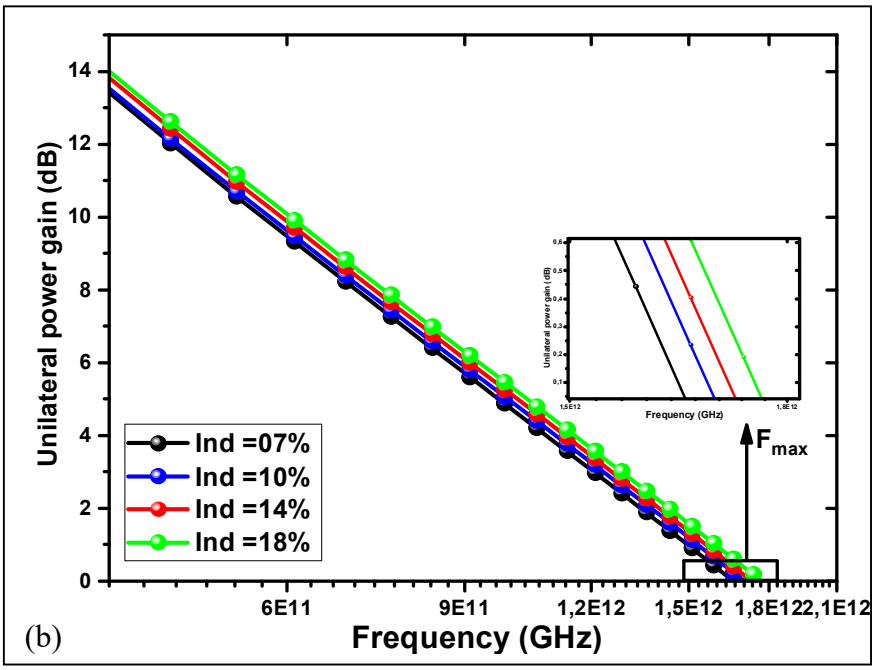

Figure III.23 Current (a) and power (b) gains at various In-content with L_g = 50nm.

III.4.2.3 Impact of temperature variation

In this section, we investigate the output/input parameters and RF performance of Device C, at elevated temperatures. In the simulation, we reduced the gate length from 50 nm to 30 nm to compare the impact of gate length when varying temperature.

- **I_{DS}-V_{DS} output Characteristics**

Figure III-24 shows the I_{DS}-V_{DS} characteristics of the C device for different temperature values ranging from: 300K, 400K, 500K and 600 K at V_{GS} = 0.5 V. As the temperature increases, the mobility of the charge carriers increases and, consequently, the interactions between the charges also increase, reducing the output current [18]. This phenomenon is clearly visible in the simulated characteristics.

A slight Kink effect is observed due to surface traps at elevated temperature. However, no self-heating phenomenon is observed up to V_{DS} = 8V, suggesting stable operation of the device, which maintains a high drain current at room temperature of 1960 mA/mm compared with 680 mA/mm at a high temperature of 600K, a decrease of about 65%.

We compare our results with an AlGaN/AlN/GaN HEMT on β-Ga_2O_3 substrate proposed by G. Purnachandra Rao[120]. At 300K, the device showed an $I_{D\ max}$ of 1100 mA/mm and at 800K the device showed an output drain current reduction of 502 mA/mm.

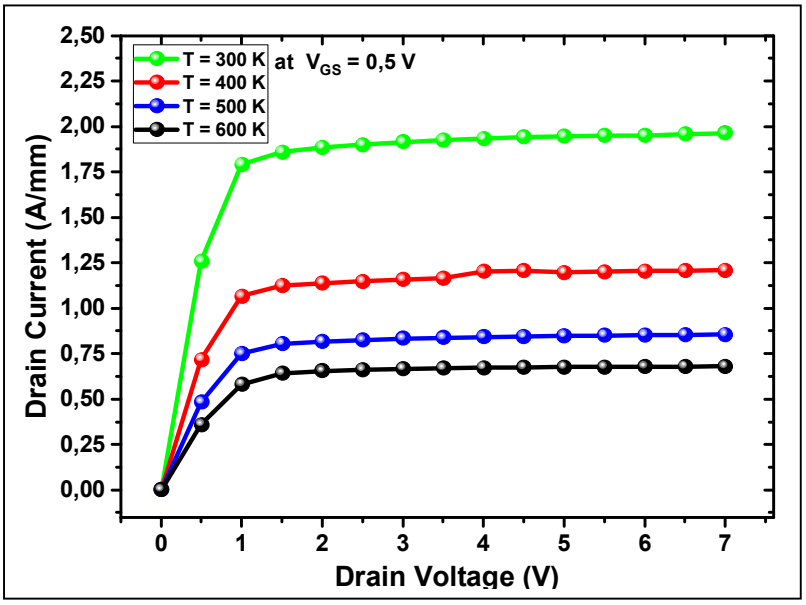

Figure III.24 I_d-V_{DS} output characteristics at different temperatures.

These results confirm the ability of these nanodevices to operate at high temperatures with good performance. In addition, at room temperature, the maximum current reached is around 1.9 A/mm with L_g=30nm at V_{GS}=0.5V, compared with 1A/mm for L_g=50nm (Figure III.21). The current increases with decreasing gate length.

- **I_{DS}-V_{GS} and g_m input characteristics**

To follow the evolution of the threshold voltage V_{TH} as a function of temperature, Figure III.25 (a) illustrates us the transfer characteristics with respect to temperature range, varied from 300K to 600 K with a step of 100 K at V_{DS} = 0.5V.

It can be seen that the increase in temperature causes the threshold voltage to shift toward positive values, −0.34V was extracted at room temperature compared with -0.12V at 600 k. We note that V_{th} is less dependent on temperature than other parameters [121].

However, it is clear that increasing temperature has a significant impact on the drain current. The transconductance variation of the proposed device is shown in Figure III.25 (b) at V_{DS} = 0.5V.

The maximum transconductance reduces from 2200 mS/mm to 520 mS/mm from 300 to 600 K, a reduction of 76% is observed.

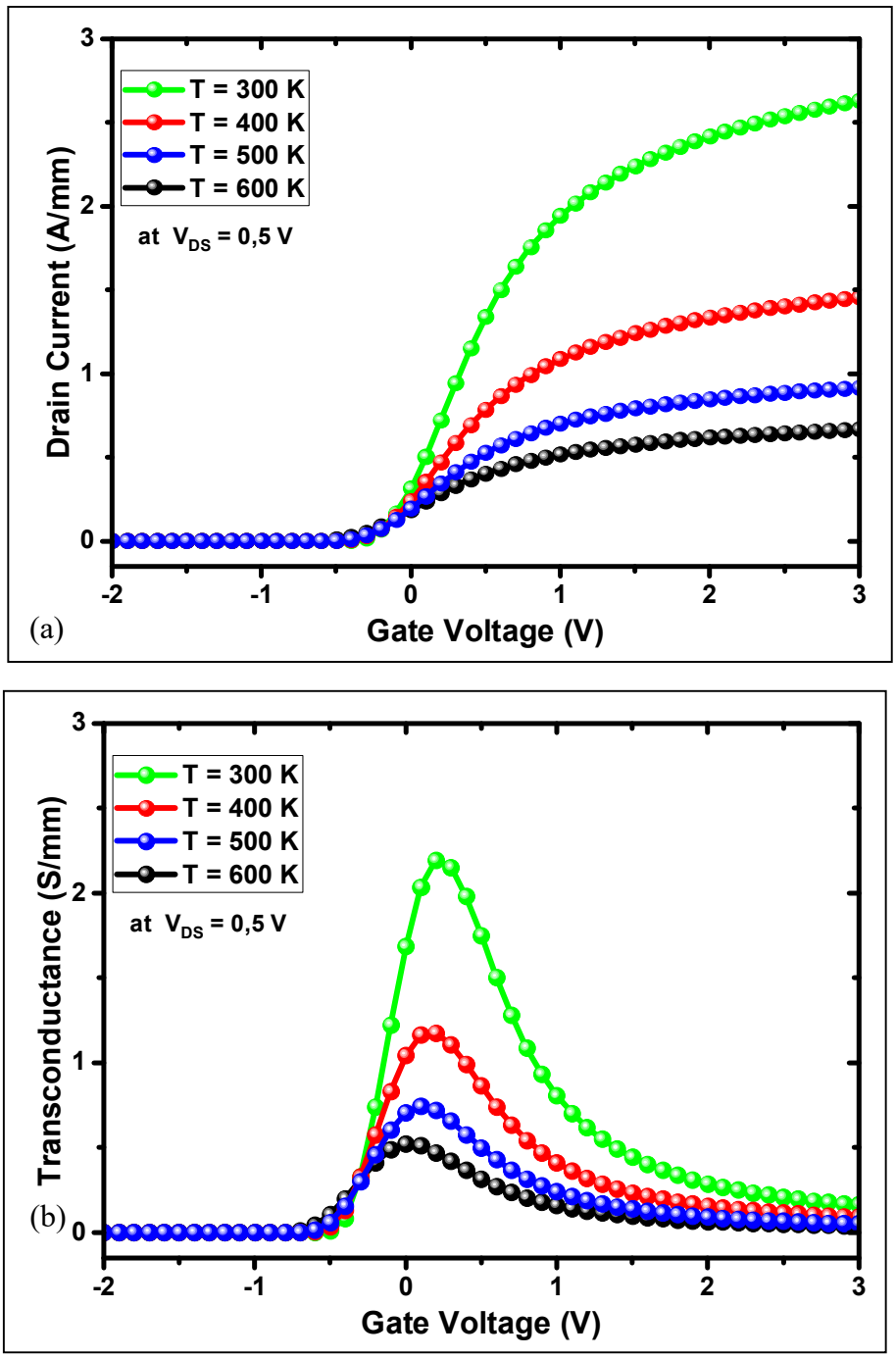

Figure III.25 (a) I_d-V_{GS}-T transfer characteristics, (b) Transconductance (g_m-T).

- **RF characteristics**

The cut-off frequency (f_t) and the maximum frequency (fmax), are inversely proportional to the higher temperature. This decrease in the value of f_t is in good agreement with theory, since the transition frequency is proportional to the electron saturation velocity (Equation III.6) and the maximum oscillation frequency is proportional to the transition frequency (Equation I.41). Overall, the speed of electrons decreases with increasing temperature.

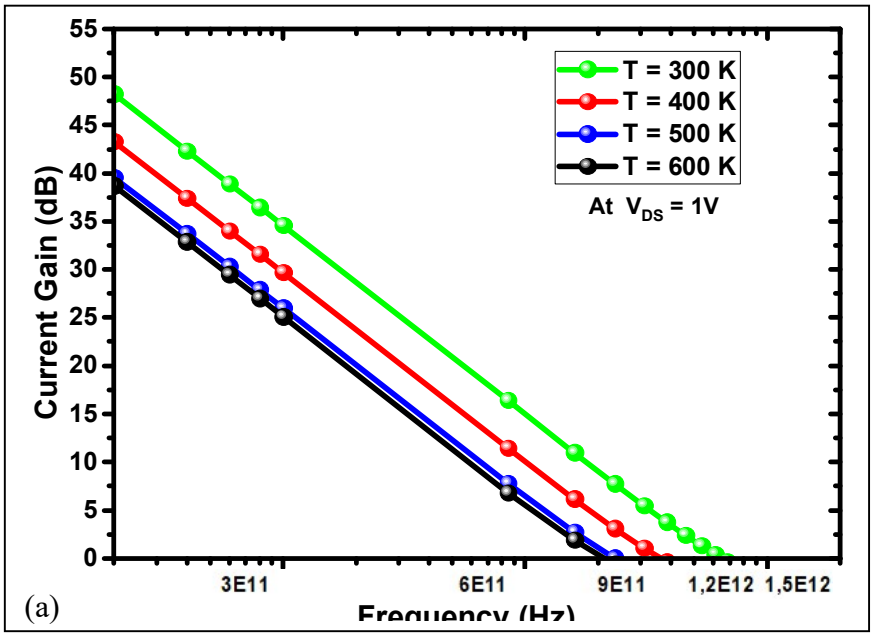

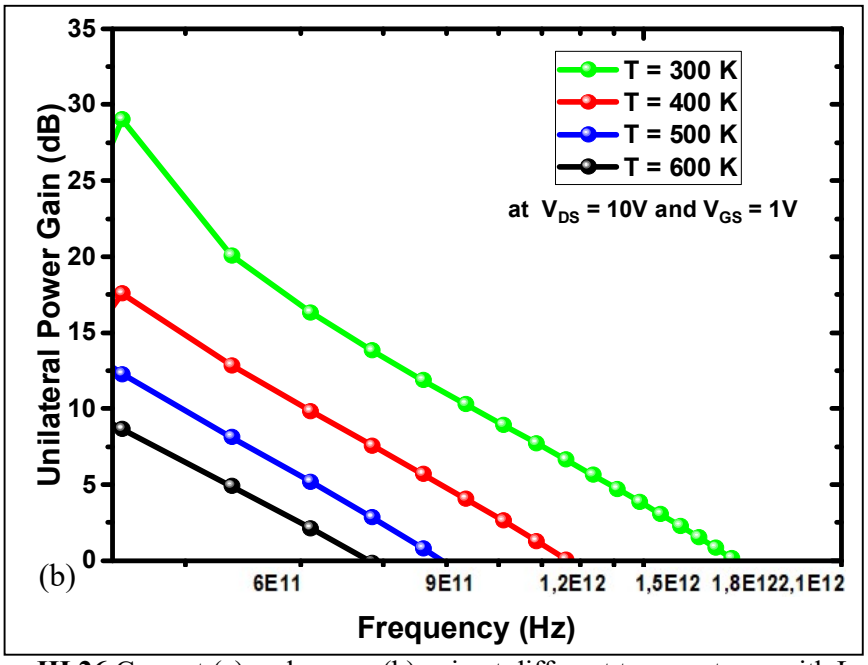

Figure III.26 Current (a) and power (b) gain at different temperatures with L_g = 30nm.

It can be seen that the device suffered a significant decrease in its operating frequency at high temperatures. From the simulation results, we inferred that the implementation of this novel HfO_2/AlGaN/GaN MOSHEMT layered on β-Ga_2O_3 substrate, enables excellent analog and microwave features at room temperature. It has a good performance under high temperature with no noticeable permanent degradation, our results are confirmed theoretically with [19].

- **Recapitulative Table**

Table III.8 compares the obtained results of our proposed MOSHEMT transistors grown on β-Ga_2O_3 substrate with other similar devices.

Table III.8 Comparison of our results with similar reports using β-Ga_2O_3 substrate.

Ref	Transistors on β-Ga_2O_3 substrate	$n_s \times 10^{13}$ cm^{-2}	I_{Dmax} A	I_{on}/I_{off}	V_{th} V	g_m mS	C_G pF	f_t GHz	f_{max} GHz
[122], 2023	AlGaN/GaN/ AlGaN HEMT	-	2	10^{19}	+0.2	-	3.47	559	851
[123] 2020,	AlGaN/GaN MOSHEMT	-	0.002	-	-	-	-	82	360
[124], 2021	AlGaN/GaN HEMT	-	0.007	-	-1.7	2	-	265	900
[125], 2021	AlN/ β-Ga_2O_3 HEMT	3.8	1.32	10^{7}	-3.8	320	-	68	142
[126], 2022	AlGaN/AlN/GaN/ AlGaN HEMT	-	1.2	10^{16}	0.51	-	3.7	420	720
[51], 2022	$Al_{0.31}GaN/Al_{0.1}GaN$ / $Al_{0.1}GaN$ HEMT	1.05	1.3	10^{14}	-4.3	270	-	-	-
[117], 2023	AlGaN/AlN/GaN HEMT	-	1.4	-	0.8	-	-	1288	1884
[127], 2021	AlGaN/GaN HEMT	-	0.004	-	0.12	6	-	470	2600
This work	AlGaN/AlInGaN/ GaN MOSHEMT	0.3	3	10^{12}	-0.13	4000	2.35	1216	1770

III.5 Conclusion

In this chapter, we have presented the various results obtained from Atlas SILVACO simulations of a new AlGaN/AlInGaN/GaN MOSHEMT structures. The fundamental objective of our research is to design a high-performance RF transistor by improving the 2DEG concentration, drain current and frequencies.

On the first hand, an AlGaN/AlInGaN/GaN MOSHEMT grown on 4H-SiC substrate (Device B) is simulated. A comparison studies is performed between a single and double barrier layer. The DC and RF results showed that the 10nm T-gate MOSHEMT's performance was considerably improved after the addition of a second AlInGaN barrier, where a sheet charge density of 0.49 $\times 10^{13}$ cm^{-2}, a maximum I_D above 3700 mA/mm, a breakdown voltage of 138V, and record F_t/F_{max} of 891/1148 GHz were obtained with relatively low leakage. The device shows excellent performance.

On the other hand, we modeled the same single barrier AlGaN/AlInGaN/GaN on another substrate, namely β-Ga_2O_3. We constate that the device with 50nm T-gate length and HfO_2 gate oxide, it exhibits an $I_{D;max}$ of 1000A/mm, high f_t/f_{max} frequencies of 1216/1770 GHz. These improvements in frequencies demonstrate the potential of AlGaN/GaN MOSHEMTs on β-Ga_2O_3 substrate.

Chapter IV Design and simulation of RF filtering block for GNSS receivers

IV.1 Introduction

Thanks to the outstanding performance of AlGaN/GaN MOSHEMT components, in particular their ability to achieve higher electron mobilities and higher frequencies than other technologies. This chapter examines an innovative architecture to meet the constraints of minimizing bandwidth and interference in satellite navigation systems while maintaining energy efficiency and reducing power loss. In particular, it discusses the use of gallium nitride technology in a microwave filtering block for GNSS receivers. In this thesis, the well-known RF design software called Advanced Design System (ADS) is used, see Appendix C.

The first section of this chapter describes the main characteristics of GNSS, their frequency bands, and the block architecture of a GNSS receiver. Section two presents the principle of electrical modeling and the extraction methods used to produce the small-signal equivalent model of the designed AlGaN/AlInGaN/GaN MOSHEMT on 4H-SiC (STR02-DB). The third section provides the simulation results of the developed filtering block for a GNSS receiver in the frequency band of interest.

IV.2 Global Navigation Satellite System (GNSS)

The GNSS (Global Navigation Satellite System) system refers to a positioning and navigation system, that combines several systems with worldwide coverage, including GPS (American), GLONASS (Russian), COMPASS (Chinese), GALILEO (European), and IRNSS (Indian) systems. All of these systems are satellite constellations used to determine the position and speed of a receiver located anywhere on earth [129].

IV. 2. 1 GNSS operating principle

Hundreds of satellites are currently orbiting the earth. These satellites constantly transmit precise radio signals containing position and time information. GNSS receivers, such as those built into smartphones or vehicle navigation systems, pick up the signals emitted by the satellites. To determine the position in terms of latitude, longitude, and altitude, the GNSS receiver must receive signals from at least three satellites, using the triangulation method. The receiver determines the distance to each satellite by measuring the time it takes for the signal emitted by the satellite to reach the receiver. Once the receiver calculates the distance to three satellites, it can determine its position. The diagram of the intersection of three spheres; the triangulation method is shown in Figure IV.1.

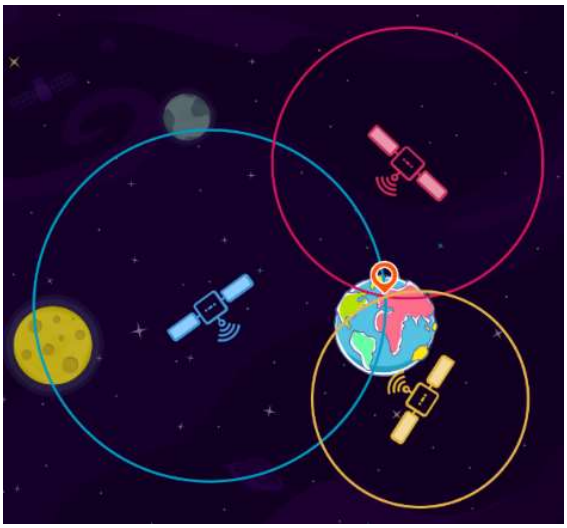

Figure IV.1 Positioning through intersecting three spheres; triangulation method.

Each GNSS system transmits signals in a fixed frequency band. The following table lists the different frequency bands allocated to GNNS systems, ranging from 1.1 to 1.6 GHz:

Table IV.1 Frequency bands allocated for GNSS signals [129].

GNSS system	Frequency band name	Frequency band (MHz)	Carrier frequency (MHz)
GPS	L1	1555-1590	1575.42
	L2	1210-1245	1227.6
	L5	1160 1195	1176.45
GALILEO	E1	1555-1595	1575.42
	E6	1260-1295	1275.75
	E5	1150-1230	1191.795
GLONASS	L1	1594-1610	1600.995
	L2	1238-1254	1248.06
	L3	1190-1212	1202.025
COMPASS	B1	1550-1610	1575.42
	B2	1160-1250	1207.14
	B3	1250-1285	1268.52
IRNSS	L5	1164-1188	1176.45

IV. 2. 2 GNSS system segments

GNSS system requires a suitable infrastructure, which is designed as follows:

- **Space segment:** It consists of a nominal constellation of operating satellites; the orbit altitude is about 20,000 km above the Earth.
- **Ground segment:** It is formed by a network of control stations, providing the user's position updating and corrections.
- **User segment:** It consists of the receiver equipment, which receives the signals from the satellites and calculates the 3D user's position.

In this thesis, we are interested in the third part of the GNSS infrastructure, which is the GNSS receiver. Figure IV.2 shows the GNSS infrastructure.

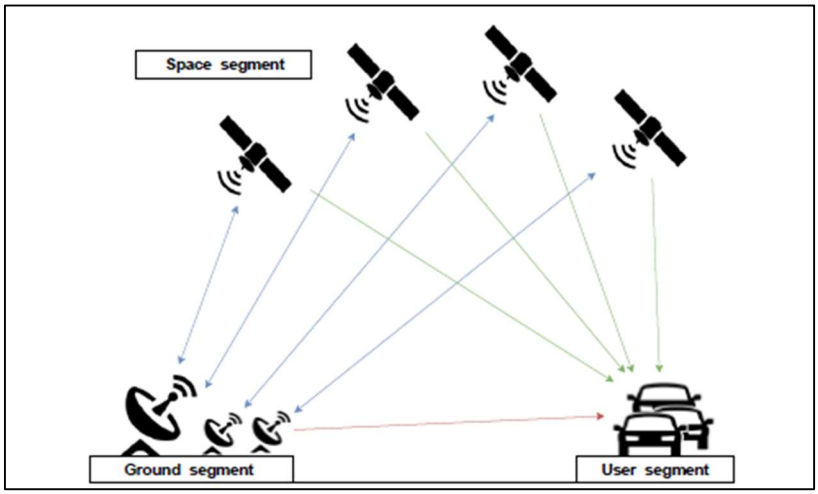

Figure IV.2 GNSS infrastructure.

IV.3 GNSS receiver

The GNSS receiver can be broken down into several blocks, each with a specific mission, all of which lead to receiving, processing, and calculating position from the signals emitted by the GNSS satellites. The block diagram of a generic GNSS receiver is illustrated in Figure IV.3 [1]. This receiver architecture is the most efficient and popular [130].

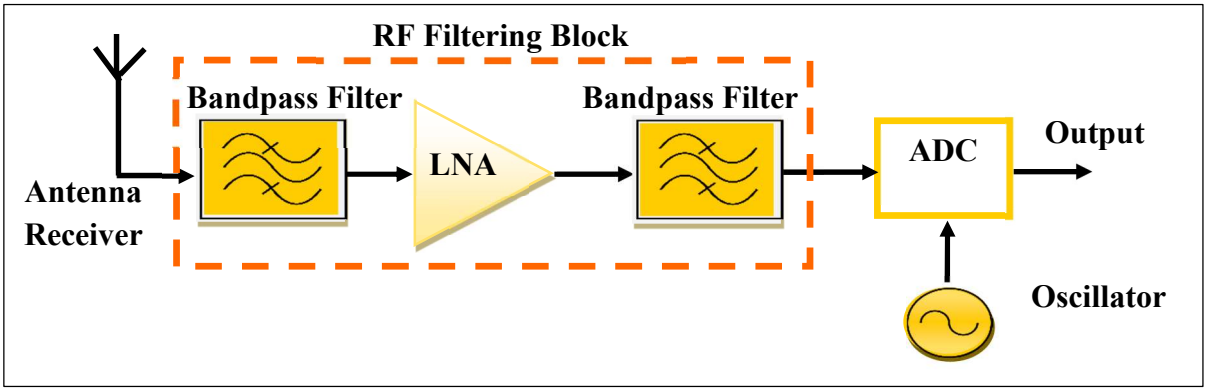

Figure IV.3 Radio frequency block diagram of the basic structure of a GNSS receiver.

The basic function of a GNSS receiver is to recover the transmitted baseband signal to guarantee navigation accuracy. Therefore, an RF signal is received by the antenna. Then the signal passes through a bandpass filter which provides some selectivity by filtering out received signals with unwanted frequencies and passing some signals in the GNSS appropriate frequency. The signal from BPF will pass through a low-noise-amplifier (LNA) to amplify the weak received signal to be treated effectively.

The output from LNA is fed to a second bandpass filter which is used to select the narrowest band of the GNSS receiver. A local oscillator (LO) is set to diminish the coming RF signal at the level of the intermediate frequency (IF) which is near to the input and the output of the (ADC) converter. Furthermore, there are other blocks such as the IF filtering block and the demodulation block, which are not of interest in our work. For more details, see [131]. Each block diagram shown in Figure IV.3 is described below.

IV. 3. 1 Receiver antenna

The receiver antenna is an essential component of a GNSS receiver. Its main function is to receive the GNSS signals coming from multiple GNSS constellation satellite and pass them along to the GNSS receiver to calculate its position.

IV. 3. 2 Bandpass filter (BPF)

Two bandpass filters are placed directly in the input and the output of the LNA amplifier to ensure high-frequency selectivity for the GNNS frequency bands from 1.2 GHz to 1.6 GHz and to reject other signals. Bandpass Filters can be made by connecting a low-pass filter with a high-pass filter [132]. Bandpass filters allow signals in a certain frequency band to pass through without distorting the input signal. A typical bandpass filter has two main parameters:

- **Cut-off Frequency (F_C):** This is the central frequency within the desired bandpass. It defines the frequency around which the filter allows maximum signal transmission.
- **Bandwidth (BW):** The bandwidth is the range of frequencies that the filter permits to pass through. It is usually specified as the difference between the upper and lower frequencies (f_L and f_H), where the output gain is reduced to -3dB of its maximum.

The frequency response of a bandpass filter is shown in Figure IV.4.

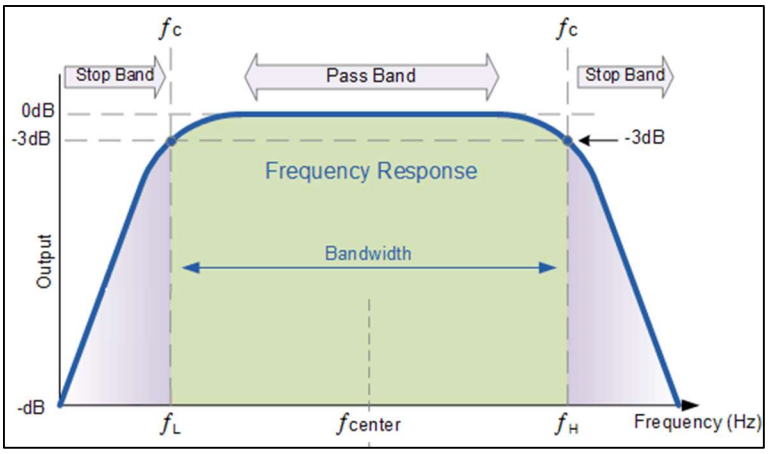

Figure IV.4 Frequency response of a bandpass filter [133].

IV.3.2.1 Bandpass filter types

Bandpass filters used in GNSS receivers can be classified according to their manufacturing technology. Here are some of the most common classifications:

a. **Passive filters:** These filters are built using passive components such as resistors (R), capacitors (C), and inductors (L). They can take various forms, such as RC filters, LC filters, or RLC filters. Passive filters are often used in applications where narrow bandwidth and high-quality selectivity are required.

b. **Active filters:** These filters use active components such as operational amplifiers or transistors. They offer better selectivity, but at the same time increase the complexity and time cost of the circuit. They are used in applications requiring amplification gain.

c. **Surface Acoustic Wave Filters (SAW):** These modern filters exploit surface acoustic waves to filter radio frequency. They are commonly used in GNSS systems due to their compact size, good performance, and low cost [134].

In this thesis, passive bandpass filters based on LC components are designed. The challenge is to ensure that the bandwidth of this filter conforms to the narrow frequency specific to GNSS, ranging from 1100 MHz to 1600 MHz.

IV.3.2.2 LC bandpass filters

LC filters combine inductors (L) and capacitors (C) to form a bandpass filter in radio frequency systems, thanks to their high rejection, low loss, small size, and simple structure. These filters are typically used when a small band of frequency needs to be passed through the filter, and all others are rejected [132].

Several topologies are used to design an LC bandpass filter. The most frequently used are π, T, and Γ, as illustrated in Figure IV.5.

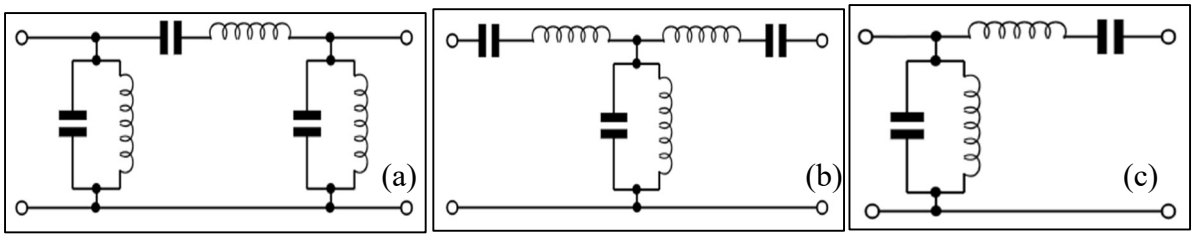

Figure IV.5 LC bandpass filter topologies (a) π format, (b) T format, (c) Γ format [135].

These topologies offer different compromises. The π and T configurations are often used in bandpass filters due to their good performance in terms of selectivity and bandwidth.

However, they can suffer from higher insertion loss than other topologies, particularly at higher frequencies. On the other hand, the Γ topology is very useful in RF applications thanks to its simplicity and ease of implementation. It can offer better impedance transformation and less insertion loss than π and T topologies [132].

IV.3.2.3 Bandpass filter design steps

Designing an RF bandpass filter involves several steps to ensure that the filter fulfills the required criteria. Figure IV.6 shows a flowchart for the main procedures involved in creating an RF filter:

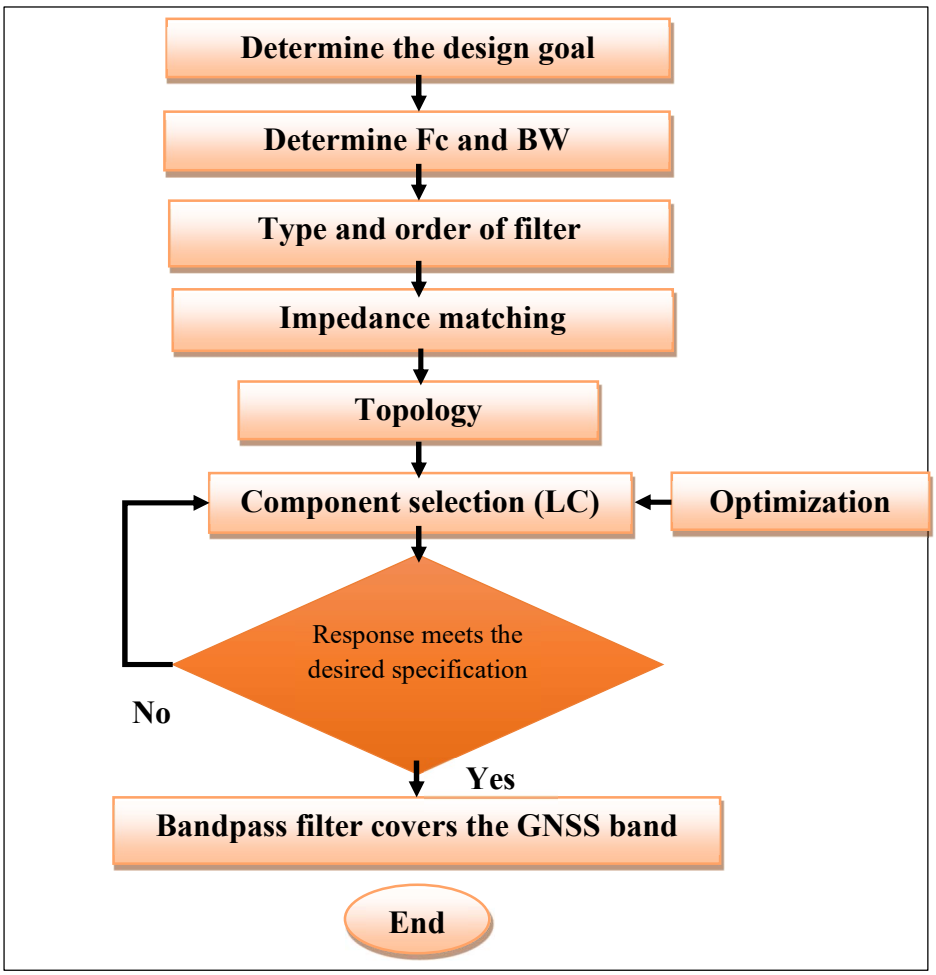

Figure IV.6 Flowchart of the various simulation steps involved in bandpass filter design.

IV. 3. 3 Low noise amplifier (LNA)

The low noise amplifier (LNA) is a key component of the GNSS receiver, used to amplify the received weak signal from the antenna by adding minimum noise to this signal. In this work, the basic discrete active component that we have designed (STR02-DB) is used as the main element for designing a low-noise amplifier (LNA).

IV.3.3.1 LNA topologies

The topologies chosen for the low-noise amplifier circuit design play an essential role in determining the desired performance.

We will present schematic diagrams of the main possibilities for implementing a single-stage LNA based on a single-transistor topology:

a. **Common-source topology:** The term “common-source comes” from the fact that the transistor's "source" electrode is connected to the ground. In this topology, the input signal is applied to the gate and collected by its drain (Figure IV.7 (a)). This is the basic structure most often used, as is the case in our LNA design.

b. **Common-gate topology:** In this circuit, the input signal is applied to the source and its output is at the drain, leaving the gate as the common point (Figure IV.7 (b)).

c. **Common-drain topology:** This circuit (Figure IV.7 (c)) is often used as an impedance adapter (Rs is the input impedance).

There are cascade and cascode circuit topologies defined with two or more transistors, but this is not the case for our study [136]. We have chosen the common-source topology because it amplifies an input voltage that reaches us from the filter, and gives us good voltage stability.

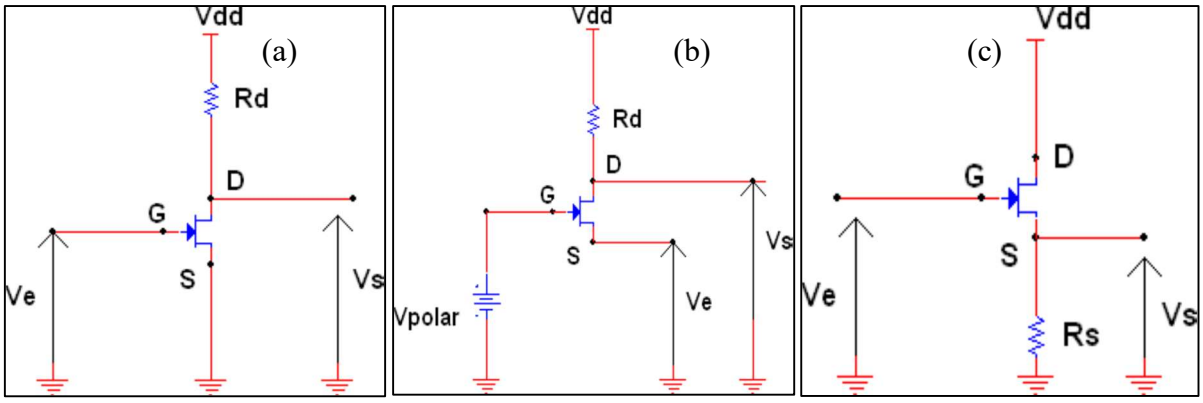

Figure IV.7 LNA topologies (a)Common source, (b)Common gate, (c)Common drain [136].

IV.3.3.2 LNA design steps

When designing a high-performance LNA circuit, several requirements must be met:

a. **Transistor technology:** There is a wide choice of transistors integrated into LNA circuits. The transistors most commonly used are silicon or silicon-germanium (SiGe) bipolar transistors, or gallium arsenide (GaAs) field-effect transistors (FETs) [137,138]. Recently,

a new technology has emerged for RF applications, based on high electron mobility GaN transistors (HEMT and MOSHEMT).

The extremely high performance of these devices enables them to operate at higher frequencies and temperatures. Once the transistor model is chosen, it is important to bias it correctly so that it operates in its linear range, providing maximum amplification with minimum distortion. In this thesis work, the MOS-HEMT transistor (STR02-DB) studied in Chapter III is chosen.

b. Noise figure: The noise figure (NF) of an LNA amplifier characterizes the degradation of the available signal-to-noise ratio at the input (SNR_{IN}) to the available signal-to-noise ratio at the output (SNR_{OUT}), which is defined by:

$$NF = \frac{SNR_{IN}}{SNR_{OUT}} \qquad \text{IV.1}$$

The noise figure must be as low as possible.

c. Stability: The stability of an LNA amplifier determines its resistance to oscillation in the frequency band under study. It is important to study the amplifier's stability to avoid stage oscillations that could cause it to malfunction [139]. One way of expressing the conditions necessary for unconditional stability is to guarantee a stability factor K greater than unity:

$$K = \frac{1 - |S_{11}|^2 - |S_{22}|^2 + |\Delta|^2}{2|S_{12}S_{21}|^2} > 1 \qquad \text{IV.2}$$

And

$$\Delta = S_{11}S_{22} - S_{12}S_{21} < 1 \qquad \text{IV.3}$$

d. Gain: Generally, the gain is defined as the power gain delivered by the component and the power delivered by the excitation source.

e. Input/output matching network: Impedance matching is necessary on the input and output sides of an LNA to minimize reflection and transmission coefficients, and achieve optimum noise figure and maximum gain by setting the load impedance equal to the source impedance, which is generally challenging [140]. Figure IV.8 shows a general transistor amplifier circuit block.

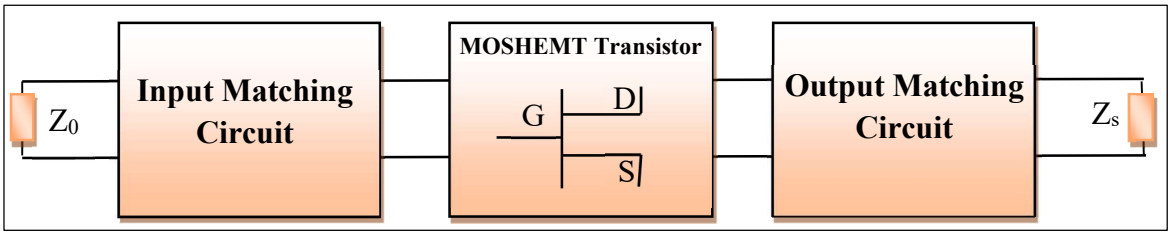

Figure IV.8 General block diagram of a single stage LNA based MOSHEMT transistor.

f. Linearity: An amplifier is subject to non-linearity as soon as a high sinusoidal input signal is applied, resulting in signal distortion. In the case of GNSS signals, the signals are co-inhabited by strong interfering cellular signals, which can overlap the operation of an LNA.

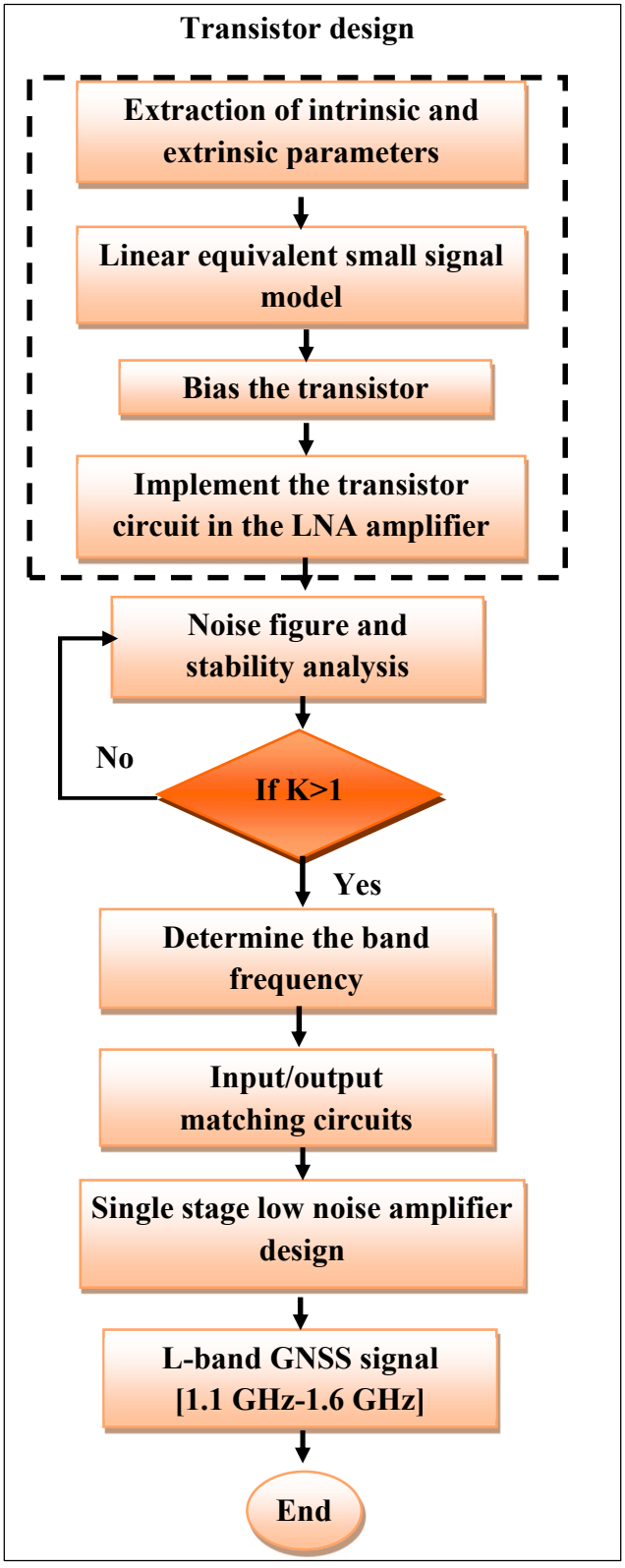

Figure IV.9 Flow chart of the different simulation steps to design an LNA.

To improve the interference immunity of GNSS systems, LNAs with high linearity characteristics are required. The following flowchart describes the main simulation steps involved in designing a single-stage LNA based on a MOSHEMT transistor:

In general, BPF and LNA are different blocks in a GNSS receiver. Here we try to compact the BPF with the LNA in a single block called the filtering block. To this end, we are interested in designing two filtering blocks with two center frequencies, corresponding to the carrier frequency of the GPS L1 and GPS L2.

IV. 3. 4 Local oscillator (LO)

The local oscillator circuit is based on the translation of the radio frequency signals to a lower intermediate frequency (IF) by multiplying the incoming signal with a sinusoid. The most obvious reason for this is to bring the frequency down to a usable range where the analog-to-digital conversion function can take place normally.

IV. 3. 5 Analog/Digital converter (ADC)

This component is dedicated to converting the analog signals into digital samples for further processing in the rest of the transmission chain.

IV.4 GNSS receiver limitation (approach to the problem)

The quality of the measurements made by the GNSS receiver may limit its ability to provide correct positions. The measurements taken by the receiver correspond to the distances separating it from the visible satellites. They may be contaminated by noise or interference, in which case the GNSS signal cannot be extracted, resulting in false position [141].

Various types of interference countermeasures have been developed since the early years of the GNSS systems. These techniques can be implemented by exploiting the different blocks of the GNSS receiver. In this context, one of the main interferences detection and suppression techniques is the use of a selective filtering block at the input of the transmission chain [141]. This block filters the incoming signal into the desired bandwidth, rejects out-of-band interferences and reduces noise [142].

In this thesis, the design of the filtering block for the GNSS receiver is studied by simulating LC bandpass filters and a first-stage LNA amplifier. The proposed AlGaN/AlInGaN/GaN MOSHEMT transistor (STR02-DB) will be integrated into the LNA design to test its performance in an RF application. ADS software simulations are performed to study the designed filter block characteristics.

IV.5 Simulation results

Modeling the elements of an MMIC integrated circuit is one of the methods used to reduce the cycle time and cost of a circuit by accurately predicting its operation through simulation. A logical step-by-step procedure was followed in this thesis work to design the filtering block circuit for a GNSS receiver. The agilent advanced design (ADS) simulation tool was used and the results are discussed below:

IV. 5. 1 Modeling the MOSHEMT (STR02-DB) small signal equivalent diagram

The aim of modeling is to develop a mathematical model equivalent to the simulated transistor, enabling its electrical behavior to be reproduced and predicted. In this section, we describe the electrical modeling principle and parameter extraction methods used for our AlGaN/AlInGaN/GaN MOSHEMT (STR02-DB) studied in the previous chapter. We chose this device because of its superior physical properties, its high transconductance, and its mode of operation (E-mode), which enables it to operate at high frequencies.

- **Description of the small-signal equivalent model**

Analog and RF analyses of the device performance parameters at high frequencies, such as gain, stability, nonlinearity, and output power can be performed with the aid of a small signal linear equivalent model. It offers a crucial connection between the electrical operations taking place inside the device and the observed port network characteristics.

The electrical behavior of two-port networks can be described by the S-parameters, which provide extensive knowledge of the intrinsic device quantities. These S-parameters can be easily transformed into admittance or impedance parameters through which the voltage quantities can be converted to currents.

Several small-signal equivalent modeling topologies have emerged to facilitate transistor performance analysis. Figure I.20 shows the basic small signal equivalent circuit of the HEMT transistor. The schematic elements are divided into two categories: intrinsic elements (C_{GS}, C_{GD}, C_{DS}, R_{GS}, R_{GD}, R_{DS}, g_m, and τ) and extrinsic elements (C_{PG}, C_{PD}, L_g, L_S, L_D, R_G, R_s, and R_d).

There are two stages to the process of extracting the small-signal equivalent model's components, and they are described as:

IV.5.1.1 Determining extrinsic elements

To extract the extrinsic elements, we place the transistor in the cold bias condition, i.e. for V_{DS}=0V. This simplifies the diagram topology shown in Figure I.20 to Figure IV.10 since

at this bias the component behaves like a reciprocal passive quadrupole (g_m=0, S_{12}=S_{21}). The determination of extrinsic elements from these cold measurements then depends on the gate polarization. This method is described in detail in [143].

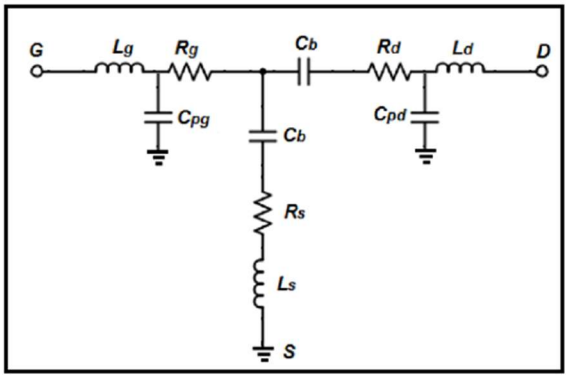

Figure IV.10 Equivalent diagram at a cold bias condition [85].

a. Inductance extraction

To extract the values of the L_S, L_G, and L_D access inductances, the transistor is biased at V_{DS}=0 V and V_{GS}>V_B, where V_B is the forward voltage of the gate source and the gate-drain (typically V_B is slightly greater than 0V so as not to damage the transistor). In this case, we use the impedance matrix (Z-parameters), which can be easily deduced from the S-parameters of the system, and is expressed as follows:

$$Z_{11}= R_S+ R_G+ \frac{R_C}{3}+ \frac{nKT}{qI_G}+ j\omega(L_S+ L_S) \quad \text{IV.4}$$

$$Z_{12}= Z_{21}= R_S+ \frac{R_C}{2}+ j\omega L_S \quad \text{IV.5}$$

$$Z_{22}= R_S+ R_D+ R_C + j\omega(L_S+ L_D) \quad \text{IV.6}$$

$$L_S= \frac{Im(Z_{12})}{\omega} \quad \text{IV.7}$$

$$L_G= \frac{Im(Z_{11})- Im(Z_{12})}{\omega} \quad \text{IV.8}$$

$$L_D= \frac{Im(Z_{22})- Im(Z_{12})}{\omega} \quad \text{IV.9}$$

Where R_C is the channel resistance under the gate and I_G is the gate current.

b. Capacitance extraction

In this case, the transistor is biased at V_{DS}=0V and V_{GS}<V_B. The equivalent circuit as follows:

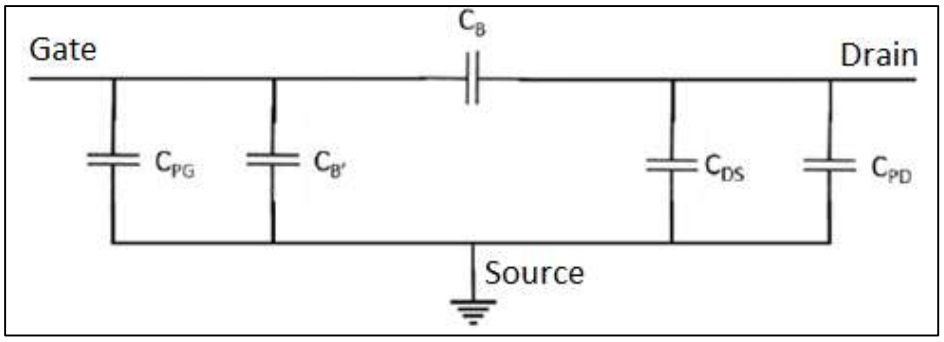

Figure IV.11 Small signal equivalent diagram at V_{DS}=0V and V_{GS}<VP [85].

In these conditions, the residual inductive and resistive effects of the access elements are masked by the contribution of the capacitors; so we can de-embed the inductances extracted previously [144]. We use the admittance matrix (Y-parameters) corresponding to the diagram above, and are given by the following expressions:

$$Y_{11} = j\omega.(C_{PG} + C_B + C_{B'}) \quad \text{IV.10}$$

$$Y_{12} = Y_{21} = -j\omega C_B \quad \text{IV.11}$$

$$Y_{22} = j\omega.(C_{PD} + C_B + C_{DS}) \quad \text{IV.12}$$

With a symmetrical gate topology as well as symmetrical polarization, we can perform the C_B=$C_{B'}$ approximation. Considering C_{DS} as negligible, we obtain:

$$Y_{11} = j\omega.(C_{PG} + 2C_B) \quad \text{IV.13}$$

$$Y_{12} = Y_{21} = -j\omega C_B \quad \text{IV.14}$$

$$Y_{22} = j\omega.(C_{PD} + C_B) \quad \text{IV.15}$$

We derive the values of the capacitances:

$$C_B = \frac{Im(Y_{12})}{\omega} \quad \text{IV.16}$$

$$C_{PD} = \frac{Im(Y_{22}) - Im(Y_{12})}{\omega} \quad \text{IV.17}$$

$$C_{PG} = \frac{Im(Y_{22}) - 2.Im(Z_{12})}{\omega} \quad \text{IV.18}$$

c. Resistors extraction

To extract access resistors, the bias conditions are the same as for inductances (series elements), i.e. V_{DS}=0 V and $V_{GS}>V_B$. Access resistors can vary according to transistor bias, so pulsed measurements may be necessary. The values of these resistances are given by:

$$R_S = R_e(Z_{12}) - \frac{R_C}{2} \quad \text{IV.19}$$

$$R_G = R_e(Z_{11}) - R_e(Z_{12}) + \frac{R_C}{6} \quad \text{IV.20}$$

$$R_D = R_e(Z_{22}) - R_e(Z_{12}) + \frac{R_C}{2} \quad \text{IV.21}$$

Where L_G and W_G are the length and width of the gate, respectively.

IV.5.1.2 Determining intrinsic elements

Once the extrinsic elements have been extracted, it is possible to isolate the intrinsic structure of the transistor using matrix manipulations to peel the extrinsic layers. The de-embedding method used is described in [143]. Intrinsic elements as a function of the components of the admittance matrix are given here:

$$C_{GD} = -\frac{\mathrm{Im}(Y_{12})}{\omega}.\left(1+\left(\frac{\mathrm{Re}(Y_{12})}{\mathrm{Im}(Y_{12})}\right)^2\right) \quad \text{IV.22}$$

$$C_{GS} = \frac{\mathrm{Im}(Y_{11})+\mathrm{Im}(Y_{12})}{\omega}.\left(1+\left(\frac{\mathrm{Re}(Y_{11})+\mathrm{Re}(Y_{12})}{\mathrm{Im}(Y_{11})+\mathrm{Im}(Y_{12})}\right)^2\right) \quad \text{IV.23}$$

$$C_{dS} = \frac{\mathrm{Im}(Y_{21})+\mathrm{Im}(Y_{12})}{\omega} \quad \text{IV.24}$$

$$R_{GS} = \frac{\mathrm{Re}(Y_{11})+\mathrm{Re}(Y_{12})}{\omega C_{GS}(\mathrm{Im}(Y_{11})+\mathrm{Im}(Y_{12}))} \quad \text{IV.25}$$

$$R_{GD} = \frac{\mathrm{Re}(Y_{12})}{\omega C_{GS}.\mathrm{Im}(Y_{12}))} \quad \text{IV.26}$$

$$R_i = \frac{\mathrm{Re}(Y_{11})}{(\mathrm{Im}(Y_{11} - \omega C_{GD})^2 + (\mathrm{Re}(Y_{11}))^2} \quad \text{IV.27}$$

$$G_m = \sqrt{(1 + R_{GS}\, C_{GS}\omega)\,(Im(Y_{21}) - Im(Y_{12}))^2 + \left(Re(Y_{21}) - Re(Y_{12})\right)^2} \quad \text{IV.28}$$

$$G_D = \frac{1}{R_{DS}}\ Re(Y_{22}) + Re(Y_{12}) \quad \text{IV.29}$$

$$\tau = \frac{1}{\omega}\left(\frac{\mathrm{Im}(Y_{12}) - \mathrm{Im}(Y_{21}) - (\mathrm{Re}(Y_{21}) - \mathrm{Re}(Y_{12}).R_{GS}\, C_{GS}\omega}{G_m}\right) \quad \text{IV.30}$$

IV.5.1.3 Extraction of the small-signal equivalent model

The small-signal linear model and parameters' extraction methods introduced in the previous section have been applied to our transistor. In the first step, polarization-independent extrinsic parameters are extracted. In the second step, all intrinsic parameters are extracted from a particular polarization point; equal to V_{DS}=5 V and V_{GS} = 1.5V.

The parameters obtained are then optimized so that our model fits the main model data as precisely as possible using ADS. The extrinsic and intrinsic elements of our MOSHEMT under study (STR02-DB) are extracted from numerical simulations on ATLAS-SILVACO software, where the Z and Y parameters are calculated automatically, and they are listed in Tables IV.2 and IV.3.

Table IV.2 Extrinsic parameters of the MOS-HEMT transistor (STR02-DB).

Extrinsic elements	**LS (pH)**	**LG (pH)**	**LD (pH)**	**CPG (Ff)**	**CPD (Ff)**	**CB (Ff)**	**RS (Ω)**	**RG (Ω)**	**RD (Ω)**
Values	4.3667	60.237	56.9	58.83	96.24	4.069	0.018	0.0967	0.211

Table IV.3 Intrinsic parameters of the MOS-HEMT transistor (STR02-DB).

Intrinsic elements	**CGS (fF)**	**CGD (fF)**	**CDS (fF)**	**Gm (S)**	**Ri (Ω)**	**τ (ps)**	**RDS (Ω)**	**Gd (S)**	**RGD (Ω)**
Values	76.18	51.31	52.695	4.47	0.09237	1.41	122.942	0.0081	126.292

Once these intrinsic and extrinsic elements are extracted, we introduce them into the ADS design software, to create the electrical small-signal equivalent model of our component, as shown in Figure IV.12.

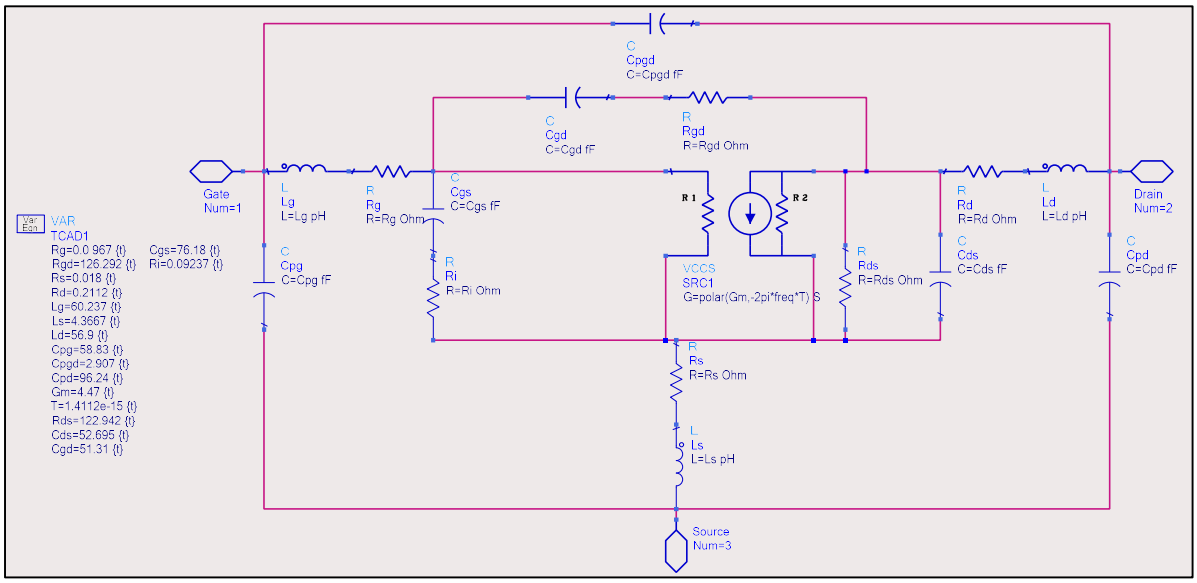

Figure IV.12 Small signal equivalent model of the STR02-DB MOSHEMT in ADS.

IV.5.1.4 S-parameters

The S-parameters of the small signal electrical model of our transistor using ADS are shown in Figure IV.13.

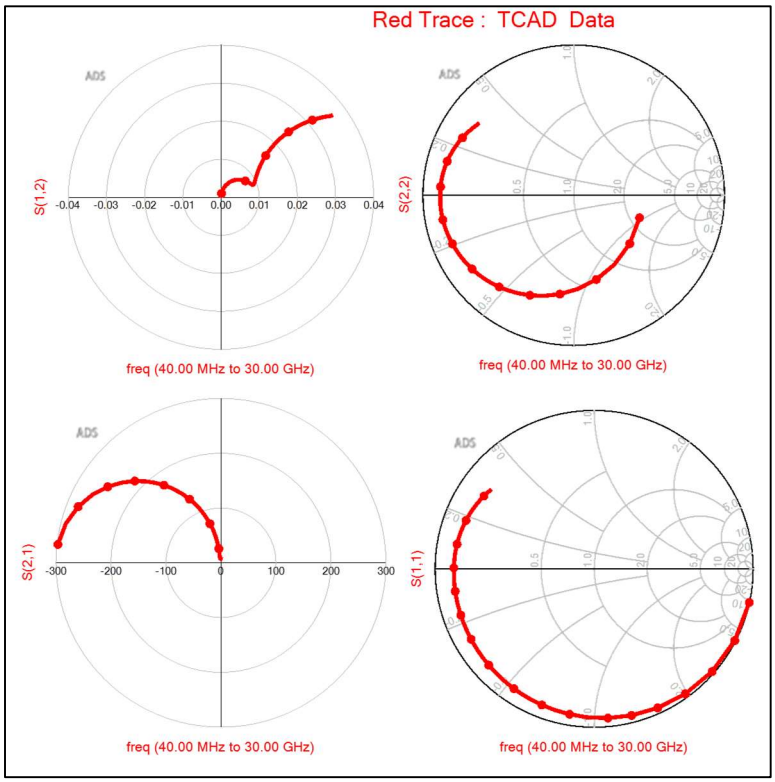

Figure IV.13 Smith charts presentation of the S-parameters of the proposed model.

These S-parameters have been first obtained by SILVACO and confirmed by ADS. Figure IV.13 shows the Smith charts comparison of the reflection and the transmission coefficients S_{11}, S_{22}, S_{12}, and S_{21} of our transistor at the bias point of V_{GS} = 1.5 V and V_{DS} =5 V. The study was carried out over a frequency range from 40 MHz to 30 GHz. Figure IV.14 shows a comparison of the inverse gain (S_{12}) and the forward maximum gain (S_{21}) as a function

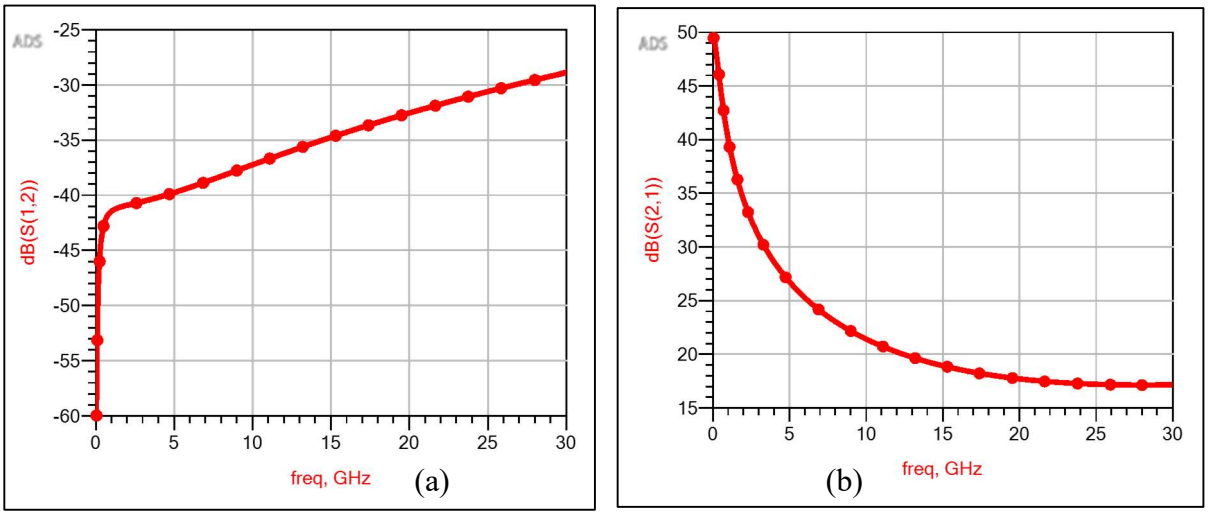

Figure IV.14 S_{12} (a) and S_{21} (b) gains vs frequency of the proposed model.

of frequency. Inverse gain shows low values, while the forward gain shows excellent values, especially in the band range of [1 to 2 GHz] which is the band of interest in our study.

The noise figure of the electrical model for our MOSHEMT transistor along the frequency range of 0 to 30GHz is calculated using the ADS tool and given in Figure IV.15. NF shows a low value of around 1.4 dB at 30 GHz.

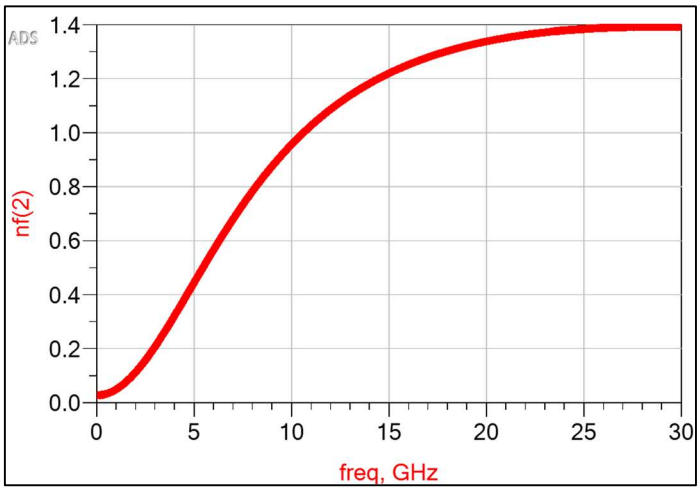

Figure IV.15 Noise figure for AlGaN/AlInGaN/GaN MOSHEMT (STR02-DB).

The physical and electrical results of our proposed MOSHEMT transistor (STR02-DB) showed that this transistor is perfectly suited to microwave applications.

IV. 5. 2 Simulation and modeling of the filtering block for GNSS receiver

The circuit of the filtering block designed as part of this thesis is shown in Figure IV.16. We note that the input filter and the output filter have the same L and C parameters.

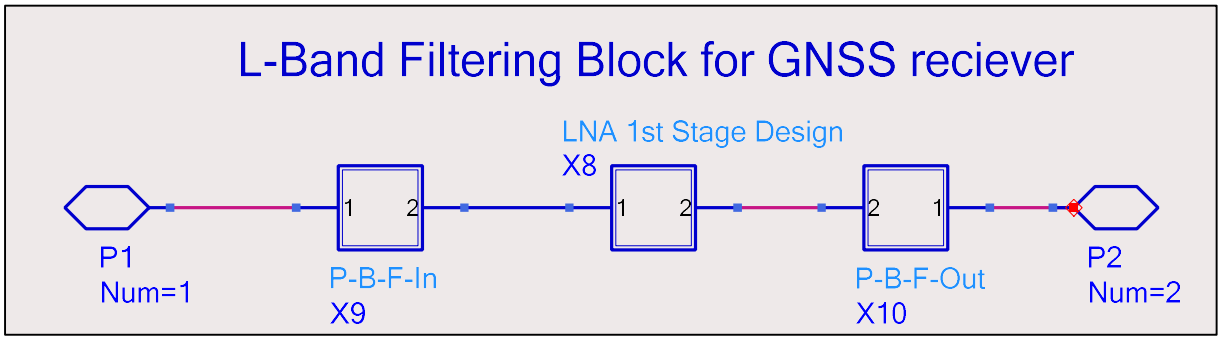

Figure IV.16 Simulations structure for the complete filtering block for a GNSS receiver.

Our objectives were:

- Test the performance of the proposed GaN-based MOSHEMT (STR02-DB) on an LNA.
- Design two selective bandpass filters with two operational frequencies. The first one is fixed at 1575 MHz corresponding to the carrier frequencies of the L1-GPS/B1-

COMPASS/E1-GALILEO bands. The second operational frequency is set at around 1234 MHz corresponding approximately to L2-GPS/L2-GLONASS bands.

- The output response of the filtering block (BPF+LNA+BPF) of a GNSS receiver should have the same operational frequencies of the filters that correspond to the GNSS signals.

The filtering block has two main subblocks, which are:

IV.5.2.1 Low noise amplifier based on STR02-DB MOSHEMT

The embedded circuit of the MOSHEMT-based LNA designed as part of this thesis is shown in Figure IV.17. This LNA is designed to operate over a frequency range from 1 GHz to 13 GHz. The transistor is biased with V_{DS} = 5V. We have taken this model for LNA from [145].

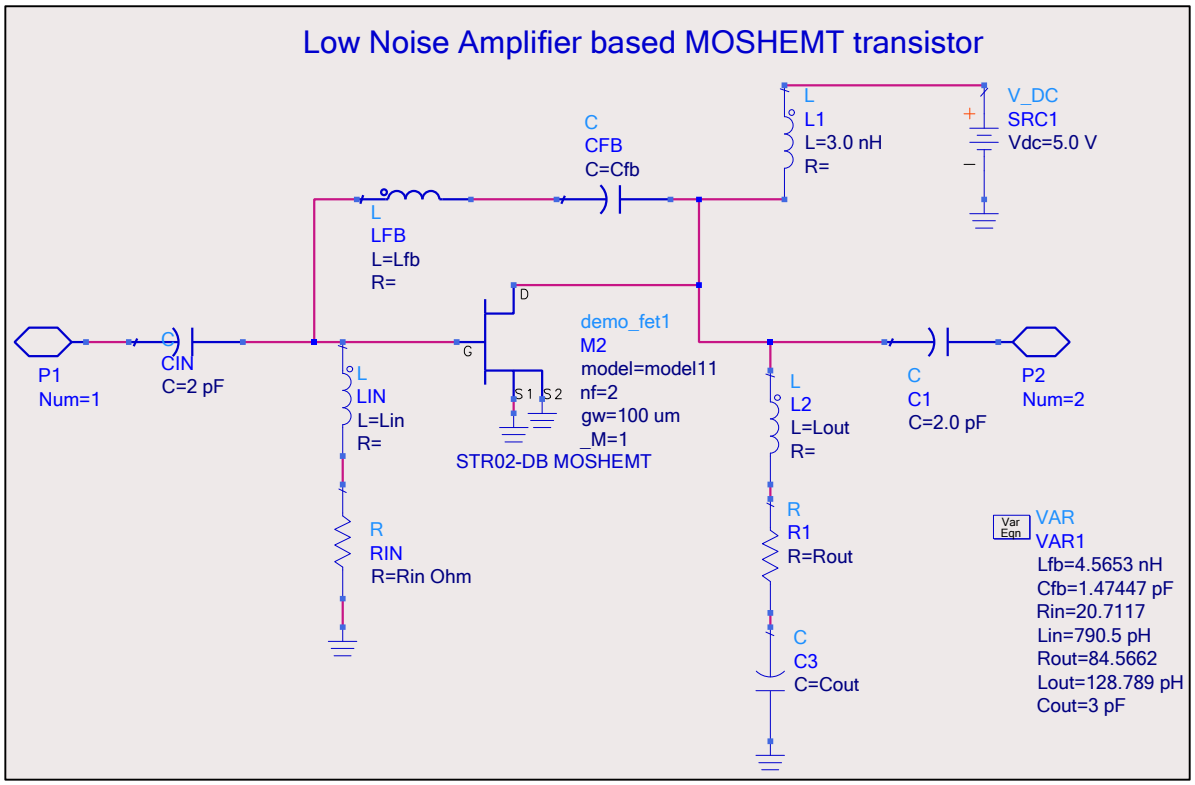

Figure IV.17 Complete single-stage LNA based on STR02-DB MOSHEMT.

The LNA circuit consists of:

- Transistor demo_fet1 shows the implementation of our small-signal diagram of the STR02-DB MOSHEMT transistor presented in Figure IV.12 into the LNA model, the transistor is polarized at V_{DS} = 5V.
- C_{IN} capacitor and L_{IN} inductor form the input matching network, which transfer the input impedance into 50 Ω.
- C_{out} capacitor and L_{out} inductor form the output matching network, which transfers the output impedance into 50 Ω.

- L_{FB} and C_{FB} ensure the transistor polarization.
- R_{IN} at the gate side prevents the flow of large currents to the input of the LNA.
- R_{OUT} at the drain side prevents oscillation at the output of the LNA.
- L1 and C1 are used to enhance the reflection coefficients.

The S-parameters, noise figures, stability, and linearity characteristics of the 1st-stage LNA with 50 Ohm matching networks are simulated between 1-13 GHz, and presented in this section.

➢ **S-parameters**

The different Sij parameters simulated are shown in Figure IV. 18. The reflection coefficients S_{11} (input return loss) and S_{22} (Output return loss) vary between -0 dB and -16 dB over the entire frequency range [1 GHz to 13 GHz]. An acceptable input match is obtained.

The reverse transmission coefficient S_{12} is less than -16 dB, which means that the isolation of the component between the input and output points is good. The forward gain transmission S_{21} reaches a maximum of 12 dB. The gain achieved meets the specification requirements [136]. As a result, the values obtained are deemed acceptable for incorporation into the RF stage of the GNSS receiver.

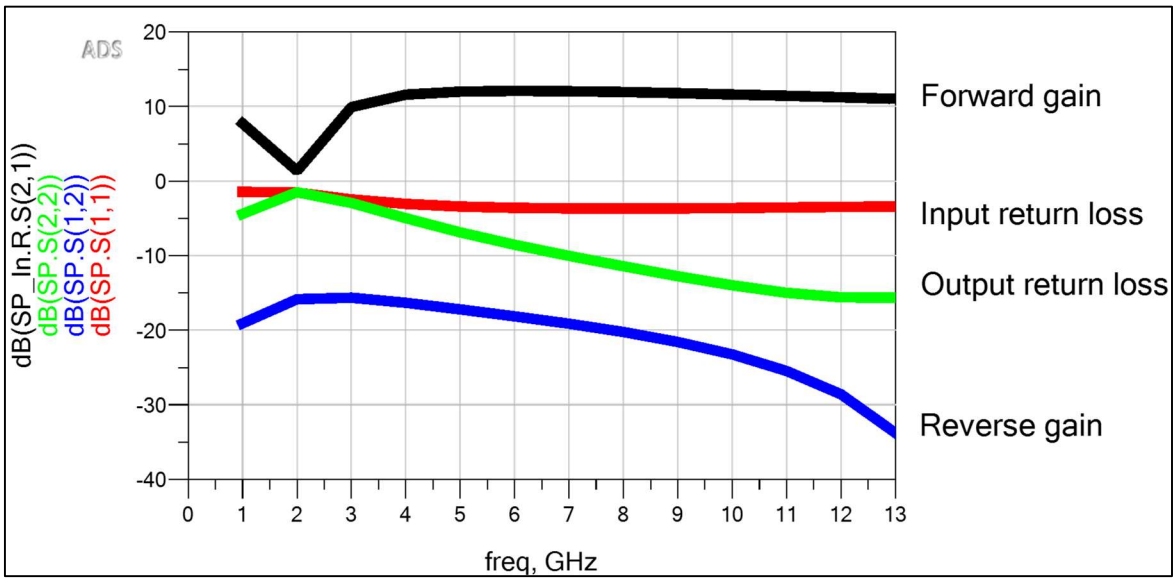

Figure IV.18 S-parameters of the designed single-stage MOSHEMT-based LNA

➢ **Noise figure**

Figure IV.19 presents the noise figure of the LNA as a function of frequency [1 GHZ – 13 GHz], as can be seen, the designed LNA has a minimum noise figure of 1.8 dB at 2 GHz.

The device shows a low noise figure thanks to the low noise MOSHEMT used and the ideal passive components.

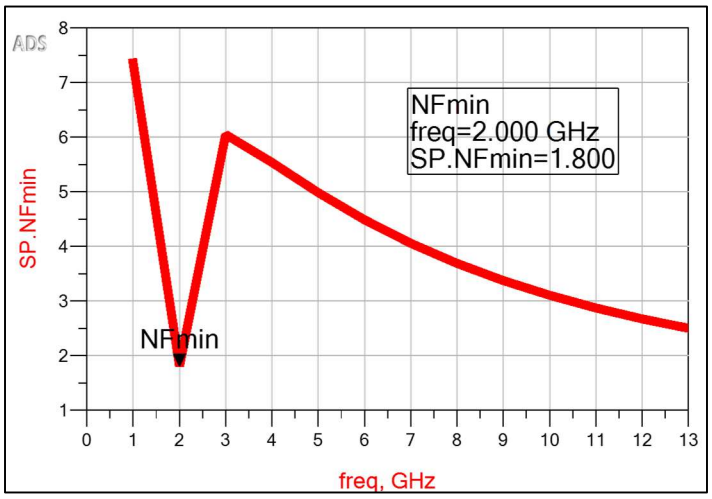

Figure IV.19 Noise figure of the designed single-stage MOSHEMT-based LNA.

- **Stability**

The simulation results of the stability factors (Δ and K) of the proposed LNA are presented in Figure IV.20. We observe that the K factor is greater than unity and Δ is less than one over the entire simulated frequency range. Hence, both the conditions for unconditional stability (K and Δ) are satisfied.

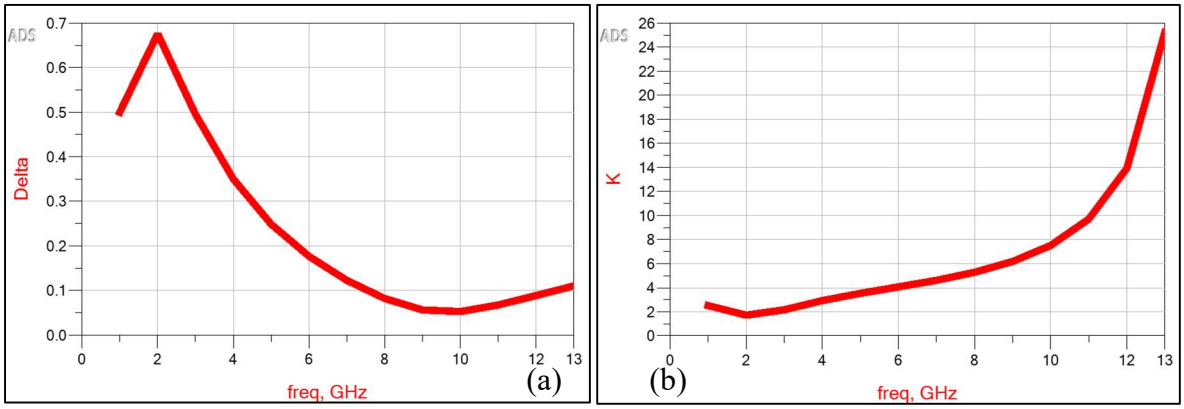

Figure IV.20 Delta (a) and K (b) stability factors.

- **Linearity**

The linearity behavior of the device is investigated by determining the compression point and the compression gain at 1dB. To calculate this point, we remove the S-parameter block, and add the harmonic balance tool from the Keysight ADS, as well as a sweeping input power to apply a variable power source to the amplifier input.

The compression point at 1dB is obtained from the variation of the input power (P_{in}) as a function of the output power (P_{out}) of the fundamental frequency (1.5 GHz). It is determined by superimposing a straight line on the linearity zone of the curve $P_{out}=f(P_{in})$, see Figure IV.21 (a), the compression point (OP1dBm, IP1dB) is defined when there is a difference of 1dB between the straight line and the curve, and is equal (13.5 dBm, 4.6 dB), which means that the amplifier is linear down to 13.5 dBm.

Similarly, the gain curve as a function of the input power shows a linear zone and a saturation zone: gain is constant in the amplifier's linearity zone, and then falls. Therefore, the LNA device shows that it has a compression gain of 7.1 dB (Figure IV.21 (b)).

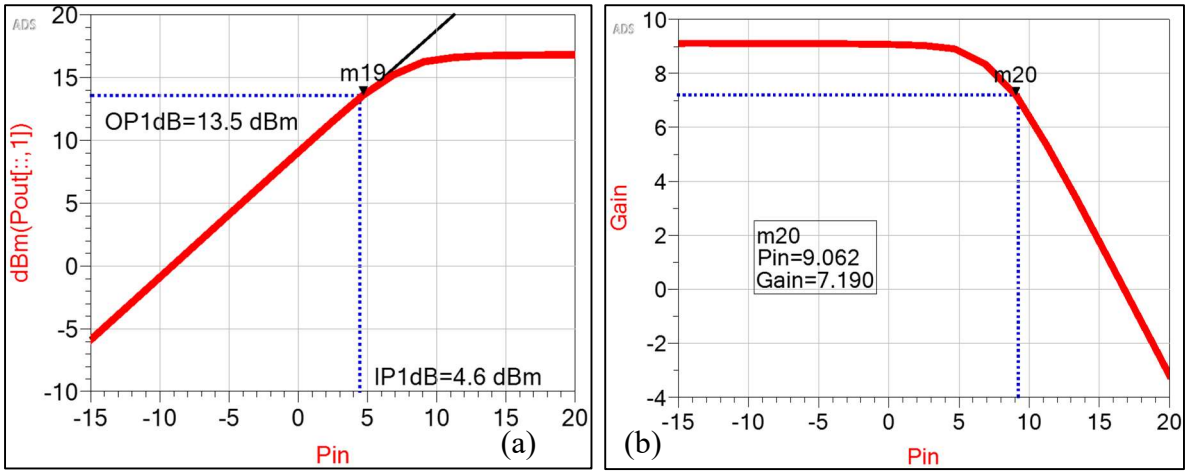

Figure IV.21 Compression point (a) and compression gain (b) at 1dB.

- **Recapitulative table**

The following table summarizes the main results obtained by integrating the proposed MOSHEMT into the LNA design and compares them with previous LNAs using the same technology.

Table IV.4 Comparison of our LNA with other previously published LNAs.

References	Transistor	Frequency band	NF (dB)	Gain (dB)	S22 (dB)	IP1dB
[145], 2014	GaN HEMT	1-14 GHz	2.5	10	-12	-
[146], 2010	GaN HEMT	1-25 GHz	3.3	13	-9	20
[147], 2012	GaN HEMT	0.25-3 GHz	2.5	20	-	32.5
[148], 2023	GaAs HEMT	1-12 GHz	1.5	23	-	-
This work	GaN MOSHEMT	1-13 GHz	1.8	12	-16	13.5

IV.5.2.2 LC bandpass filter

At first, an LC bandpass filter structure is designed with ideal components for inductances and capacitances, we then optimized these values. Figure IV.22 shows the LC bandpass filter geometry implemented in ADS.

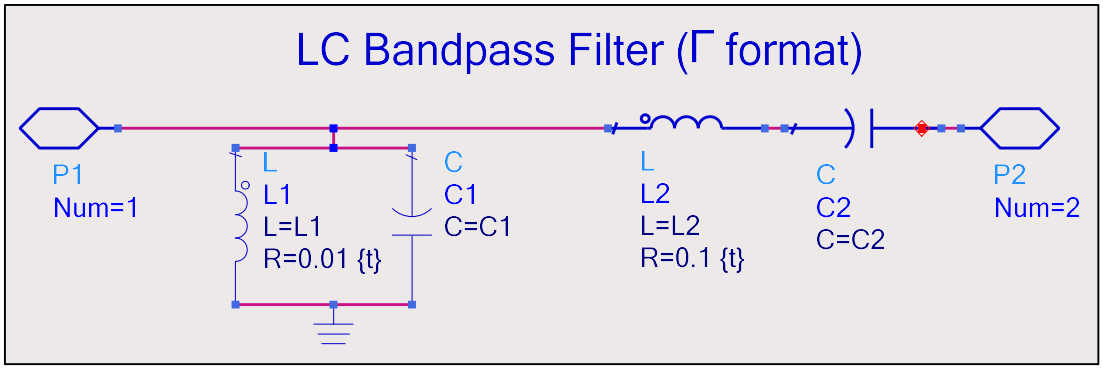

Figure IV.22 LC bandpass filter structure.

The steps that we take into account to design our filter structures are:

a. **Determine the design goal:** In our case, we are interested in the design of two bandpass filters that cover some frequency bands for GNSS signals.

b. **Center Frequency (f_c):** The operating frequency for the first filter is set at 1575 MHZ, corresponding to the carrier frequency of the L1-GPS, B1-COMPASS, and E1-GALILEO bands. For the second filter, the operating frequency is set at around 1200 MHz to cover the L2 GPS and GLONASS bands.

c. **Bandwidth (BW):** The GNSS's bandwidth is relatively narrow. It depends on the maximum and minimum frequencies of the bandpass filter.

d. **Filter type:** We are going to design two passive LC bandpass filters.

e. **Topology type:** Γ format has been chosen.

f. **Impedance matching:** The filter should be impedance-matched with other blocks to minimize signal reflection and maximize signal transfer. The input/output impedance of the designed filter is 50 Ω.

g. **Component selection:** We need to choose appropriate values for passive components (inductors, capacitors) that meet our design specifications. To do this, we choose to use the genetic algorithm as a means of optimizing these components using ADS.

IV. 5. 3 Optimization of the filtering block

To obtain the desired bandwidth at a specific operating frequency (1.1 GHz and 1.6 GHz), it is necessary to optimize the input and output filter components of the circuit. The next step is to optimize these values to obtain a bandwidth covering the GNSS bands [22].

ADS RF design software provides optimization and adjustment tools, the best values of passive components (capacitance and inductance) can be selected to ensure the desired bandpass of the filter. ADS optimization technique was used. Figure IV.23 shows the schematic block released to optimize the filter components to obtain the bandwidth required for GNSS.

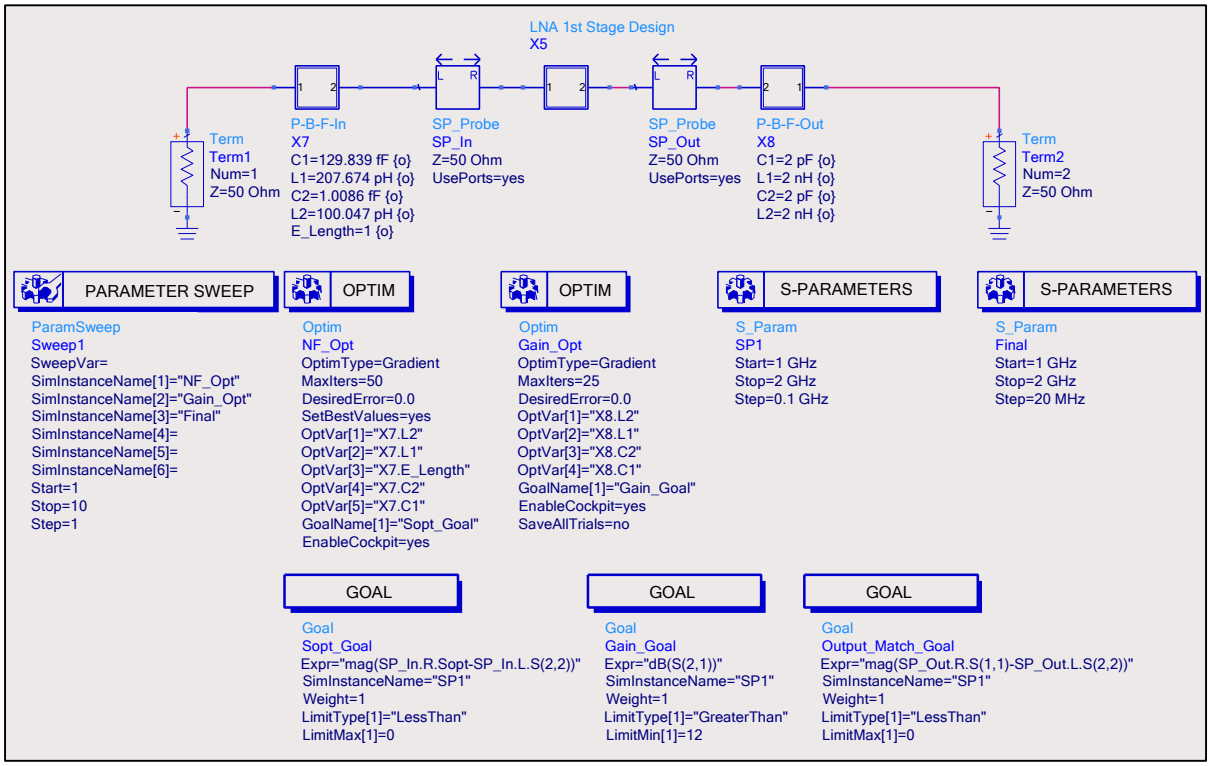

Figure IV.23 The simulated optimization scheme under ADS for the filtering block.

The sub-blocks shown are as follows:

a. **Filtering block:** It consists of input and output LC bandpass filters and LNA.

b. SP-Prob sub-block: The circuit's SP-probes are placed at the input and output of the LNA, as this is the only active component in the design since it has a transistor. SP-probe simulation is used for S-parameter analysis. It is used to calculate transmission and reflection coefficients, noise figures, and stability factors.

c. S-parameters sub-block: It enables us to plot the S-parameters in the swept frequency of a component or circuit. Performing a simulation sweep consists of selecting the start and stop points to sweep and the increments step.

d. **Port terminations:** They are used to define the transformed impedances at the source and load side to 50 ohms

e. **OPTIM sub-block:** It is used to define the optimization algorithm and the number of iterations; in our case, we have chosen the most popular algorithm, which is the genetic algorithm with 500 iteration points.

f. **GOAL sub-block**: In this sub-block, we define the desired objective of the optimization. Our goal is to optimize the LC components of the two filters in such a way as to obtain the operating frequency of the filtering block similar to that use GNSS system.

In the next section, we will present the simulated results with optimum values.

IV.5.3.1 BPF optimization results

We configured the optimization step twice, in order to have bandpass filter center frequencies around the carrier frequencies of GPS L1 (1575.42 MHz) and GPS L2 (1227 MHz). In this section, we simulate the response of the LC bandpass filters designed after optimization.

➢ **Bandpass filter model with Fc=1575 MHz**

The optimum parameters for the first filter (labeled L1-BPF) are as follows: L1 = 110.46 pH, C1 = 92.12 pF, L2 = 10.58 nH, and C2 = 28.16 fF. Figure IV.24. (a) shows the simulated transmission response (S_{21}). This figure shows that the designed BPF meets the desired bandwidth filtering specifications, the bandwidth at 3dB attenuation increases from f_1= 1.514 GHz to f_2= 1.662 GHz (BW = 148 MHZ).

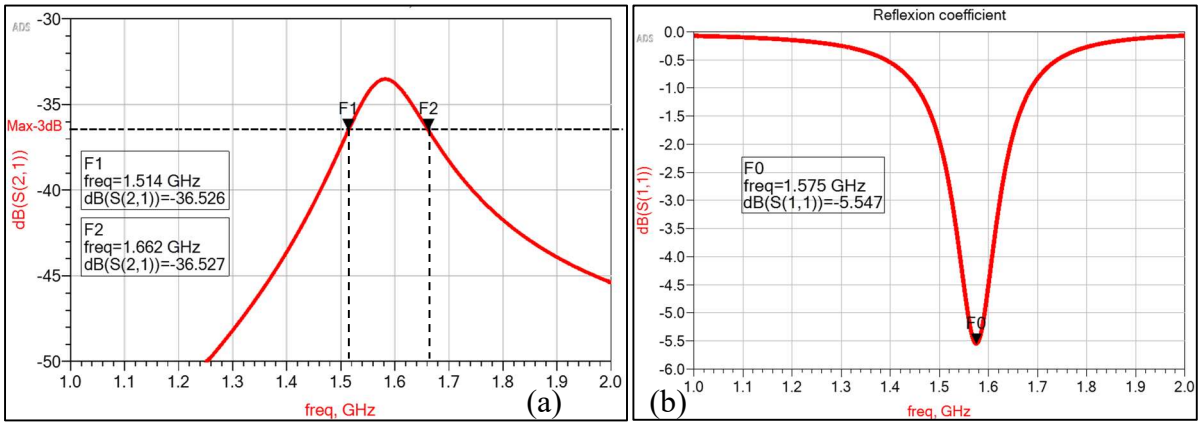

Figure IV.24 Simulated S-parameters (S_{21} (a) and S_{11} (b)) of L1-BPF with L1 = 110.46 pH, C1 = 92.12 pF, L2 = 10.58 nH, and C2 = 28.16 fF.

Figure IV.24 (b) shows the simulated reflection coefficient S_{11}. This filter has an operating frequency of fc =1.575 GHz for S_{11} =-5. 547 dB, which corresponds to the carrier

frequency of GPS-L1, GALILEO_E1, and COMPASS_B1 [1575.42 MHz]. The designed bandpass filter features high selectivity and good impedance matching.

- **Bandpass filter model with Fc=1234 MHz**

The second band bandpass filter (labeled L2-BPF) was simulated with optimum LC values of L'1 = 147.86 pH, C'1 = 112.15 pF, L'2 = 15.77 nH, and C'2 = 78.27 fF. The simulated gain transmission and reflection curves of this circuit are depicted in Figure IV.25. The main parameters for the lower and upper frequencies are 1187 MHz and 1300 MHz, respectively, giving a bandwidth equal to 113 MHz. The center frequency of this filter is about 1.234 GHz with a minimum insertion loss of -6.146 dB.

We note that this filter has a good selectivity since it has an operating frequency close to the carrier frequency of the GPS-L2 [1227.6] and GLONASS-L2 [1248.06].

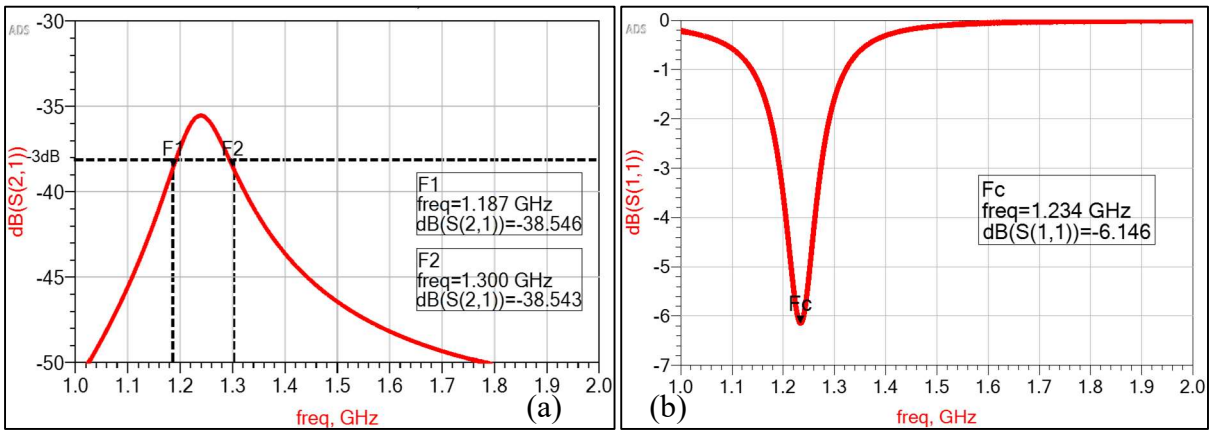

Figure IV.25 Simulated S-parameters (S_{21} (a) and S_{11} (b)) of L2-BPF with L'1 = 147.86 pH, C'1 = 112.15 pF, L'2 = 15.77 nH, and C'2 = 78.27 fF.

Table IV.5 summarizes the optimum values of LC components of the designed filters and the obtained frequency band. The two bandpass filters set specially are intended to function in the L1 and L2 bands of GPS.

Table IV.5 LC components of the designed filters and the obtained frequency bands.

Bandpass filter	LC values	Center frequency	Frequency band (MHz)	Bandwidth	Corresponding GNSS bands
L1-BPF	C1 = 92.12 pF	1575 MHz	[1514:1662]	148MHz	GPS-L1, GALILEO_E1, and COMPASS_B1
	L1 = 110.46 pH				
	C2 = 28.16 fF				
	L2 = 10.58 nH				
L2-BPF	C'1 = 112.15 pF	1234 MHz	[1187:1300]	113MHz	L2 of GPS and GLONASS
	L'1 = 147.86 pH				
	C'2 = 78.27 fF				
	L'2 = 15.77 nH				

IV. 5. 4 Filtering block (BPF + LNA+ BPF) characteristics

Finally, once the different blocks of our circuits are released, and the optimization is done, we simulate the main characteristics of the filtering block at the frequency band [1-2 GHz]. The global filtering block structure used for simulation is shown in Figure IV.26.

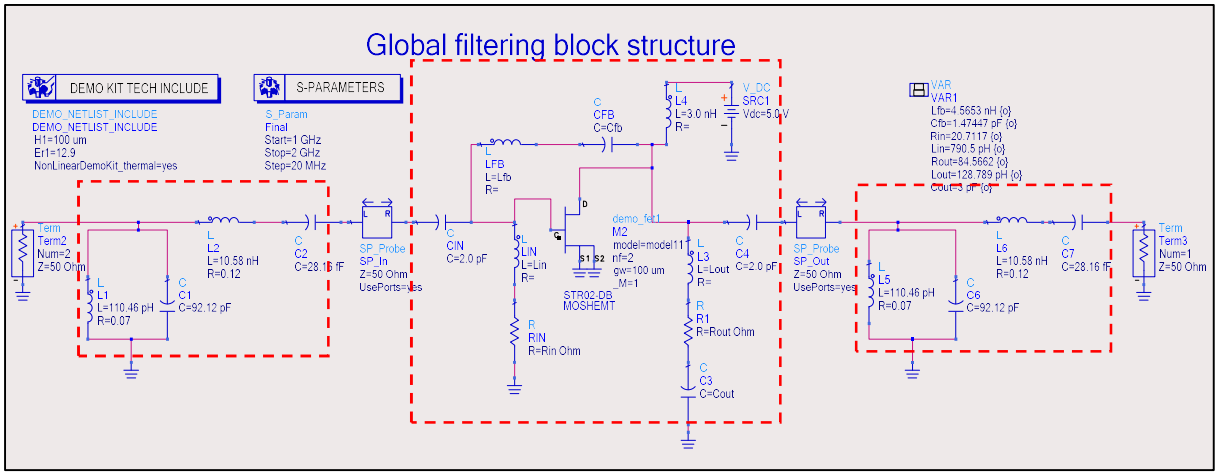

Figure IV.26 Global filtering block structure.

IV.5.4.1 Filtering block model using L1-BPF filter

In this step, we use the BPF-L1 filter with the higher band. The simulated output reflection and transmission response curves (S_{21}, S_{11}) of this circuit are shown in Figures IV.27 and IV.28. The operating frequency is found to be 1.580 GHz. At 3 dB attenuation, the bandwidth is equal to 60 MHz with f_1=1.550 GHz and f_2=1.610 GHZ.

The result is a narrow transmission band covering the GPS-L1[1555-1590 MHz], GALILEO_E1 [1555-1595 MHz], and COMPASS_B1 [1550-1610 MHz].

In our work, we focus on obtaining an output frequency band of the global simulated network that covers the frequency band of the GNSS receiver. As can be seen, there is only a slight deviation in center frequency between the simulated individual BPF (1575 MHz) and the simulated filtering block (BPF+LNA+BPF) (1580 MHz); it is offset by 0.05 from the carrier frequency of the GNSS L1 band (1575.42 MHz).

This is mainly due to the noise factor and the electromagnetic simulation process, which have not been taken into account [23].

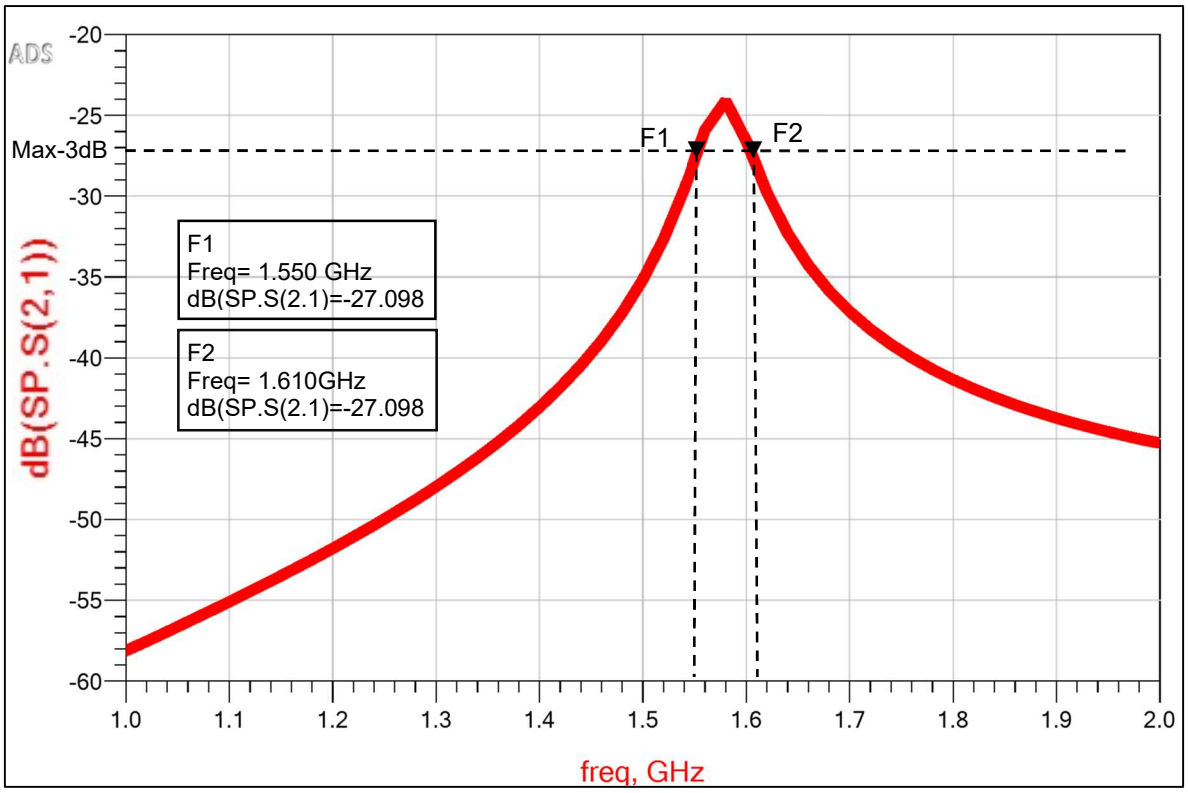

Figure IV.27 Transmission gain (S_{21}) of the filtering block using L1-BPF filter.

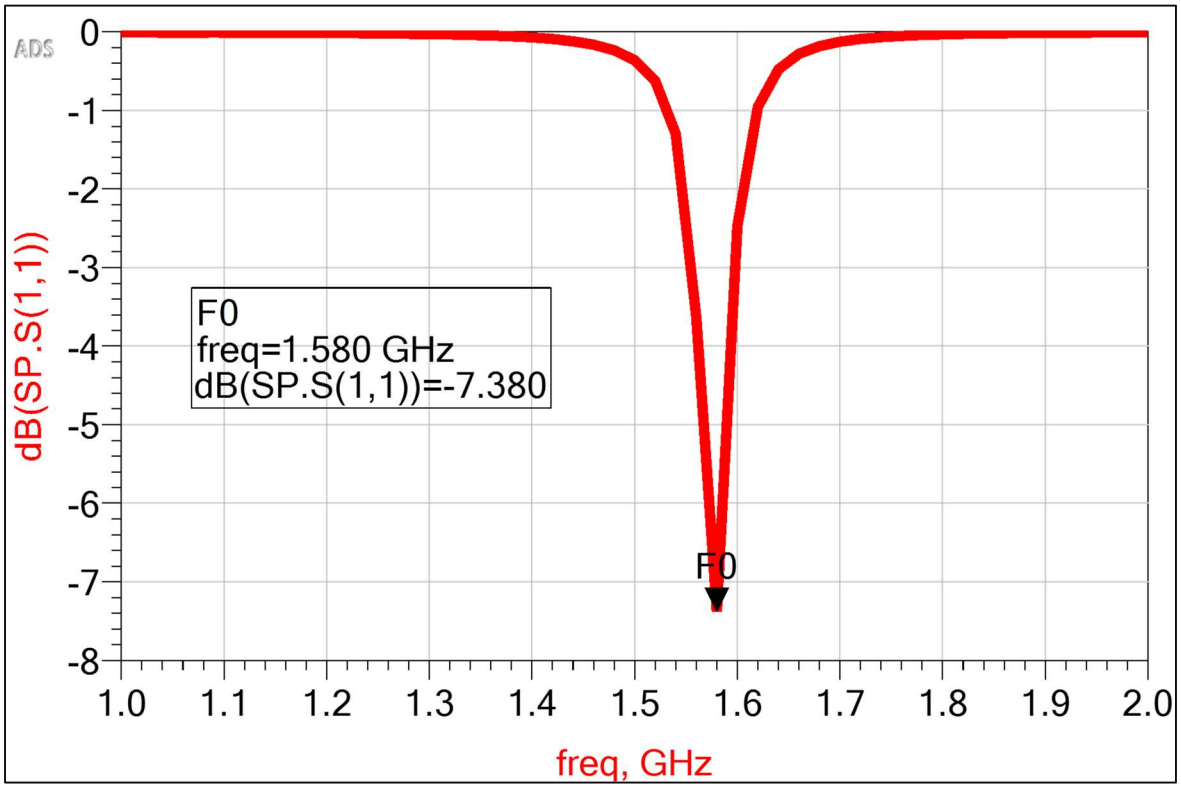

Figure IV.28 Reflection gain (S_{11}) of the filtering block using L1-BPF filter.

IV.5.4.2 Filtering block model using L2-BPF filter

Here we use a BPF-L2 filter with the lower band. The output response of the filtering block is shown in Figures IV.29 and IV.30. The -3 dB bandwidth is equal to 110 MHz with f_1=1.190 GHz and f_2=1.300 GHZ.

The operating frequency is 1.240 GHz for a reflection coefficient in dB S_{11} = -5.993 dB, which is closer to the signal carrier frequency of the L2 band of GPS and GLONASS. The result is a narrow transmission band covering the GPS-L2 [1210-1245 MHz] and GLONASS-L2 [1238-1254 MHz] bands.

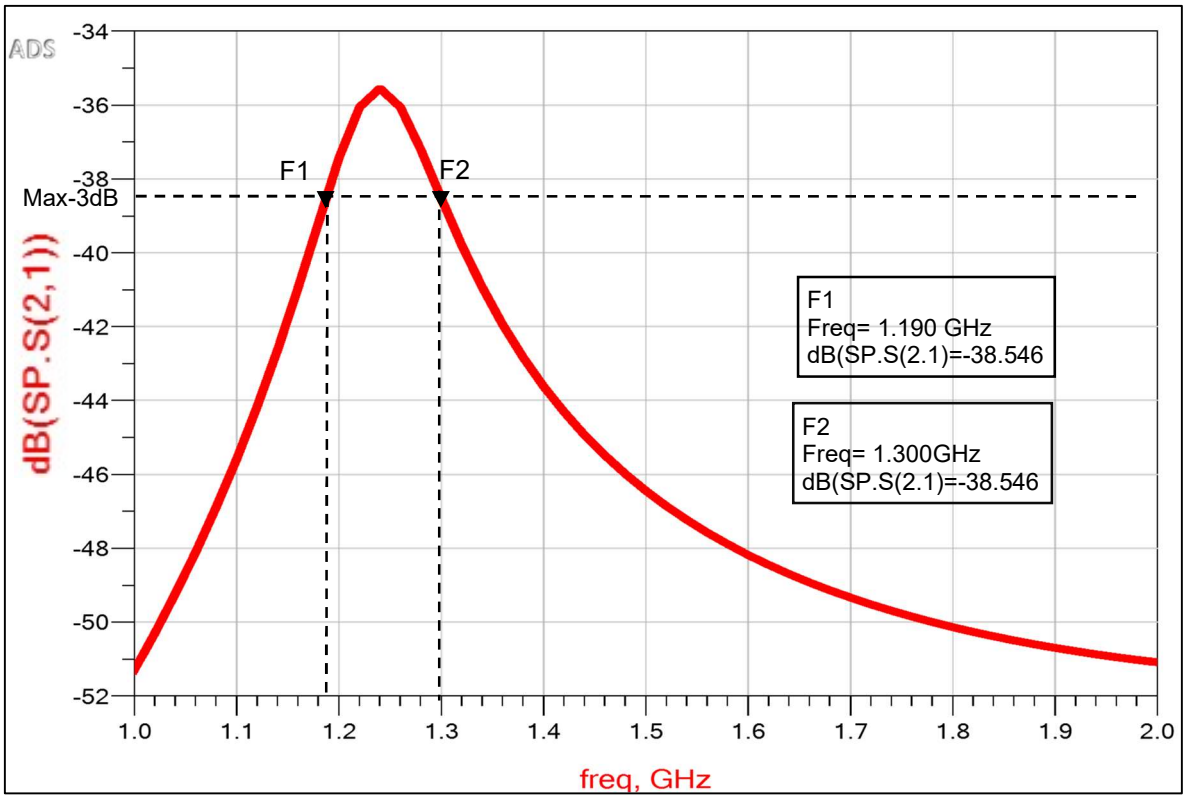

Figure IV.29 Transmission gain (S_{21}) of the filtering block using L2-BPF filter

The simulated results obtained confirm the practical validity of the BPF+LNA+BPF integrated MOSHEMT transistor for covering some of the GNSS bands.

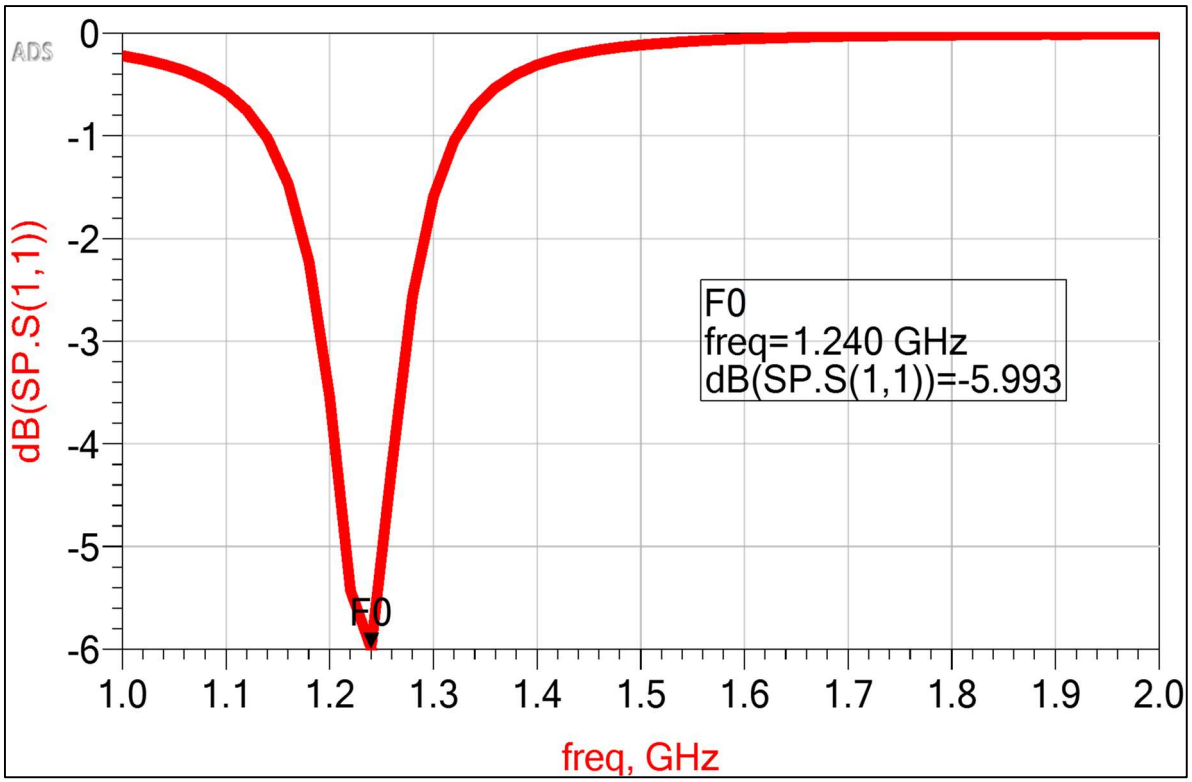

Figure IV.30 Reflection gain (S_{11}) of the filtering block using L2-BPF filter.

➢ **Filtering block stability**

The stability of the globally designed circuit (PBF+LNA+PBF) is studied through the unity Smith chart circle (<1). Figure IV.31 shows the stability circle and the transmission coefficient. We found that the circle of stability (Load_Stability_Circle) is located outside the Smith chart. Therefore, it is found that this circuit is unconditionally stable over the entire interest band (L-band).

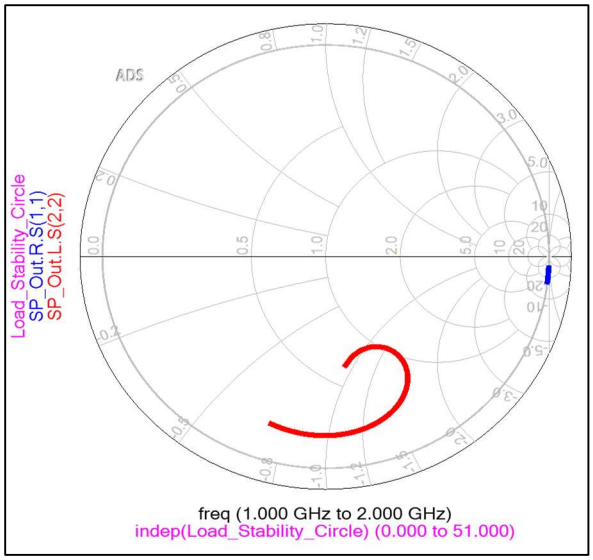

Figure IV.31 Smith chart stability circuits, S_{11} and S_{22}.

- **Recapitulative table**

The comparison between the implemented RF filtering block and other reported works is given in Table IV. 6.

Table IV.6 Comparison of our proposed RF filtering block with other reported ones.

Ref	Rf filtering block components	Technology used	Fc (MHz)	Frequency band (MHz)	Corresponding GNSS bands
[130], 2008	BSF+LNA+ BPF	GaAs HEMT	1575.42	-	L1-GPS, E1-GALILEO, and B1-COMPASS
[149], 2017	LNA+BPF	MOSFET	1200 1600	[1215-1300] [1559-1610]	L2-GPS and L2-GLONASS. L1-GPS, E1-GALILEO, and B1-COMPASS.
[150], 2011	LNA +BPF	MOSFET	1575	[1525-1625]	L1-GPS, E1-GALILEO, and B1-COMPASS
This work	BPF+LNA+BPF	GaN MOSHEMT	1240 1580	[1190-1300] [1550-1610]	L2-GPS and L2-GLONASS. L1-GPS, E1-GALILEO, and B1-COMPASS.

IV.6 Conclusion

The filtering block (PBF+LNA+PBF) for the RF stage for a GNSS receiver based on the AlGaN/AlInGaN/GaN MOSHEMT transistor (STR02-DB) was developed and tested in this chapter using ADS designer. The main objective was to optimize the implemented design to cover specified bands of the GNSS signals.

We succeeded in optimizing the design and releasing two filtering block systems that operate over the GNSS frequency bands of [1190 MHz –1300 MHz] and [1550 MHz - 1610MHz], with center frequencies of 1240MHz and 1580 MHz. It has therefore been proven that the STR02-DB transistor has the potential to provide the highest specifications of an LNA to be useful for GNSS applications.

In the future, efforts may be made to build a filter block with multiband filters for multi-frequency GNSS receiver chains, still using the famous GaN material, while reducing noise.

General Conclusion

General conclusion

The design of radio frequency filtering blocks in MMIC GNSS receivers for navigation and positioning applications requires in-depth knowledge and characterization of the components at the heart of these systems, namely the transistors. At present, a wide range of technologies is available to the designer, in terms of choice of semiconductors, substrates, and transistor types.

This thesis work focuses on the modeling and characterization of AlGaN/GaN MOSHEMT transistors based on IIIA-N semiconductor materials. We chose this type of transistor because of its superior physical properties and high 2D electron gas density, enabling it to have a high operating frequency, high breakdown voltage, and low noise.

The main objective of this research work was to design an RF filter block, containing two bandpass filters (BPF) and a low-noise amplifier (LNA) for a GNSS receiver. Among the proposed MOSHEMT structure, device B (STR02-DB) was selected for integration into the single-stage LNA circuit as an active component due to its high quality.

The first stage of this work was devoted to a review of the physical, structural, and electrical properties of IIIA-N semiconductor materials, as well as the various mechanisms governing the operation of heterojunction transistors. We then describe the structure, operation, small-signal equivalent model, limitations, and technological challenges of the standard HEMT and MOSHEMT transistor.

We then carried out a 2D simulation of three different MOSHEMT transistor structures. All simulations are performed using SILVACO ATLAS software. The proposed structures are:

1- Device A: AlGaN/GaN/AlGaN MOSHEMT grown on GaN substrate, using a novel oxide material (β-Ga_2O_3), 70nm recessed T-gate length, and back-barrier layer. Analysis of the I-V curves showed that the recessed gate is the easiest solution for achieving normally-off operation.

2- Device B: AlGaN/AlInGaN/GaN MOSHEMT grown on 4H-SiC substrate, using high-k titanium dioxide TiO_2, 10 nm T-gate length, and AlInGaN spacer layer. A comparison simulation between single barrier (STR01-SB) and double barrier (STR02-DB) structures is performed. The second barrier material used is AlInGaN. Device B operates in normally-off mode and achieves the highest current and frequency performance.

3- Device C: AlGaN/AlInGaN/GaN MOSHEMT transistor grown on β-Ga_2O_3 substrate with 50 nm T-gate length. The geometrical and physical parameters' effects on the DC and AC characteristics of the proposed MOSHEMT, including the type of oxide, the composition of the spacer (In%), and the influence of temperature are investigated. The frequency performance is improved compared with Device B, but the operating mode is the depletion mode which is undesirable in the manufacturing process.

In the last part of this work, we designed a filtering block containing two passive LC bandpass filters and a single-stage low-noise amplifier (LNA). We designed two types of filters, one with a high bandwidth at a center frequency of 1575 MHz and the other with a low bandwidth at a center frequency set at 1234 MHz. furthermore, the LNA is designed on the basis of one of the MOSHEMTs proposed in this thesis, Device B (STR02-DB) was selected thanks to its excellent performance. Simulation of the GAN MOSHEMT LNA showed unconditional stability over the frequency band of interest, a maximum gain of 12dB with a minimum noise figure of 1.8 dB, and linearity down to an output power of 13.5 dBm.

In the overall system, there are two ways of filtering the signal. The RF filtering block (BPF filter + LNA + BFP filter) used can operate at two different frequencies: 1580 MHz and 1240 MHz. Consequently, the RF filtering block can cover the L1-GPS/B1-COMPASS/E1-GALILEO bands if the filter used is set at a center frequency of 1575 MHz, and the L2-GPS-GLONASS bands if the filter used has a center frequency of 1234 MHz.

We believe that the objective of this work has been achieved and the results obtained are acceptable in relation to what has been stated in the literature.

However, certain aspects of this work remain to be developed in future work:

- Establish the equivalent small-signal model of other studied devices using β-Ga_2O_3 material (devices A and C), and integrate these models into LNA circuit.
- Design multiband filters with two or more operational frequencies to cover all the GNSS frequency bands at the same time.
- Design of active filters based on GaN MOSHEMT transistors.
- Realization and manufacture of the various structures simulated in our PhD work.

Appendix

Appendix A

The periodic table of the elements, also known as the Mendeleyev table

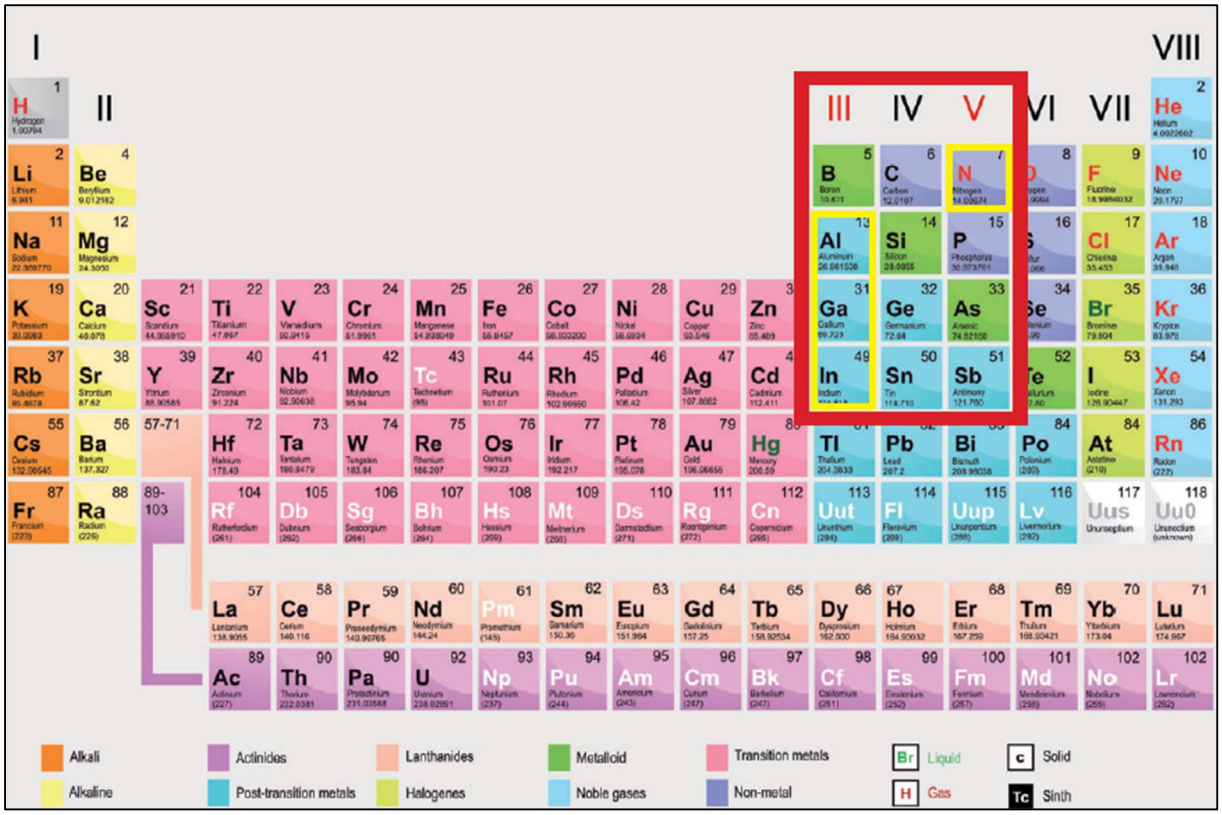

Figure A.1 Periodic table of Mendeleev showing the IIIV-A semiconductor materials.

Appendix B

1- TCAD-SILVACO software presentation

TCAD (Technology Computer Aided Design) SILVACO is a software package for designing and predicting the electrical performance of semiconductor-based devices in continuous and frequency regimes. The software consists of several programs that work together to achieve the desired results. The main programs used during this thesis are Atlas, Deckbuild, and Tonyplot, While many other sub-programs are available such as DevEdit and Athena.

In this thesis, a 2D ATLAS-SILVACO simulator is utilized, which allows for a wide range of input and output parameters, we represent these environments in Figure 1. Additionally, we consider that the input files are received by the execution environment (DeckBuild), and then ATLAS-SILVACO is called to execute the code. Tony Plot is used to visualize and display the simulation's outputs, which are shown as electrical characteristic curves.

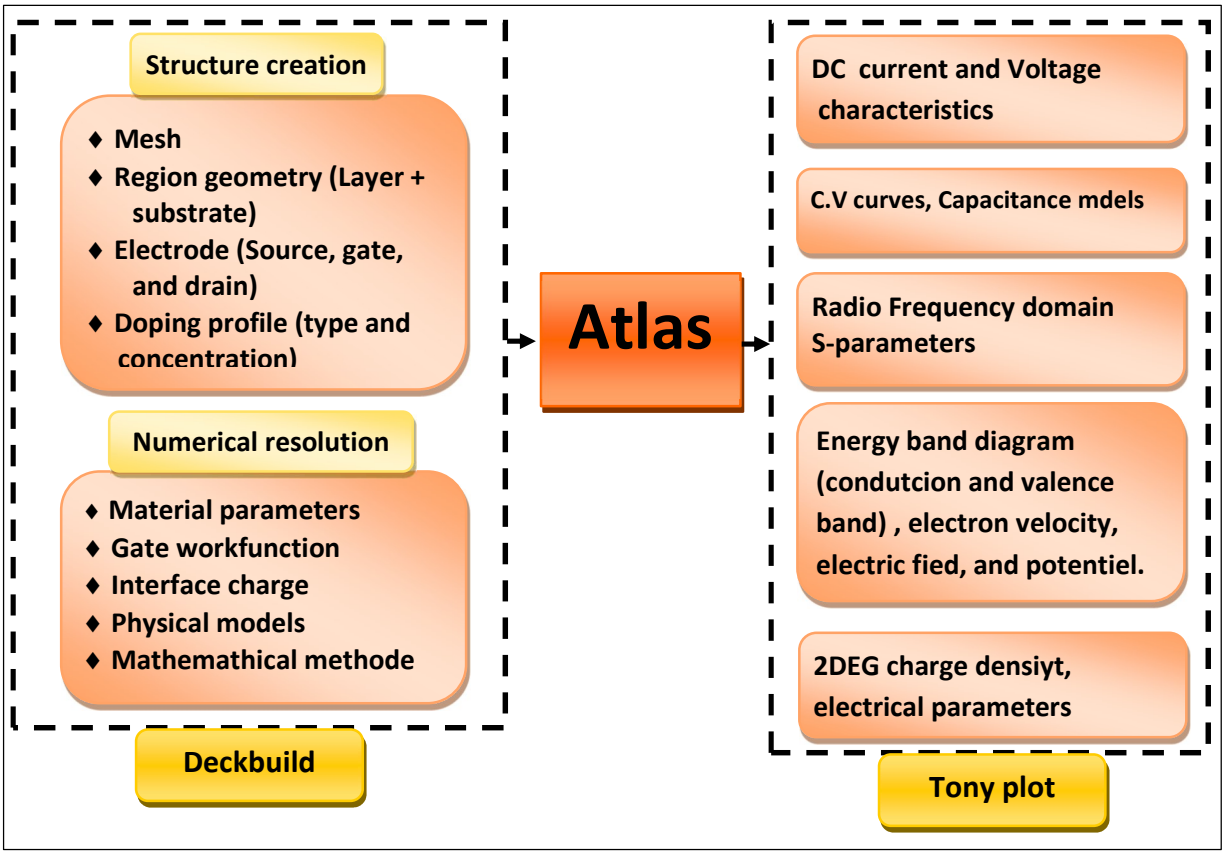

Figure B.1 Input/output Atlas modules used in the TCAD-SILVACO simulation.

2- The Basic Semiconductor Equations in ATLAS-SILVACO

The physical models in semiconductors have been modeled in the form of mathematical expressions, taking into account the probability of occupation of the energy levels, carrier mobility, and the different types of recombination generations. The physical models of TCAD used in our work will be detailed in the following paragraphs.

2.1 Physical models

The electrical properties of our designed transistors are numerically simulated using the physical models of the ATLAS-SILVACO software tool. The primary models required for all semiconductor nano-devices are:

a. Drift diffusion model

The drift diffusion model is based on Maxwell's laws, which works on all semiconductor nano-devices [128]. This model consists of a set of fundamental equations that relate electrostatic potential and the carrier densities. These equations consist of:

- **Transport equation**

The transport equations are defined based on the Boltzmann transport equation. The electron current densities $\overrightarrow{J_n}$ and the hole current densities $\overrightarrow{J_p}$ may be approximated by the drift-diffusion model [128]. In this case, the current densities are expressed in terms of the quasi-Fermi levels φ_n , φ_p and the electron/hole motilities μ_n / μ_p as:

$$\overrightarrow{J_n} = -qn\mu_n \ \nabla\varphi_n \qquad \text{B.1}$$

$$\overrightarrow{J_p} = -qp\mu_p \ \nabla\varphi_p \qquad \text{B.2}$$

- **Poisson's equation**

Poisson's equation relates variations in the electrostatic potential (Ψ) to the local space charge density (ρ), and is given by:

$$div\ (\varepsilon \nabla\ \Psi) = -\ \rho \qquad \text{B.3}$$

Where ε represents the local permittivity. The local space charge density "ρ" is the sum of contributions from all mobile and fixed charges in the device, including electrons, holes, and ionized impurities.

- **Carrier continuity equations**

The continuity equations for electrons and holes are followed by the time evolution of carrier concentrations. The following equations define these continuity equations, which show how carrier concentrations change as a function of transport, generation, and recombination processes:

$$\frac{\partial n}{\partial x} = \frac{1}{q}\, div\overrightarrow{J_n} + G_n - R_n \qquad \text{B.4}$$

$$\frac{\partial p}{\partial x} = -\frac{1}{q}\, div\overrightarrow{J_p} + G_p - R_p \qquad \text{B.5}$$

Where G_n and G_p are the elctron and hole generation rates, R_n and R_p are the electron and hole recombination rates, respectively.

b. Carrier generation and recombination model

The carrier generation and recombination model, also known as the Shockley-Read-Hall (SRH) model, is the process by which mobile charge carriers (electrons and holes) are created and eliminated within a semiconductor material, and is essentially a two-step process. The generation process occurs when electron-hole pairs are created in a semiconductor due to various mechanisms such as thermal excitation. Recombination is the process by which free electrons recombine with holes, leading to the neutralization of charge carriers. SRH model is expressed as follows:

$$U_{SRH} = \frac{np - n_i^2}{\tau_p\left(n + n_i \exp\left[\frac{E_{Trap}}{KT_L}\right]\right) + \tau_n\left(p + n_i \exp\left[\frac{E_{Trap}}{KT_L}\right]\right)} \qquad \text{B.6}$$

Where n_i is the intrinsic carrier density, E_{Trap} is the difference between the trap energy level and the intrinsic Fermi level, T_L is lattice temperature and τ_n and τ_p are the electron and hole lifetimes, k is the Boltzeman constant [128].

c. Electric field-dependent mobility model

The electric field-dependent mobility model (FLDMOB) has been applied to demonstrate the behavior of the charge carrier mobility in a low field and their behavior in a high field. **Equation** 7 shows that as the electric field increases, the electrons velocity begins to saturate at a constant velocity and then literally stagnate [128]. The default low field mobility models as a function of electric field (E) and saturation velocity (V_{sat}) is given by:

$$\mu_n(E) = \mu_{n0} \left[\frac{1}{1 + \left(\frac{\mu_{n0} \cdot E}{V_{sat}} \right)^{\delta}} \right]^{\frac{1}{\delta}} \quad \text{B.7}$$

Where μ_{n0} is the low field mobility and δ is a user defined parameter.

d. Impact ionization model

The impact ionization model is used to mimic the breakdown phenomenon of GaN HEMTs devices. When the electric field is high enough and the distance between carrier collisions is sufficient to allow high-speed acceleration, the free carriers acquire sufficient energy before colliding with the atoms in the crystal; this means that more free carriers are generated. If the rate of generation of free carriers is high, an avalanche phenomenon occurs.

The impact ionization models used during our simulation is Selberherr's Model, which is a recommended model for most cases to plot the HEMT's breakdown voltage curves.

e. Other models

The Fermi-Dirac statistical approach, also mentioned during the simulation, and integrated into the conduction and valence band states, whose energy minimum is located at the E_C and E_V energies, respectively, giving the following expressions for the electron and hole concentrations:

$$n = N_c . \exp\left(\frac{E_F - E_C}{KT_L} \right) \quad \text{B.8}$$

$$p = N_v . \exp\left(\frac{E_F - E_v}{KT_L} \right) \quad \text{B.9}$$

Where K referred to as the Boltzmann approximation, T_L is the lattice temperature, E_F is the fermi energy level. The effective density of states for these electrons and holes, abbreviated as N_c and N_v, are determined as follows:

$$N_c = 2 \left(\frac{2\pi m_e^* kT_L}{h^2} \right)^{\frac{3}{2}} \quad \text{B.10}$$

$$N_v = 2 \left(\frac{2\pi m_h^* kT_L}{h^2} \right)^{\frac{3}{2}} \quad \text{B.11}$$

Where m_e^* and m_h^* are the elementary effective masse of electron and hole, respectively. "h" displays the reduced Planck constant.

2.2 Different stages of simulation

The ATLAS-SILVACO simulation is carried out in the following steps:

2.2.1 Specification of the Structure studied

- **Mesh specification:** The mesh, a series of horizontal and vertical lines, is crucial for simulations. The intersection between the lines is called a node and represents the point where the equations are solved. the mesh must be refined in regions where there is a high carrier density such as the 2DEG channel and the gate region, whereas it may be less tight for other regions. The more refined the mesh, the more accurate the calculation, but the simulation time also increases. Consequently, the choice of mesh must balance speed and results accuracy. .
- **Specifying regions and materials:** Once the mesh has been defined, the regions making up the component. These regions are defined by declaring the type of material and its position in the two dimensions, i.e. thickness and width (x and y).
- **Electrode specification:** Electrodes (source, gate and drain) can be defined in ATLAS by identifying their position, depth and material constituents.
- **Doping specification:** The doping profile of a specific region can be of type n (donors) or p (acceptors). The type of distribution can be uniform (complete ionization) or Gaussian.
- **Material specification:** The material instruction is used to associate physical and electrical parameters of the new materials used in the simulation which are not defined by default for standard semiconductors.
- **Model specification**: it indicates the inclusions of different physical mechanisms, models or other parameters such as the temperature range during the simulation.
- **Contact specification:** indicates the physical attributes of an electrode (ohmic, Schottky or MOS contact).
- **Interface specification:** indicates the interface charge parameters at the semiconductor/insulator boundaries.

2.2.2 Method specification:

Numerical methods are used to solve the equations related to the physical models based on the iterative resolution. Two types of methods are included in ATLAS-SILVACO: the Gummel method and the Newton method.

2.2.3 Solution specification

Solutions are specified by following the instructions below: Log, Solve, Load and Save. The Log instruction is used to record all the characteristics of the terminal in a data file. The Solve instruction is used to search for a solution for one or more polarisation points. The Load instruction is used to introduce previous solutions as an initial backup, from an existing file saved with the Save instruction. The results are displayed in the TonyPlot environment.

2.2.4 Programming logic

We are now going to present the order of the commands specific to the Atlas programming logic. There are five groups of commands, which must be organized correctly as follows.

Table 0.1 Order of command groups in an Atlas program.

specification	Instruction
Structure	MESH REGION ELECTRODE DOPING
Model	MATERIAL MODEL CONTACT INTERFACE
Numerical method	METHOD
Solution	LOG SOLVE SAVE LOAD
Result analysis	EXTRACT TONYPLOT

The available options and equations are extensively introduced and discussed in the ATLAS user's manual [128]

Appendix C

ADS Software

Advanced Design System (ADS) is an electronic design automation, produced by Keysight EEsof EDA, [7] a division of Keysight Technologies. It provides an integrated design environment for designers of RF, microwave, and high speed digital products such as radar systems, mobile phones, wireless networks, satellite communications, and high-speed data links [7].

Keysight ADS supports all stages of the design process including schematic capture, layout, design rule verification, frequency and time domain circuit simulation and electromagnetic field simulation, enabling the engineer to fully characterize and optimize an RF design without changing tools.

ADS tool enables us to visualize and determine our design device whether they meet the necessary requirements and whether they can be manufactured. Tables, diagrams, and graphs are examples of data analysis and visualization sunctions in ADS software that help us to clearly interpretate and analyze data and make conclusions and modifications Additionally, we may simply fix any defects you see in your design, which boosts your trust in it.

References

[1] I. Vurgaftman and J. n. Meyer, "Band parameters for nitrogen-containing semiconductors," Journal of Applied Physics, vol. 94, pp. 3675-3696, 2003.

[2] J. Hudgins, G. Simin, and M. Khan, "A new assessment of the use of wide bandgap semiconductors and the potential for GaN," in 2002 IEEE 33rd Annual IEEE Power Electronics Specialists Conference. Proceedings (Cat. No. 02CH37289), 2002, pp. 1747-1752.

[3] H. Mathieu, T. Bretagnon, and P. Lefebvre, Physique des Semiconducteurs et des Composants Electroniques-Problèmes Résolus. Dunod, 2001.

[4] D. Brunner, H. Angerer, E. Bustarret, F. Freudenberg, R. Höpler, R. Dimitrov, et al., "Optical constants of epitaxial AlGaN films and their temperature dependence," Journal of applied physics, vol. 82, pp. 5090-5096, 1997.

[5] S. Bouzid-Driad, "Réalisation et caractérisation de transistors HEMTs GaN pour des applications dans le domaine millimétrique,", Doctoral thesis, Lille 1, 2013.

[6] E. Sichel and J. Pankove, "Thermal conductivity of GaN, 25–360 K," Journal of physics and chemistry of solids, vol. 38, p. 330, 1977.

[7] J. L. Walker, Handbook of RF and microwave power amplifiers: Cambridge university press, 2011.

[8] H. Lakhdhar, "Reliability assessment of GaN HEMTs on Si substrate with ultra-short gate dedicated to power applications at frequency above 40 GHz,", doctoral thesis Bordeaux, 2017.

[9] H. Mordoc, "Handbook of Nitride Semiconductors and Devices: Vol. 1: Materials Properties, Physics and Growth," ed: Wiley Verlag GmbH, Weinheim, 2008.

[10] W. Seifert, R. Franzheld, E. Butter, H. Sobotta, and V. Riede, "On the origin of free carriers in high-conducting n-GaN," Crystal Research and Technology, vol. 18, pp. 383-390, 1983.

[11] R. BAYA and M. CHEKARI, "Simulation Study of HEMT performance for high frequency applications,", doctoral thesis, Université Ibn Khaldoun-Tiaret, 2020.

[12] M. Abid, H. Abu Hassan, Z. Hassan, S. Ng, S. Mohd Bakhori, and N. Abd Raof, "Structural and optical properties of Al x In y Ga1− x− y N quaternary alloys grown on sapphire substrates by molecular beam epitaxy," Microelectronics international, vol. 27, pp. 148-153, 2010.

[13] S. Li and C. Ouyang, "First principles study of wurtzite and zinc blende GaN: a comparison of the electronic and optical properties," Physics letters A, vol. 336, pp. 145-151, 2005.

[14] S. Aroulanda, "Co-intégration de HEMT GaN hyperfréquence normally-off avec des normally-on,", thèse de Doctorat, Université de Lille 2020.

[15] O. Ambacher, J. Majewski, C. Miskys, A. Link, M. Hermann, M. Eickhoff, et al., "Pyroelectric properties of Al (In) GaN/GaN hetero-and quantum well structures," Journal of physics: condensed matter, vol. 14, p. 3399, 2002.

[16] M. Shur, A. Bykhovski, and R. Gaska, "Pyroelectric and piezoelectric properties of GaN-based materials," MRS Online Proceedings Library (OPL), vol. 537, 1998.

[17] F. Albany, "Evaluation de la robustesse d'une technologie HEMT GaN normally-off à implantation d'ions fluorures co-intégrée avec une technologie HEMT GaN normally-on," , thèse de Doctorat , Université de Bordeaux, 2021.

[18] O. Ambacher, J. Smart, J. Shealy, N. Weimann, K. Chu, M. Murphy, et al., "Two-dimensional electron gases induced by spontaneous and piezoelectric polarization charges in N-and Ga-face AlGaN/GaN heterostructures," Journal of applied physics, vol. 85, pp. 3222-3233, 1999.

[19] V. Fiorentini, F. Bernardini, and O. Ambacher, "Evidence for nonlinear macroscopic polarization in III–V nitride alloy heterostructures," Applied physics letters, vol. 80, pp. 1204-1206, 2002.

[20] Y. P. Varshni, "Temperature dependence of the energy gap in semiconductors," physica, vol. 34, pp. 149-154, 1967.

[21] R. Bouveyron, "Development and understanding of III-N layers for the improvement of high power transistors,", doctoral thesis, University Grenoble Alpes (ComUE), 2017.

[22] Z.-e. Touati, "Contribution à la modélisation non linéaire et l'optimisation des transistors à effet de champ à hétérojonction par des méthodes intelligentes,", thèse de doctorat, Université Mohamed Khider-Biskra, 2019.

[23] E. Malela-Massamba, "Développement et caractérisation de modules Technologiques sur semiconducteur GaN: application à la réalisation de cathodes froides et de transistor HEMT AlGaN/GAN,", thèse de doctorat, Lyon, 2016.

[24] Z. Dridi, B. Bouhafs, and P. Ruterana, "First-principles investigation of lattice constants and bowing parameters in wurtzite AlxGa1− xN, InxGa1− xN and InxAl1− xN alloys," Semiconductor Science and Technology, vol. 18, p. 850, 2003.

[25] Y. Koide, H. Itoh, M. Khan, K. Hiramatu, N. Sawaki, and I. Akasaki, "Energy band-gap bowing parameter in an Al x Ga1− x N alloy," Journal of applied physics, vol. 61, pp. 4540-4543, 1987.

[26] B. Noureeddine, "Etude ab-initio des proprietes electroniques de GaN/InN/AlN: effets de polarisation," Magister, d'Oran, 2014.

[27] F. Bernardini and V. Fiorentini, "Nonlinear macroscopic polarization in III-V nitride alloys," Physical Review B, vol. 64, p. 085207, 2001.

[28] O. Ambacher, B. Foutz, J. Smart, J. Shealy, N. Weimann, K. Chu, et al., "Two dimensional electron gases induced by spontaneous and piezoelectric polarization in undoped and doped AlGaN/GaN heterostructures," Journal of applied physics, vol. 87, pp. 334-344, 2000.

[29] J. Piprek, Nitride semiconductor devices: principles and simulation: John Wiley & Sons, 2007.

[30] T. Matsuoka, N. Yoshimoto, T. Sasaki, and A. Katsui, "Wide-gap semiconductor InGaN and InGaAlN grown by MOVPE," Journal of electronic materials, vol. 21, pp. 157-163, 1992.

[31] N. Ketteniß, "GaN-based heterostructure field effect transistors with ternary and quaternary InAl (Ga) N barrier layers," Aachen, Techn. Hochsch., PhD Dissertation., 2013, 2013.

[32] B. Reuters, F. Scholz, and A. Vescan, "Polarization-optimized heterostructures with quaternary AlInGaN layers for novel group III nitride devices," Lehr-und Forschungsgebiet GaN-Bauelementtechnologie2016.

[33] P.-T. Tu, I. Sanyal, P.-C. Yeh, H.-Y. Lee, L.-H. Lee, C.-I. Wu, et al., "Quaternary Barrier AlInGaN/GaN-on-Si High Electron Mobility Transistor with Record F T-L g

Product of 13.9 GHz-μm," in 2020 International Symposium on VLSI Technology, Systems and Applications (VLSI-TSA), 2020, pp. 130-131.

[34] I. Gorczyca, T. Suski, N. E. Christensen, and A. Svane, "Band gap bowing in quaternary nitride semiconducting alloys," Applied Physics Letters, vol. 98, 2011.

[35] B. G. Yacobi, Semiconductor materials: an introduction to basic principles: Springer Science & Business Media, 2003.

[36] D. Hull and D. J. Bacon, Introduction to dislocations vol. 37: Elsevier, 2011.

[37] C. Stampfl and C. G. Van de Walle, "Energetics and electronic structure of stacking faults in AlN, GaN, and InN," Physical Review B, vol. 57, p. R15052, 1998.

[38] Y. Li, "Theoretical investigation on electron mobility in AlInGaN/InGaN heterostructures," physica status solidi (b), vol. 256, p. 1800704, 2019.

[39] T. Zine-eddine, H. Zahra, and M. Zitouni, "Design and analysis of 10 nm T-gate enhancement-mode MOS-HEMT for high power microwave applications," Journal of Science: Advanced Materials and Devices, vol. 4, pp. 180-187, 2019.

[40] Y. Li, J. Zhang, G. Liu, R. Quan, X. Duan, J. Zhang, et al., "Theoretical analysis of the mobility of two-dimensional electron gas in the quaternary AlxInyGa1-x-yN/GaN heterojunctions limited by the alloy composition fluctuation," AIP Advances, vol. 7, 2017.

[41] J. P. Ibbetson, P. Fini, K. Ness, S. DenBaars, J. Speck, and U. Mishra, "Polarization effects, surface states, and the source of electrons in AlGaN/GaN heterostructure field effect transistors," Applied Physics Letters, vol. 77, pp. 250-252, 2000.

[42] R. Wang, G. Li, G. Karbasian, J. Guo, B. Song, Y. Yue, et al., "Quaternary Barrier InAlGaN HEMTs With $ f_ {T}/f_ {\max} $ of 230/300 GHz," IEEE electron device letters, vol. 34, pp. 378-380, 2013.

[43] P. Murugapandiyan, A. Mohanbabu, V. R. Lakshmi, M. Wasim, and K. M. J. J. o. E. M. Sundaram, "Investigation of Quaternary Barrier InAlGaN/GaN/AlGaN Double-Heterojunction High-Electron-Mobility Transistors (HEMTs) for High-Speed and High-Power Applications," vol. 49, pp. 524-529, 2020.

[44] N. M. Shrestha, C.-H. Chen, Z.-M. Tsai, Y. Li, J.-H. Tarng, and S. Samukawa, "Barrier engineering of lattice matched alingan/gan heterostructure toward high performance e-mode operation," in 2019 International Conference on Simulation of Semiconductor Processes and Devices (SISPAD), 2019, pp. 1-4.

[45] R. Brown, D. Macfarlane, A. Al-Khalidi, X. Li, G. Ternent, H. Zhou, et al., "A sub-critical barrier thickness normally-off AlGaN/GaN MOS-HEMT," vol. 35, pp. 906-908, 2014.

[46] C. Mead, "Schottky barrier gate field effect transistor," in Semiconductor Devices: Pioneering Papers, ed: World Scientific, 1991, pp. 499-499.

[47] A. Banerjee, "AlGaN/GaN based enhancement mode MOSHEMTs,", doctoral thesis, University of Glasgow, 2010.

[48] B. Hult, Design, Fabrication and Characterization of GaN HEMTs for Power Switching Applications: Chalmers Tekniska Hogskola (Sweden), 2022.

[49] H. Hahn, Threshold voltage engineering of GaN-based n-channel and p-channel heterostructure field effect transistors: Verlag Dr. Hut, 2015.

[50] M. Golio, RF and microwave semiconductor device handbook: CRC press, 2017.

[51] A. Revathy, C. Boopathi, O. I. Khalaf, and C. A. T. Romero, "Investigation of AlGaN channel HEMTs on β-Ga2O3 substrate for high-power electronics," Electronics, vol. 11, p. 225, 2022.

[52] S. Rennesson, "Développement de nouvelles hétérostructures HEMTs à base de nitrure de gallium pour des applications de puissance en gamme d'ondes millimétriques," thèse de doctorat, Université Nice Sophia Antipolis, 2013.

[53] G. Dambrine, A. Cappy, F. Heliodore, and E. Playez, "A new method for determining the FET small-signal equivalent circuit," IEEE Transactions on microwave theory and techniques, vol. 36, pp. 1151-1159, 1988.

[54] M. Sharma, R. J. I. J. o. R. Chaujar, and M. C. A. Engineering, "Ultrascaled 10 nm T-gate E-mode InAlN/AlN HEMT with polarized doped buffer for high power microwave applications," vol. 32, p. e23057, 2022.

[55] R. Wang, G. Li, J. Verma, B. Sensale-Rodriguez, T. Fang, J. Guo, et al., "220-GHz quaternary barrier InAlGaN/AlN/GaN HEMTs," vol. 32, pp. 1215-1217, 2011.

[56] I. FOUR, "Simulation et modélisation des commutateurs RF à base de composants semi-conducteurs, thèse de doctorat, " Université de Tlemcen-Abou Bekr Belkaid, 2021.

[57] C. Pavageau, M. S. Moussa, J.-P. Raskin, D. Vanhoenaker-Janvier, N. Fel, J. Russat, et al., "A 7-dB 43-GHz CMOS distributed amplifier on high-resistivity SOI substrates," IEEE transactions on microwave theory and techniques, vol. 56, pp. 587-598, 2008.

[58] M. Haziq, S. Falina, A. A. Manaf, H. Kawarada, and M. Syamsul, "Challenges and opportunities for high-power and high-frequency AlGaN/GaN high-electron-mobility transistor (HEMT) applications: A review," Micromachines, vol. 13, p. 2133, 2022.

[59] C. Ma, G. Gu, and Y. Lü, "A high performance InAlN/GaN HEMT with low Ron and gate leakage," Journal of Semiconductors, vol. 37, p. 024009, 2016.

[60] N. Islam, M. F. P. Mohamed, M. F. A. J. Khan, S. Falina, H. Kawarada, and M. Syamsul, "Reliability, Applications and Challenges of GaN HEMT Technology for Modern Power Devices: A Review," Crystals, vol. 12, p. 1581, 2022.

[61] W. Saito, Y. Takada, M. Kuraguchi, K. Tsuda, and I. Omura, "Recessed-gate structure approach toward normally off high-voltage AlGaN/GaN HEMT for power electronics applications," IEEE Transactions on electron devices, vol. 53, pp. 356-362, 2006.

[62] L. T. Xuan, "Fonction normally-on, normally-off compatible de la technologie hemt gan pour des applications de puissance, hyperfréquences," Université de Limoges, 2018.

[63] C. Gong, M. Mi, Y. Zhou, P. Wang, Y. Chen, J. Liu, et al., "InAlN/GaN HEMT With n+ GaN Contact Ledge Structure for Millimeter-Wave Low Voltage Applications," IEEE Journal of the Electron Devices Society, vol. 11, pp. 72-77, 2023.

[64] M. Vadizadeh, M. Fallahnejad, M. Shaveisi, R. Ejlali, and F. Bajelan, "Double Gate Double-Channel AlGaN/GaN MOS HEMT and its Applications to LNA with Sub-1 dB Noise Figure," Silicon, vol. 15, pp. 1093-1103, 2023.

[65] D. S. Lee, O. Laboutin, Y. Cao, W. Johnson, E. Beam, A. Ketterson, et al., "317 GHz InAlGaN/GaN HEMTs with extremely low on-resistance," physica status solidi c, vol. 10, pp. 827-830, 2013.

[66] J. Ballestín-Fuertes, J. Muñoz-Cruzado-Alba, J. F. Sanz-Osorio, and E. Laporta-Puyal, "Role of wide bandgap materials in power electronics for smart grids applications," Electronics, vol. 10, p. 677, 2021.

[67] K. Jones, T. Chow, M. Wraback, M. Shatalov, Z. Sitar, F. Shahedipour, et al., "AlGaN devices and growth of device structures," Journal of Materials Science, vol. 50, pp. 3267-3307, 2015.

[68] H. Krishna Murthy, "Characterisation of GaN HEMTs on Different Substrates for Power Electronics Applications," ed, 2022.

[69] D. J. Meyer, D. A. Deen, D. F. Storm, M. G. Ancona, D. S. Katzer, R. Bass, et al., "High electron velocity submicrometer AlN/GaN MOS-HEMTs on freestanding GaN substrates," IEEE electron device letters, vol. 34, pp. 199-201, 2013.

[70] F. Roccaforte, P. Fiorenza, G. Greco, R. L. Nigro, F. Giannazzo, F. Iucolano, et al., "Emerging trends in wide band gap semiconductors (SiC and GaN) technology for power devices," Microelectronic Engineering, vol. 187, pp. 66-77, 2018.

[71] R. Singh, G. P. Rao, T. R. Lenka, S. Prasad, N. E. I. Boukortt, G. Crupi, et al., "Design and simulation of T-gate AlN/β-Ga2O3 HEMT for DC, RF and high-power nanoelectronics switching applications," International Journal of Numerical Modelling: Electronic Networks, Devices and Fields, p. e3146, 2023.

[72] M. Higashiwaki, K. Sasaki, T. Kamimura, M. Hoi Wong, D. Krishnamurthy, A. Kuramata, et al., "Depletion-mode Ga2O3 metal-oxide-semiconductor field-effect transistors on β-Ga2O3 (010) substrates and temperature dependence of their device characteristics," Applied Physics Letters, vol. 103, p. 123511, 2013.

[73] S. Pearton, J. Yang, P. H. Cary, F. Ren, J. Kim, M. J. Tadjer, et al., "A review of Ga2O3 materials, processing, and devices," Applied Physics Reviews, vol. 5, 2018.

[74] A. Maertens, "Etude de la réalisation d'une structure transistor (FET) pour l'observation de l'exciton du ZnO sous champ électrique," CentraleSupélec, 2016.

[75] D. J. Macfarlane, "Design and fabrication of AlGaN/GaN HEMTs with high breakdown voltages, doctoral thesis, " University of Glasgow, 2014.

[76] Y. Dora, Understanding material and process limits for high breakdown voltage aluminum gallium nitride/gallium nitride HEMTs:, doctoral thesis, University of California, Santa Barbara, 2006.

[77] B. F. Zahra, "Study of the self-heating effect in the MOS-HEMT transistor," master, Universite abou bekr belkaid tlemcen, 2015.

[78] Y. Li, X. Liu, T. Sun, F. Zhang, T. Fu, P. Wang-yang, et al., "Impact of Al," 2022.

[79] J. Du, T. Pu, X. Li, L. Li, J.-P. Ao, and H. Gao, "Normally-Off Metal-Insulator-Semiconductor P-GaN gated AlGaN/GaN high electron mobility transistors with low gate leakage current," Journal of Crystal Growth, vol. 611, p. 127183, 2023.

[80] A. Hassan, Y. Savaria, and M. Sawan, "GaN integration technology, an ideal candidate for high-temperature applications: A review," IEEE Access, vol. 6, pp. 78790-78802, 2018.

[81] R. Ye, X. Cai, C. Du, H. Liu, Y. Zhang, X. Duan, et al., "An overview on analyses and suppression methods of trapping effects in AlGaN/GaN HEMTs," IEEE Access, vol. 10, pp. 21759-21773, 2021.

[82] T. Kawanago, K. Kakushima, Y. Kataoka, A. Nishiyama, N. Sugii, H. Wakabayashi, et al., "Gate technology contributions to collapse of drain current in AlGaN/GaN Schottky HEMT," IEEE Transactions on Electron Devices, vol. 61, pp. 785-792, 2014.

[83] Z. Zhang, W. Li, K. Fu, G. Yu, X. Zhang, Y. Zhao, et al., "AlGaN/GaN MIS-HEMTs of Very-Low Hysteresis and Current Collapse With In-Situ Pre-Deposition Plasma Nitridation and LPCVD-Si3N4 Gate Insulator," IEEE Electron Device Letters, vol. 38, pp. 236-239, 2016.

[84] W. Saito, T. Nitta, Y. Kakiuchi, Y. Saito, K. Tsuda, I. Omura, et al., "Suppression of dynamic on-resistance increase and gate charge measurements in high-voltage GaN-HEMTs with optimized field-plate structure," IEEE transactions on electron devices, vol. 54, pp. 1825-1830, 2007.

[85] I. Four and M. Kameche, "Comparative simulation of DC and AC performances of Al0. 26Ga0. 74N/GaN HEMT with BGaN Back-barriers," international Journal of Nanoelectronics and Materials, vol. 14, pp. 99-112, 2021.

[86] I. Jabbari, M. Baira, and H. Maaref, "Correlation between kink effect and trapping mechanism through H1 hole trap in Al 0.22 Ga 0.78 N/GaN/SiC HEMTs by current DLTS: Field effect enhancement," Applied Physics A, vol. 126, pp. 1-11, 2020.

[87] R. Lossy, H. Gargouri, M. Arens, and J. Würfl, "Gallium nitride MIS-HEMT using atomic layer deposited Al2O3 as gate dielectric," Journal of Vacuum Science & Technology A, vol. 31, 2013.

[88] O. Seok, W. Ahn, Y.-S. Kim, M.-K. Han, and M.-W. Ha, "3.2 kV AlGaN/GaN MIS-HEMTs employing RF sputtered Ga 2 O 3 films," in 2012 24th International Symposium on Power Semiconductor Devices and ICs, 2012, pp. 269-272.

[89] N. Amina, M. Zitouni, and T. Zineeddine, "RF Performance Analysis of Conventional and Recessed Gate AlGaN/GaN MOSHEMT using β–Ga 2 O 3 as Dielectric Layer," in 2023 International Conference on Advances in Electronics, Control and Communication Systems (ICAECCS), 2023, pp. 1-6.

[90] J. Shi, L. F. Eastman, X. Xin, and M. Pophristic, "High performance AlGaN/GaN power switch with HfO2 insulation," Applied Physics Letters, vol. 95, 2009.

[91] T.-Y. Wu, S.-K. Lin, P.-W. Sze, J.-J. Huang, W.-C. Chien, C.-C. Hu, et al., "AlGaN/GaN MOSHEMTs With Liquid-Phase-Deposited $\hbox {TiO} _ {2} $ as Gate Dielectric," IEEE transactions on electron devices, vol. 56, pp. 2911-2916, 2009.

[92] A. Noual, M. Zitouni, Z.-e. Touati, O. Saidani, and A. Yousfi, "Numerical study of T-Gate AlGaN/AlInGaN/GaN MOSHEMT with Single and Double Barrier for THz Frequency Applications," East European Journal of Physics, pp. 216-225, 2023.

[93] S. Hasan, M. U. Jewel, S. R. Crittenden, D. Lee, V. Avrutin, U. Ozgur, et al., "MOCVD-Grown Ga2O3 as a Gate Dielectric on Algan/Gan Based Heterojunction Field Effect Transistor," 2023.

[94] A. Kaya, H. Mao, J. Gao, R. V. Chopdekar, Y. Takamura, S. Chowdhury, et al., "An Investigation of Electrical and Dielectric Parameters of Sol–Gel Process Enabled $\beta $-Ga2O3 as a Gate Dielectric Material," IEEE Transactions on Electron Devices, vol. 64, pp. 2047-2053, 2017.

[95] C. Zhang, F. Liao, X. Liang, H. Gong, Q. Liu, L. Li, et al., "Electronic transport properties in metal doped beta-Ga2O3: A first principles study," Physica B: Condensed Matter, vol. 562, pp. 124-130, 2019.

[96] T. Scheinert, T. Mikolajick, and S. Schmult, "Critical parameters for the presence of a 2DEG in GaN/AlxGa1− xN heterostructures," AIP Advances, vol. 9, p. 125018, 2019.

[97] A. Douara, B. Djellouli, H. Abid, A. Rabehi, A. Ziane, M. Mostefaoui, et al., "Optimization of two-dimensional electron gas characteristics of AlGaN/GaN high electron mobility transistors," International Journal of Numerical Modelling: Electronic Networks, Devices and Fields, vol. 32, p. e2518, 2019.

[98] S. Xiong, W. Huang, A. Hassan, and R. Zhong, "Simulation study on electrical properties of p-GaN gate normally-off HEMT devices affected by Al mole fraction in AlGaN barrier layer," in Journal of Physics: Conference Series, 2022, p. 012073.

[99] A. N. Khan, M. Chauhan, K. Jena, and G. Chatterjee, "Improved Analog Performance of PZT Ferroelectric AlGaN/AlN/GaN E-Mode GR-MOSHEMT," in 2022 IEEE Delhi Section Conference (DELCON), 2022, pp. 1-5.

[100] H.-Y. Lee, T.-W. Chang, and C.-T. Lee, "AlGaN/GaN metal-oxide-semiconductor high-electron mobility transistors using Ga 2 O 3 gate dielectric layer grown by vapor cooling condensation system," Journal of Electronic Materials, vol. 50, pp. 3748-3753, 2021.

[101] H.-Y. Shih, F.-C. Chu, A. Das, C.-Y. Lee, M.-J. Chen, and R.-M. Lin, "Atomic layer deposition of gallium oxide films as gate dielectrics in AlGaN/GaN metal–oxide–semiconductor high-electron-mobility transistors," Nanoscale Research Letters, vol. 11, pp. 1-9, 2016.

[102] M. Ge, Y. Li, Y. Zhu, D. Chen, Z. Wang, and S. Tan, "Effects of gate work function on E-mode AlGaN/GaN HEMTs with stack gate β-Ga2O3/p-GaN structure," Journal of Physics D: Applied Physics, vol. 54, p. 355103, 2021.

[103] H. Y. Kang, M. J. Yeom, J. Y. Yang, Y. Choi, J. Lee, C. Park, et al., "Epitaxial κ-Ga2O3/GaN heterostructure for high electron-mobility transistors," Materials Today Physics, vol. 31, p. 101002, 2023.

[104] H.-Y. Lee, D.-S. Liu, J.-I. Chyi, E. Y. Chang, and C.-T. Lee, "Lattice-matched AlInN/GaN/AlGaN/GaN heterostructured-double-channel metal-oxide-semiconductor high-electron mobility transistors with multiple-mesa-fin-channel array," Materials, vol. 14, p. 5474, 2021.

[105] S. Dasgupta, D. F. Brown, F. Wu, S. Keller, J. S. Speck, and U. K. Mishra, "Ultralow nonalloyed ohmic contact resistance to self aligned N-polar GaN high electron mobility transistors by In (Ga) N regrowth," Applied Physics Letters, vol. 96, p. 143504, 2010.

[106] N. M. Shrestha, Y. Li, C.-H. Chen, I. Sanyal, J.-H. Tarng, J.-I. Chyi, et al., "Design and simulation of high performance lattice matched double barrier normally off AlInGaN/GaN HEMTs," vol. 8, pp. 873-878, 2020.

[107] H. Rahbardar Mojaver, J.-L. Gosselin, and P. Valizadeh, "Use of a bilayer lattice-matched AlInGaN barrier for improving the channel carrier confinement of enhancement-mode AlInGaN/GaN hetero-structure field-effect transistors," Journal of Applied Physics, vol. 121, p. 244502, 2017.

[108] D. Biswas, H. Fujita, N. Torii, and T. J. J. o. A. P. Egawa, "Effect of In composition on electrical performance of AlInGaN/GaN-based metal-insulator-semiconductor high electron mobility transistors (MIS-HEMTs) on Si," vol. 125, p. 225707, 2019.

[109] T. Nanjo, M. Suita, T. Oishi, Y. Abe, E. Yagyu, K. Yoshiara, et al., "Comparison of characteristics of AlGaN channel HEMTs formed on SiC and sapphire substrates," vol. 45, pp. 424-426, 2009.

[110] T.-L. Wu, S.-W. Tang, and H.-J. Jiang, "Investigation of recessed gate AlGaN/GaN MIS-HEMTs with double AlGaN barrier designs toward an enhancement-mode characteristic," Micromachines, vol. 11, p. 163, 2020.

[111] R. Kajitani, K. Tanaka, M. Ogawa, H. Ishida, M. Ishida, and T. Ueda, "Novel high-current density GaN-based normally off transistor with tensile-strained quaternary InAlGaN barrier," Japanese Journal of Applied Physics, vol. 54, p. 04DF09, 2015.

[112] N. M. Shrestha, Y. Li, C.-H. Chen, I. Sanyal, J.-H. Tarng, J.-I. Chyi, et al., "Design and simulation of high performance lattice matched double barrier normally off AlInGaN/GaN HEMTs," IEEE Journal of the Electron Devices Society, vol. 8, pp. 873-878, 2020.

[113] D. R. Androse, S. Deb, S. K. Radhakrishnan, and E. Sekar, "T-gate AlGaN/GaN HEMT with effective recess engineering for enhancement mode operation," Materials Today: Proceedings, vol. 45, pp. 3556-3559, 2021.

[114] J. Jorudas, P. Prystawko, A. Šimukovič, R. Aleksiejūnas, J. Mickevičius, M. Kryśko, et al., "Development of quaternary InAlGaN barrier layer for high electron mobility transistor structures," Materials, vol. 15, p. 1118, 2022.

[115] P. Murugapandiyan, A. Mohanbabu, V. R. Lakshmi, M. Wasim, and K. M. Sundaram, "Investigation of quaternary barrier InAlGaN/GaN/AlGaN double-heterojunction high-electron-mobility transistors (HEMTs) for high-speed and high-power applications," Journal of Electronic Materials, vol. 49, pp. 524-529, 2020.

[116] J. Bernát, P. Javorka, A. Fox, M. Marso, H. Lüth, and P. Kordoš, "Effect of surface passivation on performance of AlGaN/GaN/Si HEMTs," Solid-State Electronics, vol. 47, pp. 2097-2103, 2003.

[117] G. P. Rao, T. R. Lenka, and H. P. T. Nguyen, "Analysis of Channel length, Gate length and Gate position Optimization of III-Nitride/β-Ga2O3 Nano-HEMT for High-Power Nanoelectronics and Terahertz Applications," Materials Science and Engineering: B, vol. 293, p. 116498, 2023.

[118] G. P. Rao, T. R. Lenka, R. Singh, and H. P. T. Nguyen, "Simulation modelling of III-nitride/β-Ga2O3 HEMT for emerging high-power nanoelectronics applications," Journal of the Korean Physical Society, vol. 81, pp. 876-884, 2022.

[119] F. Sonmez, E. Arslan, S. Ardali, E. Tiras, and E. Ozbay, "Determination of scattering mechanisms in AlInGaN/GaN heterostructures grown on sapphire substrate," Journal of Alloys and Compounds, vol. 864, p. 158895, 2021.

[120] G. Purnachandra Rao, T. R. Lenka, N. E. I. Boukortt, and H. P. T. Nguyen, "Investigation of the Temperature Impact on the Performance Characteristics of the Field-Plated Recessed Gate III-Nitride HEMT on β-Ga2O3 Substrate," in International Conference on Micro/Nanoelectronics Devices, Circuits and Systems, 2023, pp. 111-121.

[121] A. M. Bhat, N. Shafi, and C. Periasamy, "AlGaN/GaN HEMT AC/DC Performance Analysis of Conventional and Gate Recessed MOS-HEMT With Temperature Variation," in 2019 3rd International Conference on Electronics, Materials Engineering & Nano-Technology (IEMENTech), 2019, pp. 1-4.

[122] R. Karpagam, S. L. S. Vimalraj, G. Sathishkumar, V. Megala, Y. Gowthami, and B. Balaji, "DC and RF Performance Analysis of Extended Field plated AlGaN/GaN/β-

Ga2O3 HEMT," Transactions on Electrical and Electronic Materials, vol. 24, pp. 459-468, 2023.

[123] B. Jacob, G. Paul, and V. Suresh Babu, "DC Characterization and High-Frequency Performance Analysis of a GaN/AlGaN HET on a β-Ga2O3 Substrate," IETE Journal of Research, vol. 69, pp. 1460-1465, 2023.

[124] S. Anju, V. S. Babu, and G. Paul, "Design optimization of high-frequency AlGaN/GaN HEMT on BGO substrates," Applied Physics A, vol. 127, p. 405, 2021.

[125] R. Singh, T. Lenka, and H. Nguyen, "T-gate shaped AlN/β-Ga2O3 HEMT for RF and high power nanoelectronics," Int. J. Numer. Modelling, Electron. Netw. Devices Fields, vol. 1, p. 34, 2021.

[126] G. Purnachandra Rao, T. R. Lenka, R. Singh, N. E. I. Boukortt, S. M. Sadaf, and H. P. T. Nguyen, "Comparative Study of III-Nitride Nano-HEMTs on different substrates for emerging high-power nanoelectronics and millimetre wave applications," Journal of Electronic Materials, vol. 52, pp. 1948-1957, 2023.

[127] S. Anju, V. S. Babu, and B. Jacob, "A nanoscale AlGaN/GaN HEMT on BGO substrate with recessed T gate for high frequency applications," Materials Today: Proceedings, vol. 80, pp. 2076-2079, 2023.

[128] A. U. s. Manual, ATLAS User's Manual: Device Simulation Software, 2008.

[129] K. Ikram, "Synthèse des Filtres Multi-bandes pour les applications GNSS MC/MF," thèse master, Université Bordj Bou Arriridj, Algérie, 2019.

[130] M. M. Hossain, ""Design of RF Front End for Multi-Band Multi-System GNSS Receiver"," ed, 2008.

[131] S. Jin, Global navigation satellite systems: signal, theory and applications: BoD–Books on Demand, 2012.

[132] G. Matthaei, L. Young, and E. Jones, "Design of microwave filters impedance-matching networks and coupling structures volume 2," vol, vol. 1, p. 526, 1963.

[133] https://www.electronics-tutorials.ws/filter/filter_4.html.

[134] P. Chen, G. Li, and Z. Zhu, "Development and application of SAW filter," Micromachines, vol. 13, p. 656, 2022.

[135] https://www.electronics-notes.com/articles/radio/rf-filters/constant-k-simple-bandpass-lc-rf-filter-design-calculations.php.

[136] Z. Hamaizia, "Conception d'un amplificateur faible bruit LNA à base d'un transistor à effet de champ à hétérojonction pHEMT,", thèse de doctorat, Université Mohamed Khider–Biskra, 2011.

[137] Ma, Pingxi, Racanelli, Marco, "A novel bipolar-MOSFET low-noise amplifier (BiFET LNA), circuit configuration, design methodology, and chip implementation", IEEE Transactions on Microwave Theory and Techniques, p. 2175-2180, 2003.

[138] Zhang, Xiaomeng, Li, Shuo, Moody, Tylor, "Multi-finger MOSFET low noise amplifier performance analysis", NAECON 2014-IEEE National Aerospace and Electronics Conference, p. 342-345, 2014

[139] M. Navneeta, "Design and Test of an L-Band (GNSS) Low Noise Amplifier and Limiter," 2015.

[140] K. Fouad, "Conception d'un amplificateur faible bruit (LNA) a base du transistor GaN HEMT sous ADS (Advanced Design System)," thèse de doctorat, Faculté des Sciences et Technologies, 2021.

[141] Z. A. KHEZZAR, "Traitement des signaux GNSS," thèse doctorat, Université de Batna 2, 2021.
[142] C. J. Hegarty, D. Bobyn, J. Grabowski, and A. Van Dierendonck, "An overview of the effects of out-of-band interference on GNSS receivers," NAVIGATION: Journal of the Institute of Navigation, vol. 67, pp. 143-161, 2020.
[143] A. Cutivet, "Caractérisation et modélisation de dispositifs GaN pour la conception de circuits de puissance hyperfréquence," Lille 1, 2015.
[144] M. Werquin, "Études théoriques et expérimentales de transistors HEMT's de la filière nitrure de gallium pour les applications de puissance hyperfréquences," Lille 1, 2005.
[145] P. Sakalas, A. Šimukovič, S. Piotrowicz, O. Jardel, S. Delage, A. Mukherjee, et al., "Compact modelling of InAlN/GaN HEMT for low noise applications," Semiconductor Science and Technology, vol. 29, p. 095014, 2014.
[146] M. Chen, W. Sutton, I. Smorchkova, B. Heying, W.-B. Luo, V. Gambin, et al., "A 1–25 GHz GaN HEMT MMIC low-noise amplifier," IEEE Microwave and Wireless Components Letters, vol. 20, pp. 563-565, 2010.
[147] K. W. Kobayashi, "An 8-W 250-MHz to 3-GHz decade-bandwidth low-noise GaN MMIC feedback amplifier with>+ 51-dBm OIP3," IEEE Journal of Solid-State Circuits, vol. 47, pp. 2316-2326, 2012.
[148] X. Yan, J. Zhang, H. Luo, S.-P. Gao, and Y. Guo, "A Compact 1.0–12.5-GHz LNA MMIC With 1.5-dB NF Based on Multiple Resistive Feedback in 0.15-μm GaAs pHEMT Technology," IEEE Transactions on Circuits and Systems I: Regular Papers, vol. 70, pp. 1450-1462, 2023.
[149] M. A. Addou, J. Lintignat, R. Gomez-Garcia, B. Barelaud, F. Torres, S. Bila, et al., "Silicon-integrated signal-interference dual-band bandpass filter for GNSS application," in 2017 IEEE MTT-S International Microwave Symposium (IMS), 2017, pp. 1675-1678.
[150] C. Barth, Subsampling GPS receiver front-end: Stanford University, 2011.

Publications and communications

Publication and Communications

- **International Publication**

1. **Noual Amina, Messai Zitouni, Touati Zine-eddine, Saidani Okba, Abderrahim Yousfi. "**Numerical Study of T-GATE AlGaN/AlInGaN/GaN MOSHEMT with Single and Double Barrier for THz Frequency Applications". East European Journal of Physics (EEJP), Scopus index, 12-2023.

- **National and International Communications**

1. **Noual Amina, Messai Zitouni, Touati Zine-eddine.** "Influence of High-k Dielectric Materials on AlGaN/AlInGaN/GaN MOS-HEMT Grown on β-Ga_2O_3 Substrate: Numerical Study". IEEE 2nd International Conference on Electrical Engineering and Automatic Control (IEEE ICEEAC 2024) May 12-14, 2024.
2. **Noual Amina, Messai Zitouni. "**Numerical Study of the Electrical Characteristics of a New AlGaN/GaN MOSHEMT Design on 4H-SiC Substrate with Quaternary AlInGaN Spacer Layer". National conference on Mechanic and Materials NCMM'2023, 6-7 December 2023.
3. **Noual Amina, Messai Zitouni, Touati Zine-eddine, Saidani Okba, Abderrahim Yousfi, Brahimi Abdelhalime. "**High-Temperature Dependent of III-Nitride Based-MOSHEMT Grown on UWBG-β-Ga_2O_3 Substrate". The 1st International Conference on Electronics Engineering, Technology of Telecommunications Advanced applications, 2ETA'23, 25-26 October 2023.
4. **Noual Amina, Messai Zitouni, Touati Zine-eddine. "**Effect of Aluminum Content on the Electrical Characteristics of Nanometric Recessed Gate AlGaN/AlN/GaN MOSHEMT using β-Ga_2O_3 as Dielectric Layer". The 3rd International conference on Electrical Engineering CEE2023, Mai 09-10, 2023.
5. **Noual Amina, Messai Zitouni, Touati Zine-eddine. "**RF Performance Analysis of Conventional and Gate Recessed AlGaN/GaN MOSHEMT using β-Ga_2O_3 as Dielectric Layer". IEEE 1st International Conference on Advances in Electronics, Control and Communication Systems, ICAECCS'23, March 6-7th, 2023.
6. **Noual Amina, Messai Zitouni, Touati Zine-eddine. "**Optimization of the Gate Length and the Gate Position of InAlGaN/GaN MOSHEMT using β-Oxide-Gallium as Dielectric Layer". National Seminar of Physics, Chemistry and Their Applications, NSPCA'23 Online Conference, March 6-7th, 2023.

7. **Noual Amina, Messai Zitouni, Touati Zine-eddine. "**Comparative Analysis of Characteristics of AlGaN/InAlGaN/GaN MOSHEMT with a Single and Double Barrier". The 1st International Conference on Materials and Energies, IC-ME '21 Online Conference, September 13-14, 2021.
8. **Noual Amina, Messai Zitouni, Touati Zine-eddine.** "DC and RF Study of AlGaN/InAlGaN/GaN MOSHEMT with a Single and Double Barrier". 2nd National Conference in Electrical Engineering, CEE '21, April 6th, 2021.